EVAPORATION AND CONDENSATION IN ANNULAR VERTICAL UPWARD FLOW OF WATER–STEAM

by

Wing Hon George Terence Chan, B.Sc.

May, 1990

A Thesis Submitted for the Degree of Doctor of Philosophy
in the Faculty of Engineering of the University of London
and for the Diploma of the Imperial College

Department of Chemical Engineering and Chemical Technology
Imperial College
London, SW7

ABSTRACT

The principal objective of this research, namely the measurement of heat transfer coefficients for evaporation and condensation in equilibrium annular vertical upward flow under identical hydrodynamic condition, was achieved. The results showed that the heat transfer coefficients in evaporation are significantly higher than in condensation. This called into question the conventional interpretation of boiling heat transfer in the high quality region as due to pure convection. The Mesler (1977) hypothesis on the effect of non-wall (secondary) nucleation on heat transfer could offer an explanation.

The experimental study was further extended to cover condensation in hydrodynamically non-equilibrium annular flow. The results showed that non-equilibrium has no significant effect on the heat transfer process for the conditions investigated, though effects may occur under more severely non-equilibrium conditions.

Film thickness measurements were also made in equilibrium and non-equilibrium annular flow using needle contact probe and flush-mounted concentric probes. The results indicated that hydrodynamic equilibrium could have been reached for the developing length given in the experiments. The combined use of needle and concentric probes proved to be a good technique for measurements of dynamic liquid film thickness in systems where specific conductance cannot be measured. A general numerical method was also developed to simulate the probe response to film thickness variation and was in good agreement with measurements on a model system.

An attempt was made to develop a complete evaporative heat transfer model for annular flow that takes account of convective heat transfer and nucleate boiling (due to wall nucleation). The model indicated that the bubble burst size should be much larger than the liquid film thickness for good comparison with heat transfer data. The high speed cine films of Hewitt et al (1963) were reanalysed and shown to be consistent with this finding. The predictions of this model for some limited amount of data from the literature are encouraging and represent, to the author's knowledge, the first complete closure of this prediction problem. However, in the light of the experimental results obtained here, further development of the model will probably be necessary in future to take account of secondary nucleation.

Acknowledgements

I would like to express my gratitude to Prof. G.F. Hewitt for his guidance in my work.

Thanks are also due to SERC and AERE Harwell for their financial support.

I would like to thank Mr. P.C. Lovegrove and his colleagues for their help in designing and building the experimental rig, and Mr. K. Bull (now retired from Harwell) for his general assistance in the experiments.

I am grateful to Mr. S. Jayanti for his assistance in calculations using the Harwell Flow 3D computer code, and Mr. D. de Silva for his participation in the work on calibration of the concentric probe and numerical simulation of the probe response.

I also want to thank Dr. H.G.D. Goyder and Dr. C.E. Teh for making available their computing facilities.

I am indebted to my family for their encouragement.

Dedicated to *Mooi Cheng*

Table of Contents

CHAPTER 1 INTRODUCTION 1
1.1 Heat transfer in annular flow 2
1.2 Objectives of present work 4

CHAPTER 2 LITERATURE SURVEY 5
2.1 Heat transfer modelling in evaporating flow 5
2.1.1 Empirical approach 6
2.1.1.1 Forced convective evaporation 6
2.1.1.2 Nucleate boiling 12
2.1.1.3 Combined forced convective and nucleate boiling ... 14
2.1.2 Semi-theoretical methods for annular flow 22
2.1.3 Conclusion 26
2.2 Theories on nucleation cycle 27
2.2.1 Incipience of nucleation in heterogeneous system 27
2.2.1.1 Gas or vapour trapping 27
2.2.1.2 Bubble at equilibrium 28
2.2.1.3 Criteria for incipience of nucleation in forced flow .. 29
2.2.2 Bubble growth without translation 31
2.2.2.1 Spherical bubble growth in an infinite superheated liquid 31
2.2.2.1.1 Inertia-limited bubble growth : Rayleigh's model 32
2.2.2.1.2 Diffusion-controlled bubble growth in uniformly superheated liquid 35
2.2.2.1.3 Numerical solution for bubble growth 37
2.2.2.2 Bubble growth at a solid surface 38
2.2.2.2.1 Spherical bubble growth adjacent to a solid surface 38
2.2.2.2.2 Effect of local heat transfer processes on growth of a spherical bubble near a heated surface 41
2.2.2.2.3 Hemispherical bubble growth on heated surface 43
2.2.2.2.4 Comparison between experimental data and theories 46

2.2.3 Bubble departure size in forced flow 46
2.2.4 Bubble growth with translation in flowing liquid film 50

CHAPTER 3 A MODEL OF EVAPORATIVE HEAT TRANSFER IN SINGLE-COMPONENT ANNULAR FLOW 52
3.1 The components of the heat flux 55
3.2 Convective Heat Transfer 56
3.2.1 Calculation of film thickness and shear stress distribution knowing film rate 58
3.2.2 Calculation of liquid film flowrate 63
3.3 Nucleate Boiling Heat Transfer 65
3.4 Analysis of heat transfer data using assumptions of hydrodynamic equilibrium 72
3.5 Predictions of the model assuming a constant bubble burst size 76
3.6 Consideration of non-equilibrium effects in annular flow 77
3.7 Conclusion 79

CHAPTER 4 EXPERIMENTS ON ANNULAR FLOW 81
4.1 Experiments on equilibrium annular flow 82
4.1.1 Description of experimental rig 82
4.1.2 Description of test section 83
4.1.3 Experimental design considerations 85
4.1.4 Instrumentation 87
4.1.5 Operation 89
4.1.6 Data analysis 91
4.1.6.1 Calculation of heat transfer coefficient 91
4.1.6.2 Calculation of frictional pressure drop 92
4.1.7 Results and discussion 93
4.1.7.1 Heat transfer results 93
4.1.7.2 Pressure drop results 97
4.2 Experiments on non-equilibrium annular up-flow 99
4.2.1 Modifications of experimental rig 100
4.2.2 Operation 101
4.2.3 Results and discussion 102
4.2.3.1 Heat transfer results 102

4.2.3.2 Pressure drop results 102
4.3 Conclusions 103

CHAPTER 5 FILM THICKNESS MEASUREMENTS IN ANNULAR FLOW 104
5.1 Needle contact probe 104
5.2 Flush-mounted concentric probe 105
5.3 Flush-mounted double concentric probe 107
5.4 Installation and instrumentation 108
5.5 Data processing 110
5.6 Results and discussion 113
5.6.1 Needle contact probe measurements 113
5.6.2 Conductance probe results 113
5.7 Conclusions 118

CHAPTER 6 CONCLUSIONS AND RECOMMENDATIONS FOR FURTHER WORK 120
6.1 Heat transfer in equilibrium annular flow 120
6.2 Heat transfer and wave characteristics in developing annular flow 121
6.3 Prediction of flow boiling 122

APPENDIX A CALIBRATION OF ANNULUS THERMOCOUPLES 123
A.1 Absolute mode 123
A.2 Differential mode 124

APPENDIX B CALIBRATION OF PRESSURE SENSORS 126
B.1 Calibration of differential pressure cells 126
B.2 Calibration of pressure transducers 126

APPENDIX C CALIBRATION OF FLOWMETERS 128

APPENDIX D SINGLE-PHASE HEAT BALANCE 130
D.1 Objectives 130
D.2 Conditions of tests 130
D.3 Results and discussions 131

APPENDIX E EFFICIENCY TEST ON WATER-STEAM SEPARATOR USING WATER AND AIR 134

APPENDIX F CALIBRATION OF FLUSH-MOUNTED CONCENTRIC PROBES 136

F.1 Calibration equipment and procedure 136

F.2 Calibration results and predictions by numerical method 138

APPENDIX G ASSESSMENT OF THE EFFECT OF INCONDENSIBLES ON CONDENSATION HEAT TRANSFER UNDER NORMAL OPERATION 141

G.1 Analysis 142

G.2 Calculation 145

APPENDIX H FORMATION OF BUBBLES IN A LIQUID FILM : ANALYSIS OF EXPERIMENTS OF HEWITT ET AL (1963) 147

H.1 Theory 148

H.2 Results and discussion 150

REFERENCES 152

NOMENCLATURE 161

CHAPTER 1

INTRODUCTION

Heat transfer in two-phase flow is a common process that occurs in a diversity of industrial equipment such as evaporators and condensers. A good understanding of the mechanisms in this process is obviously desirable. To achieve this, one has to consider many important governing factors and their complex interactions in two-phase flow. A considerable simplification of the treatment of such system is achieved by classification of the type of interfacial distribution, namely the "flow patterns" or "flow regimes".

Visual studies of evaporative two-phase flow in circular tubes (Hsu and Graham 1963, Dickson and Gouse 1966) have identified various major flow patterns, namely bubbly, slug, annular and drop flow. For vertical tubes of large inside diameter, churn flow can be observed in the transition from slug to annular flow. Whether a certain flow pattern will prevail depends on many factors such as : the mass flow rates of each of the phases, their physical properties which in turn are functions of temperature and pressure, the geometry and orientation of the channel, etc.

Of particular interest in the present research project is the annular pattern in single component saturated vertical upward flow. This is the dominant flow pattern in evaporation and condensation for qualities (vapour mass flow fraction) greater than a few percent. To put the annular flow pattern in perspective in the broad context of two-phase flow, we can consider a vertical tube subject to a moderate input of uniform heat flux with subcooled liquid fed from the bottom (see Fig. 1.1).

Starting from the bottom, the enthalpy of the single-phase liquid is increasing. At a certain point, the first bubble will evolve from the tube wall when the required local superheat temperature is reached. For a certain distance from this point, some of the bubbles generated at the wall

Figure 1-1 Flow patterns in a vertical evaporator tube

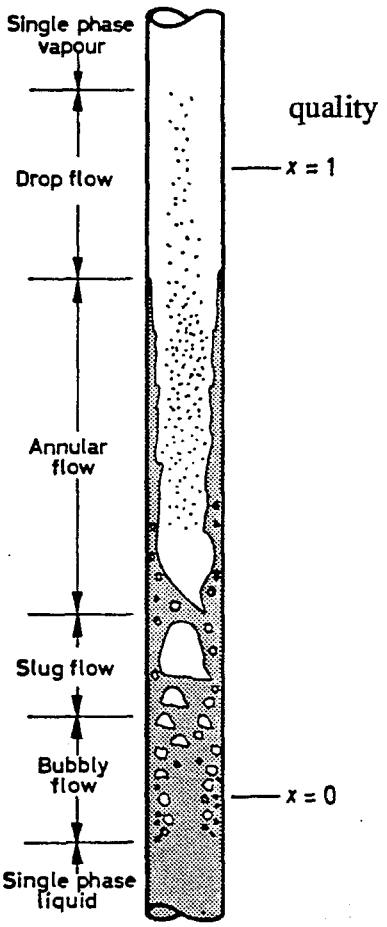

may drift into the still-subcooled liquid in the central region of the tube and collapse. As the saturation condition is approached and passed, fully developed bubble flow is established.

Due to the difference in density between the liquid and vapour phase, the increase of enthalpy continuously accelerates the flow. The net increase of number of bubbles leads to bubble coalescence, increase of void fraction, then the transition to slug flow, followed possibly by churn flow for a large diameter tube.

Ultimately, the prevailing pattern is annular flow, which basically consists of a liquid film on the tube wall and a vapour core with entrained liquid droplets. The liquid film can dry out (as shown in figure 1-1) if the depletion of the liquid film due to evaporation and droplet entrainment outbalances the replenishment of the liquid film by droplet deposition. Beyond dryout, the wall temperature rises and the droplets gradually evaporate until the flow is completely converted to vapour.

Annular flow occurs in many types of heat transfer equipment, and prevails over a considerable length of the flow channel. The liquid film has a complex interfacial structure with interfacial waves which have been classified into two main types, namely ripple waves and disturbance waves. In most flow situations of engineering interest, disturbance waves are dominant. These waves move with different frequencies and velocities over a continuous layer of liquid substrate on the tube wall.

1.1 Heat transfer in annular flow

Heat transfer in annular flow is normally considered as being governed by two mechanisms :

(a) Forced convective heat transfer : Here, heat is conducted and convected between the channel wall and the interface and the heat transferred causes (evaporation) or results from (condensation) a phase change at the interface. For condensation, this is the dominant mechanism

(b) Nucleate boiling : Here, bubbles are formed at the wall at nucleation sites and the creation and transport of these bubbles causes an enhancement of the heat transfer.

The forced convective mechanism is dominant at high velocity and low heat flux whereas the nucleate boiling mechanism is dominant at low velocity and high heat flux. Over most of the practical range, both mechanisms play a significant role in evaporating flow.

The usual route to prediction of the forced convective region is via application of single-phase-flow-based turbulent diffusivity theories. However, these often overpredict the heat transfer coefficient, possibly due to turbulence damping at the interface. Thus, empirical correlations are normally used for design purposes. Prediction of nucleate boiling is formidably difficult and the normal procedure is to use empirical correlations. The heat transfer coefficients are very strongly affected by the number and size distribution of the nucleation sites at the wall. For pool boiling, some progress has been made (Mikic and Rohsenow, 1969) in taking account of the surface characteristics. However, for forced convective boiling, no complete theory exists spanning both regimes.

A major new controversy about forced convective boiling was initiated by Mesler (1977). He postulated that heat transfer in this regime was affected by secondary nucleation, i.e. nucleation on bubbles entrained by wave action etc.. Aounallah et al (1983) report measurements in fully equilibrium annular flow which attempted to refute this hypothesis by showing that the heat transfer coefficient was constant at low heat fluxes. However, it is not clear that the heat transfer would be dependent on the heat flux if secondary rather than wall nucleation was dominant. The Mesler mechanism needed further examination and this was the main objective of the work described in the present thesis.

Another area requiring investigation is the reason why the convective heat transfer theories tend to overpredict the data. This could possibly reflect essential differences between the effective frequency of turbulence-related disturbances between single-phase flow (on which the film heat transfer models are based) and annular film flow. In the latter case, there is some evidence (Martin and Azzopardi, 1985), that there is a link between initial disturbance wave frequency in annular flow and turbulence burst frequency in the equivalent single-phase flow case. For air-water flows, it has been shown that the disturbance wave frequency decreases with distance from the injector, requiring considerable distance to reach equilibrium (Hall Taylor et al 1963). Could the reduction of disturbance

wave frequency give (in effect) a reduction in turbulence disturbance frequency and cause the observed discrepancy ? Again, investigation of this possibility was an objective of the present work.

1.2 Objectives of present work

The main objectives of the present work were as follows :

(1) To assess the available information on flow boiling and to classify it. The selective literature review is given in Chapter 2

(2) To provide a direct check of the Mesler hypothesis. Here, experiments were carried out under exactly the same condition (namely equilibrium annular flow) for both condensation and evaporation. If secondary nucleation is important in the forced convective regime, then this could result in higher heat transfer coefficients for evaporation than for condensation. Implementing the experiments involved a major reconstruction of the Harwell low pressure boiling facility and the development of a novel fluid heated and cooled test section. The results of this work are described in Chapter 4.

(3) To investigate heat transfer in non-equilibrium flow with the aim of evaluating the influence of disturbance wave frequency on heat transfer. Here, it was important to measure both the heat transfer characteristics (in this case with condensation) and the interfacial wave characteristics. The heat transfer measurements are reported in Chapter 4 and the interfacial wave characteristics measurement (obtained using conductance methods) are described in Chapter 5.

(4) To develop a complete theory for flow boiling, covering both forced convective evaporation and nucleate boiling. This work was done in parallel with the experimental work (objective 2 and 3). The route followed was to specify the distribution of potential nucleation sites, to determine which were active and to determine the latent heat released at each site. This latent heat was added to the heat transfer by forced convection to give the total heat flux. This work is described in Chapter 3.

CHAPTER 2

LITERATURE SURVEY

In this present chapter, the objective will be to survey the published information on evaporative heat transfer in sufficient detail to provide a context for the presentation of the author's own analytical and experimental work. Section 2.1 describes the empirical and semi-theoretical approaches which have been followed to provide prediction methods for evaporative heat transfer. Section 2.2 focuses more specifically on theories for the bubble nucleation cycle, including incipience of nucleation, bubble growth and bubble departure.

2.1 Heat transfer modelling in evaporating flow

Though only single-component evaporating flow is to be discussed here, the number of variables that need consideration is more than double that in heat transfer in single-phase flow. Experimental visual studies of diabatic single-component two-phase flow (e.g. steam and water) have revealed that the flow patterns are qualitatively similar to those observed in adiabatic two-phase two-component flow (e.g air and water). As a result, many findings concerning hydrodynamics in the adiabatic case have been applied to evaporating flow. However, the fact that heat transfer in evaporating flow gives rise to a change in the quality (mass flow fraction of the vapour phase) along the channel means that the heat flux affects the hydrodynamic development of the flow. "Fully developed conditions" as defined in single-phase flow have no counterpart in evaporating flow since the flow conditions are continually changing.

In any heat transfer analysis, the primary concern is the estimation of the heat transfer coefficient, which is conventionally defined as the ratio of the difference between the wall temperature and a reference temperature to the wall heat flux, i.e. $\dot{q}_w/(T_w - T_{ref})$. Local values are preferred for accurate design calculations. For saturated evaporating flow, $T_{ref} = T_{sat}$. In order to

provide consistent data for testing theories, any experimental study of two-phase heat transfer must involve direct or indirect measurement of the variables in the above definition.

Experimental results have shown that annular flow prevails over a considerable length of the heated flow channel over the quality range from a few percent up to dry-out. Consequently, a lot of correlations, either empirical or semi-empirical, are specially suited to this particular flow pattern.

In general terms, the heat transfer mechanisms in annular evaporating flow are classified as convective (where heat is transferred from the wall through the liquid leading to evaporation at the liquid-vapour interface) or nucleate boiling (where bubbles are formed at nucleation centres on the channel surface). However, given a heat transfer condition, there is no clear cut criterion to determine the dominance of either mechanism. In fact, under some conditions, they both can have significant contributions to heat transfer. The conventional interpretation of experimental results to-date is that, for a given heat flux, nucleate boiling is important in the low quality region whereas the convective mechanism becomes dominant with increasing quality.

In modelling heat transfer in evaporating flow, whether by an empirical or by a theoretical approach, the resulting correlation should reflect the mechanism(s) involved.

A vast amount of work has been done on two-phase heat transfer in channel flows and a very detailed review would fill a volume many times the size of this thesis. What is done here, therefore, is to present a structured classification (with selected examples) of the approaches which have been followed. The review starts with a discussion of empirical correlations (forced convection, nucleate boiling and combined convection and nucleate boiling) and then goes on to discuss semi-theoretical methods for estimating forced convective situations.

2.1.1 Empirical approach

2.1.1.1 Forced convective evaporation

It has been the usual practice to define the forced convective region as one in which the heat transfer coefficient at a given quality is essentially

independent of heat flux. The heat transfer coefficient in this region increases with both quality and mass flux. The interpretation of this increase has generally been that the liquid film thins due to evaporation and increased vapour shear. However, it should be remembered that the alternative explanation due to Mesler (1977) ascribes the increase to the increased effect of secondary nucleation. Correlations for forced convective evaporation fall into two main categories, namely those based on the Martinelli parameter X_{tt} and those based on other correlation approaches.

Correlations based on Martinelli parameter X_{tt}

The first correlation of this type was due to Dengler and Addoms (1956). Following the success of Lockhart and Martinelli (1949) in correlating their adiabatic two-phase flow data for pressure drop and void fraction by using the so-called Martinelli parameter, X_{tt}, Dengler and Addoms (1956) employed the same parameter in correlating their heat transfer data. They obtained good correlation for those data which they regarded as predominantly due to convective heat transfer. Their result is

$$\frac{\alpha_{tp}}{\alpha_{Lo}} = 3.5\left(\frac{1}{X_{tt}}\right)^{0.5} \qquad (2.1.1.1\text{-}1)$$

where α_{tp} is the two-phase heat transfer coefficient defined as

$$\alpha_{tp} = \frac{\dot{q}_w}{(T_w - T_{sat})} \qquad (2.1.1.1\text{-}2)$$

where T_{sat} is the saturation temperature, $\dot{q}_w$ the wall heat flux and T_w the wall temperature.

α_{Lo} is calculated from the well known Dittus-Boelter equation for the total flow with liquid properties.

X_{tt} is Martinelli parameter defined as

$$X_{tt} = \sqrt{\left(\frac{dp_F}{dz}\right)_L \Big/ \left(\frac{dp_F}{dz}\right)_G} \qquad (2.1.1.1\text{-}3)$$

where $(dp_F/dz)_L$ and $(dp_F/dz)_G$ are the frictional pressure gradients for the liquid and vapour phases flowing alone in the channel.

Assuming a Blasius type friction relation with the exponent of the Reynolds number equal to 0.2 for both the vapour and liquid phase, equation 2.1.1.1-3 leads to

$$X_{tt} = \left(\frac{1-x}{x}\right)^{0.9}\left(\frac{\rho_G}{\rho_L}\right)^{0.5}\left(\frac{\eta_L}{\eta_G}\right)^{0.1} \qquad (2.1.1.1\text{-}4)$$

where x is the quality (flow mass fraction of the vapour phase).

Subsequently, other experimentalists also used X_{tt} to correlate their own two-phase convective data in a format similar to equation 2.1.1.1-1 as follows :

$$\frac{\alpha_{tp}}{\alpha_{Lo}}\left(\text{or}\frac{\alpha_{tp}}{\alpha_L}\right) = a\left(\frac{1}{X_{tt}}\right)^b \qquad (2.1.1.1\text{-}5)$$

where α_L is the heat transfer coefficient for the liquid phase flowing alone in the channel.

Chen (1963) also correlated the convective component, α_{con} , of his combined correlation (see below) in terms of X_{tt}. He assumed the form of α_{con} to be of the Dittus-Boelter type, i.e.

$$\alpha_{con} = 0.023 Re_{tp}^{0.8} Pr_{tp}^{0.4} \frac{\lambda_{tp}}{D} \qquad (2.1.1.1\text{-}6)$$

Chen argued that since heat is transferred from the wall to the liquid film, λ_L can replace λ_{tp}. Moreover, for ordinary fluids, the Prandtl numbers of the liquid and the vapour are normally of the same magnitude. Therefore, Pr_L can substitute Pr_{tp}. By defining a parameter F as

$$F = \left[\frac{Re_{tp}}{Re_L}\right]^{0.8} \qquad (2.1.1.1\text{-}7)$$

where Re_L is based on the liquid fraction, he showed that

$$\alpha_{con} = \alpha_L F \qquad (2.1.1.1\text{-}8)$$

F is called the enhancement factor. Being a function of Reynolds number, it was also correlated by Chen as a function of X_{tt} . It should be noted that for single-phase liquid flow, F must equal unity.

Whalley (1988) has given an explanation for X_n being a good correlating factor. For annular flow, he considered the case of the liquid fraction flowing as a liquid film on the channel wall and the case of the same liquid fraction flowing as single phase in the same channel. It is assumed that only convective heat transfer takes place in the liquid film. The hydraulic diameter for the liquid film is 4 times the ratio of film cross sectional area to its "wetted perimeter", i.e. $D_h = 4A/S = (4\pi D\,\delta)/(\pi D) = 4\delta$. Based on D_h, the Reynolds number for the liquid film turned out to be the same as in the single-phase case. As the resistance to heat transfer lies in the liquid film on the wall, the appropriate physical properties are those of the liquid. Therefore, both cases should have the same Nusselt number, i.e $Nu_{tp} = Nu_L$ and as a result

$$\frac{\alpha_{tp}}{\alpha_L} = \frac{D}{4\delta} \qquad (2.1.1.1\text{-}9)$$

Since the liquid film thickness is small compared with the tube diameter. The liquid void fraction can be expressed as

$$1 - \varepsilon_G = \frac{4\delta}{D} \qquad (2.1.1.1\text{-}10)$$

Therefore

$$\frac{\alpha_{tp}}{\alpha_L} = \frac{1}{1 - \varepsilon_G} \qquad (2.1.1.1\text{-}11)$$

It can be seen that the success of Lockhart and Martinelli (1949) in correlating ε_G as a function of X_n justified the use of X_n to correlate two-phase convective heat transfer.

Chen (1966) made use of Reynolds' momentum and heat transfer analogy to produce a theoretical basis for the enhancement factor, F which is defined in equation 2.1.1.1.7 . For the thin liquid film in saturated annular flow, the one-dimensional momentum and energy equations are sufficient to describe the transfer process :

$$\tau = \rho_L(\upsilon_L + \varepsilon_m)\frac{du}{dy} \qquad (2.1.1.1\text{-}12)$$

$$\dot{q} = -\rho_L C_{pL}(\kappa_L + \varepsilon_h)\frac{dT}{dy} \qquad (2.1.1.1\text{-}13)$$

where ε_m and ε_h are the eddy diffusivities of momentum and heat, υ_L is the kinematic viscosity, κ_L is the thermal diffusivity and y is the distance from the wall.

Chen chose to define the two-phase Reynolds number with liquid properties and the average velocity which is unknown.

$$Re_{tp} = \frac{\rho_L u_{tp} D}{\eta_L} \qquad (2.1.1.1\text{-}14)$$

Following the Reynolds' analogy which assumes the same non-dimensional profile for shear stress and heat flux in the liquid film, i.e.

$$\frac{\dot{q}}{\dot{q}_w} = \frac{\tau}{\tau_w} = \mathrm{fn}(y) \qquad (2.1.1.1\text{-}15)$$

and further assuming parity between the effective viscosity and the effective thermal conductivity, Chen combined equations 2.1.1.1-12 and 2.1.1.1-13 to give

$$\frac{\dot{q}_w}{C_{pL}} \mathrm{d}u = -\tau_w \mathrm{d}T \qquad (2.1.1.1\text{-}16)$$

For a turbulent liquid film, Chen considered it reasonable to assume that, at the value of y where $u = u_{tp}$, then $T = T_{sat}$. Therefore, integration of equation 2.1.1.1-16 yields

$$\frac{\dot{q}_w}{C_{pL}} u_{tp} = \tau_w (T_w - T_{sat}) \qquad (2.1.1.1\text{-}17)$$

Rearranging the equation 2.1.1.1-17 shows that

$$\alpha_{tp} = \frac{\dot{q}_w}{T_w - T_{sat}} = \frac{\tau_w C_{pL}}{u_{tp}} \qquad (2.1.1.1\text{-}18)$$

For the liquid fraction flowing alone in the channel, a similar argument yields

$$\alpha_L = \frac{\tau_L C_{pL}}{u_L} \qquad (2.1.1.1\text{-}19)$$

From equations 2.1.1.1-7 , 2.1.1.1-8 ,2.1.1.1-18 and 2.1.1.1-19 , it can be shown that

$$F = \frac{\tau_w}{\tau_L}\frac{u_L}{u_{tp}} \qquad (2.1.1.1\text{-}20)$$

$$= \frac{\tau_w}{\tau_L}\frac{Re_L}{Re_{tp}}$$

$$= \left(\frac{\tau_w}{\tau_L}\right)^{\left(\frac{1}{2.25}\right)}$$

By definition $\tau_w/\tau_L = (dp_F/dz)_{tp} \;/\; (dp_F/dz)_L$, which Lockhart and Martinelli (1949) have defined as

$$\left(\frac{dp_F}{dz}\right)_{tp} \;/\; \left(\frac{dp_F}{dz}\right)_L = \phi_{Ln}^2 \qquad (2.1.1.1\text{-}21)$$

where ϕ_{Ln} has already been correlated as a function of X_n.

From equations 2.1.1.1-20 and 2.1.1.1-21 , Chen showed that

$$F = \phi_{Ln}^{0.89} = \text{fn}(X_n) \qquad (2.1.1.1\text{-}22)$$

Chen (1966) then confirmed again that F is indeed a function of X_n as he has demonstrated empirically in his previous paper (1963).

Chen's analysis is more rigorous than Whalley's simple argument. His result not only justifies previous empirical approaches but also provides an alternative and more direct way to calculate heat transfer if pressure drop data is available for a system in question.

Strictly speaking, the Reynolds analogy employed by Chen is valid for a Prandtl number of unity. Bennett and Chen (1980) have attempted more elaborate analysis in considering the ratio of total momentum diffusivity to total thermal diffusivity for the case of the liquid fraction flowing alone as single-phase. They argued that since nucleation at the wall continues to break up the laminar sublayer, the ratio of the total momentum diffusivity to the total thermal diffusivity for the two-phase can be assumed equal to a two-phase turbulent Prandtl number. They derived several Prandtl number dependent expressions for the F factor. The numerical value of these expressions is similar for a Prandtl ranging from 1 to 12. One of these expressions is as follows :

$$F = Pr_L^{0.296}\left[\left(\frac{dp_F}{dz}\right)_{tp} \;/\; \left(\frac{dp_F}{dz}\right)_L\right]^{0.444} \qquad (2.1.1.1\text{-}23)$$

Equation 2.1.1.1-23 reduces to equation 2.1.2-22 for Prandtl number equal to unity.

Other correlations for forced convective evaporation

A correlation which is widely used in the refrigeration industry is that of Shah (1976). The general form of this correlation (including simultaneous nucleate boiling) will be introduced later. The forced convective component is correlated as follows:

$$\frac{\alpha_{tp}}{\alpha_L} = \frac{1.8}{Co^{0.8}} \qquad (2.1.1.1\text{-}24)$$

where

$$Co = \left(\frac{1-x}{x}\right)^{0.8}\left(\frac{\rho_G}{\rho_L}\right)^{0.5} \qquad (2.1.1.1\text{-}25)$$

Another generic line of development of boiling correlations is that of Winterton and coworkers at the University of Birmingham. We shall discuss their combined nucleate boiling / forced convective evaporation correlation in section 2.1.1.3 below. Here, we state the pure forced convective correlation used by Liu and Winterton (1988). This is in the form :

$$\frac{\alpha_{tp}}{\alpha_L} = \left[1 + xPr_L\left(\frac{\rho_L}{\rho_G} - 1\right)\right]^{0.35} \qquad (2.1.1.1\text{-}26)$$

2.1.1.2 Nucleate boiling

When the evaporation process is controlled by nucleate boiling, alternative correlations must be used. Two types can be identified, namely those based on pool boiling and those based directly on forced convective nucleate boiling data. In the first category, one may distinguish between correlations based directly on physical properties and ones based on reduced pressure.

A vast number of correlations exist in the literature and, here, only a few examples will be given which are useful in what follows. Before doing this, however, an important general point should be made. Experimental work has clearly demonstrated that nucleate boiling heat transfer is strongly dependent on solid surface properties which dictate the number of active nucleation sites under any given conditions (Berenson, 1962).

Indeed, the modelling methodology reported in Chapter 3 is arrived at by taking proper account of this fact. However, many of the most widely used correlations do not include any allowance for surface effects.

Pool boiling correlations based on physical properties

A wide variety of correlations have been developed based on fluid physical properties, often combined in dimensionless group. Useful reviews of such correlations are given by Collier (1983) and Cooper (1983). Here, we cite as examples the correlations of Forster and Zuber (1955) and Stephan and Abdelasalam (1980). The Forster and Zuber correlation is used as a component of the widely used Chen (1963) combined forced convective / nucleate boiling correlation. The Forster-Zuber correlation for the heat transfer coefficient, α_{np} , in nucleate pool boiling is as follows :

$$\alpha_{np} = 0.00122\left[\frac{\lambda_L^{0.79} C_{pL}^{0.45} \rho_L^{0.49}}{\sigma^{0.5} \eta_L^{0.29} h_{LG}^{0.24} \rho_G^{0.24}}\right] \Delta T_{sat}^{0.24} \Delta P_{sat}^{0.75} \qquad (2.1.1.2\text{-}1)$$

where $\Delta T_{sat} = (T_w - T_{sat})$ and Δp_{sat} is the saturation pressure difference corresponding to ΔT_{sat}.

Stephan and Abdelasalam (1980) have established different expressions of α_{np} for different fluids. They also constructed a general expression applicable to all fluids but with less accuracy in comparison with the specific ones. The expression for all fluids in terms of dimensionless groups is valid in the pressure range of $0.0001 \le p/p_{cr} \le 0.97$ and is given as

$$\frac{\alpha_{np} d}{\lambda_L} = 0.23\left(\frac{\dot{q}_w d}{h_{LG} T_{sat}}\right)^{0.674}\left(\frac{\rho_G}{\rho_L}\right)^{0.297}\left(\frac{h_{LG} d^2}{\kappa_L^2}\right)^{0.371}\left(\frac{\rho_L}{\rho_L - \rho_G}\right)^{1.73}\left(\frac{\kappa_L^2 \rho_L}{\sigma d}\right)^{0.35} \qquad (2.1.1.2\text{-}2)$$

where d is the bubble break-off diameter, which can be calculated by the following expression

$$d = 0.0204 b \theta \qquad (2.1.1.2\text{-}3)$$

where θ is the contact angle and b is the Laplace constant defined as

$$b = \sqrt{\left(\frac{\sigma}{g(\rho_L - \rho_G)}\right)} \qquad (2.1.1.2\text{-}4)$$

Pool boiling correlations based on reduced pressure

It has been shown by Cooper (1983) that the physical property based correlations exemplified by equations 2.1.1.2-1 and 2.1.1.2-2 . can be expressed with surprising accuracy in terms only of reduced pressure. This led Cooper (1984) to propose the following general correlation :

$$\alpha_{np} = 55 p_r^{0.12-0.2\log_{10} R_p} (-\log_{10} p_r)^{-0.55} M^{-0.5} \dot{q}_w^{0.67} \qquad (2.1.1.2\text{-}5)$$

Here, R_p is the roughness of the surface specified according to Glättungstiefe DIN 4762 in terms of μm. If not known it is assumed to be unity.

Nucleate boiling correlations for channel flow

Rather than correlate nucleate boiling in channel flow in terms of pool boiling correlations (which are derived from quite different geometries and conditions), it may seem sensible to use direct correlation of data for which nucleate boiling is considered dominant. This approach was followed by Shah (1976) in developing his general boiling correlation which is described in section 2.1.1.3 below. Nucleate boiling dominated boiling coefficients were correlated by the relationship :

$$\frac{\alpha_{tp}}{\alpha_L} = 230 Bo^{0.5} \qquad (2.1.1.2\text{-}6)$$

where Bo is the " boiling number " defined as

$$Bo = \frac{\dot{q}_w}{\dot{m} h_{LG}} \qquad (2.1.1.2\text{-}7)$$

It is unlikely that such a simple correlation would have wide applicability. Again, no account is taken of surface effects.

2.1.1.3 Combined forced convective and nucleate boiling

In most practical situations, both nucleate boiling and forced convective heat transfer are important in determining the overall evaporation rate. Various methods have been developed for predicting heat transfer coefficients under these conditions and those reviewed here fall into three categories, namely simple correction factors, boiling number (Bo) based correlations and superposition models

Simple correction factors

The heat transfer coefficient calculated on the basis of pure forced convective or pure nucleate boiling can be corrected for the presence of the other mechanism by introducing a correction factor.

The correction factor used by Dengler and Addoms is a multiplier to the convective term. Their correlation accounting for both mechanisms then becomes

$$\frac{\alpha_{tp}}{\alpha_{Lo}} = 3.5\left(\frac{1}{X_{tt}}\right)^{0.5} F_{D\&A} \qquad (2.1.1.3\text{-}1)$$

where

$$F_{D\&A} = 0.67\left\{(\Delta T_{sat} - \Delta T_i)\left[\left(\frac{dp}{dT}\right)\frac{D}{\sigma}\right]_w\right\}^{0.1} \qquad (2.1.1.3\text{-}2)$$

$F_{D\&A}$ takes effect when it is calculated to be larger than unity, but is set to equal one otherwise. This factor implies that nucleate boiling is sustained when the wall superheat temperature, ΔT_{sat} , exceeds that required for incipience of nucleation, ΔT_i. dp/dT is the slope of the saturation pressure-temperature line. It together with the surface tension are evaluated at the wall temperature. Using their own data, Dengler and Addoms correlated the nucleation incipience temperature with the average two-phase velocity. The result is

$$\Delta T_i = 10 U_{tp}^{0.3} \qquad (2.1.1.3\text{-}3)$$

Guerieri and Talty (1956) also included a nucleate boiling multiplier in their correlation as follows :

$$\frac{\alpha_{tp}}{\alpha_L} = 3.4\left(\frac{1}{X_{tt}}\right)^{0.45} F_{G\&T} \qquad (2.1.1.3\text{-}4)$$

where

$$F_{G\&T} = 0.187\left(\frac{R_E}{\delta_{Lam}}\right)^{-5/9} \qquad (2.1.1.3\text{-}5)$$

R_E is the radius of an equilibrium bubble corresponding to the wall superheat and can be calculated from

$$R_E = \frac{2RT_{sat}^2\sigma}{p_{sat}h_{LG}\Delta T_{sat}} \qquad (2.1.1.3\text{-}6)$$

Guerieri and Talty chose the dimensionless thickness of the laminar sublayer to be

$$\delta^{+}_{Lam} = \frac{\delta_{Lam}(\tau_w/\rho_L)^{0.5}\rho_L}{\eta_L} = 10 \qquad (2.1.1.3\text{-}7)$$

If $F_{G\&T}$ is less than unity, it is set to equal one. This nucleate boiling factor implies that active nucleation sites are those with a dimension smaller than the thickness of the laminar sublayer and their number is inversely proportional to the turbulence intensity in the liquid.

Alternatively, one may correct the nucleate boiling coefficient by a factor to take account of forced convection effects. This approach has been followed by Stephan and Auracher (1981) who used a correction term, which takes into account the effect of forced convection, as a multiplier to the correlations developed by Stephan and Abdelsalam (1980) for natural convection (pool) nucleate boiling (see equation 2.1.1.2-2). The general form of their correlation is

$$\alpha_{tp} = \alpha_{nuc} F_{S\&A} \qquad (2.1.1.3\text{-}8)$$

Stephan and Auracher calculated $F_{S\&A}$ from a correlation proposed by Chawla (1967) as follows :

$$F_{S\&A} = 29 Re_L^{-0.3} Fr_L^{0.2} \qquad (2.1.1.3\text{-}9)$$

where

$$Re_L = \frac{\dot{m} D (1-x)}{\eta_L} \qquad (2.1.1.3\text{-}10)$$

$$Fr_L = \frac{[\dot{m}(1-x)]^2}{\rho_L^2 g D} \qquad (2.1.1.3\text{-}11)$$

Boiling number correlations

Schrock and Grossman (1959) defined the ratio of the mass flux normal to the wall due to evaporation to the total mass flux through the channel as the boiling number, i.e. $Bo = \dot{q}_w/(\dot{m} h_{LG})$. A number of correlations in the literature use this number.

Schrock and Grossman's own correlation was as follows :

$$\frac{\alpha_{tp}}{\alpha_{Lo}} = C\left[Bo + a\left(\frac{1}{X_{tt}}\right)^{b}\right]^{n} \qquad (2.1.1.3\text{-}12)$$

where C = 7.39 x 10^3 , a = 1.5 x 10^{-4} ; b = 0.67 and n = 1 . Some later experimentalists also adopted the general form of equation 2.1.1.3-12 to correlate their own data.

Shah (1976) has analysed heat transfer data for water and freons from 19 sources with 780 data points in total. He found that the Chen correlation over-predicts the data at low mass flow rates. He also pointed out that the Chen correlation should not be expected to predict well for horizontal tubes.

Shah then employed four dimensionless variables to develop a graphical correlation (referred to as Shah correlation hereafter). The parameters are as follows :

$$\Psi = \frac{\alpha_{tp}}{\alpha_L} \qquad (2.1.1.3\text{-}13)$$

$$Co = \left(\frac{1-x}{x}\right)^{0.8}\left(\frac{\rho_G}{\rho_L}\right)^{0.5} \qquad (2.1.1.3\text{-}14)$$

$$Bo = \frac{\dot{q}_w}{\dot{m} h_{LG}} \qquad (2.1.1.3\text{-}15)$$

$$Fr_L = \frac{\dot{m}^2}{\rho_{LG}^2 g D} \qquad (2.1.1.3\text{-}16)$$

The Froude number was introduced to take account of the data from horizontal tubes.

From those data with the characteristic nucleate boiling effect, his best fit line can be expressed as

$$\Psi = 230 Bo^{0.5} \qquad (2.1.1.3\text{-}17)$$

For the apparently convection dominant data, he established the following expression

$$\Psi = \frac{1.8}{Co^{0.8}} \qquad (2.1.1.3\text{-}18)$$

Equations 2.1.1.1-17 and 2.1.1.1-18 represent the asymptotes for the nucleation dominant region and the convection dominant region respectively. The Shah correlation presented in chart form is basically a plot of Ψ against Co with the Bo and Fr as parameters. The gaps between the asymptotes were bridged by lines smoothing out the data points. In a subsequent paper, Shah (1982) presented a set of equations to replace the chart. In addition, he suggested the use of larger value of the calculated heat transfer coefficients for nucleate and convective boiling.

Superposition correlations

In this class of correlations, the coefficients for forced convective heat transfer and nucleate boiling are derived separately and then are superposed using appropriate rules. The best known and most widely used correlation of this type is that of Chen (1963).

Chen (1963) found that those correlations available at his time worked well only with the data from which they were derived, but performed poorly in comparing with other data sets. Based on data from five different sources for liquids including water and organic fluids, he used the additive method to establish a correlation which was superior than others. The form of the correlation is :

$$\alpha_{tp} = \alpha_{con} + \alpha_{nuc} \qquad (2.1.1.3\text{-}19)$$

where α_{con} and α_{nuc} are the forced convective and nucleate boiling coefficients respectively.

Chen based the nucleate term on the nucleate pool boiling correlation introduced by Forster and Zuber (1955) (see equation 2.1.1.2-1). He argued that since the temperature profile in the liquid film of annular flow is much steeper than that in nucleate pool boiling, the mean superheat of the liquid in which the bubble grows can no longer be represented by the wall superheat. Therefore an effective superheat, ΔT_e , and the associated effective pressure difference, Δp_e , should replace the wall superheat and its related pressure difference term in the original Forster and Zuber correlation. As a result,

$$\alpha_{nuc} = 0.00122\left[\frac{\lambda_L^{0.79} C_{pL}^{0.45} \rho_L^{0.49}}{\sigma^{0.5} \eta_L^{0.29} h_{LG}^{0.24} \rho_G^{0.24}}\right] \Delta T_e^{0.24} \Delta p_e^{0.75} \qquad (2.1.1.3\text{-}20)$$

Then Chen defined the so-called suppression factor, S, as the ratio of the mean superheat to the wall superheat as follows :

$$S = \left[\frac{\Delta T_e}{\Delta T_{sat}}\right]^{0.99} \qquad (2.1.1.3\text{-}21)$$

The exponent 0.99 allows S to appear to the first power in the final equation. Using the Clausius-Clapeyron equation, it can be shown that

$$S = \left[\frac{\Delta T_e}{\Delta T_{sat}}\right]^{0.24} \left[\frac{\Delta p_e}{\Delta p_{sat}}\right]^{0.75} \qquad (2.1.1.3\text{-}22)$$

Substituting this expression into equation 2.1.1.3-20 gives

$$\alpha_{nuc} = 0.00122\left[\frac{\lambda_L^{0.79} C_{pL}^{0.45} \rho_L^{0.49}}{\sigma^{0.5} \eta_L^{0.29} h_{LG}^{0.24} \rho_G^{0.24}}\right] \Delta T_{sat}^{0.24} \Delta p_{sat}^{0.75} S \qquad (2.1.1.3\text{-}23)$$

Chen assumed S to be a function of the two-phase Reynolds number and indeed succeeded in establishing such a function. It should be noted that stagnant liquid ($Re_{tp} = 0$) corresponds to pool boiling with S equal to unity. S will decrease and approach zero with increasing Re_{tp}.

The convective term, α_{con} , is calculated from equation 2.1.1.1-8 .

Gungor and Winterton (1985) have set up a data bank which consists of 3700 data points for evaporating flow in vertical and horizontal tubes. This data bank covers water, freons and ethylene glycol from 28 authors. They adopted Chen's approach to correlate data in the data bank. The basic form of their correlation is :

$$\alpha_{tp} = E\alpha_L + S_{G\&W}\alpha_{np} \qquad (2.1.1.3\text{-}24)$$

Gungor and Winterton included the boiling number, Bo, in addition to the usual Martinelli parameter to correlate the convection enhancement factor, E. They argued that generation of vapour in the boiling process results in significant disturbance of the boundary layer next to the heat transfer surface which improved heat transfer. It is certainly true. But it is clearly a mechanism due to nucleate boiling and has nothing to do with forced convection.

For the nucleate component, Gungor and Winterton have compared the Stephen and Abdelsalam equation (equation 2.1.1.2-2) and the correlation by Cooper (1984) (equation 2.1.1.2-5). They found that the two correlations give similar results. Since the Cooper correlation required far fewer physical properties, it is preferred for calculating α_{np}.

The correlations established by Gungor and Winterton for E and $S_{G\&W}$ are as follows :

$$E = 1 + 24000 Bo^{1.16} + 1.37\left(\frac{1}{X_{tt}}\right)^{0.86} \qquad (2.1.1.3\text{-}25)$$

$$S_{G\&W} = \frac{1}{1 + 1.15 \times 10^{-6} E^2 Re_L^{1.17}} \qquad (2.1.1.3\text{-}26)$$

For horizontal tubes, if Fr_L (see equation 2.1.1.3-16)is less than 0.05, then the following modified multiplying factors apply

$$E' = EFr_L^{(0.1-2Fr_L)} \qquad (2.1.1.3\text{-}27)$$

$$S'_{G\&W} = S_{G\&W} \sqrt{Fr_L} \qquad (2.1.1.3\text{-}28)$$

Gungor and Winterton compared their correlation and others against the data bank. Their own correlation gives the least mean deviation of 25% . The Shah correlation ranks second with a mean deviation of 35.5% . All the others give unacceptable mean deviations.

In a subsequent paper, Gungor and Winterton (1987) proposed an even simpler correlation

$$\alpha_{tp} = E\alpha_L \qquad (2.1.1.3\text{-}29)$$

where

$$E = 1 + 3000Bo^{0.86} + 1.12\left(\frac{x}{1-x}\right)^{0.75}\left(\frac{\rho_L}{\rho_G}\right)^{0.41} \qquad (2.1.1.3\text{-}30)$$

The previously proposed correction for horizontal tube still applies (see equation 2.1.1.3-27).

In view of the obscure physical meaning of the Gungor and Winterton correlations (1985, 1987), Liu and Winterton (1988) attempted another correlation which placed more emphasis on the heat transfer mechanisms. To stress the respective dominance of each mechanism, they chose a form for the correlation with additive squared terms as follows :

$$\alpha_{tp}^2 = (E_{L\&W}\ \alpha_L)^2 + (S_{L\&W}\ \alpha_{np})^2 \qquad (2.1.1.3\text{-}31)$$

where α_{np} is calculated from equation 2.1.1.2-5.

They chose the following functional forms for the enhancement factor and the suppression factor

$$E_{L\&W} = \left[1 + xPr_L\left(\frac{\rho_L}{\rho_G} - 1\right)\right]^n \qquad (2.1.1.3\text{-}32)$$

$$S_{L\&W} = \frac{1}{1 + aE_{L\&W}^{m_0} Re_L^{m_1}} \qquad (2.1.1.3\text{-}33)$$

Based on the same data bank as used by Gungor and Winterton, Lui and Winterton evaluated the empirical constants in equations 2.1.1.3-32 and 2.1.1.3-33 . These constants were found to be : $n = 0.35$, $a = 0.055$, $m_0 = 0.1$ and $m_1 = 0.16$. The inclusion of Pr_L in equation 2.1.1.3-32 follows Bennett and Chen's analysis (1980) that indicated a dependence of the F factor on Prandtl number. For horizontal tubes, the correction factors from equations 2.1.1.3-27 and 2.1.1.3-28 also apply.

When compared with the same data bank from which both correlations were derived, the Liu and Winterton gives more uniform mean deviations for different fluids than that of Gungor and Winterton, although the overall performance is similar. When used to predict data in a data bank for cryogenic fluids, the Liu and Winterton correlation showed better prediction.

Bennett and Hertzler (1980) have attempted to provide a rational basis for the Chen's suppression factor, S. In their analysis, they assumed that the temperature profile near the wall can be approximated by an exponential function. They further postulated that there exists a region extending a distance X_0 from the wall, and that the average superheat within this region governs the heat transfer associated with nucleate boiling. Then they derived an expression for the suppression factor, which is defined as the ratio of the average superheat within the region X_0 to the wall superheat, consistent with the original definition by Chen. The resulting expression of the suppression factor is

$$S = \frac{\lambda_L}{\alpha_{con} X_0}\left\{1 - \exp\left[-\left(\frac{\alpha_{con} X_0}{\lambda_L}\right)\right]\right\} \qquad (2.1.1.3\text{-}34)$$

Unfortunately, X_0 is unknown. Bennett and Hertzler had to evaluate it from experimental data. They plotted the calculated values of X_0 against the two-phase Reynolds number and found no apparent relationship. They then proposed a correlation for X_0 as follows :

$$X_0 = 0.041\left[\frac{\sigma}{g(\rho_L - \rho_G)}\right]^{0.5} \qquad (2.1.1.3\text{-}35)$$

Despite being defined by Bennett and Hertzler as the thickness of the bubble growth region, X_0 should be viewed only as an empirical factor. Its apparent independence from the two-phase Reynolds number should be

interpreted as showing that it is not what it was defined. The thickness of the bubble growth region should rather be dependent on the ratio λ_L/α_{con} than X_0 which is just a convenient length scale.

2.1.2 Semi-theoretical methods for annular flow

Many models have been developed for heat transfer through the liquid film in annular flow. The assumptions usually made in these models include :

(1) The liquid film can be treated as having a planar surface, the influence of the interfacial waves being introduced only by their influence in enhancing the interfacial shear stress, τ_i .

(2) If the film is turbulent, it is assumed that the turbulence characteristics follow those occurring in single-phase flow of the liquid for the same wall shear stress.

(3) Interfacial resistance to heat transfer is ignored with the interface being at the saturation temperature.

The solution proceeds by first developing a relationship between film flow rate, film thickness and pressure gradient, via which, from a knowledge of any two of these parameters, the third can be calculated (hence the description " triangular relationship " for this analysis)

Although the triangular relationship is a useful model, it does not provide a closed solution for annular flow. Further models are required for the interfacial shear stress and, since part of the liquid phase is usually entrained as droplets, for the liquid flow rate in the film.

Once the hydrodynamic characteristics of the liquid film have been established, then the heat transfer coefficient can be calculated.

The triangular relationship

In a turbulent liquid film, the local shear stress at distance y from the wall can be related to the velocity gradient by the expression :

$$\tau = \rho_L(\upsilon_L + \varepsilon_m)\frac{du}{dy} \qquad (2.1.2\text{-}1)$$

For a laminar film, equation 2.1.2-1 becomes

$$\tau = \eta_L \frac{du}{dy} \qquad (2.1.2\text{-}2)$$

Integration of the above equation yields the velocity profile in the liquid film. Further integration will give the film flow rate, i.e.

$$\dot{M}_{LF} = \int_0^{\delta} 2\pi r \rho_L u \, dy \qquad (2.1.2\text{-}3)$$

To effect these integrations the shear stress distribution in the liquid film must be found from a force balance on the gas core and the liquid film. It can be shown that the force balance (Hewitt and Hall-Taylor, 1970) leads to :

$$\tau_i = \left(-\frac{dp}{dz} - \rho_G g \right) \frac{(r_0 - \delta)}{2} \qquad (2.1.2\text{-}4)$$

$$\tau = \tau_i \left(\frac{r_i}{r} \right) + \frac{1}{2} \left(\rho_L g + \frac{dp}{dz} \right) \left(\frac{r_i^2 - r^2}{r} \right) \qquad (2.1.2\text{-}5)$$

The result of the integrations can then be written as

$$\dot{M}_{LF} = \frac{2\pi\rho_L}{\eta_L} \left\{ \begin{array}{c} \left[\tau_i r_i + \frac{1}{2} \left(\rho_L + \frac{dp}{dz} \right) r_i^2 \right] \left[\frac{1}{4}(r_0^2 - r_i^2) - \frac{1}{2} r_i^2 \ln\left(\frac{r_0}{r_i} \right) \right] \\ - \frac{1}{16} \left(\rho_L g + \frac{dp}{dz} \right) (r_0^2 - r_i^2)^2 \end{array} \right\} \qquad (2.1.2\text{-}6)$$

In practice, laminar liquid films are rarely encountered. This means that the effective or total viscosity has to be considered. In the literature, there is an abundance of expressions for the turbulent momentum diffusivity, ε_m . These expressions have been derived from mixing length theory (Prandtl 1933), mixing length theory modified by eddy damping (van Driest 1956), dimensional analysis (Von Karman 1930), empirical approach (Deissler 1952) or the so-called universal velocity profile (Von Karman 1939). Though these expressions are intended for boundary layer analysis in single-phase flow, they are often applied directly to the liquid film in annular flow.

Analysis of hydrodynamics and heat transfer in liquid film flow have been carried out by many researchers. For instance, Dukler (1959) analysed downward film flow for calculation of heat transfer coefficients in condensation. He used the turbulent momentum diffusivity expression due to Deissler (1959) for $y^+ \leq 20$ and that due to Von Karman (1930) for

$y^+ > 20$ where y^+ is the friction distance parameter given by $(u^* y \rho_L)/\eta_L$ and where u^* is the friction velocity, $\sqrt{\tau_w/\rho_L}$. Later, Hewitt (1961) extended Dukler's theory to climbing film flow.

Interfacial friction

In annular flow, the interfacial shear stress is usually much higher than it would be for flow over a smooth film due to the presence of a complex pattern of waves on the interface. The effect of the waves is analogous to that of pipe wall roughness in single phase flow. A number of relationships have been published for the effect of interfacial roughness, both directly in terms of the roughness itself and indirectly in terms of interfacial friction factor. The most widely used of these latter correlations is that of Wallis (1970) who defines a "superficial interfacial friction factor", f_i as follows :

$$f_i = \frac{\tau_i}{\frac{1}{2}\rho_C U_C^2} \qquad (2.1.2\text{-}7)$$

where ρ_C is the density of the gas core (i.e. of the droplet / gas mixture, calculated on a homogeneous mixture basis) and U_C is the velocity of gas core. Wallis correlated f_i as follows :

$$f_i = f_{sgc}\left(1 + 360\frac{\delta}{D}\right) \qquad (2.1.2\text{-}8)$$

where δ is the film thickness and f_{sgc} is the friction factor for a single phase flow with a Reynolds number :

$$Re_{sgc} = \frac{U_C \rho_C D}{\eta_G} \qquad (2.1.2\text{-}9)$$

Many alternative correlations have been proposed for interfacial friction, for instance that of Whalley and Hewitt (1978) :

$$f_i = f_{sgc}\left[1 + 24\left(\frac{\rho_L}{\rho_G}\right)^{1/3}\frac{\delta}{D}\right] \qquad (2.1.2\text{-}10)$$

However, as Whalley and Hewitt (1978) showed, these relationships are not very accurate, particularly when a large fraction of the liquid phase is entrained as droplets. More recently, therefore, Owen and Hewitt (1987) have developed a model which takes more detailed account of the influence of droplet on core turbulence. This model formed one of the

"building blocks" of the new heat transfer model developed in the work described in this thesis and, as such, it will be introduced in more detail in Chapter 3.

Droplet entrainment and deposition

In predicting the behaviour of annular flows, it is essential to know the extent of liquid entrainment. In equilibrium annular flow, the rates of deposition and entrainment are equal and opposite. However, for most practical situations, and particularly in flows with phase change (i.e. evaporation or condensation), the flow is not in equilibrium and it is essential to know the rates of entrainment and deposition so that the variation of entrained fraction along the channel can be calculated.

Some of the early correlations for entrainment and deposition are summarised by Hewitt (1982). Though these correlations were useful in developing models for annular flow, they are of restricted accuracy and, for the theory developed in the work described in the present thesis, the recent correlations of Govan et al (1988) have been used. Again, for consistency, these correlations are described in more detail in Chapter 3.

Combined hydrodynamic models

The above models can be combined together to estimate hydrodynamic behaviour in annular flow. Whalley et al (1974) developed a computer code (HANA - Harwell ANnulAr flow model) which combined the various models (triangular relationship, interfacial friction, deposition and entrainment) to produce a predictive tool for non-equilibrium annular flow. As improved relationships have been developed (and in particular for deposition and entrainment), these have been incorporated into the code which has proved effective in predicting both adiabatic and diabatic annular flows. The HANA code was used extensively in the present work to predict local hydrodynamic parameters (film flow rate, film thickness, etc) to form a basis for the calculation of heat transfer coefficient

Calculation of forced convective heat transfer coefficient

Having established the film thickness, film flowrate and interfacial shear stress from the analysis described above, the heat transfer coefficient can then be calculated. For a thin laminar film, for instance, we have :

$$\alpha_{tp} = \frac{\lambda_L}{\delta} \qquad (2.1.2\text{-}11)$$

The more usual case, however, is that of a turbulent film and, for this case, equation 2.1.1.1-13 has to be integrated across the film, taking account of the variation of effective thermal conductivity with distance from the wall. The usual assumption is to take $\varepsilon_h = \varepsilon_m$ and to use similar relationships as those used in the hydrodynamic calculations. Examples of this approach are the analysis of Anderson and Mantzouranis (1961) and Kosky and Staub (1971) in which the von Karman Universal Velocity Distribution was used as a basis and those of Dukler (1959) and Hewitt (1961) in which the Deissler and von Karman relationships were used. Since all of these relationships are fitted to velocity profile data in single phase turbulent flow, it is not surprising that (at least for Prandtl numbers of the order of unity), all of the models give rather similar results. In view of this, there has been a tendency in recent years to use simpler models, not requiring numerical solution, such as those using the Universal Velocity Profile. This is the approach followed in the present work.

Although models for annular flow heat transfer which are based on single phase turbulent flow profiles all tend to give about the same answer, they all overpredict the heat transfer coefficient, particularly for the evaporation of water, typically by 30 - 50%. This overprediction has called into question the applicability of relationships based on single phase turbulent profiles to the case of film flows where an interface exists. Specifically, it has been suggested that the interface damps the turbulence and that the eddy diffusivity peaks at a point intermediate between the wall and the interface. Attempts to correct the analysis for these effects are described by Levich (1962), Blangetti et al (1981), Mudawwar and El-Masri (1986) and others. In the analytical work described in Chapter 3, the Levich (1962) approach has been followed.

2.1.3 Conclusion

The empirical correlations for heat transfer in evaporating flows leave much to be desired. Clearly, a majority of practical cases require correlations which span both nucleate boiling and forced convection. The semi-theoretical models are specific to the forced convective (annular flow) regime. Thus, it would be very desirable to predict heat transfer

coefficients over the full range of quality and to establish a sound analytical basis for combined nucleate boiling and forced convection. An attempt to do this is described in Chapter 3 which, we believe, throws considerable light on the processes involved. However, the situations in forced convective evaporation may be much more complex than had previouly been believed and the difference between evaporation and condensation (as revealed by the experiments described in Chapter 4) may call into question the whole basis of the present and previous analysis.

2.2 Theories on nucleation cycle

2.2.1 Incipience of nucleation in heterogeneous system

2.2.1.1 Gas or vapour trapping

Most practical solid surfaces are bound to have irregularities such as pits, scratches and cracks which provide cavities from which bubble may grow. Their topology and size distribution depend on the way in which the surface of the material was formed during manufacture and subsequent treatment and usage of the material. When the surface is wetted with a liquid, the topology of the irregularities and the properties of both the surface and the liquid determine whether gas or vapour will be trapped in the irregularities. It is these trapped gas or vapour embryos that make incipience of nucleation possible.

Bankoff (1958) studied the mechanism of gas trapping by spreading liquids on solid surfaces. He proposed a simple criterion for an irregularity which was idealised as a two dimensional inverted isosceles triangle on a surface. This irregularity represents a long triangular groove. The criterion for gas to be trapped when the liquid front is advancing over such idealised irregularity is as follows :

$$\theta > \phi \qquad (2.2.1.1\text{-}1)$$

The criterion for the cavity not to be flooded after the passage of the liquid front is

$$\theta > 180^{\circ} - \phi \qquad (2.2.1.1\text{-}2)$$

where θ is the contact angle between the liquid and solid surfaces, ϕ the included angle of the cavity

This criterion is assumed to hold for cavities of conical shape. For cavities of cylindrical shape, the depth is also important for gas trapping (Singh et al, 1977). The shape that favours gas trapping and retains the trapped gas for all conditions is a re-entrant cavity.

2.2.1.2 Bubble at equilibrium

In the following discussion, an equilibrium bubble is assumed to be a spherical segment resting on a conical cavity with a circular mouth. The equilibrium state implied that the pressure inside and outside the bubble must satisfy the Gibbs equation

$$p_b - p_L = \frac{2\sigma}{R_E} \qquad (2.2.1.2\text{-}1)$$

Consider first a system at uniform temperature. At equilibrium, the temperature, T_b , inside the bubble must be the same as that of surrounding liquid, T_L . In addition, the pressure, p_b , inside the bubble must be at the saturation value corresponding to T_b. Since the pressure inside the bubble is greater than that in the liquid (see equation 2.2.1.2-1), this means that the liquid is superheated. The saturated state inside the bubble can be related to the liquid pressure and its saturation temperature by the Clausius-Clapeyron equation :

$$\frac{dp}{dT} = \frac{h_{LG}}{v_G T} \qquad (2.2.1.2\text{-}2)$$

Assuming that the ideal gas law applies inside the equation 2.2.1.2-2 can be written as

$$\frac{dp}{dT} = \frac{h_{LG} p \mathcal{M}}{\mathcal{R} T^2} \qquad (2.2.1.2\text{-}3)$$

Assuming h_{LG} is constant over the integration limits, equation 2.2.1.2-3 can be integrated from (p_L, T_{sat}) to (p_b, T_b) to give the following expression.

$$\ln\left(\frac{p_b}{p_L}\right) = \frac{h_{LG}}{\mathcal{R}}\left(\frac{1}{T_{sat}} - \frac{1}{T_b}\right)\mathcal{M} \qquad (2.2.1.2\text{-}4)$$

Rohsenow (1970) has discussed different assumptions in effecting an analytical integration of the Clausius-Clapeyron equation. He compared the analytical solutions which involved different assumptions and found that they agree over a pressure range from 0.1 MPa to 6.8 MPa.

For the same temperature, the saturation pressure on a curved surface is different from that on a plane surface. However, a straight substitution of the Gibbs equation into equation 2.2.1.2-4 will cause only a small error (Collier 1978). Experimental results showed that the superheat temperature required for initiating heterogeneous nucleation can be as low as a few degrees in contrast to several hundred degrees for homogeneous nucleation. With the assumption of $T_{sat}T_b \approx T_{sat}^2$, the substitution of the Gibbs equation into equation 2.2.1.2-4 results in the following expression

$$T_b - T_{sat} = \frac{\mathcal{R}T_{sat}^2}{\mathcal{M}h_{LG}} \ln\left(1 + \frac{2\sigma}{R_E p_L}\right) \qquad (2.2.1.2\text{-}5)$$

It is clear from equation 2.2.1.2-5 that the maximum superheat barrier to be overcome corresponds to the smallest equilibrium radius of the bubble. Including the pre-equilibrium life of the bubble when it is emerging from the cavity, the smallest radius is reached as the bubble becomes hemispherical resting on the mouth of the cavity. This implies that at equilibrium, the contact angle is always 90° and the radius of the cavity is equal to the distance between the wall and the tip of the equilibrium bubble, i.e. $r_c = y_b = R_E$. Davis and Anderson (1966) argued that the equilibrium bubble can assume different shapes from the hemisphere and have a contact angle other than 90° because for heat transfer with nucleation, the equilibrium bubble on the heating surface is exposed to a temperature gradient. As a result, the surface tension on the bubble surface can vary from point to point. In addition, the flow field surrounding the bubble also has an effect on the shape and the contact angle of the equilibrium bubble.

2.2.1.3 Criteria for incipience of nucleation in forced flow

Most investigations on incipience of nucleation are focused on subcooled full-pipe flow. Experimental data from studies of incipience of nucleation are often plotted as heat flux against the wall superheat, i.e. $T_w - T_{sat}$. . Based on experimental data, there are two possible definitions of

incipience of nucleation. One definition is that nucleation is considered to have been initiated at the point where deviation from the single-phase convection line occurs (Bergles and Rohsenow 1964, Davis and Anderson 1966). The second definition chooses the point of intersection between the extrapolated single-phase convection line and the fully developed boiling line (McAdams et al 1949, Sato and Matsumura 1964). The former definition involves lower heat flux and smaller superheat, and thus is conservative and preferred.

Hysteresis effects have been observed in some experiments (Hodgson 1969, Yin and Abdelmessih 1977). In these experiments, as heat flux was increased, the wall superheat increased smoothly along the single-phase convection line until a point where a sudden drop of wall temperature occurred. Subsequently, the trend followed the fully developed boiling line. Upon decreasing power, nucleate boiling continues at heat fluxes lower than that at which it began. Yin and Abdelmessih (1977) proposed two empirical correlations for the two distinct points of transition into and out of nucleate boiling.

Most analytical work has been aimed at predicting incipience of nucleation based on the first definition. It became customary to assume that the presence of the equilibrium bubble does not distort the temperature field in the surrounding liquid; an exception is the analysis of Kenning and Cooper (1965). Assuming the heating surface has potentially active nucleation sites of wide ranging size, the criterion for incipience of nucleation is defined as that in which the whole bubble surface is surrounded by liquid at the equilibrium temperature or above. If there is a continuous spectrum of cavity sizes on the surface, then a plot of equilibrium temperature against bubble radius will become tangential to the temperature profile at a critical bubble radius at which the first bubble growth will occur. Mathematically, this criterion is expressed as

$$\left(\frac{dT}{dy}\right)_{con} = \left(\frac{dT}{dy}\right)_{b} \qquad (2.2.1.3\text{-}1)$$

with $T = T_b$ at $y = y_b = r_c = R_E$.

Experimental findings showed that bubble size at incipience of nucleation is in the order of 1 μm. Therefore, most analysis assumed that the convection temperature profile is linear from the wall to the point of tangency, i.e.

$$\dot{q}_w = \lambda_L \frac{(T_w - T)}{y} \qquad (2.2.1.3\text{-}2)$$

Equations 2.2.1.2-5 and 2.2.1.3-2 can be differentiated with respect to y and substituted into equation 2.2.1.3-1 . The result is

$$\dot{q}_{wi} = \frac{2\lambda_L \sigma T_{sat}}{h_{LG}\rho_G y_b^2 [1 + (2\sigma)/(p_{sat} y_b)]} \qquad (2.2.1.3\text{-}3)$$

From equation 2.2.1.2-3, y_b can be expressed as an explicit function of $\dot{q}_{wi}$, that is

$$y_b = -\frac{\sigma}{p_{sat}} + \sqrt{\left(\frac{\sigma}{p_{sat}}\right)^2 + \frac{2\sigma T_{sat}\lambda_L}{h_{LG}\rho_G \dot{q}_{wi}}} \qquad (2.2.1.3\text{-}4)$$

By eliminating T_b from both equations 2.2.1.2-5 and 2.2.1.3-2, one can also obtain an explicit expression for the wall superheat

$$T_{wi} - T_{sat} = \frac{\mathcal{R} T_{sat}^2}{\mathcal{M} h_{LG}} \ln\left(1 + \frac{2\sigma}{p_{sat} y_b}\right) + \frac{\dot{q}_{wi} y_b}{\lambda_L} \qquad (2.2.1.3\text{-}5)$$

2.2.2 Bubble growth without translation

We discuss here the processes of growth of a static bubble in a superheated liquid. Two situations are reviewed, namely the growth of spherical bubbles in an infinite superheated liquid (Section 2.2.2.1) and the growth of bubbles at a solid surface, such as occurs in nucleate boiling (Section 2.2.2.2.3).

2.2.2.1 Spherical bubble growth in an infinite superheated liquid

Two extreme cases can be recognized for the growth of a vapour bubble in a superheated liquid, namely inertia controlled growth and conduction controlled growth. These cases are discussed in Sections 2.2.2.1.1 and

2.2.2.1.2 respectively. Treatment of cases where both inertia and conduction are important can be achieved numerically and this is discussed in Section 2.2.2.1.3.

2.2.2.1.1 Inertia-limited bubble growth : Rayleigh's model

A simple case, which involved only hydrodynamics, was considered by Rayleigh (1917). The case was that, in an infinite volume of liquid, a vacuum spherical void of initial radius R_0 with its centre fixed in space is collapsing under an external pressure p_∞ at infinity. Rayleigh formulated the problem based on the following laws.

Continuity in the liquid phase :

$$\frac{u}{U}=\frac{R^2}{r^2} \qquad (2.2.2.1.1\text{-}1)$$

where u is the local liquid velocity at distance r from the centre of the void and U is the velocity at the edge of the void at distance R from its centre.

Mechanical energy balance :

Kinetic energy of the liquid in motion = Work done by the external pressure at infinity

Assuming incompressibility, the kinetic energy of the liquid phase is

$$\frac{1}{2}\rho_L\int_R^\infty u^2 4\pi r^2 dr = 2\pi\rho_L U^2 R^3 \qquad (2.2.2.1.1\text{-}2)$$

where ρ_L is the liquid phase density.

The work done by the external pressure at infinity is

$$\frac{4}{3}\pi p_\infty(R_o^3-R^3) \qquad (2.2.2.1.1\text{-}3)$$

Equating the two energy expressions

$$U^2=\frac{2p_\infty}{3\rho_L}\left(\frac{R_o^3}{R^3}-1\right) \qquad (2.2.2.1.1\text{-}4)$$

Since $U = dR/dt$, the above expression can be integrated to obtain a relation between the void size and time.

Rayleigh further consider the case of a gas bubble, also with its centre fixed in space, expanding in the liquid without phase change (i.e. gas phase and liquid phase of different components is implied). The pressure in the bubble follows Boyle's law and is initially at p_{bi}. The mechanical energy balance then becomes

Kinetic energy in liquid = Work done by gas against external pressure at infinity, that is :

$$2\pi\rho_L U^2 R^3 = \int_{R_o}^{R} (p_b - p_\infty) 4\pi R^2 dR \qquad (2.2.2.1.1\text{-}5)$$

where Boyle's law requires that the instantaneous pressure p_b is given by

$$p_b = p_{bi}\frac{R_o^3}{R^3} \qquad (2.2.2.1.1\text{-}6)$$

After integration

$$U^2 = \frac{2p_{bi}}{\rho_L}\frac{R_o^3}{R^3}\ln\frac{R}{R_o} - \frac{2p_\infty}{3\rho_L}\left(1 - \frac{R_o^3}{R^3}\right) \qquad (2.2.2.1.1\text{-}7)$$

Again this expression can be integrated to produce a relation between the bubble radius and time.

Combining the continuity equation and kinetic energy balance with the momentum balance in the liquid phase, Rayleigh also obtain the pressure distribution in the liquid phase. The momentum equation that he used is

$$\frac{dp}{dr} = -\rho_L\left(\frac{\partial u}{\partial t} + u\frac{\partial u}{\partial r}\right) \qquad (2.2.2.1.1\text{-}8)$$

Substituting the continuity equation, it can be shown that

$$\frac{1}{\rho_L}\frac{dp}{dr} = \frac{2R^4U^2}{r^5} - \frac{1}{r^2}\left(2RU^2 + R^2\frac{dU}{dt}\right) \qquad (2.2.2.1.1\text{-}9$$

Integrating from infinity up to the liquid boundary of the bubble, and using $U = \dot{R}$ and $dU/dt = \ddot{R}$

$$\frac{p - p_\infty}{\rho_L} = \frac{3}{2}\dot{R}^2 + R\ddot{R} \qquad (2.2.2.1.1\text{-}10)$$

which is called the Rayleigh equation.

Rayleigh did not extend his bubble growth analysis to involve any thermal process. However, by making some assumptions and with the help of the Clausius-Clapeyron equation, his analysis can be applied to bubble growth with phase change (i.e. when the gas phase and liquid phase are of the same component).

Consider the case of a bubble growing from a very small size ($R_0 \approx 0$) and in which the pressure in the bubble is maintained at a constant value p_G as a result of the evaporation process at the interface. Equation 2.2.2.1.1-5 then becomes :

$$2\pi\rho_L\left(\frac{dR}{dt}\right)^2 R^3 = \int_0^R (p_G - p_\infty)4\pi R^2 dR \qquad (2.2.2.1.1\text{-}11)$$

which can be integrated to give :

$$\frac{dR}{dt} = \sqrt{\frac{2}{3}\frac{p_G - p_\infty}{\rho_L}} \qquad (2.2.2.1.1\text{-}12)$$

Integrating from $R = 0$ when $t = 0$ gives :

$$R = \sqrt{\frac{2}{3}\frac{p_G - p_\infty}{\rho_L}}\,t \qquad (2.2.2.1.1\text{-}13)$$

Suppose that the saturation temperature corresponding to p_∞ is T_{sat} and that the vapour temperature in the bubble is T_G, the saturation pressure corresponding to p_G, then the linearised Clausius-Clapeyron relationship gives :

$$p_G - p_\infty = \frac{T_G - T_{sat}}{T_{sat}}\rho_G h_{LG} \qquad (2.2.2.1.1\text{-}14)$$

If the bulk temperature of the liquid is T_∞ (which must be higher than T_{sat} if the bubble is to grow), then T_G would be lower than T_∞ to allow heat to be conducted to the interface to cause evaporation there. However, if the growth of the bubble is being controlled by inertia effect (the case being considered) then $T_G \approx T_\infty$ and we can write :

$$\left(\frac{dR}{dt}\right)^2 = \frac{2}{3}\frac{T_\infty - T_{sat}}{\rho_L T_{sat}}\rho_G h_{LG} \qquad (2.2.2.1.1\text{-}15)$$

Integrating from $R = 0$ when $t = 0$ gives :

$$R = \left[\frac{2}{3} \frac{h_{LG} \rho_G (T_\infty - T_{sat})}{\rho_L T_{sat}} \right]^{\frac{1}{2}} t \qquad (2.2.2.1.1\text{-}16)$$

which is the limiting case for inertia controlled growth.

2.2.2.1.2 Diffusion-controlled bubble growth in uniformly superheated liquid

Plesset and Zwick (1954) found that equation 2.2.2.1.1-16 did not predict the data of Dergarabedian (1953) well. The heat transfer from the liquid phase towards the interface to sustain evaporation, hence bubble growth, must be considered in a more rigorous way than by the simple argument presented above, i.e. $T_G \approx T_\infty$. In fact, the heat transfer process was found to be predominant over much of the bubble live span except a short period immediately following the bubble incipience.

In 1954, Forster & Zuber and Plesset & Zwick published papers in the same edition of the same journal on the subject of bubble growth in a superheated liquid. Both papers discussed the Rayleigh equation and extended it to include surface tension. The extended Rayleigh's equation then became

$$\rho_L \left(R\ddot{R} + \frac{3}{2}\dot{R}^2 \right) = p_G - p_\infty - \frac{2\sigma}{R} \qquad (2.2.2.1.2\text{-}1)$$

They also used the Clausius-Clapeyron equation to relate the pressure difference $(p_G - p_\infty)$ to $(T_G - T_{sat})$ where T_{sat} is the saturation temperature corresponding to p_∞. The heat transfer problem was first solved to obtain the temperature gradient in the thermal boundary layer surrounding the bubble as a function of the bubble radius (Plesset and Zwick) or as a function of the bubble radius and its derivative with time (Forster and Zuber). The mathematical methods employed in the two papers are quite different. In principle, this temperature gradient function together with the Clausius-Clapeyron equation can be substituted into the extended Rayleigh equation to obtain a solution for bubble growth. But an exact solution seemed impossible because of the non-linearity of the resulting differential equation.

It was argued that the hydrodynamic terms on the left hand side of the extended Rayleigh equation and the surface tension term on the right hand side lose their importance shortly after bubble incipience at times of the order of 10^{-4} seconds (Forster and Zuber). Then, an asymptotic analytical solution can be obtained for bubble growth controlled by thermal diffusion. Due to different mathematical approaches, the results from the two papers are slightly different. The respective solutions are as follows :

$$R = \sqrt{\frac{12\kappa_L}{\pi}} Ja\, t^{\frac{1}{2}} \quad \text{(Plesset and Zwick)} \qquad (2.2.2.1.2\text{-}2)$$

$$R = \sqrt{\pi\kappa_L}\, Ja\, t^{\frac{1}{2}} \quad \text{(Forster and Zuber)} \qquad (2.2.2.1.2\text{-}3)$$

where Ja , the Jacob number, is given by :

$$Ja = \frac{C_{pL}\rho_L(T_\infty - T_{sat})}{h_{LG}\rho_G} \qquad (2.2.2.1.2\text{-}4)$$

Both analysis showed good agreement with Dergarabedian's data. Plesset & Zwick mentioned the uncertainty in identifying the time origin of the bubble growth data and admitted that a time translation of their equation has been made to fit the data, since the time origin of their asymptotic curve is also arbitrary.

The same problem was tackled by Scriven (1959) in a much more general way. He took account of the phase change at the interface in making mass balance for the liquid phase. The continuity equation for the liquid phase thus becomes

$$ur^2 = \varepsilon \dot{R} R^2 \qquad (2.2.2.1.2\text{-}5)$$

where

$$\varepsilon = 1 - \frac{\rho_G}{\rho_L} \qquad (2.2.2.1.2\text{-}6)$$

Including the effect of viscosity, Scriven modified the extended Rayleigh equation into the following form

$$\varepsilon\rho_L\left(R\ddot{R} + \frac{3}{2}\dot{R}^2 + 4\mu\frac{\dot{R}}{R}\right) = p_G - p_\infty - \frac{2\sigma}{R} \qquad (2.2.2.1.2\text{-}7)$$

In his analysis, he obtained an asymptotic solution of the following form

$$R = \sqrt{\frac{12\kappa_L}{\pi}} \frac{(T_\infty - T_G) C_{pL} \rho_L}{\rho_G [h_{LG} + (C_{pL} - C_{pG})(T_\infty - T_G)]} t^{\frac{1}{2}} \qquad (2.2.2.1.2\text{-}8)$$

If $(C_{pL} - C_{pG})(T_\infty - T_G)/h_{LG} \ll 1$ then this expression equation is reduced to the Plesset-Zwick equation.

It will be noted that the thermal conduction controlled solutions indicate that the bubble radius varies with $t^{1/2}$ in contrast to the inertial controlled case where the bubble radius varies linearly with time.

2.2.2.1.3 Numerical solution for bubble growth

There have been a number of published numerical solutions for bubble growth in an infinite volume of superheated liquid. Saitoh and Shima (1977) employed a finite-difference method in solving the general momentum and energy equations coupled with a set of boundary conditions. They made the same assumption that the bubble interfacial temperature is in equilibrium with the bubble pressure. However, with numerical solutions, this assumption can also be relaxed though sig nificant differences across the interface would only be expected in liquids of high conductivity, namely liquid metals. Thus, Dwyer (1976) has examined different prediction methods for bubble growth in superheated liquid metals. He noted that the numerical solution due to Theofanous et al (1969) accounted for the interfacial mass transfer resistance. The net molar rate of evaporation, $\dot{n}_{int}$, per unit area of interface during bubble growth is given by the equation :

$$\dot{n}_{int} = C \sqrt{\frac{\mathcal{M}}{2\pi \mathcal{R}}} \left(\frac{p_{intL}}{\sqrt{T_{intL}}} - \frac{p_G}{\sqrt{T_G}} \right) \qquad (2.2.2.1.3\text{-}1)$$

where C is called the accommodation coefficient. The assumption of previous analysis that $p_G = p_{intL}$ and $T_G = T_{intL}$ is mathematically equivalent to saying that $C = \infty$ for a finite $\dot{n}_{int}$, although theoretically C cannot exceed unity. The numerical solution of Theofanous et al thus predicts a lower bubble growth rate.

2.2.2.2 Bubble growth at a solid surface

The analysis referred to in Section 2.2.2.1 were for the growth of a free bubble in an infinite fluid. However, the more important case (and the one which is considered here) is that of bubble growth adjacent to a solid surface. First, in Section 2.2.2.2.1 , we describe the analysis of Mikic et al (1970) for the growth of a spherical bubble adjacent to a solid surface. In Section 2.2.2.2.2, we present a model (namely that of Fyodorov and Klimenko, 1989) which also considers spherical bubble growth near a surface but which attempts to take account of the heat transfer processes in the wall and in the liquid between the bubble and the wall. In practice, however, bubbles growing at a solid surface are often hemispherical rather than spherical in shape. Furthermore, they are separated from the surface by a thin evaporating liquid layer often referred to as the "microlayer". In Section 2.2.2.2.3, we consider the analytical solutions for such bubbles (namely that of Cooper & Lloyd 1969, and Cooper & Vijuk 1970) for this situation. Finally, we present information (in Section 2.2.2.2.4) on comparison between these models and actual growth rate measurements.

Bubble departure size in flowing systems is discussed in Section 2.2.3. In Section 2.2.4 the (limited) information on bubble formation with liquid forced flow is discussed. The even more limited information on bubble formation in liquid films is reviewed.

2.2.2.2.1 Spherical bubble growth adjacent to a solid surface

Mikic et al (1970) modified the Plesset-Zwick equation to take account of the inertial force and the wall effect for bubble growth on a heated surface. This refinement brought about a more realistic model.

In their derivation, instead of starting formally with the momentum equation, they made use of a total kinetic energy expression (Witze et al, 1968) for the liquid phase surrounding a spherical bubble that grows on a plane surface. This kinetic energy is equated to the work done by the pressure difference between the bubble interior and infinity and the resultant equation is :

$$9.35\rho_L\left(\frac{dR}{dt}\right)^2 R^3 = 4\pi\int_0^R (p_G - p_\infty)R^2 dR \qquad (2.2.2.2.1\text{-}1)$$

which is similar to equation 2.2.2.1.1-11.

Integration of equation 2.2.2.2.1-1 yields :

$$9.35\rho_L\left(\frac{dR}{dt}\right)^2 R^3 \approx \frac{4}{3}\pi R^3(p_G - p_\infty) \qquad (2.2.2.2.1\text{-}2)$$

$$\left(\frac{dR}{dt}\right)^2 = \frac{\pi}{7}\left(\frac{p_G - p_\infty}{\rho_L}\right) \qquad (2.2.2.2.1\text{-}3)$$

Using the linearised Clausius-Clapeyron equation to relate the pressure difference term to its corresponding temperature difference term, the above equation can be changed to

$$\left(\frac{dR}{dt}\right)^2 = A^2\frac{T_G - T_{sat}}{\Delta T} \qquad (2.2.2.2.1\text{-}4)$$

where $\Delta T = T_\infty - T_{sat}$

and

$$A = \left(\frac{\pi}{7}\frac{h_{LG}\rho_G\Delta T}{\rho_L T_{sat}}\right)^{\frac{1}{2}} \qquad (2.2.2.2.1\text{-}5)$$

Equation 2.2.2.2.1-4 is arrived at by considering the inertial effect on a growing bubble on a heated surface. Mikic et al pointed out that the pressure and corresponding temperature T_G inside the bubble is usually not known but it must fall between the limits T_{sat} and T_∞.

The effect of conduction in the superheated liquid surrounding the bubble is accounted for by the Plesset-Zwick equation (see equation 2.2.2.1.2-18), which can be differentiated to give :

$$\frac{dR}{dt} = \frac{1}{2}\sqrt{\frac{12\kappa_L}{\pi}}\frac{C_{pL}\rho_L(T_\infty - T_{sat})}{h_{LG}\rho_G}\frac{1}{\sqrt{t}} \qquad (2.2.2.2.1\text{-}6)$$

The Plesset-Zwick equation is valid in the asymptotic condition (purely conduction controlled) with $T_G \approx T_{sat}$ in equation 2.2.2.2.1-6. In the actual situation, T_G should replace T_{sat}. Then, equation 2.2.2.2.1-6 can be modified to become :

$$\frac{dR}{dt} = \frac{1}{2}\frac{B}{\sqrt{t}}\frac{T_\infty - T_G}{\Delta T} \qquad (2.2.2.2.1\text{-}7)$$

$$\frac{dR}{dt} = \frac{1}{2}\frac{B}{\sqrt{t}}\left(1 - \frac{T_G - T_{sat}}{\Delta T}\right) \qquad (2.2.2.2.1\text{-}8)$$

where

$$B = \sqrt{\frac{12\kappa_L}{\pi}}Ja \qquad (2.2.2.2.1\text{-}9)$$

Since the inertial and conduction effect are simultaneous, equations 2.2.2.2.1-4 and 2.2.2.2.1-8 can be combined to eliminate the unknown T_G. The resulting expression is as follows

$$\frac{1}{A^2}\left(\frac{dR}{dt}\right)^2 + \frac{2\sqrt{t}}{B}\frac{dR}{dt} - 1 = 0 \qquad (2.2.2.2.1\text{-}10)$$

Then, solving for dR/dt and expressing the result in non-dimensional form

$$\frac{dR^+}{dt^+} = (t^+ + 1)^{\frac{1}{2}} - (t^+)^{\frac{1}{2}} \qquad (2.2.2.2.1\text{-}11)$$

where

$$R^+ = \frac{AR}{B^2} \qquad (2.2.2.2.1\text{-}12)$$

$$t^+ = \frac{A^2 t}{B^2} \qquad (2.2.2.2.1\text{-}13)$$

Mikic et al integrated equation 2.2.2.2.1- 11 from $R^+ = 0$ (instead of $R^+ = R_0^+$) when $t^+ = 0$ to give the following expression :

$$R^+ = \frac{2}{3}[(t^+ + 1)^{3/2} - (t^+)^{3/2} - 1] \qquad (2.2.2.2.1\text{-}14)$$

When $t^+ \ll 1$

$$R^+ = t^+ \qquad (2.2.2.2.1\text{-}15)$$

$$R = At = \left(\frac{\pi h_{LG}\rho_G \Delta T}{7\ \rho_L T_{sat}}\right)^{\frac{1}{2}} t \qquad (2.2.2.2.1\text{-}16)$$

which is analogous to the Rayleigh equation (see equation 2.2.2.1.1-16) for the infinite fluid case.

When $t^+ \gg 1$

$$R^+ = \sqrt{t^+} \qquad \text{(2.2.2.2.1-17)}$$

$$R = B\sqrt{t} \qquad \text{(2.2.2.2.1-18)}$$

which is the Plesset-Zwick equation.

Mikic et al also extended their analysis to include effects of subcooling and initially non-uniform temperature profile around the bubble. The equation that resulted in non-dimensional form is as follows.

$$\frac{dR^+}{dt^+} = \left[t^+ + 1 - \theta\left(\frac{t^+}{t^+ + t_w^+} \right)^{\frac{1}{2}} \right]^{\frac{1}{2}} - (t^+)^{\frac{1}{2}} \qquad \text{(2.2.2.2.1-19)}$$

where

$$\theta \equiv \frac{T_w - T_{bulk}}{T_w - T_{sat}} \qquad \text{(2.2.2.2.1-20)}$$

where T_{bulk} is the bulk liquid temperature and t_w^+ is the waiting time (non-dimensionalised as in equation 2.2.2.2.1-13) for bubble incipience. When $t_w^+ \to \infty$, equation 2.2.2.2.1-19 will be reduced to equation 2.2.2.2.1-11 for the uniformly superheated case.

2.2.2.2.2 Effect of local heat transfer processes on growth of a spherical bubble near a heated surface

Fyodorov and Klimenko's model (1989) takes into account the temperature field in the wall under the growing bubble. This model is intended for wetting liquids whose contact angle with the surface is close to zero; cryogens and some organic fluids such as ethanol, benzene and propanol fall into this category. The unsteady state heat conduction equation in the wall is :

$$\frac{\partial T}{\partial t} = \kappa_w \nabla^2 T \qquad \text{(2.2.2.2.2-1)}$$

For slow bubble growth and high values of wall thermal diffusivity, κ_w it is possible to ignore the term $\partial T/\partial t$ in equation 2.2.2.2.2-1, which then becomes

$$0 = \nabla^2 T \qquad (2.2.2.2.2\text{-}2)$$

This means that the unsteady heat transfer is approximated by an infinite number of steady states, each of which corresponds to the size of the bubble in each instance during growth. Among the boundary conditions set for solving 2.2.2.2.2-2 is the heat flux continuity at the wall surface

$$q_w = \lambda_w \frac{\partial T}{\partial z} = q_L = \frac{\lambda_L}{\delta}(T_w - T_{sat}) \qquad (2.2.2.2.2\text{-}3)$$

Here δ is defined as the distance between the lower half of the spherical bubble and the wall. δ varies from zero at the contact point to R at the bubble equator.

After the temperature field in the wall under the growing bubble was found, the total heat transfer between the wall and the bubble interface, Q_w , can be calculated. A non-dimensional heat transfer rate was defined as such that

$$\hat{Q}_w = \frac{Q_w}{\lambda_L R \theta_s} \qquad (2.2.2.2.2\text{-}4)$$

where $\theta_s = T_{w\infty} - T_{sat}$ and $T_{w\infty}$ is the wall temperature far from the contact point between the bubble and the wall. $\hat{Q}_w$ was shown to be a unique function of $\xi = \frac{\lambda_w}{\lambda_L}$. Tabulated values of this function were presented in the original paper.

A heat balance for the bubble results in the following expression :

$$h_{LG}\rho_G \frac{d}{dt}\left(\frac{4}{3}\pi R^3\right) = \hat{Q}_w \kappa_L R \theta_s \qquad (2.2.2.2.2\text{-}5)$$

Assuming $R = 0$ when $t = 0$, integration of equation 2.2.2.2.2-5 from 0 to t gives

$$R = \sqrt{\frac{\hat{Q}_w}{2\pi} Ja \kappa_L}\; t^{\frac{1}{2}} \qquad (2.2.2.2.2\text{-}6)$$

Fyodorov and Klimenko defined $Ja = [C_{pL}\rho_L(T_w - T_{sat})]/[h_{LG}\rho_G]$, though the definition should probably include $T_{w\infty}$ rather than T_w.

During bubble growth, the layer of superheated liquid originally formed on the wall was stretched around the bubble. When the heat transfer from this superheated layer was also considered, Fyodorov and Klimenko derived the following equation :

$$R = \left\{ \left[\sqrt{\frac{3}{\pi}} Ja \right]^{3/2} + \left[\sqrt{\left(\frac{\hat{Q}_w}{2\pi} + 1 \right) Ja} \right]^{3/2} \right\}^{2/3} \sqrt{\kappa_L} t^{1/2} \qquad \text{(2.2.2.2.2-7)}$$

where $\sqrt{3/\pi} \approx 1$. Since $\hat{Q}_w$ is a unique function of ξ , it was shown that :

$$\left(\frac{\hat{Q}_w}{2\pi} + 1 \right)^{\frac{3}{4}} \approx \frac{6.9}{(1 + 1070/\xi)^{0.23}} = \gamma \qquad \text{(2.2.2.2.2-8)}$$

Then equation 2.2.2.2.2-7 can be written as :

$$R = (Ja^{3/2} + \gamma Ja^{3/4})^{2/3} \sqrt{\kappa_L} t^{1/2} \qquad \text{(2.2.2.2.2-9)}$$

Equation 2.2.2.2.2-9 is applicable when $\xi \geq 10$ and $Ja \leq 100$

2.2.2.2.3 Hemispherical bubble growth on heated surface

Another noteworthy bubble growth model was advanced by Cooper (1969). This model considered bubble growth on a heated surface covered by a large volume of initially stagnant liquid. For conditions under which the inertial force is much larger than the forces of surface tension, buoyancy and viscosity, then the bubble shape is hemispherical. Prompted by experimental evidence of the existence of a microlayer underneath the hemispherical bubble, Cooper and Lloyd (1969) developed a liquid trapping model for calculating the thickness of such a layer. The resulting expression is strikingly simple.

$$\delta_0 = C_2 \sqrt{\nu_L t_g} \qquad \text{(2.2.2.2.3-1)}$$

Where δ_0 is the initial thickness of the microlayer at any point (radius r) under the bubble, ν_L the kinematic liquid viscosity, t_g the time for the bubble to grow to r , and C_2 is equal to 0.8.

With equation 2.2.2.2.3-1 incorporated in his bubble growth analysis, Cooper assumed the general form of the growth rate as $R = C_1 t^n$ and then proceeded to derive expressions for C_1 and the value for n. Cooper and Vijuk (1970) noted that C_2 depends on n but the relation is not strong. C_2 = 0.8 is used in all their analysis.

For the case where $\lambda_w \gg \lambda_L$, the change in saturation temperature inside the bubble due to inertia force is much less than the wall superheat or $(T_w - T_{sat}) \gg \rho_L\left(R\ddot{R} + \frac{3}{2}\dot{R}^2\right)(dT/dP)_{sat}$. It can then be assumed that T_w remains constant and the interfacial temperature equals T_{sat} throughout the bubble life. Furthermore, the model assumed the only contribution to bubble growth comes from evaporation at the microlayer. The result of Cooper's analysis (1969) is :

$$R = \frac{2}{C_2}\frac{T_{wo} - T_{sat}}{\phi}(v_L t)^{\frac{1}{2}} \qquad (2.2.2.2.3\text{-}2)$$

where

$$\phi = \psi\left[1 + \frac{2}{C_2^2}\frac{C_{pL}(T_{wo} - T_{sat})}{h_{LG}}\frac{1}{Pr_L}\right] \qquad (2.2.2.2.3\text{-}3\ a)$$

$$\psi = \frac{v_L h_{LG}\rho_G}{\lambda_L} = \frac{\rho_G}{\rho_L}\frac{h_{LG}}{C_{pL}}Pr_L \qquad (b)$$

where T_{wo}

is the initial wall temperature when bubble growth begins. $T_{wo} \approx T_w$ for $\lambda_w \gg \lambda_L$

For most non-metallic liquids boiling with typical wall superheat, the second term in the bracket of equation 2.2.2.2.3-3a is much less than unity. It then follows that

$$R \approx 2.5\sqrt{\frac{\kappa_L}{Pr_L}}Ja_{wo}\, t^{\frac{1}{2}} \qquad (2.2.2.2.3\text{-}4)$$

where

$$Ja_{wo} = \frac{C_{pL}\rho_L(T_{wo} - T_{sat})}{\rho_G h_{LG}} \qquad (2.2.2.2.3\text{-}5)$$

If T_∞ is written for T_w, then for many non-metallic liquids on a highly conducting heated wall, the numerical value predicted by equation 2.2.2.2.3-4 is similar to those predicted by equations 2.2.2.1.2-2 ,2.2.2.1.2-3 and 2.2.2.1.2-8 ,although the mechanism and theory are quite different.

The theory of hemispherical bubble growth on heated surfaceswas further developed by Cooper and Vijuk (1970). Account was taken of the evaporation at the curved bubble surface. When the liquid is initially superheated uniformly at T_{bulk} and evaporation at the curved surface is significant, Cooper and Vijuk suggested that contributions from the superheated layer at the curved surface and that from the microlayer to bubble growth are additive, resulting in the following expression for a highly conducting wall.

$$R=\left(MJa_{wo}+2\sqrt{\frac{3}{\pi}Ja_{bulk}}\right)\sqrt{\kappa_L}t^{\frac{1}{2}} \qquad (2.2.2.2.3\text{-}6)$$

where

$$Ja_{bulk}=\frac{C_{pL}\rho_L(T_{bulk}-T_{sat})}{\rho_G h_{LG}} \qquad (2.2.2.2.3\text{-}7)$$

$$M=\frac{2}{C_2\sqrt{Pr_L}} \qquad (2.2.2.2.3\text{-}8)$$

For a heated wall with low conductivity, i.e. $\lambda_L \gg \lambda_w$

$$R=\left(\frac{2}{\sqrt{\pi}}\beta Ja_{wo}+2\sqrt{\frac{3}{\pi}Ja_{bulk}}\right)\sqrt{\kappa_L}t^{1/2} \qquad (2.2.2.2.3\text{-}9)$$

where

$$\beta=\left(\frac{\lambda_w C_{pw}\rho_w}{\lambda_L C_{pL}\rho_L}\right)^{1/2} \qquad (2.2.2.2.3\text{-}10)$$

For combinations of liquid and wall with thermal conductivities of the same order of magnitude, Cooper and Vijuk derived the following bubble growth equation.

$$R=\left(\frac{Ja_{wo}}{1/M+\sqrt{\pi}/(2\beta)}+2\sqrt{\frac{3}{\pi}Ja_{bulk}}\right)\sqrt{\kappa_L}t^{1/2} \qquad (2.2.2.2.3\text{-}11)$$

With inertial force taken into consideration, Cooper and Vijuk obtained the following bubble growth equation.

$$R = \frac{1}{\frac{1}{t}\sqrt{\frac{3}{2}\frac{\rho_L}{\rho_G}\frac{T_{sat}}{h_{LG}(T_{wo}-T_{sat})}+\frac{1}{MJa_{wo}\sqrt{\kappa_L t^{1/2}}}}} \qquad (2.2.2.2.3\text{-}12)$$

2.2.2.2.4 Comparison between experimental data and theories

Stewart and Cole (1972) have obtained some experimental data on bubble growth on a heated surface (non-uniform temperature field implied) at 0.048 bar with the wall superheat ranging from 19.35 to 22.54°C corresponding to Jakob numbers from 955 to 1112. They used these data to test some the well known models. Although the model of Mikic et al (1970) and that of Cooper and Vijuk (1970) fared better than others, none agreed satisfactorily with the data. They all over-predicted.

However, Saitoh et al (1977) have compared Mikic et al's model with the data of Dergarabedian (1953) and Hooper & Abdelmessih (1966), both sets taken at pressure of 1 bar with uniform superheat. In this comparison, Mikic et al's model showed increasing over-prediction with increasing superheat.

Although Mikic et al's theory seems to be the best among the analytical models, there is now evidence which showed that this theory has not taken proper account of the effect of the Jakob number. Due to the complex nature of bubble growth, a completely satisfactory mechanistic model of bubble growth is not yet available.

2.2.3 Bubble departure size in forced flow

Now we consider the case of vapour bubble behaviour in a flowing system. Bubbles normally start from a fixed site on the channel wall and a crucial issue (determining the frequency of bubble formation) is the bubble size at the point of departure from the original site.

The forces acting on the attached bubble can be classified as : (1) buoyancy force due to gravity; (2) surface tension force; (3) drag force due to the motion of the surrounding liquid around the bubble; (4) inertia forces of the vapour and the liquid and (5) pressure gradient force. At the moment

just before the bubble departs from the nucleation site, all the forces acting on the bubble must be balanced. The bubble departs when this force balance is upset.

The complexity of the forces involved in bubble departure has left many of the problems insolved, even in pool boiling. This has perhaps discouraged workers from studying the flow situation, but there have been some useful contributions, two of which (namely those of Koumoutsos et al, 1968 and Al-Hayes and Winterton, 1981) are described here as a basis for the description of the evaporative heat transfer model in Chapter 3.

Correlation of Koumoutsos et al for bubble departure in horizontal flow

The scarcity of information on bubble departure in forced flow was pointed out by Koumoutsos et al (1968). They studied bubble departure in horizontal forced flow over a heated wall at atmospheric pressure in a duct with a 15 mm x 26 mm rectangular cross section. Based on the hydraulic diameter, the Reynolds number in their experiments ranged from 2300 to 22000. They observed that as the centre of gravity of the bubble rose, its base attached to the wall was narrowed and formed a near cylindrical stem or "neck" with decreasing radius. They observed that the bubble inclined in the direction of flow. Bubble departure was defined by them as the point of break-off of the bubble neck.

In their theoretical analysis, Koumoutsos et al considered bouyancy, surface tension and drag forces. The volume of vapour in the bubble neck was found negligible and the angle made by the plane parallel to the wall and the tangent of the bubble surface where necking starts was approximately equal to the contact angle, θ_o, without necking.

The force balance on the bubble is :

$$F_s^2 = F_b^2 + F_d^2 \qquad (2.2.3\text{-}1)$$

where F_s, F_b and F_d are the forces due to surface tension, buoyancy and drag respectively.

The buoyancy force, F_b was expressed as

$$F_b = \frac{\pi R^3}{3} \rho_L g (1 + \cos\theta_0)^2 (2 - \cos\theta_0) \qquad (2.2.3\text{-}2)$$

The drag force, F_d , was expressed as

$$F_d = C_d \frac{1}{2} \rho_L u^2 R^2 (\pi - \theta_0 + \sin\theta_0 \cos\theta_0) \qquad (2.2.3\text{-}3)$$

where u is the average liquid velocity seen by the bubble.

The surface tension force, F_s was expressed as

$$F_s = C_s 2\pi R \sigma \sin^2\theta_0 \qquad (2.2.3\text{-}4)$$

where C_s is an adjustable constant which take into account uncertainties in geometry and contact angle. The value of C_s can be determined by considering pool boiling data for the same solid / liquid system where surface tension and buoyancy forces are in balance at the point of bubble departure. Using boundary layer theory and invoking the standard drag law, Koumoutsos et al related the departure radius R_d in flow boiling to its value R_{dnp} in pool boiling by the expression :

$$\frac{R_d}{R_{dnp}} = \left(1 - a \frac{\rho_G U v_L}{\sigma}\right)^{n/2} \qquad (2.2.3\text{-}5)$$

where a and n are adjustable constants. From their own data, Koumoutsos et al found that $n = 4$ and $(a\rho_G v_L/\sigma) = 0.015$ sec/cm.

It should be noted that equation 2.2.3-5 satisfied the pool boiling condition for $U = 0$ and gives negative bubble departure radius (which is impossible) when $U > 66.67$ cm/s.

Al-Hayes and Winterton's correlation for bubble departure

Based on their experiment, in which bubble growth was initiated by gas diffusion, a correlation for bubble departure in forced flow was proposed by Al-Hayes and Winterton (1981). They also considered the buoyancy force, surface tension force and drag force. In their analysis, the bubble was assumed to be a truncated sphere, but distorted under the forces. All the forces were resolved in the flow direction parallel to the wall. The surface tension force arising from the difference between the advancing and receding bubble was accounted for.

For vertical upward flow, a force balance yields

$$F_s = F_b + F_d \qquad (2.2.3\text{-}6)$$

For vertical downward flow, the buoyancy force has a negative sign.

The expression of the buoyancy force for the truncated sphere was given as

$$F_b = \frac{1}{3}\pi R^3 \rho_L g (2 + 3\cos\theta_0 - \cos^3\theta_0) \qquad (2.2.3\text{-}7)$$

The expression of the drag force was given as

$$F_d = C_d \frac{1}{2}\rho_L u^2 R^2 (\pi - \theta_0 + \sin\theta_0 \cos\theta_0) \qquad (2.2.3\text{-}8)$$

which is the same as equation 2.2.3-3, but Al-Hayes and Winterton calculated C_d and u in ways different from that proposed by Koumoutsos et al. Based on their own data, Al-Hayes and Winterton proposed the following expressions for C_d :

$$C_d = 1.22 \qquad 20 < Re_b < 400 \qquad (2.2.3\text{-}9\ a)$$

$$C_d = \frac{24}{Re_b} \qquad 4 < Re_b < 20 \qquad (b)$$

where

$$Re_b = \frac{2R\rho_L u}{\eta} \qquad (2.2.3\text{-}10)$$

u is calculated from the appropriate velocity profile at a distance equal to one half the distance the bubble projects from the wall, i.e. at a distance $R(1+\cos\theta_0)/2$.

Assuming a reasonable variation in contact angle at intermediate points around the circumference of the line of contact, the net surface tension force in a direction parallel to the wall is (Winterton 1972) :

$$F_s = \frac{1}{2}\pi R \sigma \sin\theta_0 (\cos\theta_r - \cos\theta_a) \qquad (2.2.3\text{-}11)$$

With a multiplying factor attached to fit their own data, equation 2.2.3-11 became

$$F_s = \frac{1}{2}\pi R \sigma \sin\theta_0 (\cos\theta_r - \cos\theta_a)\left(\frac{58}{\theta_0 + 5} + 0.14\right) \qquad (2.2.3\text{-}12)$$

where θ_0 is in degrees.

Al-Hayes and Winterton (1981) claimed that their bubble departure correlation is also applicable to horizontal flow, and indeed, showed good comparison with data from horizontal flow. However, in their paper, there was no mention of how to account for forces normal to the wall, bearing in mind that the buoyancy force is normal to the wall in horizontal flow and should be balanced by the normal component of the surface tension force.

2.2.4 Bubble growth with translation in flowing liquid film

To the present author's knowledge, there have been no systematic studies of bubble growth in the liquid film in annular flow, despite this being the most important practical case. Some observations of nucleate boiling in climbing films were reported by Hewitt et al (1963) but their study was primarily concerned with the onset and suppression of nucleation and with observing the dryout phenomenon . Fortunately, the high speed cine films taken by Hewitt et al were still available and, in the present work, these have been analysed to give some information on bubble frequencies and sizes. Though this information was limited, it proved crucial in giving a more rational basis to the theory described in Chapter 3.

Though there are obvious differences to the case of annular flow, information on bubble growth in nucleate boiling in free falling liquid films may also be helpful. Cerza and Sernas (1985) have conducted an experiment to measure growth rate of bubbles formed in falling superheated laminar water films. They found that expressions of bubble growth rate for pool boiling underestimated their data.

In their experiment, Cerza and Sernas observed three stages in the bubble growth cycle. The first stage is the time between the departure of the previous bubble from a given site and the appearance of the next bubble. The second is the time between the appearance of a bubble at its site and its departure from that site. The third and the final stage is the time between the departure of a bubble and its burst. At the end of the second stage, the bubbles were seen to detach from their sites at diameters larger than the ambient film thickness. During the third stage, they grew to diameters that were an order of magnitude larger than the liquid film thickness. This relatively large bubble size was also reported by Fujita and Ueda (1976) from an experiment in which an annular flow channel was

used with downward flow of water film ranging from laminar to turbulent on the center tube. As we shall see in Chapter 3, as evidenced from the present anaylsis of the Hewitt et al (1963) cine film, bubble departure sizes in annular flow may also be an order of magnitude greater than the film thickness and, in this sense, the evidence from free falling films and annular flow situations show a similar pattern.

Cerza and Sernas attempted to model the bubble growth in the third stage. The bubble was assumed to be hemispherical with its base embedded in the liquid film, the thickness of the thin liquid film separating the bubble base from the wall being unknown in their experiment. For analysis purposes, the bubble was sliced from the top into strips with their length parallel to the flow direction. The velocity profile was relatively easy to solve for a laminar film, but with a slight complication that the bubble velocity had to be superimposed. The energy equation was then solved in the base film for each strip by applying appropriate boundary conditions. The heat flux at the bubble base was then calculated from the temperature gradient at the wall. Since the heat flux must be related to the bubble size through evaporation, the bubble growth rate and the bubble size could be calculated. The derivation of the model was lengthy and the solution was not in closed form. In predicting the third stage bubble growth, the initial size (at the end of the second stage) and the bubble velocity were input from experimental data into the model. Furthermore, a thickness of the bubble base film, which could not be measured in the experiment, had to be assumed to fit the bubble growth measurements.

CHAPTER 3

A MODEL OF EVAPORATIVE HEAT TRANSFER IN SINGLE-COMPONENT ANNULAR FLOW

As will have been seen from the survey in Chapter 2, there exists no comprehensive model for heat transfer in evaporating flow which covers the full range of quality and which includes both forced convective and nucleate boiling. This present chapter describes a new analytical approach which was developed in parallel with the experimental work which is described in Chapter 4. Though the surprising results of these experiments raise new questions which will have to be addressed in the future, it is felt that the analytical approach described in this present chapter does provide a new route to the calculation of heat transfer in evaporating flows.

The model described here follows the traditional interpretation of evaporative heat transfer, namely that of forced convective film heat transfer which is enhanced by the creation of bubbles at the wall by the nucleation process. The description of the forced convective heat transfer in the present model has the following new features :

(1) Recent Harwell developments in the modelling of annular flows are included to determine the local conditions prevailing in the channel. Specifically, the Owen and Hewitt (1987) model is used to calculate the interfacial shear stress, and the entrainment and deposition correlations of Govan et al (1988) are used to determine the local film flowrate. The iterative solution of these relationships gives a value of local film thickness and leads naturally to the determination of the forced convective heat transfer coefficient.

(2) Nearly all models have assumed that the turbulence properties vary with distance from the wall in a manner similar to that found in single phase flow. These models tend to overpredict the heat transfer coefficients and this has been interpreted as resulting from damping of turbulence at the interface. In the present model, account has been taken of this effect by using the model of Levich (1962).

The main problem is in calculating the contribution to the overall heat transfer arising from the nucleation, growth and release of bubbles formed at nucleation sites at the wall. The principal features of the model developed here are as follows :

(1) It was assumed that the additional heat transfer arising from bubble formation (nucleate boiling) was due to latent heat transport. That is, the additional heat flux was simply the mass of vapour bubbles formed per unit area per unit time multiplied by the latent heat of vaporisation. It is recognised that this is probably an oversimplication; the interaction of the flowing film with the growing bubbles will give an enhancement of the forced convective heat transfer. However, the area occupied by the growing bubbles is relatively small and it is assumed that any enhancement arising from their presence is roughly offset by the reduction of area for forced convection heat transfer which also results from their presence. Thus, the calculation of the additional heat flux arising from the nucleate boiling process involves a knowledge of the number of nucleation sites, the frequency of bubble departure from these sites and size of these bubbles on departure from the liquid film. It was assumed (in line with the Al-Hayes and Winterton 1981 analysis, see Section 2.2.3) that the bubble remained hemispherical during it's full growth cycle.

(2) The number of active nucleation sites was calculated by assuming that there is a fixed cumulative distribution of conical potentially active nucleation sites on the surface. It is postulated that incipient nuclei exist at these sites in the form of hemispherical bubbles which will only grow when the whole of their surface is at a temperature which exceeds the equilibrium temperature corresponding to the given bubble radius. The temperature profile within the liquid film can be calculated from the forced convective heat transfer analysis. Thus, if a specification is given of the cumulative distribution of potentially active nucleation site sizes, the number which are active can be calculated . This form of analysis is similar to that used by Davis and Anderson (1966) for subcooled boiling, except that these authors assumed a linear temperature gradient near the wall. For any given mass and heat

flux, it is of course possible to choose a cumulative distribution of potentially active nucleation sites which will fit the variation of heat transfer coefficient with quality. The acid test of any analysis is whether the variation of heat transfer coefficient with mass flux and heat flux can be correctly predicted.

(3) The bubble frequency is, by definition, the reciprocal of the time between the bubble departures from the nucleation sites. This time consists of a "waiting time" before the bubble growth is initiated and a "growth time" between initiation and bubble departure from the nucleation site. The waiting time was calculated from the Mikic and Rohsenow (1969) model and the subsequent bubble growth rate was calculated using the Plesset and Zwick (1954) equation. This growth period was terminated at the point where bubble departure was predicted by the Al-Hayes and Winterton (1981) model.

(4) Having established a methodology for calculating the number of active nucleation sites and bubble departure frequency from each site the remaining parameter to be determined was that of bubble size on release from the liquid film. There are no systematic experimental data for bubble release sizes and no established correlations. Using the above modelling methods for cumulative active site distribution and bubble frequency, it quickly became apparent that the data could only be reconciled if it were assumed that the bubble radius on release from the liquid film was about an order of magnitude greater than the thickness of the liquid film. This was surprising and , to check the physical reality of this finding, some measurements were made of some high speed cine films produced in the experiments of Hewitt et al (1963). In these experiments, a climbing water film was set up on the inner surface of an annular channel in which an upward steam flow had been set up. The inner surface was heated electrically and nucleate boiling on the inner surface could be viewed through the outer (glass) wall of the annulus. By analysing the resultant cine films, it was possible in the present work to estimate the bubble radius on release and also to estimate the bubble frequency. The liquid film thickness in the Hewitt et al experiments was estimated analytically and it was indeed found that the bubble release diameter was an

order of magnitude greater than the film thickness. Details of these measurements and calculations are given Appendix H. Though the estimated bubble release sizes are thus confirmed as being physically reasonable, there remains the problem (in developing a general prediction method) of correlating them. Some tentative attempts were made to produce a correlation but it was found that the assumption of a constant release size gave reasonable results for a given system.

It is believed that the model given here presents, for the first time, a rational basis for predicting heat transfer in evaporating flows. The complexity of the phenomena involved would make it foolish to claim any kind of generality for the models but at least a consistent framework has been developed. This development work will now be discussed in more detail in the same order as the above summary.

3.1 The components of the heat flux

The total heat flux in terms of the heat transfer coefficients can be expressed as :

$$\dot{q}_w = (\alpha_{con} + \alpha_{nuc})(T_w - T_{sat}) \qquad (3.1\text{-}1)$$

Equation 3.1-1 can also be written as :

$$\dot{q}_w = \dot{q}_{con} + \dot{q}_{nuc} \qquad (3.1\text{-}2)$$

Therefore

$$\dot{q}_{con} = \alpha_{con}(T_w - T_{sat}) \qquad (3.1\text{-}3)$$

$$\dot{q}_{nuc} = \alpha_{nuc}(T_w - T_{sat}) \qquad (3.1\text{-}4)$$

As both mechanisms determine the wall temperature or the wall heat flux, the calculation proceeds in an iterative manner.

In the calculation done here, the assumption is made that temperature profile is fully developed within the liquid film; that is, the rate of change of temperature with axial distance is constant independent of distance from the wall at any location. Since the film is very thin, this is a reasonable assumption. However, it does not mean that, at a given quality, the film flowrate is fixed. The value of film flowrate will depend on the up-stream history of the flow which will determine the extent of to which the liquid has been entrained

3.2 Convective Heat Transfer

For equilibrium annular flow with evaporation taking place at the vapour-liquid interface, the heat flux due to convection through the liquid film can be described by the following one dimensional heat transfer equation.

$$\dot{q} = -C_{pL}\rho_L(\kappa_L + \varepsilon_h)\frac{dT}{dy} \qquad (3.2\text{-}1)$$

In many "film heat transfer" theories, the common assumptions have been that the interface is planar and the eddy thermal diffusivity is equal to the eddy momentum diffusivity, i.e. $\varepsilon_m/\varepsilon_h = Pr_t = 1$. These assumptions are also adopted in the following analysis.

If the heat flux at the wall is $\dot{q}_{con}$, then the heat flux at distance y from the wall in a circular channel is given as :

$$\frac{\dot{q}}{\dot{q}_{con}} = \frac{r_o}{r_o - y} \qquad (3.2\text{-}2)$$

where $\dot{q}_{con}$ has been defined by equation 3.1-3, r_o is the tube internal radius and y is the distance from wall.

After combining equations 3.2-1 and 3.2-2 and expressing the result in non-dimensional form, it follows that

$$\left(\frac{r_o^+}{r_o^+ - y^+}\right) = \left(\frac{1}{Pr_L} + \frac{\varepsilon_m}{\upsilon_L}\right)\frac{dT^+}{dy^+} \qquad (3.2\text{-}3)$$

where the non-dimensional variables are defined as follows :

$$T^+ = \frac{C_{pL}\rho_L u^*(T_w - T)}{\dot{q}_{con}} \qquad (3.2\text{-}4)$$

$$y^+ = \frac{y u^*}{\upsilon_L} \qquad (3.2\text{-}5)$$

$$u^* = \sqrt{\frac{\tau_{avg}}{\rho_L}} \qquad (3.2\text{-}6)$$

$$\tau_{avg} = \frac{1}{\delta}\int_0^{\delta} \tau dy \qquad (3.2\text{-}7)$$

$$r_o^+ = \frac{r_o u^*}{\upsilon_L} \qquad (3.2\text{-}8)$$

If the film thickness δ and average shear stress are known, then equation 3.2-3 can be integrated to give :

$$T_i^+ = \int_0^{\delta^+} \left(\frac{r_o^+}{r_o^+ - y^+} \right) \frac{1}{1/Pr + \varepsilon_m/\upsilon_L} dy^+ \qquad (3.2\text{-}9)$$

In general, film heat transfer analysis overpredicts the heat transfer coefficient; an example of such comparisons is that of Aounallah (1983) who compared his data for water with the film heat transfer analysis of Hewitt (1961). However, for refrigerants (which are often used in experimental studies), the agreement with the predictions is often much closer.

It can be argued that the presence of the vapour-liquid interface would restrict the freedom of the eddies in the liquid film. For the same shear stress, the turbulence intensity at the vapour-liquid interface is less than that in single-phase flow at the same distance from the wall. Hence, the velocity gradient at the interface should be larger. By the same argument, for the same wall heat flux, the temperature gradient at the interface would be larger than predicted by a theory that does not account for some eddy damping in the liquid film.

Following Levich's (1962) suggestion, a damping factor is introduced here as a multiplier to the eddy diffusivity. Its general form is expressed as $(1 - y/\delta)^n$, where the exponent n is not a universal constant; its value has been varied in different analysis to fit experimental data (Mudawwar and EL-Masri, 1986). As a result, equation 3.2-9 is modified to :

$$T_i^+ = \int_0^{\delta^+} \left(\frac{r_0^+}{r_0^+ - y^+} \right) \frac{1}{1/Pr + \varepsilon_m/\upsilon_L (1 - y^+/\delta^+)^n} dy^+ \qquad (3.2\text{-}10)$$

Once T_i^+ is known, the convective heat transfer coefficient can be calculated from equation 3.2-4 .

$$\alpha_{con} = \frac{C_{pL} \rho_L u^*}{T_i^+} \qquad (3.2\text{-}11)$$

In order to solve equation 3.2-10, we need a value for δ and also information on the variation of τ with y in order to solve equation 3.2-7 to calculate τ_{avg} . To calculate δ and τ_{avg} , therefore, we must invoke the equivalent hydrodynamic model of annular flow and this will be described in section 3.2.1; in order to close this model, we need a value of the film flowrate $\dot{M}_{LF}$ and this involves prediction of entrainment and deposition of droplets to determine the flow ($\dot{M}_{LF}$) which remains in the film. The determination of deposition and entrainment rates is discussed in section 3.2.2

3.2.1 Calculation of film thickness and shear stress distribution knowing film rate

To calculate film thickness and shear stress in annular flow, we invoke the Owen and Hewitt (1987) model. In this model, new relationships were proposed for both the liquid film and the gas-droplet core. The development of such models is an evolutionary process, the Owen-Hewitt model being one of the latest (but almost certainly not the last) manifestation. However, the model contains sufficient new features to make it worthwhile including here.

The film model

In the film region of a vertical upward annular flow, ignoring the change of momentum of the liquid, a force balance results in the following expression :

$$\tau = \tau_i\left(\frac{r_i}{r}\right) - \frac{1}{2}\left(\frac{dp}{dz} + \rho_L g\right)\left(\frac{r^2 - r_i^2}{r}\right) \qquad (3.2.1\text{-}1)$$

where τ_i is the interfacial shear stress and r_i the interfacial radius.

Taking into account eddy damping in the liquid film, the shear stress distribution in the liquid film can be expressed by

$$\tau = \rho_L\left[\upsilon_L + \varepsilon_m\left(1 - \frac{y}{\delta}\right)^n\right]\frac{du}{dy} \qquad (3.2.1\text{-}2)$$

In non-dimensional form equation 3.2.1-2 becomes :

$$\frac{du^+}{dy^+} = \frac{\tau}{\tau_{avg}}\left[\frac{1}{1+\varepsilon_m/\upsilon_L(1-y^+/\delta^+)^n}\right] \qquad (3.2.1\text{-}3)$$

where

$$u^+ = \frac{u}{u^*} \qquad (3.2.1\text{-}4)$$

In equation 3.2.1-3 , ε_m is the single-phase eddy diffusivity, which can be derived, for instant, from Von Karman's universal velocity profile :

$$\frac{\varepsilon_m}{\upsilon_L} = 0 \qquad y^+ \le 5$$

$$\frac{\varepsilon_m}{\upsilon_L} = \frac{y^+}{5} - 1 \qquad 5 < y^+ \le 30 \qquad (3.2.1\text{-}5)$$

$$\frac{\varepsilon_m}{\upsilon_L} = \frac{y^+}{2.5} - 1 \qquad 30 < y^+$$

After substituting equation 3.2.1-1 and equation 3.2.1-5 into equation 3.2.1-3 and performing the integration, the non-dimensional velocity profile can be found.

The film flow rate can be calculated from the velocity profile by the following expression :

$$\dot{M}_{LF} = \int_{r_i}^{r_0} 2\pi r \rho_L u \, dr \qquad (3.2.1\text{-}6)$$

In non-dimensional form and with a change of variable, equation 3.2.1-6 can be written as :

$$\dot{M}_{LF}^+ = \int_0^{\delta^+}\left(1 - \frac{y^+}{r_0^+}\right)u^+ dy^+ \qquad (3.2.1\text{-}7)$$

where

$$\dot{M}_{LF}^+ = \frac{\dot{M}_{LF}}{2\pi r_0 \eta_L} \qquad (3.2.1\text{-}8)$$

$$y^+ = r_o^+ - r^+ \qquad (3.2.1\text{-}9)$$

It can be shown that if a Reynolds number based on the full pipe cross sectional area is defined for the film flow rate, we have the following relationship :

$$Re_{LF} = 4\dot{M}_{LF}^{+} \qquad (3.2.1\text{-}10)$$

The core model

In the core region, ignoring the change of momentum, a force balance gives the following expression :

$$\tau_i = -\frac{r_i}{2}\left(\frac{dp}{dz} + \rho_C g\right) \qquad (3.2.1\text{-}11)$$

where ρ_C is the homogeneous density in the core region and defined as :

$$\rho_C = \frac{\dot{M}_G + \dot{M}_E}{\dot{M}_G/\rho_G + \dot{M}_E/\rho_L} \qquad (3.2.1\text{-}12)$$

A homogeneous velocity in the core region can also be defined as :

$$U_C = \frac{1}{\pi r_i^2}\left(\frac{\dot{M}_G}{\rho_G} + \frac{\dot{M}_E}{\rho_L}\right) \qquad (3.2.1\text{-}13)$$

Then the interfacial friction factor can be defined in the conventional form as :

$$f_i = \frac{\tau_i}{\frac{1}{2}\rho_C (U_C - u_i)^2} \qquad (3.2.1\text{-}14)$$

Due to the presence of interfacial waves, which act like a rough pipe wall on the gas core flow, f_i is greater than for a smooth tube. Owen modified Nikuradse's single phase friction factor equation in deriving the following expression for calculating the interfacial friction factor, which is consistent with equation 3.2.1-14 :

$$\sqrt{\frac{2}{f_i}} = \frac{1}{K_{tp}}\ln\left(\frac{r_i}{e_E}\right) + A_r - \frac{1.5}{K_{tp}} + \frac{1}{K_{tp}}\left[\frac{2\delta}{r_0}\ln\left(\frac{r_0}{\delta}\right) - \frac{\delta}{r_0}\right] \qquad (3.2.1\text{-}15)$$

where K_{tp} is the two-phase Von Karman constant and e_E is the effective roughness defined as

$$e_E = e - y_{Lam} \qquad (3.2.1\text{-}16)$$

y_{Lam} is the thickness of the laminar sublayer of the vapour phase flowing alone and is calculated by the following equation :

$$y_{Lam} = \frac{5D}{Re_G}\sqrt{\frac{2}{f_G}} \qquad (3.2.1\text{-}17)$$

where f_G is the friction factor for the vapour phase flowing alone and is calculated by the Blasius equation :

$$f_G = 0.079 Re_G^{-0.25} \qquad (3.2.1\text{-}18)$$

A_r is a function, given by Nikuradse in graphical form, of the "roughness Reynolds number", Re^*, which was defined by Owen as :

$$Re^* = \frac{e u_i^* \rho_C}{\eta_G} \qquad (3.2.1\text{-}19)$$

where

$$u_i^* = \sqrt{\frac{\tau_i}{\rho_C}} \qquad (3.2.1\text{-}20)$$

The present author fitted a polynomial to the graphical roughness correlation of Nikuradse. The polynomial is presented as follows:

$$A_r = 4.0700142 + 13.416356 Re^* - 12.642043 Re^{*2} + 7.1099155 Re^{*3} - 2.9138685 Re^{*4} + 0.55962556 Re^{*5} \qquad 0.2 \le Re^* \le 2 \qquad (3.2.1\text{-}21\ a)$$

$$A_r = 8.5 \qquad 2 \le Re^* \qquad (b)$$

Correlations are required for e_E and K_{tp} in equation 3.2.1-15. Based on their own experimental data and others', Owen and Hewitt established some correlations for e in terms of the following non-dimensional parameters :

$$e^* = \frac{2e}{D} \qquad (3.2.1\text{-}22)$$

$$\delta^* = \frac{2\delta}{D} \qquad (3.2.1\text{-}23)$$

$$We_C = \frac{\rho_C U_C^2 (D - 2\delta)}{\sigma} \qquad (3.2.1\text{-}24)$$

The correlations are :

$$e^* = \mathrm{fn}_1(\delta^*) \qquad 0.011 < \delta^* \qquad (3.2.1\text{-}25\ a)$$

$$\frac{e^*}{\sqrt{Re_F}} = \mathrm{fn}_2\left(\sqrt{\frac{\delta^*}{We_C}} \times 10^{-4}\right) \qquad \delta^* < 0.008 \qquad (b)$$

$$e^* = \frac{(0.011-\delta^*)}{0.003} e^*_{0.011<\delta^*} + \frac{(\delta^*-0.008)}{0.003} e^*_{\delta^*<0.008} \quad 0.008 \le \delta^* \le 0.011 \qquad \text{(c)}$$

where equation 3.2.1-25c is an interpolation between equations 3.2.1-25a and 3.2.1-25b .

Owen also derived a correlation for the two-phase Von Karman constant as follows :

$$K_{tp} = \mathrm{fn}_3\left(\frac{\rho_G U_G^2}{\rho_H U_H^2}\right) \qquad \text{(3.2.1-26)}$$

where ρ_H and U_H are the homogeneous density and velocity of the two-phase flow.

The present author also fitted polynomials to fn_1 , fn_2 and fn_3. The coefficients in the polynomials are tabulated as follows :

	fn_1	fn_2	fn_3
a_0	8.7039779×10^{-3}	4.7951855×10^{-4}	0.13891391
a_1	7.4347371×10^{-1}	2.2001327×10^{-3}	0.12340717
a_2	2.2349825×10^{2}	$-5.5105181 \times 10^{-4}$	8.4672053×10^{-2}
a_3	-3.6609360×10^{3}	1.1973976×10^{-4}	3.407797×10^{-3}
a_4	2.1583735×10^{4}	$-9.0818094 \times 10^{-6}$	
a_5	-3.8516048×10^{4}		
a_6	-2.9827505×10^{4}		

The subscripts of the coefficients represent the exponents of their respective variables.

Since e_E and K_{tp} were actually derived from experimental data, equation 3.2.1-15 has taken proper account of the influence of interfacial waves on the shear stress.

From equation 3.2.1-1 , it can be seen that the film model requires values of pressure gradient and interfacial shear stress, which are calculated from the core model. Equally, equation 3.2.1-14 and equation 3.2.1-15 show that

the core model requires values of film thickness and interfacial velocity, which are calculated from the film model. Thus, the two models have to be solved simultaneously and iteratively for a given liquid film flowrate.

3.2.2 Calculation of liquid film flowrate

Interfacial waves in annular flow can be classified into ripple and disturbance waves (Hall Taylor et al 1963). The prevalence of each type of wave depends more on the flow rate of the liquid phase than that of the vapour phase. The disturbance waves, interacting with the vapour phase, are the source of liquid entrainment. On the other hand, the droplets in the gas core are constantly being deposited back onto the liquid film. The fraction of liquid entrained depends on the dynamic processes of entrainment and deposition. In equilibrium annular flow, the entrainment rate and deposition rate become equal and the net amount of liquid entrainment remains unchanged.

Asali (1984) proposed a correlation that relates the critical liquid film flow rate for the onset of droplet entrainment to the physical properties of the liquid and vapour phase. Later, Owen (1986) introduced a correlation similar in form to that of Asali but with different empirical constants. This correlation is as follows:

$$Re_{LFC} = \frac{\dot{m}_{LFC} D}{\eta_L} = \exp\left(5.8504 + 0.4249 \frac{\eta_G}{\eta_L} \sqrt{\frac{\rho_L}{\rho_G}} \right) \qquad (3.2.2\text{-}1)$$

where $\dot{m}_{FC}$ is the critical film mass flux based on the full pipe area.

For the region where droplet entrainment is taking place, there has again been an evolutionary development of empirical correlations for deposition and entrainment. Here, we use one of the most recent sets of correlations, namely those of Govan et al (1988). For droplet deposition, Govan et al defined a droplet mass transfer coefficient in the usual way by the following rate equation :

$$D_d = kC \qquad (3.2.2\text{-}2)$$

where D_d is the deposition rate, k the mass transfer coefficient and C the droplet concentration in the gas core, calculated assuming a homogeneous gas / droplet mixture.

Based on data from experiments where only deposition took place, Govan et al derived correlations for the mass transfer coefficient as follows :

$$k\sqrt{\frac{\rho_G D}{\sigma}} = 0.18 \qquad C/\rho_G \le 0.3 \qquad \text{(3.2.2-3 .a)}$$

$$k\sqrt{\frac{\rho_G D}{\sigma}} = 0.083\left(\frac{C}{\rho_G}\right)^{-0.65} \qquad 0.3 < C/\rho_G \qquad \text{(b)}$$

At equilibrium,

$$D_d = E = kC_E \qquad \text{(3.2.2-4)}$$

where C_E is calculated using the equilibrium entrained flow fraction. Govan et al were able to used data from equilibrium annular flow to calculate the entrainment rate, E , for which they then established a correlation as follows :

$$\frac{E}{\dot{m}_G} = 5.75\times 10^{-5}\left[(\dot{m}_{lF}-\dot{m}_{lFC})^2\frac{D\rho_L}{\sigma\rho_G^2}\right]^{0.316} \qquad \dot{m}_{lF} > \dot{m}_{lFC} \qquad \text{(3.2.2-5)}$$

For equilibrium annular flow, the equilibrium droplet concentration, C_E , can be expressed explicitly by substituting equations 3.2.2-3 and 3.2.2-5 into equation 3.2.2-4 . After some algebraic manipulations, the following expression can be written :

$$C_E = 5.75\times 10^{-5}\left[\frac{(\dot{m}_{lF}-\dot{m}_{lFC})^2 D\rho_L}{\sigma\rho_G^2}\right]^{0.316} \times \frac{\dot{m}_G}{0.18}\sqrt{\frac{\rho_G D}{\sigma}} \qquad C_E/\rho_G \le 0.3 \quad \text{and} \quad \dot{m}_{lF} > \dot{m}_{lFC} \qquad \text{(3.2.2-6 .a)}$$

$$C_E = \{5.75\times 10^{-5}\left[\frac{(\dot{m}_{lF}-\dot{m}_{lFC})^2 D\rho_L}{\sigma\rho_G^2}\right]^{0.316} \times \frac{\dot{m}_G}{0.083\rho_G^{0.65}}\sqrt{\frac{\rho_G D}{\sigma}}\}^{1/0.35} \qquad 0.3 < C_E/\rho_G \quad \text{and} \quad \dot{m}_{lF} > \dot{m}_{lFC} \qquad \text{(b)}$$

$$C_E = 0 \qquad \dot{m}_{lF} < \dot{m}_{lFC} \qquad \text{(c)}$$

By definition,

$$U_H C_E \pi r_i^2 = \dot{m}_E \pi r_0^2 \qquad \text{(3.2.2-7)}$$

where U_H is the average velocity of the core homogeneous flow and $\dot{m}_E$ is the mass flux of the entrained liquid based on the tube cross sectional area. Therefore,

$$\dot{m}_E = U_H C_E \left(\frac{r_i}{r_0}\right)^2 \qquad (3.2.2\text{-}8)$$

Then the film flow rate $\dot{M}_{LF}$ in equilibrium flow is given by :

$$\dot{M}_{LF} = \dot{M}_L - \pi r_o^2 \dot{m}_E \qquad (3.2.2\text{-}9)$$

The value of $\dot{M}_{LF}$ can then be used in the film analysis to calculate δ and τ_{avg} which can in turn be used in the heat transfer analysis.

3.3 Nucleate Boiling Heat Transfer

A nucleation cycle which forms part of the overall heat transfer model will be described. Then equations and correlations will be presented for calculating various parameters which are related to the heat transfer process involved in such a nucleation cycle.

Consider a single active nucleation site. From the moment when an equilibrium bubble starts to grow, latent heat is released at the bubble surface, this heat arising from the sensible heat in the layer of superheated liquid surrounding the bubble. The bubble does not have any translational motion during this attached growth stage. But, as the bubble grows larger, the drag force, imposed by the liquid flow on the bubble, increases. The bubble will detach when the drag force outbalances the surface tension force and the buoyancy force. Bubble departure usually takes place while the bubble size is still smaller than the mean liquid film thickness. Subsequent to bubble departure, two things happen simultaneously. One thing is that the detached bubble continues to grow when it travels up the liquid film flow, convected by the liquid flow. The moving bubble eventually bursts. The other thing is that, by transient conduction, a temperature profile over the active nucleation site starts to develop in the liquid that replaces the detached bubble. When this temperature profile satisfies the required superheat for incipience of nucleation, a new bubble starts to grow.

Heat transfer within one nucleation cycle over a single active nucleation site is modelled. Time average values of the variables involved are considered. According to the above description, a nucleation cycle consists of the waiting stage, the attached growth stage and the detached growth stage. The bubble frequency is based on the time taken in the waiting stage and the attached growth stage. For calculating the latent heat transferred, the bubble burst size in the detached growth stage must be known.

Assuming a hemispherical shape just before the bubble bursts, the nucleate boiling heat transfer coefficient is calculated from the following expression :

$$\alpha_{nuc} = \frac{\frac{1}{2}\left(\frac{4}{3}\pi R_B^3\right) h_{LG} \rho_G f_b n_a}{(T_w - T_{sat})} \qquad (3.3\text{-}1)$$

The estimation of the parameters in equation 3.3-1 will be discussed next.

Cumulative size distribution of potential nucleation sites

It is customary to idealise a potential nucleation site as a conical cavity in a flat surface. The parameters necessary to characterise such a cavity will be the included angle at the bottom ϕ and the radius at the cavity mouth r_c. Given a surface, the functional relationship between these parameters and the number of cavities is usually not known and has to be found either by direct observation or indirect methods such as heat transfer experiments or gas diffusion experiments (Brown, 1967). It must be pointed out that, in practice, direct observation may not find any cavity that has such an idealised shape. In general,

$$n = \text{fn}(\phi, r_c) \qquad (3.3\text{-}2)$$

where n is the cumulative number of cavities for the cavity included angles from ϕ up to ϕ_{max} and for the cavity mouth radius from r_c up to $r_{c\,max}$.

It is assumed that the Bankoff (1958) criteria for potentially active nucleation site applies for conical cavities (see Section 2.2.1.1). Since those cavities that do not satisfy the Bankoff criteria are swamped upon contact between the surface and the liquid, the included angle will not be considered in characterising the distribution of active nucleation sites. Equation 3.3-2 then becomes

$$n_a = \mathrm{fn}(r_c) \qquad (3.3\text{-}3)$$

where n_a is the cumulative number of potential nucleation sites for r_c up to $r_{c\max}$.

Brown's experiment (Brown 1967) showed that the cumulative size distribution of the potential nucleation sites can be described by a power law. This functional form was later adopted by Mikic and Rohsenow (1969) in proposing a pool boiling correlation. When written as a power law, equation 3.3-3 becomes

$$n_a = \left(\frac{r_{c\max}}{r_c} \right)^s \qquad r_c < r_{c\max} \qquad (3.3\text{-}4)$$

It should be noted that when $r_c \to 0 \quad n_a \to \infty$, which is not physically possible. $r_{c\max}$ is the maximum mouth radius, above which the number of potential nucleation sites is zero. Therefore, for a given surface, $r_{c\max}$ and s are the characterising factors.

Number of active nucleation sites

An equilibrium bubble will grow when the superheat of the surrounding liquid exceeds the critical (metastable equilibrium) value. The critical superheat temperature for bubble growth can be calculated from equation 2.2.1.2-5 in Section 2.2.1.2 :

$$T_b - T_{sat} = \frac{\mathcal{R} T_{sat}^2}{\mathcal{M} h_{LG}} \ln\left(1 + \frac{2\sigma}{R_E p_{sat}} \right) \qquad (3.3\text{-}5)$$

Here, a hemispherical shape is assumed for the equilibrium bubble. Therefore the bubble height is equal to the bubble radius and the mouth radius of the cavity, i.e. $y_b = R_E = r_c$.

Following the usual assumption, it is postulated that the incipient bubble will grow if the temperature around its surface is everywhere greater then the metastable equilibrium temperature T_b given by equation 3.3-5. Since heat is being transferred into the fluid, there is a temperature gradient from the wall. Thus, bubble growth will occur if the temperature at y_b (the top of the bubble) exceeds T_b.

Assuming that there is no effect of the presence of the bubble on the temperature profile in the liquid film, the local superheat temperature can be calculated from the convective model described in Section 3.2. The temperature profile in the liquid film is expressed as :

$$T = T_w - \frac{\dot{q}_{con}}{C_{pL}\rho_L u^*}\int_0^{y^+}\left(\frac{r_0^+}{r_0^+ - y^+}\right)\frac{1}{1/Pr + \varepsilon_m/\upsilon_L(1-y^+/\delta^+)^n}dy^+ \qquad (3.3\text{-}6)$$

If $\dot{q}_{con}$ is too low, then T is lower than T_b over the full range of site sizes; no bubble growth occurs. As $\dot{q}_{con}$ is increased, a condition occurs at which T at y_b (calculated from equation 3.3-6) reaches T_b (calculated from equation 3.3-5). Bubbles having this particular value of $y_b(=R_E)$ will then grow. As the heat flux is further increased, then a range of cavity sizes from r_{c1} to r_{c2} is activated, where $r_{c1} < r_{c2}$. Within, this range of site sizes, the specified condition is obeyed. Provided the cumulative size distribution of the potential nucleation sites is known, then one can calculate the total number of active nucleation sites.

In some boiling incipience analysis, the value of $r_{c\,max}$ was considered to be in the order of a few microns (1×10^{-6} m). On the other hand, the liquid film thickness is in the region from 1×10^{-4} m up to a few millimetres. The rather flat temperature profile in the turbulent liquid film can result in a upper size limit of potential nucleation site being larger than the maximum size of available active nucleation sites, i.e. $r_{c2} > r_{c\,max}$. Therefore, the number of active nucleation sites is only determined by r_{c1}

Bubble frequency

Since the superheated layer starts to develop immediately after the bubble has detached, bubble frequency depends on the waiting time and the attached growth time and is defined as :

$$f_b = \frac{1}{t_w + t_g} \qquad (3.3\text{-}7)$$

Based on a transient conduction model, Mikic and Roshenow (1969) have derived an implicit equation for the waiting time :

$$T_b - T_{sat} = (T_w - T_{sat})\,\mathrm{erfc}\left(\frac{R_E}{2\sqrt{\kappa t_w}}\right) \qquad (3.3\text{-}8)$$

where κ_L is the thermal diffusivity of the liquid. Here, it is assumed that heat transfer by conduction from the wall dominates over heat transfer by convection along the wall. The term in the complementary error function is usually small and equation 3.3.8 can be written as

$$T_b - T_{sat} = (T_w - T_{sat})\left(1 - \frac{R_E}{\sqrt{\pi \kappa t_w}}\right) \qquad (3.3\text{-}9)$$

Due to the small size of the active nucleation site, the equilibrium bubble is still within the region of linear temperature profile, i.e.

$$\dot{q}_w = \frac{\lambda_L (T_w - T_b)}{R_E} \qquad (3.3\text{-}10)$$

The use of $\dot{q}_w$ in equation 3.3-11 is consistent with the fact that transient conduction during this waiting period contributes in effect to the total heat flux.

Combining equations 3.3-9 and 3.3-10 gives

$$t_w = \frac{1}{\pi \kappa_L}\left[\frac{\lambda_L (T_w - T_{sat})}{\dot{q}_w}\right]^2 \qquad (3.3\text{-}11)$$

It is interesting to see that the waiting time is independent of the cavity size provided the equilibrium bubble is within the linear temperature region.

Once bubble growth starts, then it continues for a period t_g with the bubble still attached to the nucleation site. The growth behaviour has been calculated, in the current model, from the Plesset-Zwick equation (see Section 2.2.2.1.2). This equation is for a spherical bubble but is used here for the hemispherical bubble; for a given fluid temperature surrounding the bubble, symmetry dictates that the radial growth rate will be the same. The non-dimensional form of the Plesset-Zwick equation is as follows :

$$R_b^+ = \sqrt{t_g^+} \qquad (3.3\text{-}12)$$

where

$$R_b^+ = \frac{A R_b}{B^2} \qquad (3.3\text{-}13)$$

$$t_g^+ = \frac{A^2 t_g}{B^2} \qquad (3.3\text{-}14)$$

and

$$A = \left(\frac{\pi h_{LG} \rho_G \Delta T}{7 \rho_L T_{sat}} \right)^{\frac{1}{2}} \qquad (3.3\text{-}15)$$

$$B = \left(\frac{12}{\pi} \kappa_L \right)^{\frac{1}{2}} Ja \qquad (3.3\text{-}16)$$

$$Ja = \frac{\Delta T C_{pL} \rho_L}{h_{LG} \rho_G} \qquad (3.3\text{-}17)$$

ΔT is assumed to be half the temperature difference across the liquid film, i.e.

$$\Delta T = (T_w - T_{sat})/2 \qquad (3.3\text{-}18)$$

Equation 3.3-12 is applicable to bubble growth controlled by heat diffusion when $t_g^+ \gg 1$.

Bubble departure size

Calculation of the bubble departure size is based on the Al-Hayes and Winterton (1981) criterion, which was established from a force balance for a bubble departing from the heated surface (see Section 2.2.3). The forces acting on the bubble include buoyancy force, surface tension force, and drag force. For a vertical surface and upward flow, the force balance gives :

$$F_s = F_b + F_d \qquad (3.3\text{-}19)$$

where

$$F_s = \frac{\pi \sigma R_d \sin\theta_0}{2} (\cos\theta_r - \cos\theta_a) \left(\frac{58}{\theta_0 + 5} + 0.14 \right) \qquad (3.3\text{-}20)$$

$$F_b = \frac{\rho_L g \pi R_d^3}{3} (2 + 3\cos\theta_0 - \cos^3\theta_0) \qquad (3.3\text{-}21)$$

$$F_d = \frac{C_d \rho_L u_b^2 R_d^2}{2} (\pi - \theta_0 + \cos\theta_0 \sin\theta_0) \qquad (3.3\text{-}22)$$

F_s is the surface tension force, F_b the buoyancy force and F_d the drag force, R_d the bubble departure radius. θ_0 is the equilibrium contact angle for no flow. θ_a and θ_r are the advancing and receding angles respectively. The advancing angle is on the side of the bubble that faces the coming flow. The receding angle sees the wake of the flow. All the angles are in terms of degrees. u_b is the local fluid velocity at half the bubble height, i.e. $R_d(1+\cos\theta_0)$ and C_d is the drag coefficient. Assuming the bubble can be approximated by a solid sphere on the wall of a close conduit with single phase flow, the drag coefficient can be calculated using the correlation proposed by Idelcik (1986).

$$C_d = \left(\frac{24}{Re_b} + \frac{4.565}{3\sqrt{Re_b}} - \frac{0.491}{\sqrt{Re_b}}\right)[1-\tanh(2.5\times10^{-4}Re_b) \qquad (3.3\text{-}23)$$

$$+0.42\tanh(2.5\times10^{-4}Re_b)+0.02\tanh(1\times10^{-4}Re_b)]$$

where

$$Re_b = \frac{2R\rho_L u_b}{\eta_L} \qquad (3.3\text{-}24)$$

Bubble burst size

There are no published correlations (or even data) for bubble burst size in annular flow nucleate boiling. The procedure followed here has been to predict the bubble burst size by applying the above models for the number of nucleation sites and the frequency of bubble generations from these sites; the bubble burst size required to satisfy the measured heat flux was determined. As was mentioned in the introduction to this chapter, the burst sizes predicted by this method were typically an order of magnitude greater then the liquid film thickness. This seemed surprising and the cine films produced by Hewitt et al (1963) were reanalysed to investigate bubble release sizes and frequency. This analysis is described in Appendix H. The film thickness was also estimated and it was shown that, indeed, the bubble burst size was an order of magnitude greater than the film thickness

In order to have a general model, a correlation of bubble burst diameter is required and an attempt to produce such a correlation is described in Section 3.4

3.4 Analysis of heat transfer data using assumptions of hydrodynamic equilibrium

The refrigerant-12 data of Steiner (1988) and Bandel (1973) and the water data of Bennett (1976) were selected for analysis using the methodology described above. In this analysis, it was assumed that hydrodynamic equilibrium prevailed at the location of the heat transfer measurement (i.e. the rate of droplet deposition equals the rate of entrainment and the film flow rate can be calculated directly using equations 3.2.2-6 and 3.2.2-9). This is probably a reasonable assumption for the Steiner and Bandel data sets, but less so for the Bennett set. We shall discuss the case of non-equilibrium annular flow in Section 3.5.

Since the literature could not provide reliable data for the required values of contact, advancing and receding angles for the Al-Hayes and Winterton bubble departure criteria, in all the analysis described below, the values of the contact, advancing and receding angles were assumed to be 90°, 100° and 80° respectively.

Analysis of Steiner's data

The data set of Steiner (1988) was for evaporating flow of R12 in a horizontal tube. Though it would have been preferable to use data for a vertical tube, there is a surprising dearth of comprehensive data sets for this case. In view of the fact that the mass fluxes in the Steiner (and Bandel) data sets were high enough to minimise gravitational stratification, it was decided to use this (very comprehensive) data. At the qualities in Steiner's data set (0.3 to 0.8) annular flow was very well established. In the analysis, the gravity term in equations 3.2.1-1 and 3.2.1-11 and the buoyancy force in the Al-Hayes and Winterton criteria (equation 3.3-21) were dropped since the tube was horizontal.

The experimental rig in Steiner's experiment had a preheater that generated and controlled the quality, a 1.5 m long calming section for equilibrium development, and a 0.5 m long test section subject to electric heating.

The following values were established for the parameters in the models described above :

Damping factor : The exponent n in equation 3.2-10 was set to zero implying no interface damping of the turbulence. This was consistent with the finding that analytical predictions without damping have previously been found to be in better agreement with result for refrigerants than they were for water. However, the choice of a non-zero value for n could probably have given an even closer fit to the data.

Cumulative size distribution of potential nucleation site :The values used in equation 3.3-4 were $s = 4$ and $r_{c\,max} = 10$ μm (1×10^{-5} m). The calculations showed that y_b^+ corresponding to $y_b (= r_{c\,max})$ was always less than 5, i.e. within the laminar sublayer and justifying the assumption of a linear temperature profile in the fluid adjacent to the incipient bubble.

Using the above values, the bubble burst size could be calculated from the experimental heat transfer coefficients. These calculated values are plotted in figure 3.4-1. against the liquid film thickness (which was calculated in the hydrodynamic part of the analysis described above). The bubble burst size would have to be an order of magnitude greater than the film thickness for consistent prediction. As was mentioned above, this surprising result is consistent with measurements made on the Hewitt et al (1963) cine film (see Appendix H). Other results calculated in the analysis of the Steiner data are shown in figures 3.4-2 to 3.4-4 and are as follows :

(a) Bubble departure diameter (figure 3.4-2) : Again, this was plotted against film thickness and, as will be seen, the departure diameter is much less than the film thickness over the whole range, thus justifying the use of the drag coefficient expressed in equation 3.3-23

(b) Bubble frequency (figure 3.4-4) : Here, the calculated bubble frequency from a given site is plotted against heat flux. The frequencies are of the order of several hundred bubbles per second and generally increase with increasing heat flux. The order of magnitude of bubble frequency is also in accord with

Figure 3.4-1

Bubble burst radius plotted against mean liquid film thickness

based on Steiner's evaporation data of R12 in horizontal tube with 14 mm inside diameter

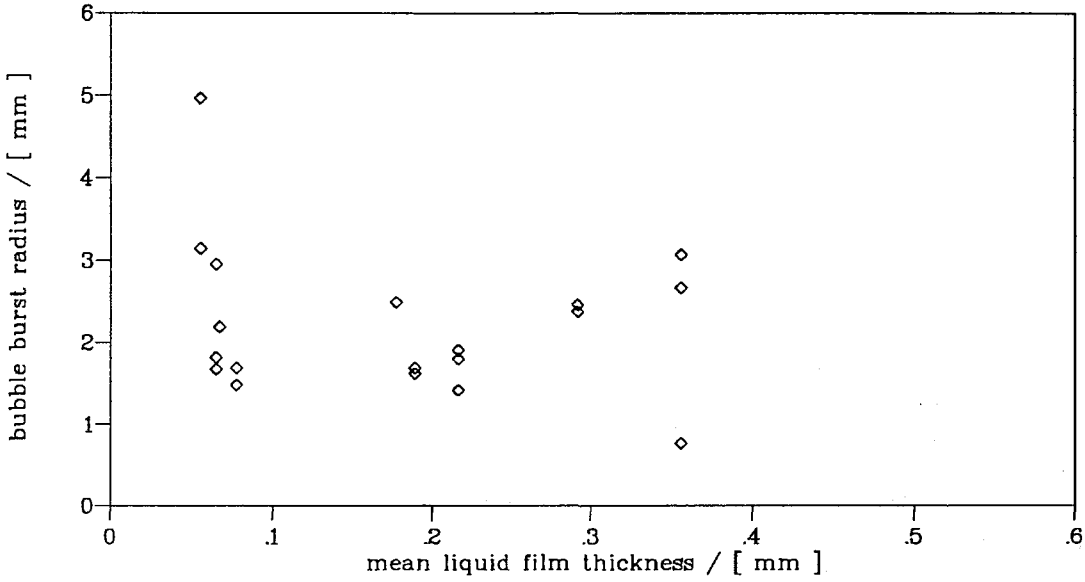

saturation temperature range (C) : -20 to 0
mass flux range (kg/m~2/s) : 128 to 241
quality range : 0.3 to 0.8

Figure 3.4-2

Bubble departure radius plotted against mean liquid film thickness

based on Steiner's evaporation data of R12 in horizontal tube with 14 mm inside diameter

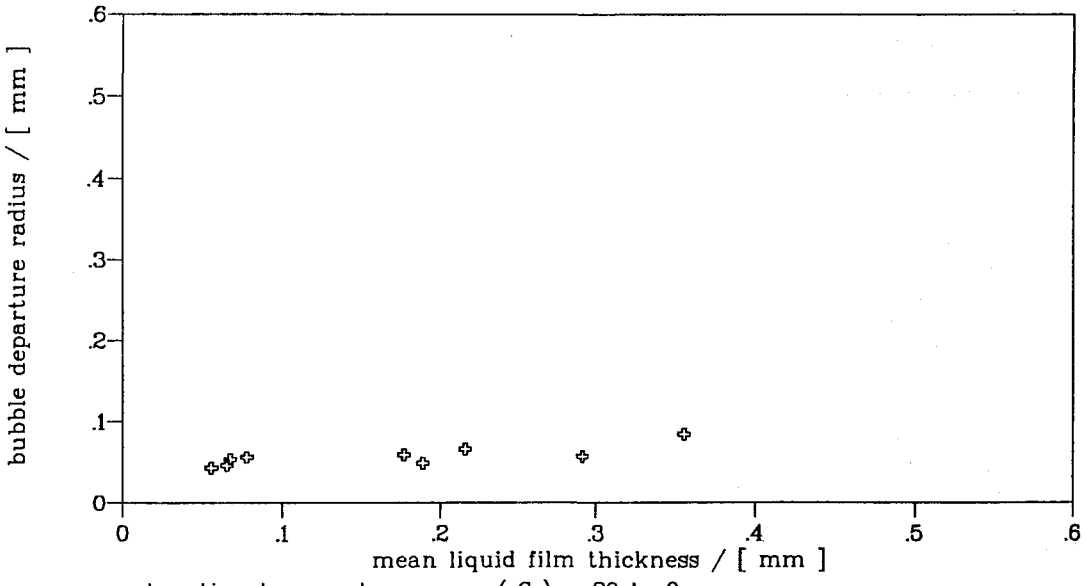

saturation temperature range (C) : -20 to 0
mass flux range (kg/m~2/s) : 128 to 241
quality range : 0.3 to 0.8

Figure 3.4-3

Bubble frequency plotted against total heat flux
based on Steiner's evaporation data of R12 in
horizontal tube with 14 mm inside diameter

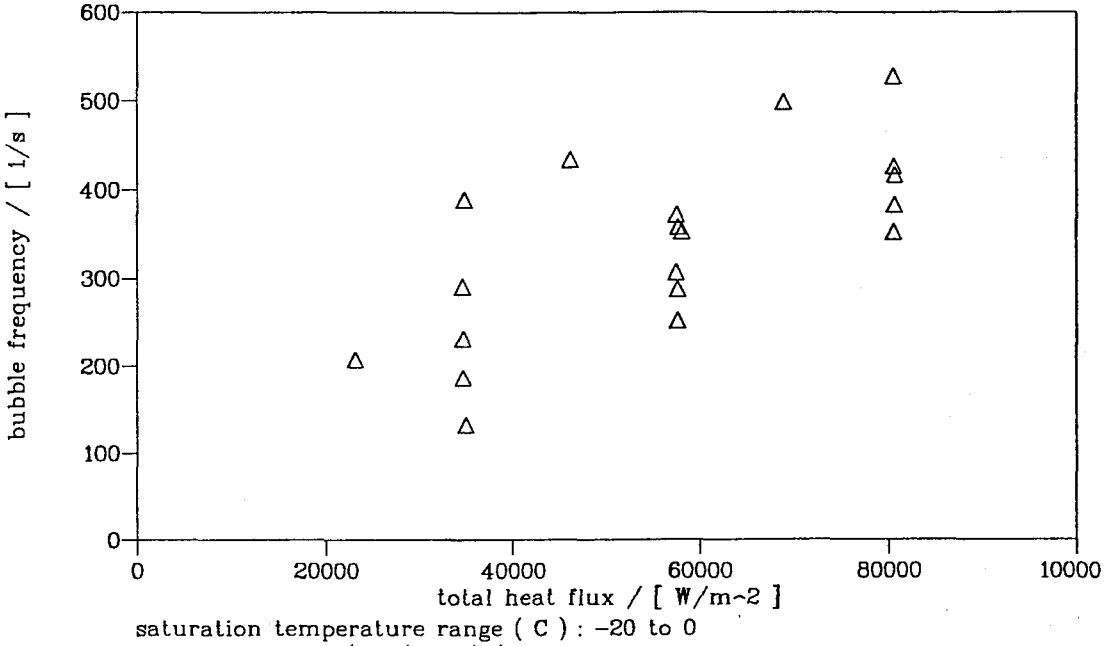

saturation temperature range (C) : -20 to 0
mass flux range (kg/m^2/s) : 128 to 241
quality range : 0.3 to 0.8 (see point labels)

Figure 3.4-4

Experimental and calculated heat transfer
coefficients plotted against total heat flux
based on Steiner's evaporation data of R12 in
horizontal tube with 14 mm inside diameter

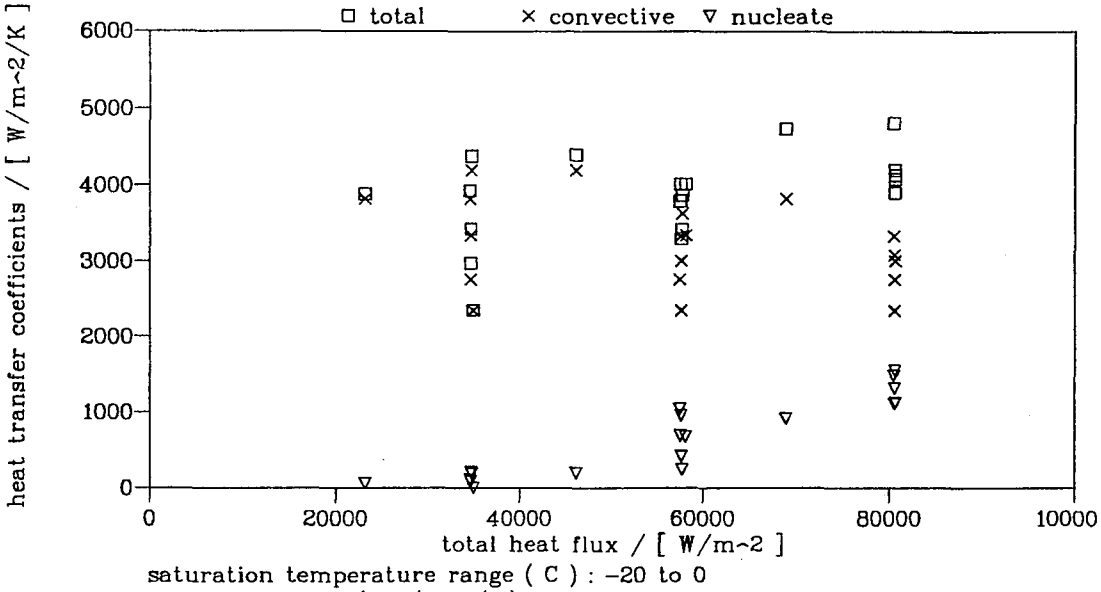

saturation temperature range (C) : -20 to 0
mass flux range (kg/m^2/s) : 128 to 241
quality range : 0.3 to 0.8

the analysis of the Hewitt et al (1963) cine films (see Appendix H) and also with the frequency measurements of Fujita and Ueda (1976).

(c) Components of heat transfer coefficient (figure 3.4-4) : Here, the total , convective and nucleate boiling heat transfer coefficients are plotted for reference for this data. Since the total coefficient comes from the data and the convective coefficient is calculated from the model, the nucleate boiling coefficient represents the residual. This residual value increases generally with increasing heat flux reflecting mainly the increasing number of active nucleation sites and the increasing bubble frequency.

Analysis of Bandel's data

The Bandel (1973) data was extracted from a University of Birmingham data bank for data [1] of evaporation heat transfer. Bandel's (1973) data was also for horizontal flow of R12 and was taken using the same experimental rig as Steiner's but with a wider range of mass flow rates. Comparison of the Steiner and Bandel data sets reveals some surprising differences as illustrated in figure 3.4-5. Though the measured heat transfer coefficient are similar at low heat fluxes where convection dominates, there are large differences at high heat fluxes probably reflecting the effect of differences in the tube surface condition on the nucleation site distribution. This illustrates one of the main recurrent problems of predicting heat transfer for this region. In predicting the Bandel data, the following parameters were assumed:

(a) Damping factor : n in equation 3.2-10 was taken as zero, as with the Steiner data.

(b) Cumulative size distribution of active nucleation sites : The values used in equation 3.3-4 were $s = 8$ and $r_{c\,max} = 10$ μm. The s value is twice that used for the Steiner data, attempting to reflect the obvious change in surface characteristics.

---

1 I am grateful to Mr. D. Kennedy who, working as a consultant in Harwell, helped me in obtaining some data from the data bank.

Figure 3.4-5

Comparison of evaporation data from Bandel and Steiner under similar conditions
horizontal test section ; tube i.d. 14 mm
saturation temperature at 0 C

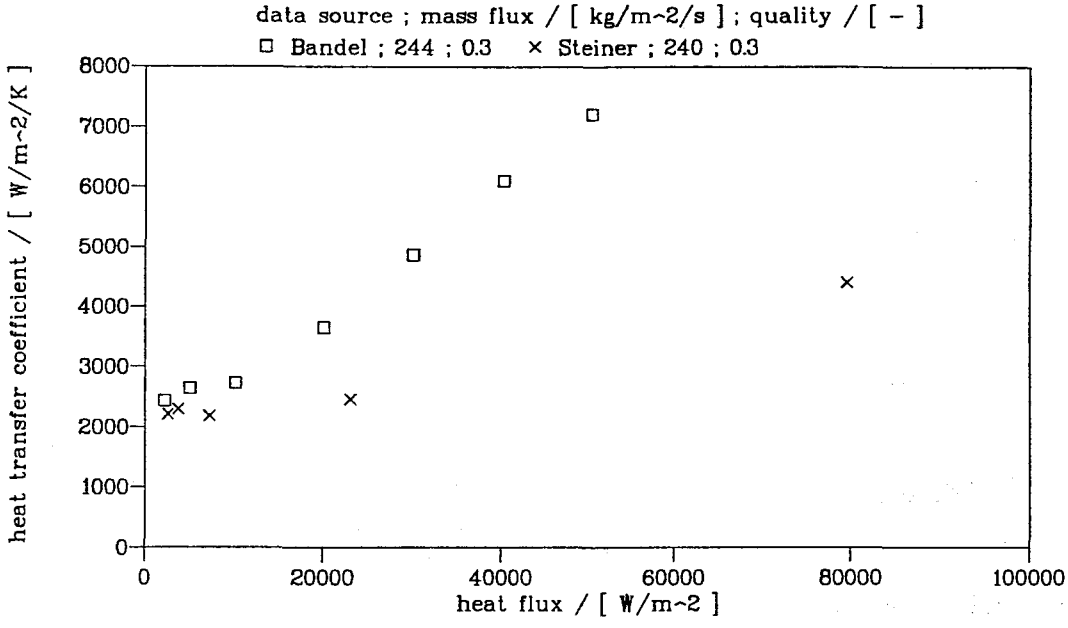

Figure 3.4-6

Bubble burst radius plotted against mean liquid film thickness
based on Bandel's evaporation data of R12 in horizontal tube with 14 mm inside diameter

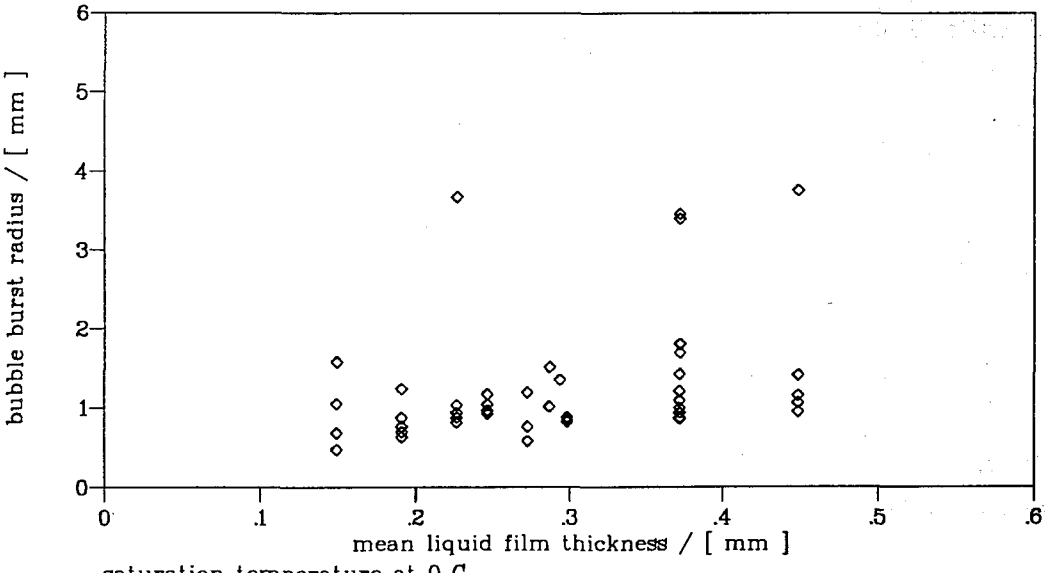

saturation temperature at 0 C
mass flux range (kg/m~2/s) : 104 to 706
quality range : 0.3 to 0.5

The bubble burst sizes calculated (see figure 3.4-6) are of a similar order of magnitude to those predicted from the Steiner data as are the other predicted parameters.

Analysis of Bennett's data

The Bennett (1976) data were also taken from the University of Birmingham data bank. These data were for vertical up-flow of water and steam and have a wide range of heat flux, though the maximum quality is not more than 0.13. The Wallis (1961) correlation for prediction of flow reversal was used to sort out the data points for annular flow. For annular flow to prevail, the following criteria must be satisfied :

$$V_G^* = \frac{V_G \rho_G^{0.5}}{\sqrt{gD(\rho_L - \rho_G)}} > 1 \qquad (3.4\text{-}25)$$

Before going any further, it should be pointed out that Bennett's data were not taken under equilibrium conditions. The test section in his experiment was 0.076 m long mounted at the exit of a 1.08 m long preheater. There was no calming section for equilibrium development.

In predicting the Bennett data set, the following parameters were used :

(a) Damping factor : To reflect the known overprediction of water data by convective heat transfer models not taking account of interface damping, a value of n = 1.5 was taken in 3.2-10

(b) Cumulative size distribution of active nucleation sites : The values used in equation 3.3-4 were s = 4 and $r_{c\,max}$ = 10 μm.

The calculated bubble burst radius, plotted against heat flux due to nucleate boiling, is shown in figure 3.4-7. Again, the general trend and the average bubble burst radius are similar to that for the R12 data. The bubble frequency (see figure 3.4-8) is calculated to be somewhat higher in the case of the Bennett data.

Attempted correlation for bubble burst diameter

As was pointed out above, to obtain complete closure of the model, a correlation would be required for bubble burst radius. Many forms of

Figure 3.4-7

Bubble burst radius plotted against heat flux due to nucleate boiling
using Bennett's evaporation data for vertical up-flow of water and steam

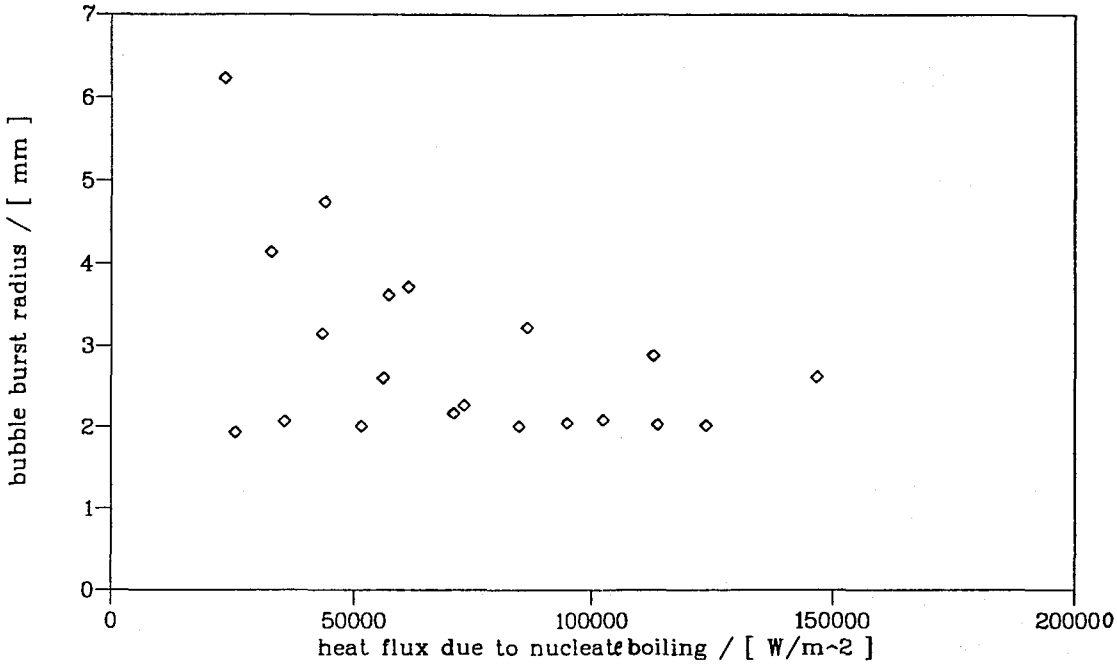

Figure 3.4-8

Bubble frequency plotted against heat flux due to nucleate boiling
using Bennett's evaporation data for vertical up-flow of water and steam

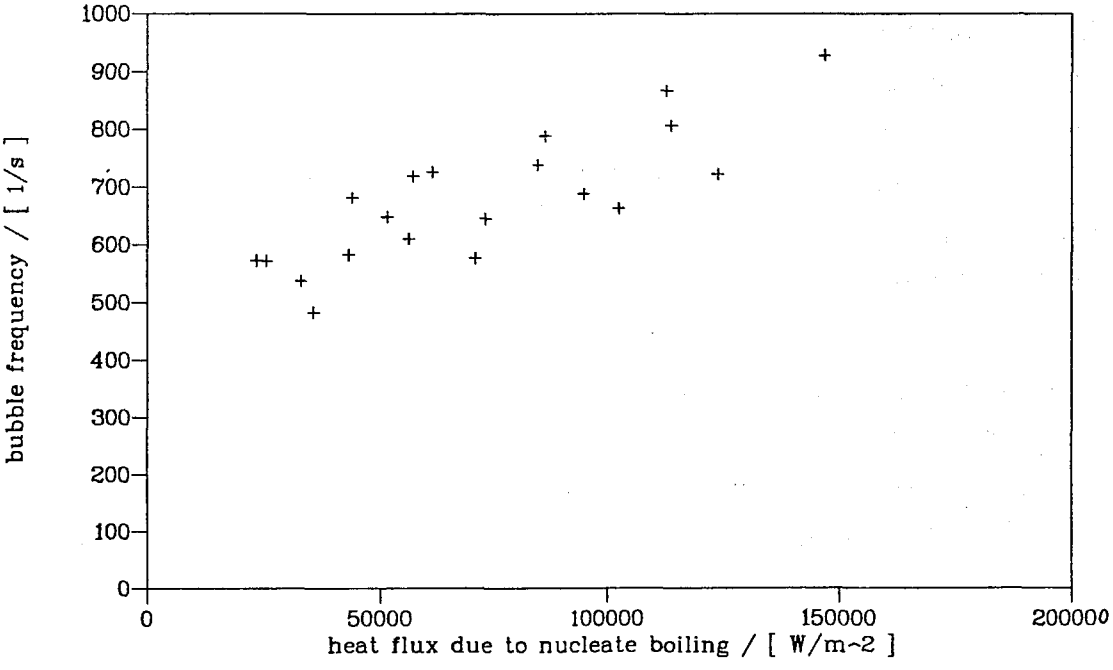

correlation were explored but, none which appeared rational were successful. Perhaps the least unsuccessful was in terms of the following groups

$$We = \frac{\rho_G U_G^2 D_B}{\sigma} \qquad (3.4\text{-}26)$$

$$Re_{Lo} = \dot{m} D / \eta_L \qquad (3.4\text{-}27)$$

$$Bo_G = \frac{\dot{q}_{nuc}}{h_{LG} \dot{m} x} \qquad (3.4\text{-}28)$$

and the density ratio ρ_G/ρ_L where D_B is the bubble burst diameter. A plot of $We(\rho_G/\rho_L)^4/Re_{Lo}$ against Bo_G shows a reasonable correlation for the R12 data but, unfortunately, gives a rather poor representation of the Bennett water data as is seen in figure 3.4-9

There is an obvious need for a comprehensive correlation for bubble burst diameter but the matter was not pursued further in the present work. The differences between boiling and condensation, as revealed by the experiments presented in Chapter 4, may necessitate a radical rethink of bubble initiation and growth in annular flow.

3.5 Predictions of the model assuming a constant bubble burst size

The calculation reported in Section 3.4 showed that the bubble burst size required for closure did not vary too greatly with the flow quality and heat flux and, as an interim measure, it was decided to perform comparison calculations using a constant bubble size, namely 1.5 mm. Using the value of D_B, the overall model was used to predict the data sets of Steiner, Bandel and Bennett. The values of the interfacial damping and active site distribution parameters were those stated for the respective data sets in Section 3.4.

The predicted heat transfer coefficients are compared with the Bandel data in figure 3.5-1. Reasonable agreement is observed but perhaps the most important result is that the correct form of the curves has been predicted on a rational basis. The the author's knowledge, this is the first time that such curves have been predicted using a combination of forced convective and nucleation site activation models.

Figure 3.4-9

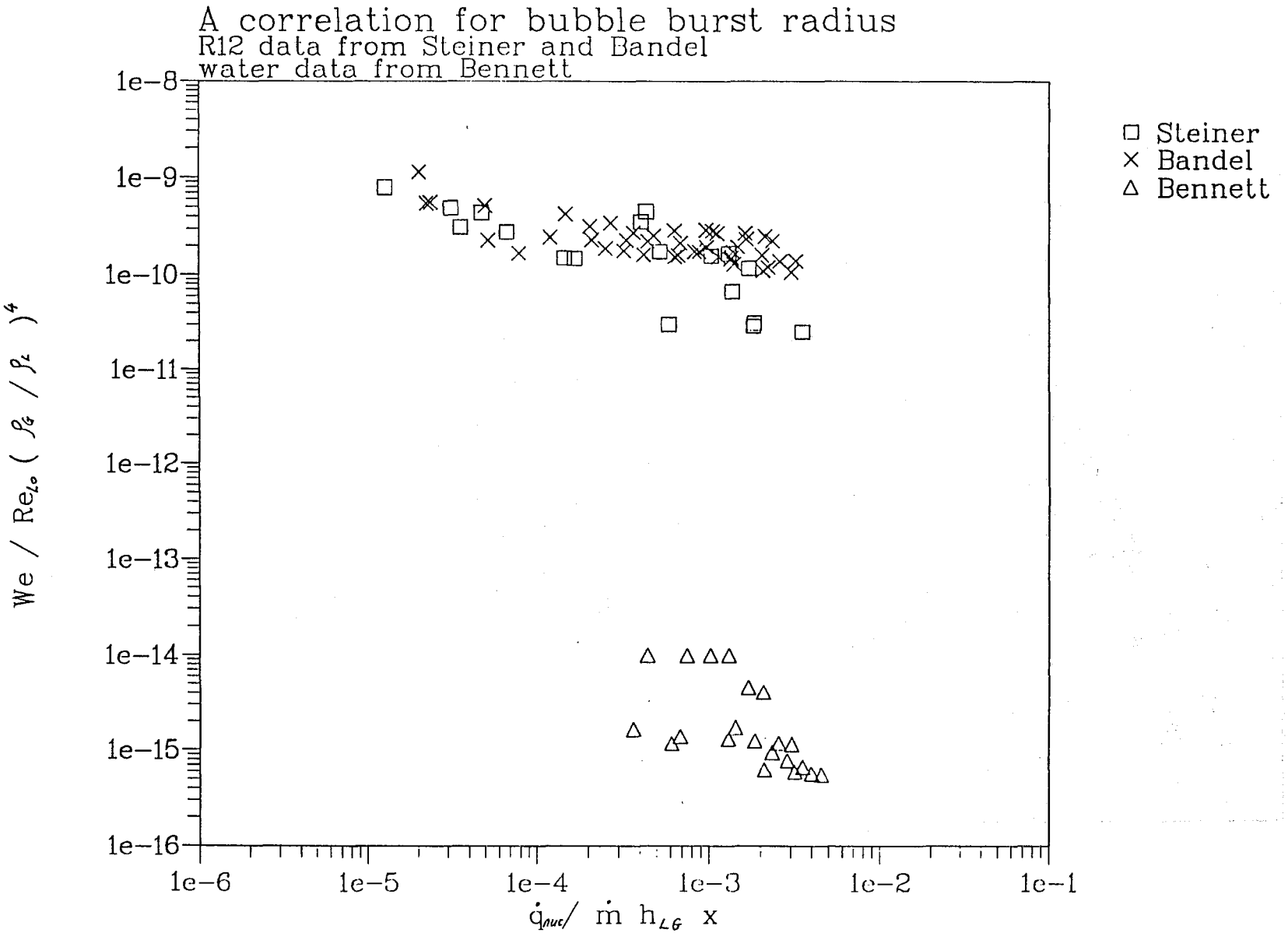
A correlation for bubble burst radius
R12 data from Steiner and Bandel
water data from Bennett
Steiner
Bandel
Bennett
1e−8
1e−9
1e−10
1e−11
1e−12
1e−13
1e−14
1e−15
1e−16
1e−6
1e−5
1e−4
1e−3
1e−2
1e−1
We / Re_Lo (ρG / ρL)^4
q̇nuc/ ṁ h_LG x

Figure 3.5-1

Predicted heat flux effect on heat transfer coefficient for a data set of Bandel
horizontal evaporating flow of R12 in tube with
14 mm inside diameter

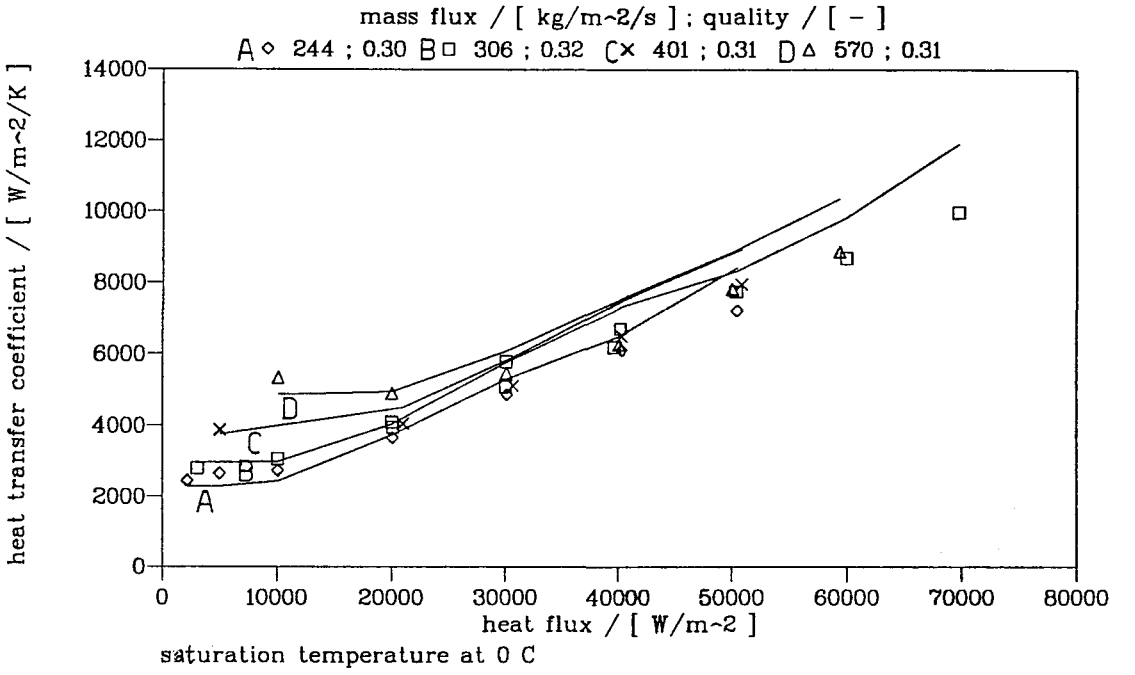

Figure 3.5-2

Predicted heat transfer coefficients compared with data sets of Bandel and Steiner
(1.5 mm bubble burst radius assumed)

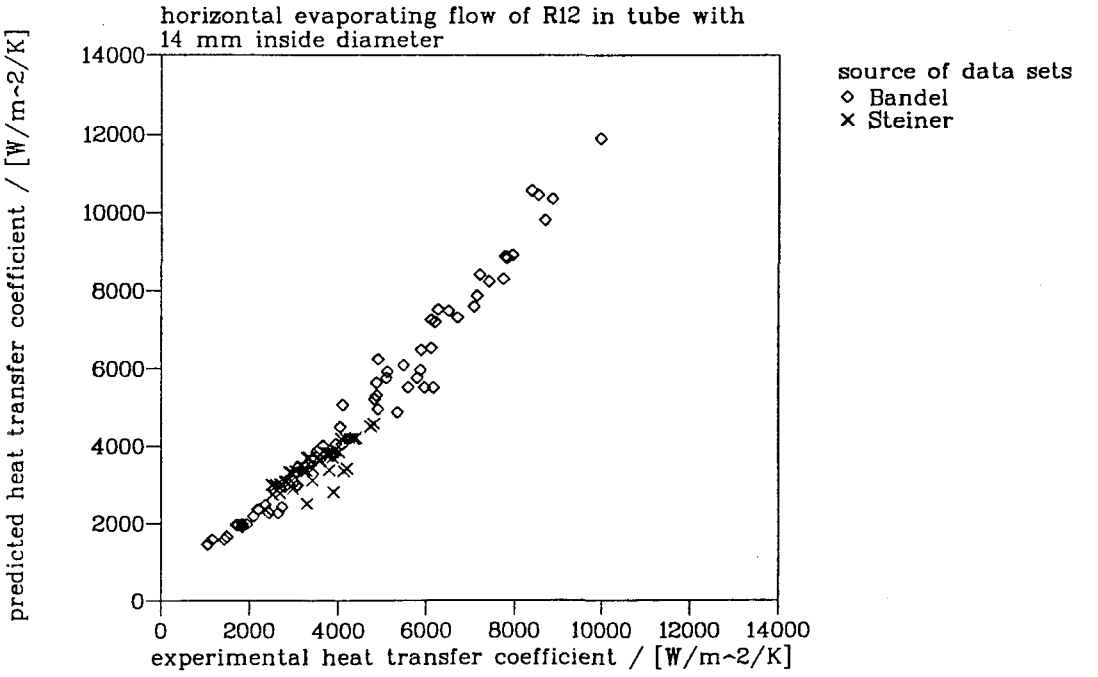

Figure 3.5-2 shows a comparison of the Steiner and Bandel experimental values with those calculated. The model slightly overpredicts the data but this could be adjusted, of course, by taking a non-zero value of the damping coefficient.

For the water data of Bennett, the agreement is less satisfactory as is shown in figure 3.5-3. A contributory factor may be that the conditions in the Bennett experiments are likely to be significantly away from hydrodynamic equilibrium, as mentioned above. The prediction of data under non-equilibrium conditions is discussed in the next Section.

3.6 Consideration of non-equilibrium effects in annular flow

Wadekar (1988) has obtained some data for the evaporation of ethanol flowing in a 3 m long vertical tube subjected to uniform electric heating. The inside diameter of the tube was 10 mm. Wall temperatures and two-phase pressures were measured along the heated tube.

As a starting point, calculationsof exactly the same form as those described in Section 3.4 were carried out for this ethanol data. The following parameterswere assumed:

(a) Damping factor : n in equation 3.2-10 was taken as zero consistent with the R12 data rather than with the water data.

(b) Cumulative size distribution of active nucleation site : The values used in equation 3.3-4 were $s = 4$ and $r_{c\,max} = 10\ \mu m$.

The calculated bubble burst radii are shown in figure 3.6-1. They lie in the same order of magnitude as those calculated for the other data sets, though there is a distinct effect of heat flux. In these calculations, local hydrodynamic equilibrium was assumed.

Since the flow quality changes along the channel, the flow would only adventitiously be at hydrodynamic equilibrium at any point. Thus at given quality, the film flow rate would vary with upstream history, namely with heat flux. Such non-equilibrium effects are discussed, for instance, by Hewitt (1982).

Figure 3.5-3

Measured heat transfer coefficients compared with prediction of Bennett's data for evaporating up-flow of water and steam

mass flux 310 kg/m^2/s ; pressure 2 bar

tube i.d. 25.4 mm

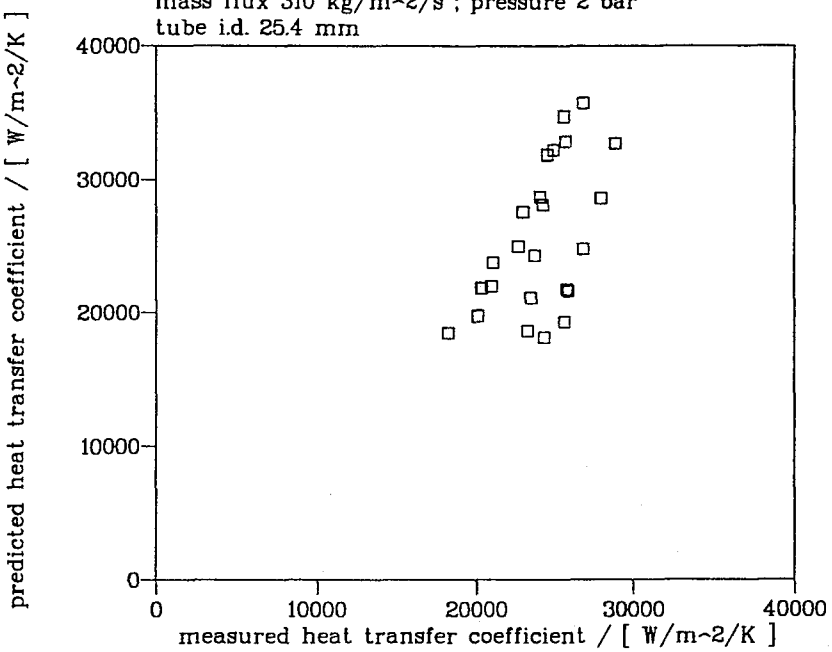

Figure 3.6-1

Bubble burst radius plotted against mean liquid film thickness
based on Wadekar's evaporation data for ethanol
pressure 1.5 bar ; mass flux 145 kg/m~2/s
vertical annular up-flow

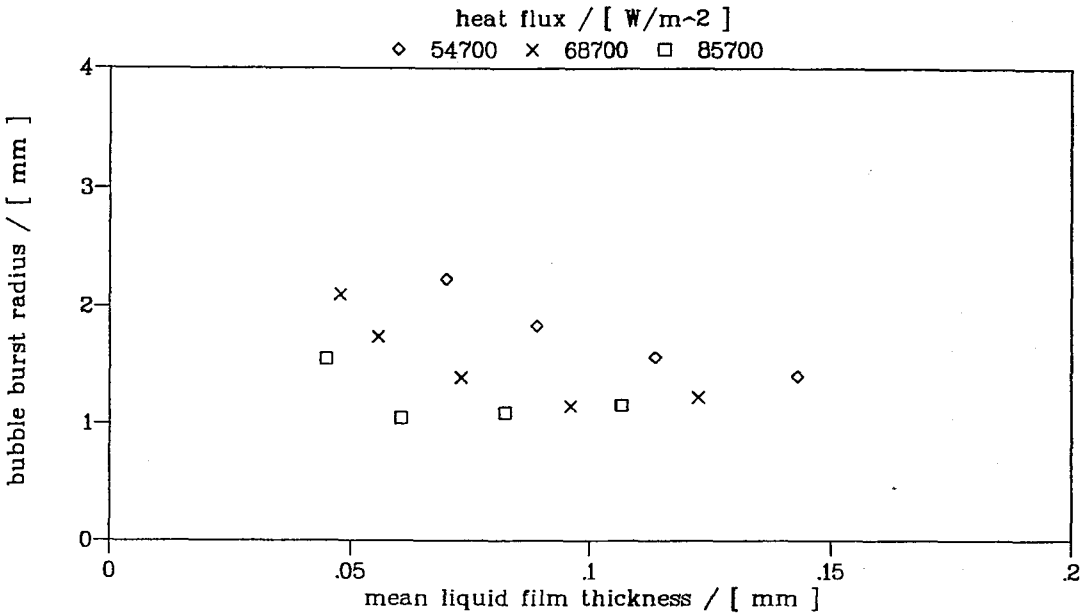

Figure 3.6-2 Wadekar's heat transfer data for ethanol

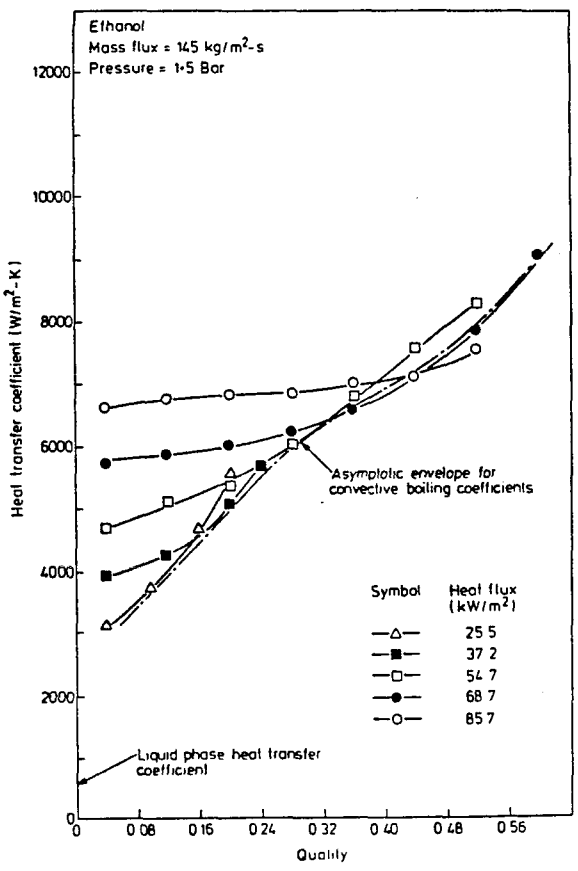

It was considered possible that such departure from equilibrium could explain the effects seen in some of Wadekar's data as illustrated in figure 3.6-2. As will be seen, the heat transfer coefficient increases with heat flux at low quality as would be consistent with the influence of nucleate boiling. However, it decreases with heat flux at high quality which is surprising since this region is one in which convection would be expected to be dominant and in which the influence of heat flux at a given quality would be expected to be small. However, the departure from equilibrium would give variation of film flowrate and film thickness with heat flux at a given quality. Would these be sufficient to explain the effect of heat flux seen in Wadekar's data ? To investigate this question, calculations were done using the Harwell non-equilibrium annular flow code HANA (Whalley et al, 1974).

The conditions of Wadekar's experiment were used as input to HANA. The code calculates the variation of pressure gradient, film flowrate and film thickness along the channel using the methods described in Chapter 2. Maximum non-equilibrium was simulated in HANA by specifying 99% entrainment at the tube inlet. The calculated local values of liquid film flow rate, interfacial shear stress and liquid film thickness were used in the present heat transfer model to calculate the local convective heat transfer coefficient using the same parameter as those specified above for the equilibrium calculation. Equilibrium heat transfer coefficients were also calculated using Wadekar's experimental conditions as direct input to the present heat transfer model.

The calculated values of film thickness, film flowrate and convective heat transfer coefficient are shown in figures 3.6-3, 3.6-4 and 3.6-5 respectively. As expected, the film thickness and film flowrate differ strongly from the equilibrium value. It should be noted that the equilibrium is calculated for a local pressure of 1.5 bar whereas the non-equilibrium is calculated for an inlet pressure of 1.5 bar. Because of the pressure drop along the channel,this adds to the discrepancy as the quality increases along the channel. Furthermore, there is a strong heat flux effect on film flow rate and film thickness at a given local quality. This is not a local effect but rather one that arises due the effect of heat flux on the rate of change of quality along the channel. However, the convective heat transfer coefficient calculations show little effect of heat flux on heat transfer

Figure 3.6-3

Calculated mean liquid film thickness in equilibrium and non-equilibrium annular up-flow
based on conditions of Wadekar's experiment on evaporating flow of ethanol

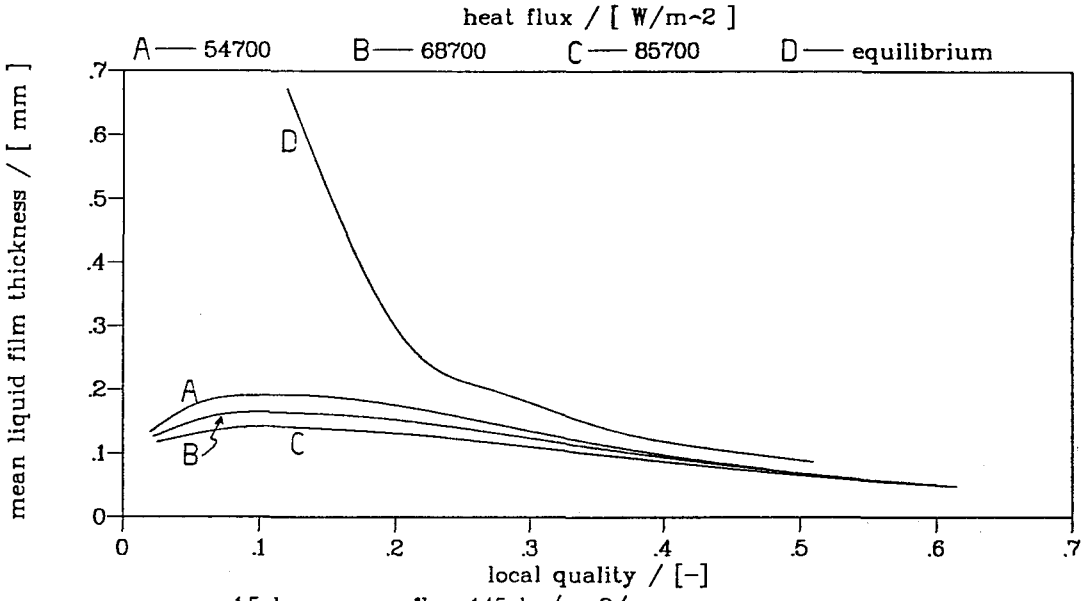

pressure 1.5 bar ; mass flux 145 kg/m~2/s
tube length 3 m ; tube i.d. 10 mm

Figure 3.6-4

Calculated liquid film flow rate in equilibrium and non-equilibrium annular up-flow
based on conditions of Wadekar's experiment on evaporating flow of ethanol

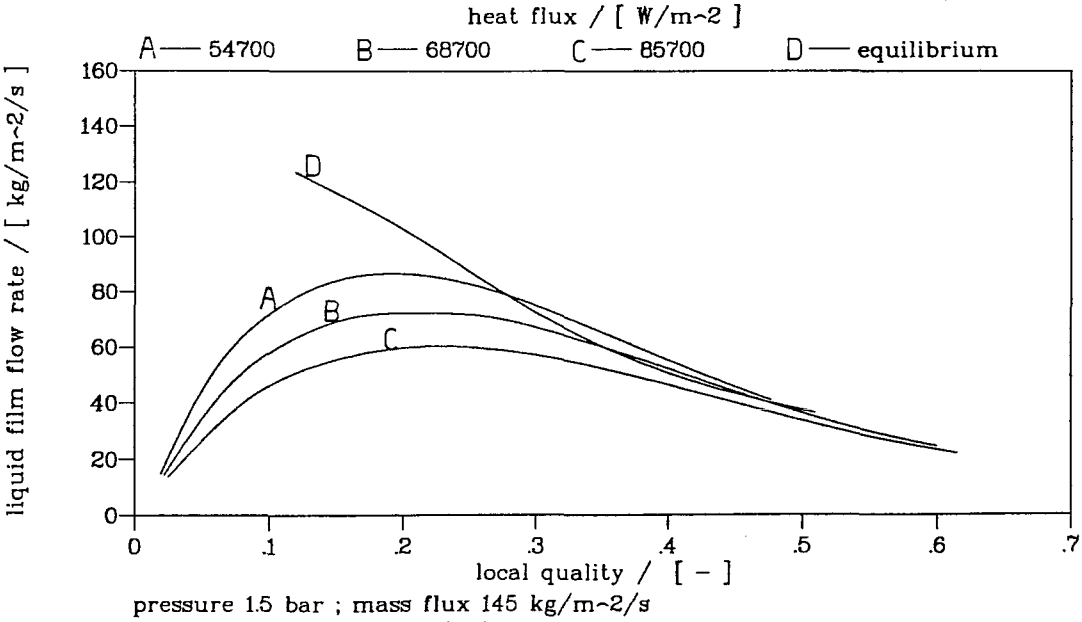

pressure 1.5 bar ; mass flux 145 kg/m~2/s
tube length 3 m ; tube i.d. 10 mm

Figure 3.6-5

Convective heat transfer coefficients calculated for equilibrium and non-equilibrium annular flow

based on conditions of Wadekar's experiment on evaporating flow of ethanol

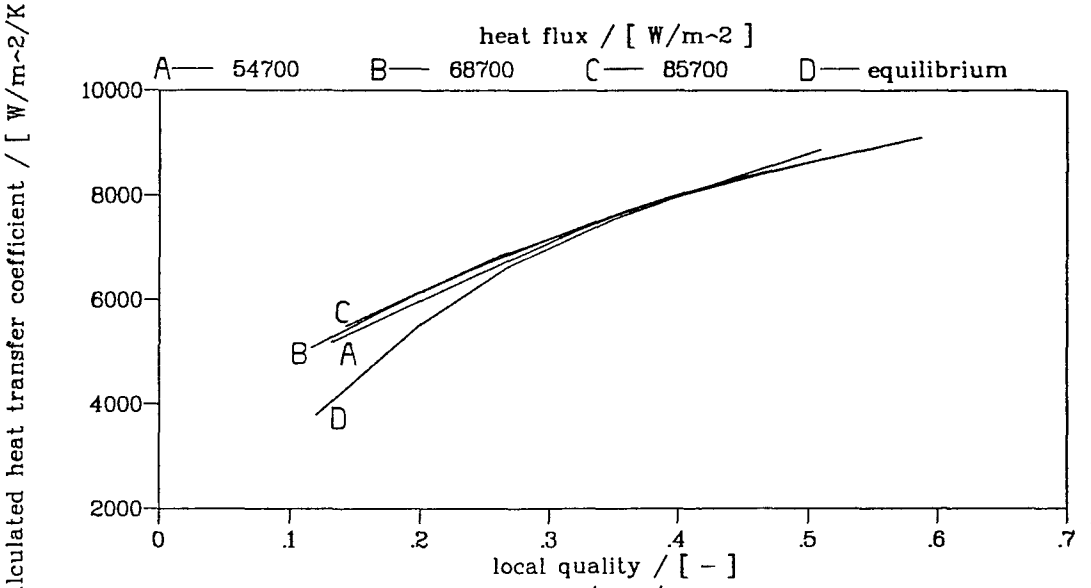

pressure 1.5 bar ; mass flux 145 kg/m~2/s

vertical up-flow of ethanol subject to uniform heat flux

coefficient as is illustrated in figure 3.6-5. This is because of the turbulent temperature profile in the outer part of the film which makes the heat transfer coefficient insensitive to change in film thickness. Thus, the Wadekar observation cannot be immediately ascribed to non-equilibrium effects. However, the difference between forced convective evaporation and condensation which emerge from the experiments described in Chapter 4 may imply that, if the heat transfer is influenced by nucleation which occurs from bubbles entrained in waves, then the heat transfer coefficient may be much more sensitive to film flow and thickness than would be expected from convective heat transfer theory.

3.7 Conclusion

(1) A phenomenological model for heat transfer in evaporating single-component annular flow has been developed. It takes detailed account of the hydrodynamics and the nucleation process that have direct bearing on heat transfer.

(2) There is a lack of information on some key parameters in this model regarding the bubble burst size, the size distribution of potential nucleation sites and the extent of eddy damping in the liquid film. Despite this disadvantage, and with some reasonable assumptions made for the last two aspects, analysis made on some data sets from the literature indicated reasonable prediction could be made by assuming a constant bubble burst radius. A value of 1.5 mm for the bubble burst radius has been used for some predictions which produced some encouraging results. Some non-dimensional variables were chosen in an attempt to establish a correlation for the bubble burst size, but they were found to be inadequate. Further work is desirable on this aspect.

(3) Surprisingly, the indicated bubble burst size was an order of magnitude larger than the calculated film thickness, Analysis if the cine films of Hewitt et al (1963) (see Appendix H) showed that this was consistent with experiment.

(4) The data of Wadekar (1988) show an inverse effect of heat flux on heat transfer coefficient. It was thought that this could be due to departure from hydrodynamic equilibrium and calculation for

non-equilibrium annular flow carried out using the Harwell HANA code showed that , indeed, for a given local quality the film flow rate and film thickness varied considerably with heat flux. However, using the convective heat transfer part of the present theory together with the predicted film flow and thickness showed that these was little commensurate change in the heat transfer coefficient. This probably explains why quality-based heat transfer correlation are reasonably successful despite non-equilibrium effects.

CHAPTER 4

EXPERIMENTS ON ANNULAR FLOW

This chapter describes two principal types of experiment on heat transfer in annular flow :

(a) Experiments in which equilibrium annular flow has been set up and convective heat transfer coefficients measured near equilibrium condition for both evaporation and condensation.

(b) Experiments in which annular flows in various states of departure from equilibrium have been set up and the heat transfer coefficient again measured, this time only with condensation.

The rationale behind experiments (a) was explained in Chapter 1. At high quality and low heat fluxes, the mechanism of heat transfer has been classically interpreted as being convective, with nucleation playing no part. However, Mesler (1977) has suggested that secondary nucleation (arising for instance from bubble entrainment in waves rather than from wall nucleation sites) can have an important role. A very direct way of assessing the role of secondary nucleation is to compare evaporation and condensation under identical conditions. In condensation, the secondary nuclei would have no role and, if their role is negligible in evaporation, a similar heat transfer coefficient would be obtained for both evaporation and condensation. If secondary nucleation is import, then evaporation coefficients would be significantly higher even if wall nucleation is completely suppressed. In defining "identical conditions" for condensation and evaporation, it is not sufficient to merely specify the mass flux and quality. At given quality, due to hydrodynamic non-equilibrium effects, the film flow rate, film thickness and interfacial wave structure can vary widely depending on the upstream history of the flow. In the present experiments, identical conditions are ensured by first generating the required quality in an electrically heated section of the channel. This was followed by a long adiabatic section in which equilibrium annular flow

was established. Finally, a short heat transfer section was introduced in which measurements for both evaporation and condensation could be made. It was vital to have exactly the same tube for both cases to avoid any ambiguity and this dictated that fluid heating rather than electrical heating was used for the boiling case. Considerable experimental difficulties are presented by this requirement and by the requirement that reasonably local values of heat transfer coefficient needed to be measured .

In experiments (b), a two-phase separator was installed immediately following the electrically heated section. The phases were then recombined downstream, but zero initial droplet entrainment was ensured by reinjecting the liquid through a porous wall section. Various degree of non-equilibrium could be achieved in a controlled manner at the heat transfer section by varying the length of an adiabatic section of channel placed between the injector and the heat transfer section.

Conditions of the experiments are as follows:

Experiments (a)	(i)	Total mass flux (kg/m^2s) : 125, 183 and 241
	(ii)	Quality from 0.1 to 0.5 approximately
	(iii)	Pressure near atmospheric
	(iv)	Heat transfer section : copper and nickel
	(v)	Thermal conditions : evaporation and condensation
Experiments (b)	(i)	Total mass flux (kg/m^2s) : 241
	(ii)	Quality from 0.1 to 0.5 approximately
	(iii)	Pressure near atmospheric
	(iv)	Heat transfer section : nickel
	(v)	Thermal conditions : condensation

4.1 Experiments on equilibrium annular flow

4.1.1 Description of experimental rig

The experimental rig consisted of two flow circuits, namely the two-phase circuit and the single-phase circuit as shown in figure 4.1.1-1.

Figure 4.1.1-1 Evaporation and condensation rig flow diagram

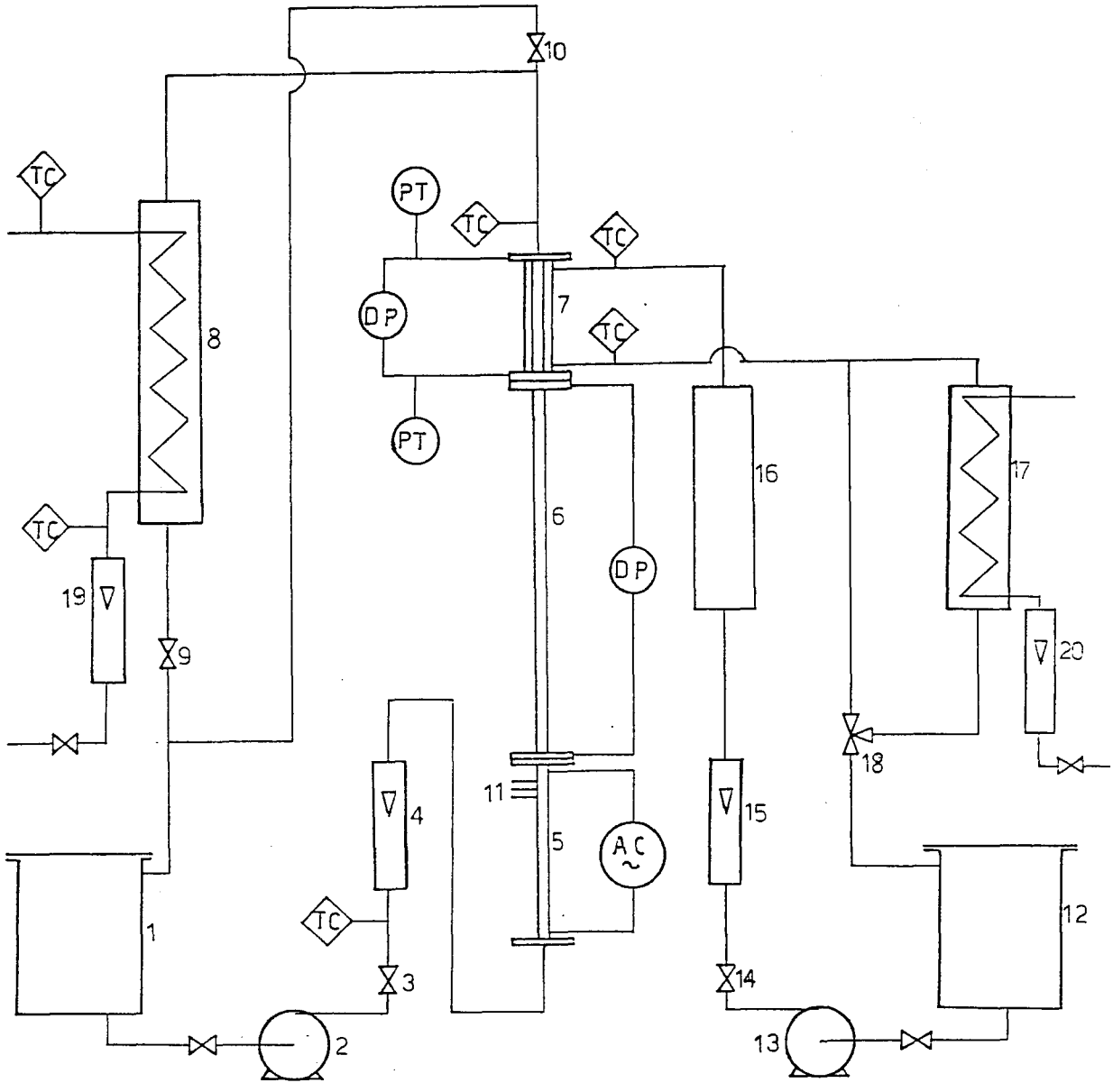

Two-phase circuit

1 storage tank
2 pump
3 flowrate control valve
4 rotameter
5 quality generating section
6 calming section
7 test section
8 condenser
9 pressure control valve
10 bleed valve
11 burn-out detector

Single-phase circuit

12 storage tank
13 pump
14 flowrate control valve
15 rotameter
16 pre-heater
17 cooler
18 by-pass valve

Cooling water supply

19 rotameter
20 rotameter

TC thermocouple
DP pressure differential cell
PT pressure transducer

The fluid used in the two-phase circuit was demineralised water stored in a tank open to atmosphere. The water temperature in the tank was maintained at about 50°C by an immersion heater. The water was pumped by a gear pump through a 1 m long electrically heated stainless steel section, where water/steam mixture was generated at the required quality. The two-phase mixture then passed through a 2 m long stainless steel calming section to reach hydrodynamic equilibrium. Then it entered a 0.3 m long test section, which will be described in the following section. The heating section, calming section and test section all had an inside diameter of 9.5 mm and were vertically aligned. After the test section, the two-phase mixture flowed through a condenser where it was totally condensed and subcooled before returning to the tank.

The fluid used in the single-phase circuit was demineralised water for condensation experiment and was glycerol for the evaporation experiments. When filled with demineralised water, the storage tank was left open to atmosphere. When glycerol was used, the tank was sealed and blanketed with nitrogen to prevent the glycerol from absorbing water vapour from the atmosphere. The tank temperature was maintained by an immersion heater at about 60°C for water or 160°C for glycerol. The single-phase fluid was pumped by a centrifugal pump through a pre-heater to the annular channel of the test section, where it flowed downwards in counter-current flow to the two-phase mixture in the centre tube. Due to their temperature difference, heat exchange took place between the single-phase and two-phase fluids. On returning to the tank, the single-phase fluid passed through either a cooler during the condensation experiments or a by-pass line during evaporation experiments.

Copper pipes were used to connect the major components of the rig. All parts of the rig were insulated by 1 in thick fibre glass. The bases of the storage tanks were insulated by foam glass.

4.1.2 Description of test section

The first test section consisted of a central copper tube with an outside diameter of 14.5 mm and a wall thickness of 2.5 mm and a stainless-steel housing (called the jacket hereafter) with an inside diameter of 19.5 mm (see figure 4.1.2-1a). Hence, an annular channel (called the annulus

Figure 4.1.2-1 Test section

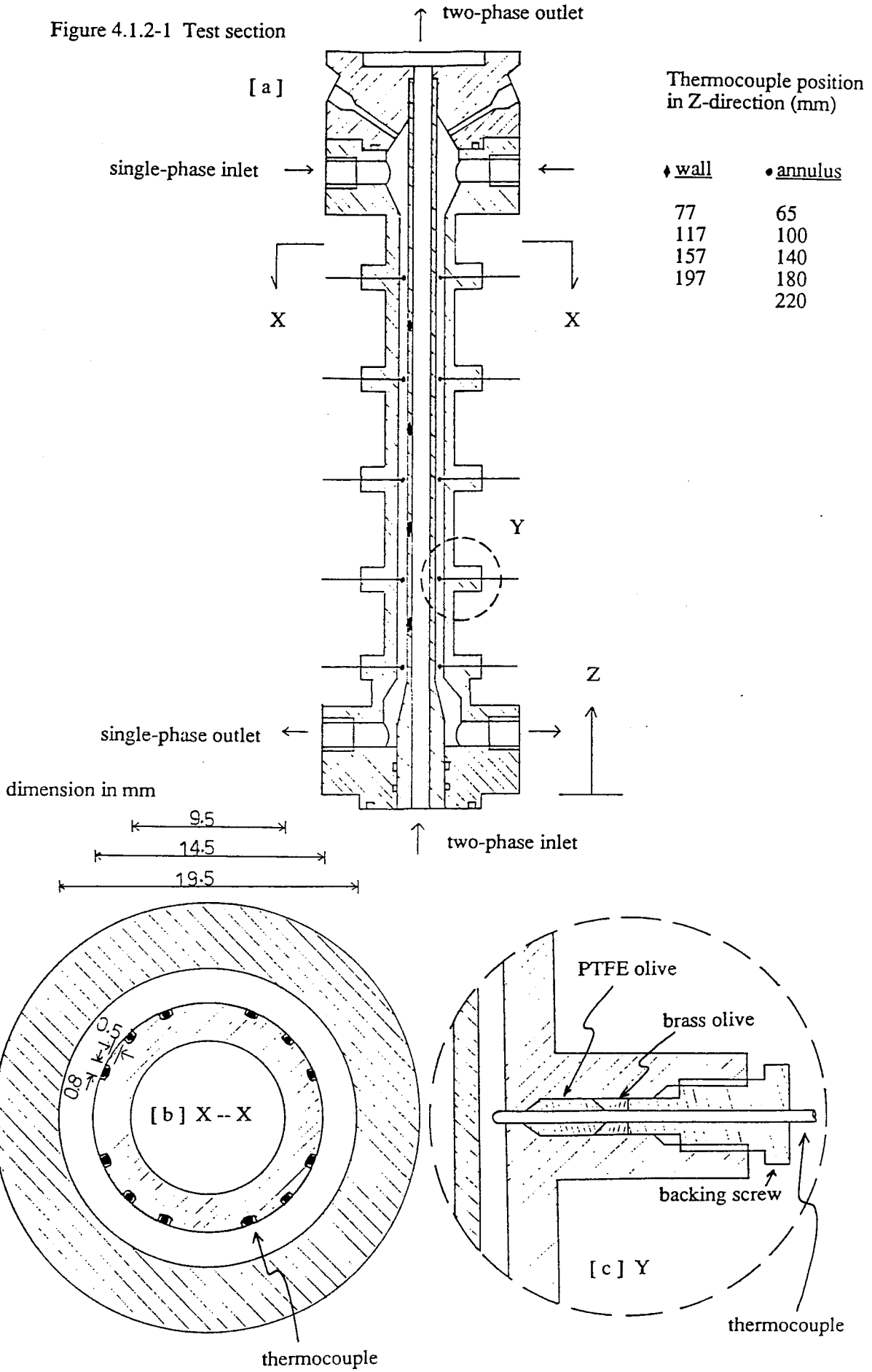

hereafter) with an equivalent diameter of 5 mm was formed. The test section had an overall length of 0.3 m. The length exposed to the single-phase fluid was 0.225 m. The centre tube was removable from the jacket. "O" rings were used to seal the two flows from each other. The inlet manifold had four feed-lines lying in a plane perpendicular to the axis of the test section. The outlet manifold had an identical arrangement. The copper tube was electroplated with nickel on its inner surface, the nickel being of negligible (several micron) thickness.

Twelve stainless-steel sheathed chromel-alumel thermocouples with a diameter of 0.5 mm were embedded with soft-solder in grooves on the outside wall of the copper tube. They lay flush with the outer wall surface with their leads coming out through sealed holes at the top flange of the test section. The hot junctions of the thermocouples were evenly spaced round the circumference (see figure 4.1.2-1b) at each of four axial positions at distances of 77, 117, 157 and 197 mm from the base of the test section. The position nearest to the base of the test section will be called the 'fourth station' and the position nearest to the top the test section will be called the 'first station'.

A total of 10 chromel-constantan thermocouples were divided into two arrays and inserted radially into the annulus on opposite sides of the jacket. On each side, their hot junctions were positioned at the mid-point of the annular gap in the same axial plane so that each of the wall thermocouple stations was approximately mid-way between a consecutive pair of annulus thermocouples along the axis. The ports for the annulus thermocouples were sealed by PTFE and brass olives (see figure4.1.2-1c). All the thermocouples were calibrated in a thermal bath.

In order to prevent corrosion, the copper tube had been electroplated with nickel. After some preliminary experiments, the tube inner surface was examined and found to be,nevertheless, showing slight signs of corrosion products, perhaps resulting from imperfections in the plating or perhaps arising from corrosion products from other parts of the rig. To address this problem, the following actions were taken:

(a) The tube was mechanically cleaned.

(b) The rig was flushed out generously with dimineralised water.

(c) Some single phase heat transfer experiments were carried out, with subcooled water flowing in the centre tube. These showed that the calculated heat transfer coefficients were in good agreement with published correlations, indicating that excessive fouling was not occurring.

In view of the great sensitivity of two phase heat transfer measurement to fouling, it was thought prudent to manufacture a second centre tube, manufactured entirely of nickel, so that the results could be checked with two independent surfaces. Like the copper tube, the wall-thermocouples on the nickel tube were of chromel-alumel type. They were calibrated before being soldered into the grooves on the outer wall of the tube. Both centre tubes were used in the experiments.

4.1.3 Experimental design considerations

This section could have been presented earlier. However, in the author's opinion, a general picture of the rig should be given first for the reader to appreciate its design principles.

The space available in the laboratory obviously limited the overall height of the rig, hence the size of different components. The dimensions of the rig in turn have some bearing on the achievable flowrates and the thermodynamic quality of the two-phase flow.

The tube inside diameter of the heating section, the calming section and the test section was chosen to be 9.5 mm. The length of the heating section was chosen to be 1 m. Then for any desired flowrate, the maximum obtainable quality would be determined by the critical heat flux. To determine the available range of quality, the Harwell HANA code was used to determine the critical conditions (i.e. the limiting quality) as a function of flowrate. This determined the operating range but, actually, quite a wide range of quality was possible over the range of flowrate available. However, to protect against overheating due to dryout, a "burnout detector" was installed at the upper end of the electrically heated section; this consisted of voltage tappings which were connected to a bridge circuit. Sudden overheating of the upper part of the electrically heated section (arising from dryout) causes a bridge imbalance which trips the power.

The design of the adiabatic section for the present experiment had to be such as to ensure that hydrodynamic equilibrium was attained. Absolute hydrodynamic equilibrium in annular flow can never be reached even under adiabatic conditions because the pressure gradient causes the gas to continue to accelerate. However, one can define an equilibrium condition as one in which, for a given outlet pressure, the local flow parameters no longer depend on up-stream length or on the generator of the two-phase mixture. Brown et al (1975) performed two-phase experiments using central jet and porous wall liquid injectors for air-water annular flow. He found that the position where equilibrium is reached depends on the individual phase flowrates. However, in general, this point is about 200 diameters down-stream of the mixer. Therefore, the length of the calming section was chosen to be 2 m for this present experiment.

The design of the test section was governed by the following requirements:

1) The annular flow can be either evaporated or condensed in the same test section by adjusting the wall temperature.
2) The test section should be sufficiently short to ensure that departure from the equilibrium condition occurring at the tube inlet is small.
3) The length of the test section should be sufficient to allow the single-phase flow in the annulus to become fully developed.
4) Measurement devices (i.e. thermocouples and pressure tappings) should be such as to give minimal disturbance of the flow and temperature field.

Requirement (1) dictates the use of a fluid as the heat source or sink. There are fluids that can be used for the full temperature range required. But with their toxicity and flammability and with the costs for necessary safety measures taken into consideration, their use was precluded. Water is certainly a safe liquid to work with. However, at low pressure, it can only be used for condensation. For evaporation, glycerol was chosen as a heating medium.

With a single-phase fluid as heat transfer medium, the test section was envisaged as a "concentric double pipe" type of heat exchanger. The flow direction of the single-phase fluid was chosen to be counter-current to the two-phase flow so that the fully developed single-phase heat transfer is

achieved at the two-phase inlet end. Local heat flux can be deduced from measurement of temperature profile in the jacket. Requirement (4) demands that the annulus thermocouples should be small and separated far enough. The thermocouples on the outer wall of the centre tube must be flush. Otherwise, they would not only disturb the temperature fluid in the single-phase fluid, but also cause error in deducing the inner wall temperature.

Obviously, a long test section would have less end effects than a short one. It seems that requirement (2) and (3) are in conflict. However, requirement (2) can be accommodated by optimising the operating conditions for the single-phase fluid to some extent. For a given single-phase flowrate, the narrower the annulus is, the higher the Reynolds number and the better the mixing and the shorter the thermal entrance length. The minimum limit on the annulus size is determined by the size of the annulus thermocouple in order to satisfy requirement (4). The annulus gap was chosen to be of 2.5 mm.

Since the heat transfer coefficient in annular flow is higher than that in single-phase flow, the thermal entrance length of the single-phase is critical in determining the length of the test section. Harwell has a general-purpose computer code called FLOW-3D for analysing fluid flow and heat transfer. It was used to calculate the thermal entrance length for the single-phase flow in the annulus. The Flow-3D calculations showed that for a range of typical operating conditions, the thermal entrance length is about 40 times the annulus gap, i.e. 100 mm approximately. The exposed heating length used was 0.225 m, which should certainly give fully developed flow by the third thermocouple station.

The two-phase circuit pump was a gear pump. Being of a positive-displacement type, the flowrate should be insensitive to any pressure fluctuation in the heating section. The pump in the single-phase circuit was of centrifugal type. Its gland seals were made from special material that could stand the high temperature.

4.1.4 Instrumentation

Rotameters in the two-phase circuit and cooling water supply line for the condenser were calibrated in situ at a fluid temperature of 50°C and 13°C

respectively. In addition, the two-phase circuit rotameter was also calibrated at a fluid temperature of 20°C specifically for the single-phase heat balance tests (see Appendix D).

The rotameter in the single-phase circuit was calibrated in situ at 60 °C but for water only. For glycerol, calibration curves provided by the rotameter manufacturer was used. A PTFE float was used for evaporation experiments with the copper tube mounted in the test section. Later, with the nickel tube in place, a stainless steel float was used for higher glycerol flowrates.

Being used only as a flow indicator, the rotameter in the cooling water supply line for the single-phase circuit cooler was not calibrated

Stream bulk temperatures were measured by copper-constantan thermocouples in pockets with intrusion length of about 50 mm at the positions as shown in Fig.4.1-1All the thermocouples were calibrated in a thermal bath.

Pressure differentials in the calming section and test section were measured by D.P. cells, which were calibrated by the 'dead weight' method. It was essential to ensure that the pressure tapping lines were full of single-phase water. This was achieved by using purge-lines which were attached at the point where the D.P. cell sensing lines joined the flanges with pressure tapping holes. The purge was tapped from the pump discharge. Absolute pressures were measured by pressure transducers at the inlet and outlet of the test section. These pressure transducers were calibrated by a "dead weight" system coupled with a vacuum system to cover sub-atmospheric condition. Later they were checked by a 'water column' method. All the pressure transducers and D.P. cells were of the strain gauge type.

The electrically heated quality generating section was fed with single-phase, low voltage alternating current via two split copper blocks 0.8 m apart, which were clamped onto the stainless steel tube. To protect against dryout and, hence, overheating and possible physical damage of the electrically heated section, a burnout detector was installed. Three metal pins, spaced at intervals of 30 mm along the electrically heated section with the top pin close to the upper copper block, were pressed onto the tube by mounting them in a split Tufnell block. The tube length

between the connecting pins form two arms of a Wheatstone bridge. Any temperature excursion between the pins would upset the balance in the Wheatstone bridge and trigger a power-cut to the heating section. The electronic system used is described in detail by Jackson (1976).

The voltage difference between the copper blocks was fed directly to a wattmeter. One of the bus bars was encircled by a current transformer with a step-down ratio of 500 : 1. The signal from this current transformer was fed to the wattmeter. The accuracy of the electrical equipment was checked by single-phase heat balance tests and proved to be satisfactory.

The voltage signals of the thermocouples and the D.P. cells were read by a scanner and then passed by it to a computer, which converted the signals into temperature and pressure readings taking account of the relationships obtained from the calibrations. The scanning rate was optimised to avoid signal attenuation. Readings of the rotameters, pressure transducers and wattmeter were taken manually and typed into the computer.

4.1.5 Operation

For each series of experiments, the mass flow rate was set constant and the quality varied in steps over the required range by adjusting the power input into the electrically heated section. Each series of experiments was started by first priming the two main flow circuits including the D.P. cell sensing lines. Then the heating section was energised and the power input was raised until the required quality was reached for the given total mass flowrate. At the same time, the flowrate of the cooling water to the condenser was adjusted to keep the condensate subcooled. Normally, the pressure in the test section was controlled by the valve in the condensate return line.

In principle, provided the annulus heat transfer is fully developed, it does not matter whether the annulus flow is laminar or turbulent. In fully developed flow, the axial temperature gradient ($\partial T/\partial z$) at any given radial position is constant. However, there is also a radial temperature gradient and, though every effort was made to position the successive annulus thermocouples accurately (i.e. by controlling the location of the annulus thermocouples by using accurate dial gauges), slight errors in position can give errors in axial temperature differences and hence in heat flux

calculation. It is therefore preferable to have turbulent flow in the annulus to minimise the radial temperature gradient at the (central) thermocouple location. However, if the flow velocity is too high, then the axial temperature gradient falls and the accuracy of the heat flux measurement may not be adequate. This rather delicate balance of requirements, together with the need (to achieve the objective of the experiment) for local measurement, presented a formidable problem in the present work. For the condensation case, where water was used as the annulus fluid, fully turbulent flows could be obtained. However, with the glycerol used in the evaporation experiments, the viscosity was higher and the Reynolds number was often only just in the turbulent regime, typically 3000. An increase in velocity would result in a decrease in axial temperature gradient and a decrease in the accuracy of the heat flux measurement. Reducing throughput by reducing the annulus gap would make accurate placing of the thermocouples more problematic. Thus, the design had to be a compromise. The experimental challenge was to make sufficiently accurate measurement to compare the evaporation and condensation cases; a relatively large scatter (compared, say, to electrical heating) was inevitable. A further limitation is that of measurement error in the thermocouples. The calibration of the annulus thermocouples is discussed in Appendix A.

During each run, the computer continuously read the temperature and pressure differential measurements and always kept the latest 9 scans, of which standard deviations were calculated for each measurement. Those measurements not readable by the computer were taken manually at appropriate time intervals. When it was judged that steady state was reached, the mean values of the latest 9 scans and those manually read measurements were stored on floppy disc. Then another run for a different quality was started by changing the power input to the heating section. The flowrate of the cooling water to the condenser had to be adjusted accordingly.

Although it would have been desirable to maintain a constant pressure at the test section for all the runs, operational difficulties prevented this and the pressure varied between typically 0.9 and 1.2 bar from run to run, though it was kept constant in any given run.

4.1.6 Data analysis

4.1.6.1 Calculation of heat transfer coefficient

The quality at the test section inlet was calculated from a heat balance over the heating section. To account for flashing due to the pressure drop in the adiabatic section, h_{LG} was based on the test section inlet conditions and C_{pL} was taken the mean of the C_{pL} values at T_{tsi} and T_{hsi}, which are the test section and heating section inlet temperatures respectively. Thus :

$$\dot{Q}_{hs} = \frac{\pi D_i^2}{4} \dot{m}_{tp} [x h_{LG} + C_{pL}(T_{tsi} - T_{hsi})] \qquad (4.1.6.1\text{-}1)$$

Where $\dot{Q}_{hs}$ is the heat input rate to the heating section and $\dot{m}_{tp}$ is the total test section mass flux. Assuming constant pressure gradient in the test section, the D.P. cell and pressure transducer readings were used to calculate the saturation temperature profile in the test section. The temperature change is related to the pressure drop in the test section by the Clasius-Clapeyron equation in difference form :

$$\frac{\Delta p_{ts}}{\Delta T_{ts}} = \frac{h_{LG}}{T_{sat} v_G} \qquad (4.1.6.1\text{-}2)$$

The inlet temperature, T_{tsi} , and the outlet temperature, T_{tso} , of the test section are related to the inlet and outlet pressure readings respectively by the saturation line.

The local saturation temperature can then be calculated by.

$$T_{sat} = T_{tsi} - \frac{z}{z_{ts}} \Delta T_{ts} \qquad (4.1.6.1\text{-}3 .a)$$

$$T_{sat} = T_{tso} + \left(1 - \frac{z}{z_{ts}}\right) \Delta T_{ts} \qquad (4.1.6.1\text{-}4 .b)$$

During the course of the condensation experiments, the test section outlet pressure transducer was found giving incorrect readings. Hence, only the reading of the inlet pressure transducer was used. The outlet pressure transducer was sent back to the manufacturer for repair and re-installed for the evaporation experiments. Then, the inlet pressure transducer

failed. It was not repaired this time. Calculation had to rely on the outlet pressure transducer for subsequent experiments coupled with an estimate of the pressure gradient.

The ratio of the wall thickness of the centre tube to its length is small. Furthermore, experimental results showed only a small temperature change along the outer wall of the centre tube. Therefore, the local heat flux was assumed to be entirely radial and was calculated from the temperature change and mass flowrate of the single-phase in the annulus.

$$\dot{q} = \frac{C_{pL}\dot{M}_a \Delta T_a}{2\pi r_i \Delta z} \qquad (4.1.6.1\text{-}5)$$

Knowing the heat flux and the thermal resistance of the centre tube, the temperature on the inner wall of the centre tube can be calculated by.

$$T_{wi} = T_{wo} \pm \dot{q}\left[\frac{r_i}{\lambda_w}\ln\left(\frac{r_o}{r_i}\right)\right] \qquad (4.1.6.1\text{-}6)$$

The sign preceding $\dot{q}$ is positive for condensation and negative for evaporation.

The local heat transfer coefficient is defined as :

$$\alpha_{tp} = \frac{\dot{q}}{|T_{sat} - T_{wi}|} \qquad (4.1.6.1\text{-}7)$$

In terms of the temperature readings, it can be expressed as :

$$\alpha_{tp} = \frac{b\Delta T_a}{|T_{sat} - T_{wo}| - c\Delta T_a} \qquad (4.1.6.1\text{-}8)$$

where

$$b = \frac{C_{pL}\dot{M}_a}{2\pi r_i \Delta z} \qquad (4.1.6.1\text{-}9)$$

$$c = \frac{C_{pL}\dot{M}_a}{2\pi\lambda_w \Delta z}\ln\left(\frac{r_o}{r_i}\right) \qquad (4.1.6.1\text{-}10)$$

4.1.6.2 Calculation of frictional pressure drop

Pressure drop calculation is based on the one-dimensional momentum equation, which can be expressed as

$$-\frac{dp}{dz}=-\frac{dp_F}{dz}-\frac{dp_a}{dz}-\frac{dp_g}{dz} \qquad (4.1.6.2\text{-}1)$$

where

$$-\frac{dp_F}{dz}=\frac{4\tau_w}{D} \qquad (4.1.6.2\text{-}1.a)$$

$$-\frac{dp_a}{dz}=G^2\frac{d}{dz}\left[\frac{x^2}{\alpha\rho_G}+\frac{(1-x)^2}{(1-\alpha)\rho_L}\right] \qquad (4.1.6.2\text{-}1.b)$$

$$-\frac{dp_g}{dz}=[\alpha\rho_G+(1-\alpha)\rho_L]g \qquad (4.1.6.2\text{-}1.c)$$

Void fraction in annular flow is quite large and, therefore, insensitive to the correlation chosen for its calculation. Butterworth (1974) has compared several void fraction correlations and found that they can be represented by the following basic form

$$\alpha=\frac{1}{1+A\left(\frac{1-x}{x}\right)^p\left(\frac{\rho_G}{\rho_L}\right)^q\left(\frac{\eta_L}{\eta_G}\right)^r} \qquad (4.1.6.2\text{-}2)$$

The Lockhart and Martinelli void fraction correlation can be fitted by putting A = 0.28 , p = 0.64 , q = 0.36 and r = 0.07 . Equation 4.1.6.2-2 with these given values for the constants is used to calculate the void fraction for the experimental data. The frictional pressure drop in the calming section and the test section can then be calculated from the measured total pressure drop using equation 4.1.6.2-1. Since only the inlet and outlet conditions are known, the difference instead of the differential form of equation 4.1.6.2-1 is used. Mean void fraction and thermodynamic properties are used in equation 4.1.6.2-2.

4.1.7 Results and discussion

4.1.7.1 Heat transfer results

The most critical measurement in this experiment is that of fluid temperature in the annulus because of the small temperature changes involved. The calculation of the local heat flux, the correction for the tube wall temperature drop, and hence the calculation of heat transfer coefficients depend on these temperature measurements. Some typical

temperature profiles in the annulus are shown in figures 4.1.7.1-1 and 4.1.7.1-2. These are the annulus thermocouple readings whose difference has been used in the heat transfer calculation; two lines of thermocouples were used on opposite sides of the annulus. The temperature change between a pair of annulus thermocouples for the evaporation experiments was about 0.2°C. For condensation experiments, this temperature change was about 0.6°C. It can be seen that the third and fourth (from the inlet) pairs of annulus thermocouples showed very consistent readings in terms of temperature difference.

To give an independent check on the annulus temperature change, a general purpose computer code (Harwell Flow 3D) was used to predict the temperature profile in the annulus. This code can predict developing flows. A detailed description of the theoretical basis of this computer code can be found in the literature (Burns et al 1986). Since the annulus is axisymetric, polar coordinates were adopted for the fluid flow in a sector of the annulus. The wall temperature was assumed constant, as is reasonably consistent with the measurements on the outer wall of the centre tube. It was also assumed that the fluid velocity at the entrance has only the axial component with a uniform radial profile. The calculated and experimental results are compared in figure 4.1.7.1-3 in terms of difference between the local (measured at the centre of the annulus gap) and inlet temperature. The agreement is very encouraging, particularly in terms of the slope of the line in the fully developed region. This gives confidence in the use of temperature differences in determining heat flux. The computer code predicted a heat transfer rate of 1500 W in the annulus which is also in good agreement with the experimental value.

Only the heat transfer coefficients at station three are presented. The reasons are that the measurements from the first and second stations of annulus thermocouples are susceptible to entrance effect and the fourth station may be susceptible to exit effects as the flow leaves the annulus.

Figures 4.1.7.1-4 and 4.1.7.1-5 show the measured outside wall and estimated inside wall and saturation temperatures for typical repeat series of runs for condensation and evaporation respectively. The temperature readings are scattered somewhat, though consistent. These temperatures, together with the heat fluxes calculated from the axial temperature difference in the annulus, are used in calculating the heat transfer

Figure 4.1.7.1-1

Typical annulus thermocouple readings for evaporation experiments.
(End points are inlet and outlet thermocouple readings.)

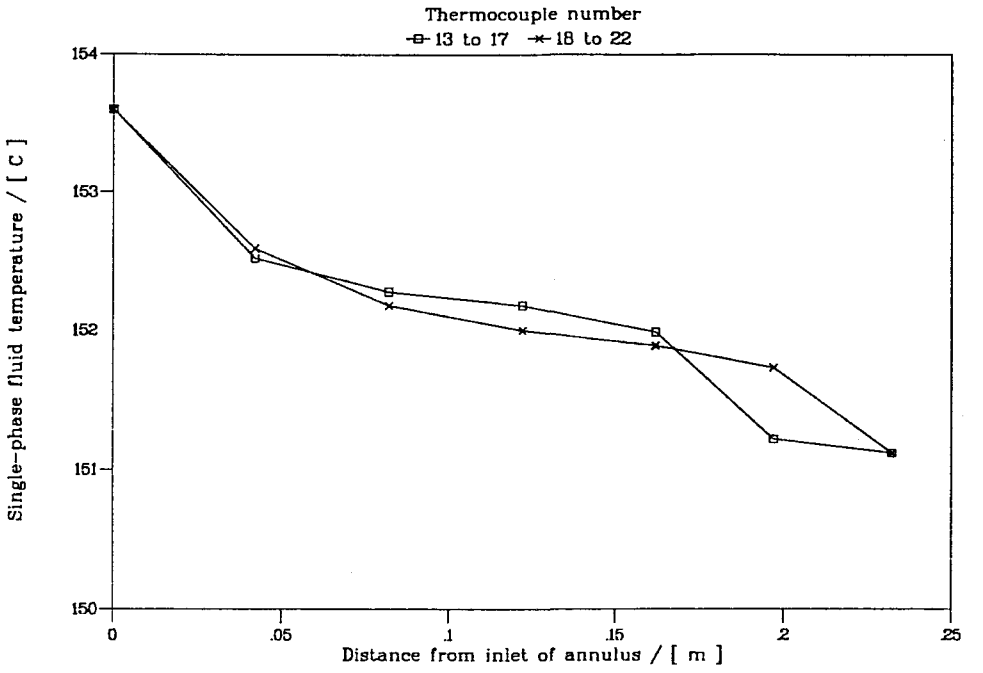

Figure 4.1.7.1-2

Typical annulus thermocouple readings for condensation experiments.
(End points are inlet and outlet thermocouple readings.)

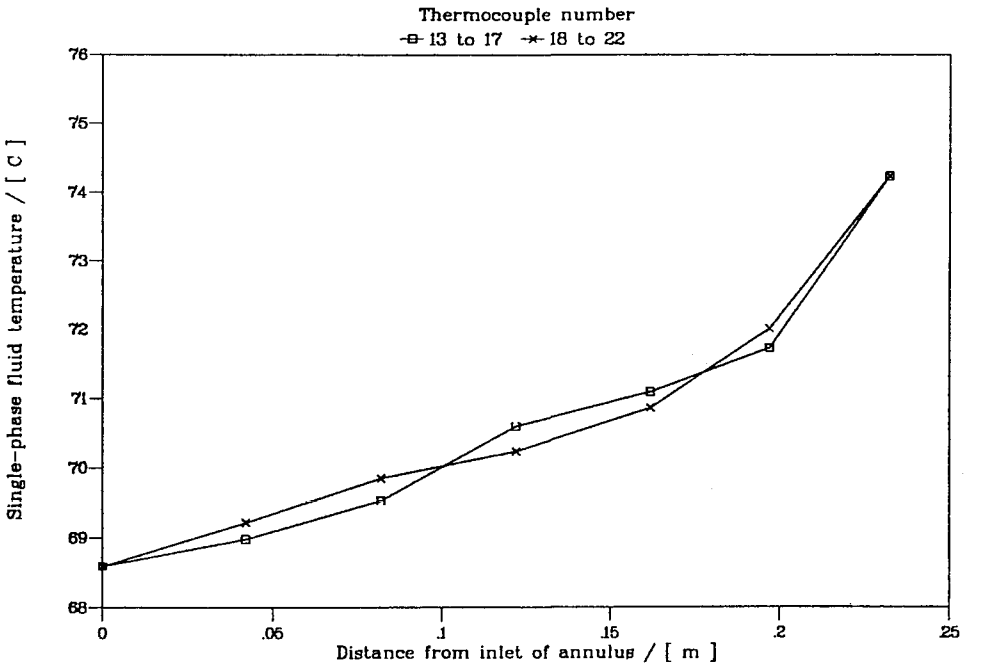

Figure 4.1.7.1-3

Temperature difference between annulus and inlet thermocouples .
(using the same data as in Fig.4.1.7.1-1 from a condensation experiment)

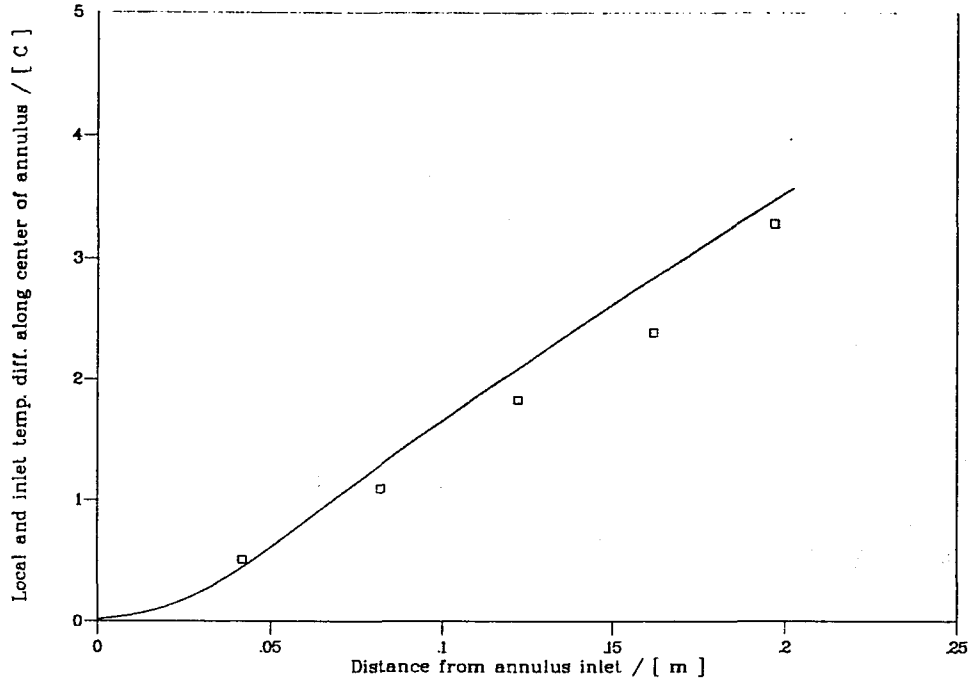

Figure 4.1.7.1-4

Inside and outside wall temperatures and two-phase saturation temperature plotted against quality at the third station with condensation in nickel tube test section
mass flux 241 kg/m^2/s

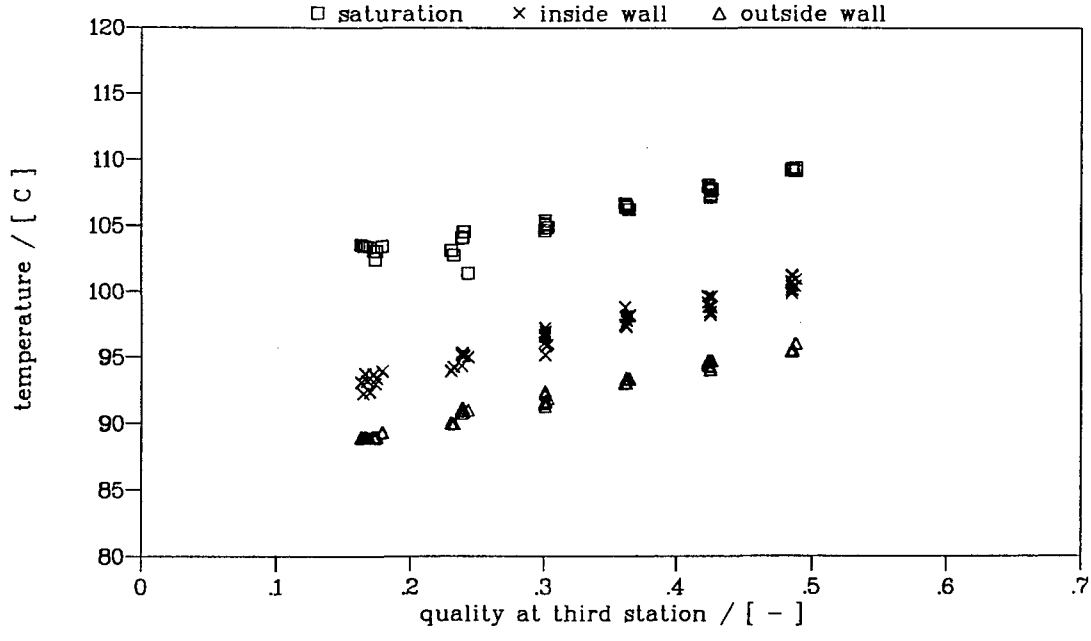

Figure 4.1.7.1-5

Inside and outside wall temperatures and two-phase saturation temperature plotted against quality at the third station with evaporation in nickel tube test section
mass flux 241 kg/m^2/s

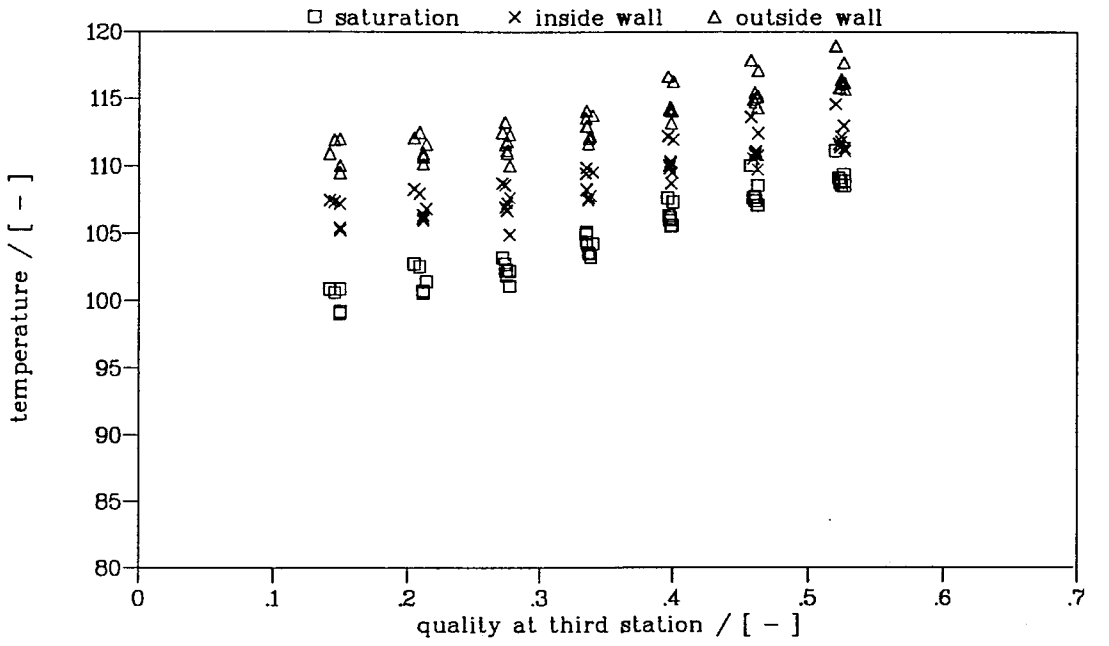

coefficients as illustrated in figures 4.1.7.1-6, 4.1.7.1-7 and 4.1.7.1-8 for the three mass fluxes (125, 183 Ind 241 kg/m^{2}s) used. As will be seen, despite the expected scatter in the data, the evaporation data are consistently higher (by up to 100%) than the condensation data, the difference increasing with increasing mass flux. This result, the most important in the work described in this thesis, has such far reaching implications that it needs to be examined carefully. The examination has focussed on the following aspects :

(1) Pressure effects : Because of operational difficulties, it was not possible to control the pressure at a given value for all the runs (though the pressure was constant and accurately measured in each individual run). The small difference in pressure would certainly not account for all the difference in heat transfer coefficient. However, the pressure effect can be to some extent accounted for by plotting the results in the variables of the earlier forced convective correlations, namely $F = \alpha_{tp}/\alpha_L$ against $1/X_{tt}$ (see Section 2.1.1.1). This is done for the present data in figures 4.1.7.1-9 and 4.1.7.1-10. As will be seen, though there is some considerable scatter, the mass flux and pressure effects are reasonably closely correlated (with the results from the two test sections agreeing with each other); however, the evaporation data still lie well above the condensation data.

(2) Fouling effects : Fouling resistance in boiling can be lower than in condensation due to the " wick boiling" effect (Macbeth et al, 1971). However, this applies to the nucleate boiling region and not the forced convective region. Moreover, it would be very surprising if the two tubes exhibited similar fouling behaviour. These facts, coupled with consistent results obtained in single-phase flow, lead one to conclude that fouling was not the cause of the evaporation / condensation difference

(3) Consistency of data : In the present experiments, in order to obtain direct comparison between evaporation and condensation, fluid heating was used for evaporation. However, if only evaporation data are required then it is certainly more accurate to use electrical joule heating of the tube wall. Fortunately, data under comparable conditions have been

Figure 4.1.7.1-6

Experimental heat transfer coefficient in equilibrium vertical annular up-flow of water and steam

total mass flux 241 kg/m^2/s

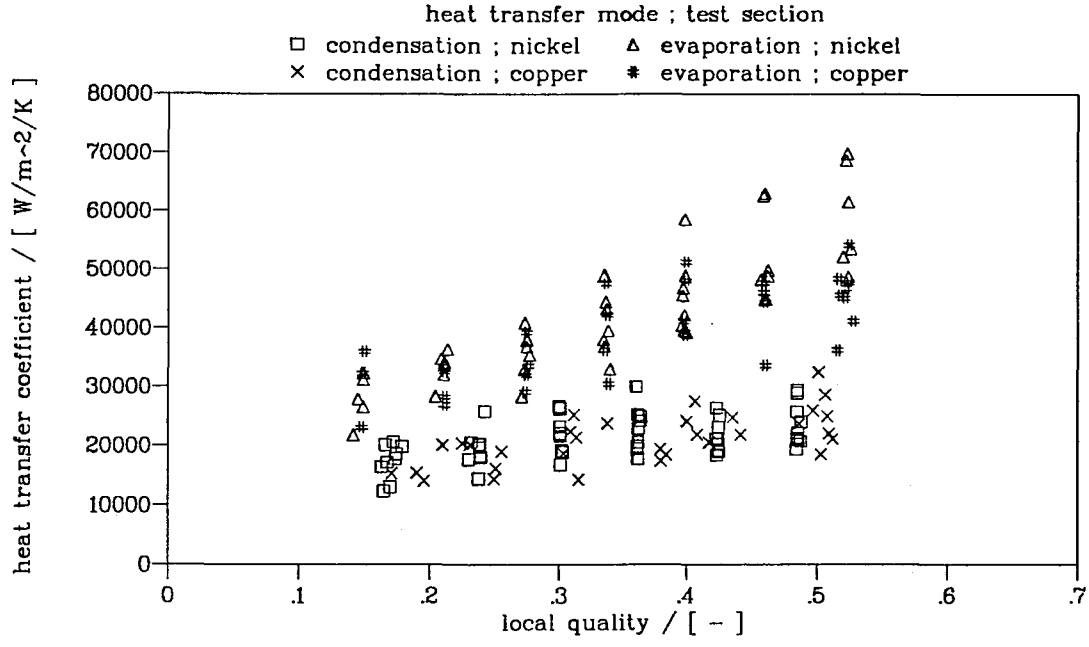

Figure 4.1.7.1-7

Experimental heat transfer coefficient in equilibrium vertical annular up-flow of water and steam

total mass flux 183 kg/m^2/s

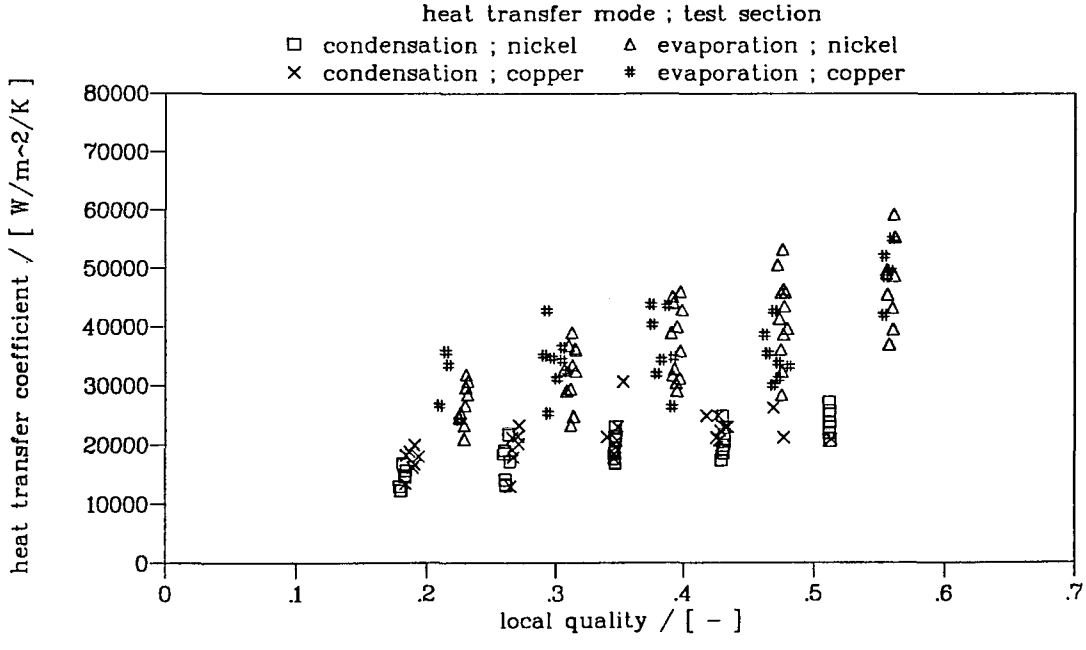

Figure 4.1.7.1-8

Experimental heat transfer coefficient in equilibrium vertical annular up-flow of water and steam
total mass flux 125 kg/m~2/s

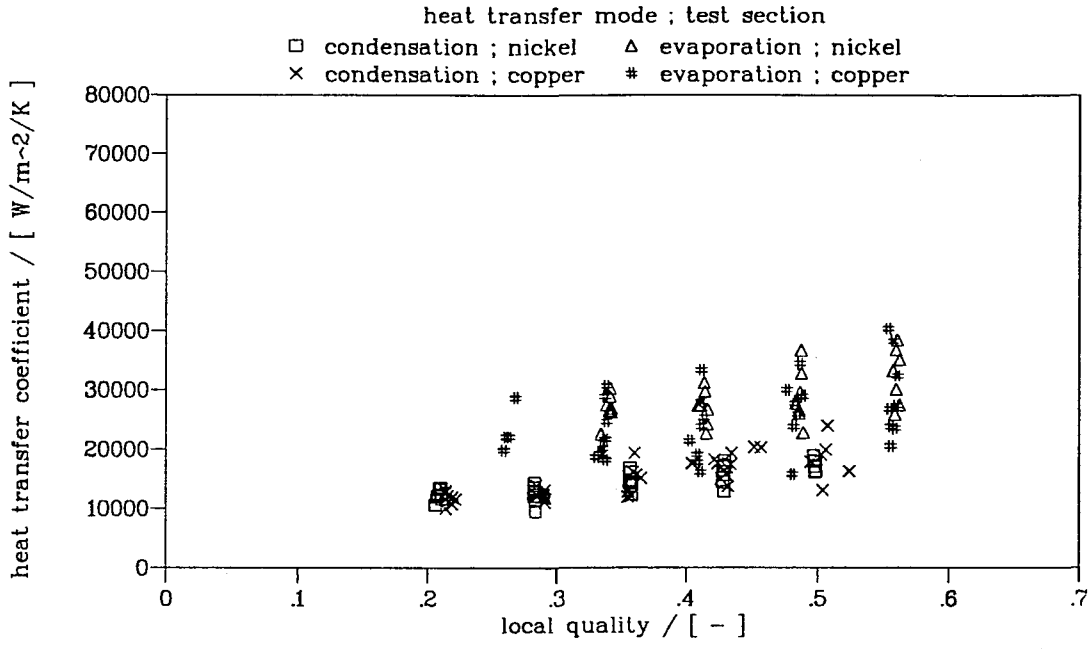

Figure 4.1.7.1-9

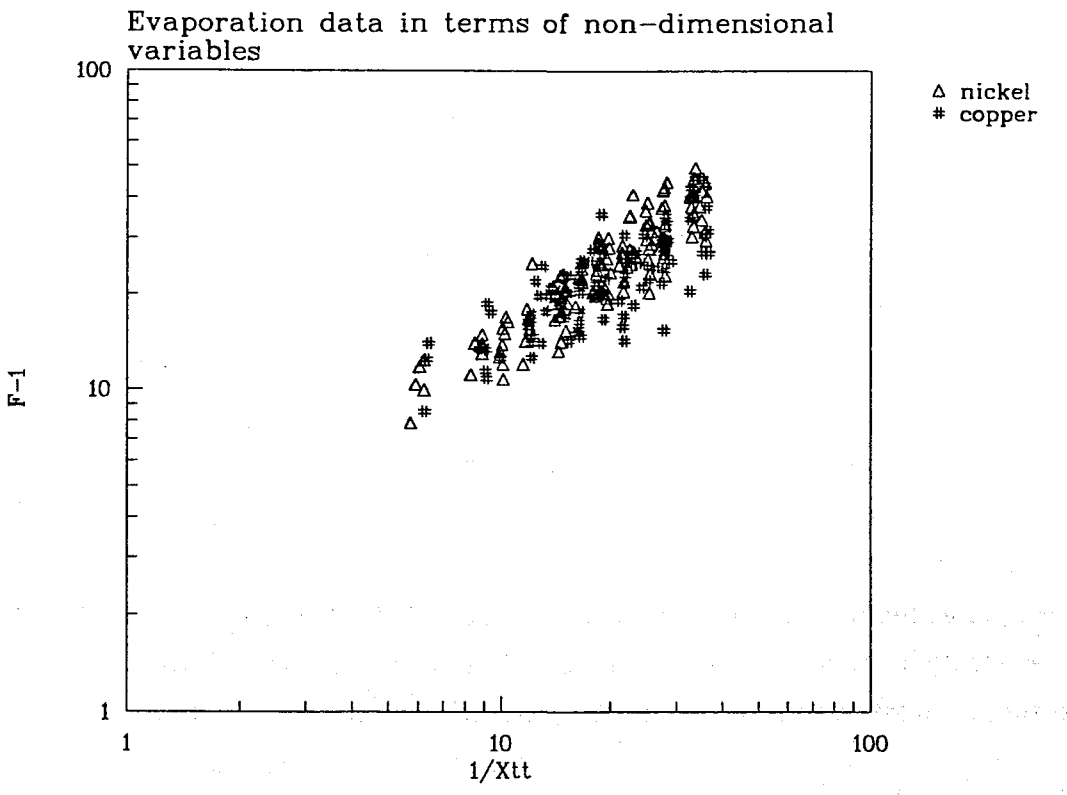

Figure 4.1.7.1-10

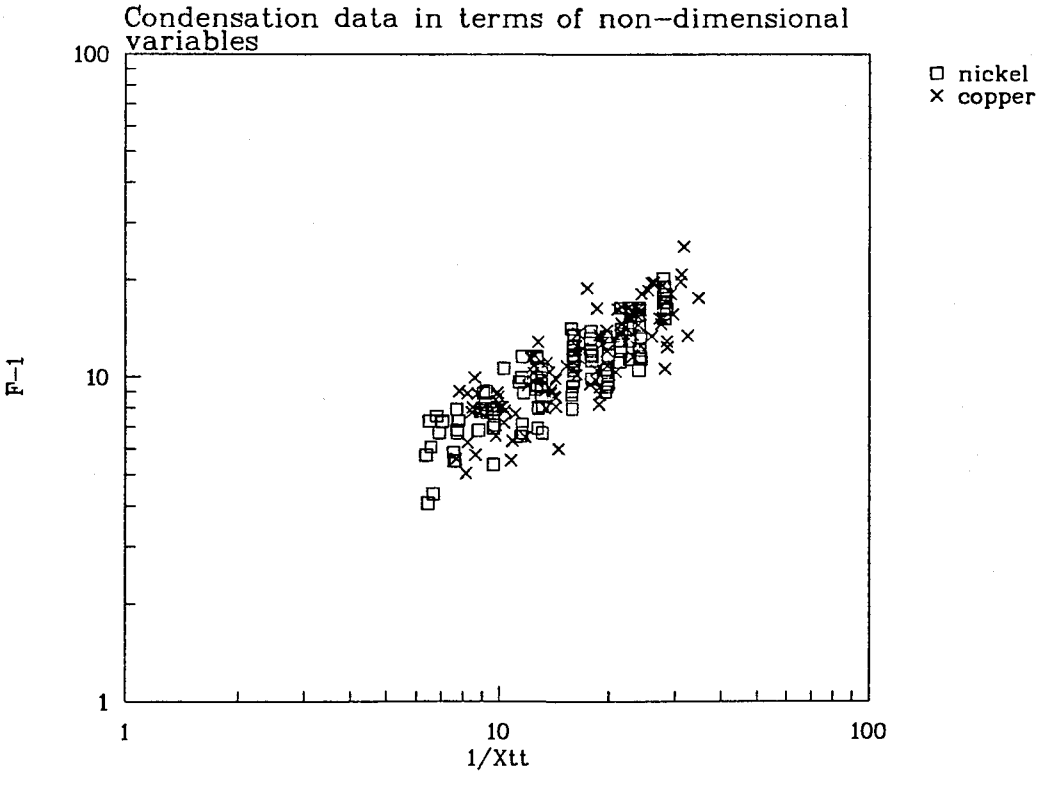

obtained from a facility at Oxford University (Kenning and Cooper, 1989). Some comparison between the Oxford data and the present data are shown in figure 4.1.7.1-11. Obviously, the present fluid heated data exhibit much more scatter, but it will be seen that they are quite consistent with the data from the Oxford electrically heated experiments.

(4) Measurement accuracy : The key measurement limiting the accuracy of the present experiments is that of the temperature difference between the annulus thermocouples at the third station. The calibration of the thermocouples is discussed in Appendix A. If the error in heat transfer coefficient is $d\alpha_{tp}$ and the error in annulus thermocouple temperature difference is $d(\Delta T_a)$, then the following equation (derived from equation 4.1.6.1-8) relates the two :

$$\frac{d\alpha_{tp}}{\alpha_{tp}} = \left(\frac{|T_{sat} - T_{wo}|}{|T_{sat} - T_{wo}| - c\Delta T_a} \right) \frac{d\Delta T_a}{\Delta T_a} \qquad 4.1.7.1\text{-}1$$

In Appendix A, the calibration of the thermocouples is discussed. A maximum error in the calibrated thermocouples of ±0.04°C was estimated. Combining the two thermocouples would give a maximum (pessimistic) error in difference of ±0.08°C. The differentials in the condensation experiments were of the order of 0.6°C which means an error of around ±15 %. In the case of the evaporation experiments, the need for a larger throughput of glycerol to ensure turbulent flow in the annulus meant that the temperature change at the third station was only of the order of 0.15°C, imply a maximum error range in the coefficient of around ±50%. This difference in accuracy is certainly reflected in the data plotted in figures 4.1.7.1-6 to 4.1.7.1-8, but the data for evaporation and condensation are still well separated and the difference between evaporation and condensation are certainly not accounted for by these potential errors.

(5) Incondensible gases : In condensation systems, one always has to be wary of the influence of incondensible gases. These can concentrate near the interface and reduce heat transfer

Figure 4.1.7.1-11

Evaporation data compared with Oxford data

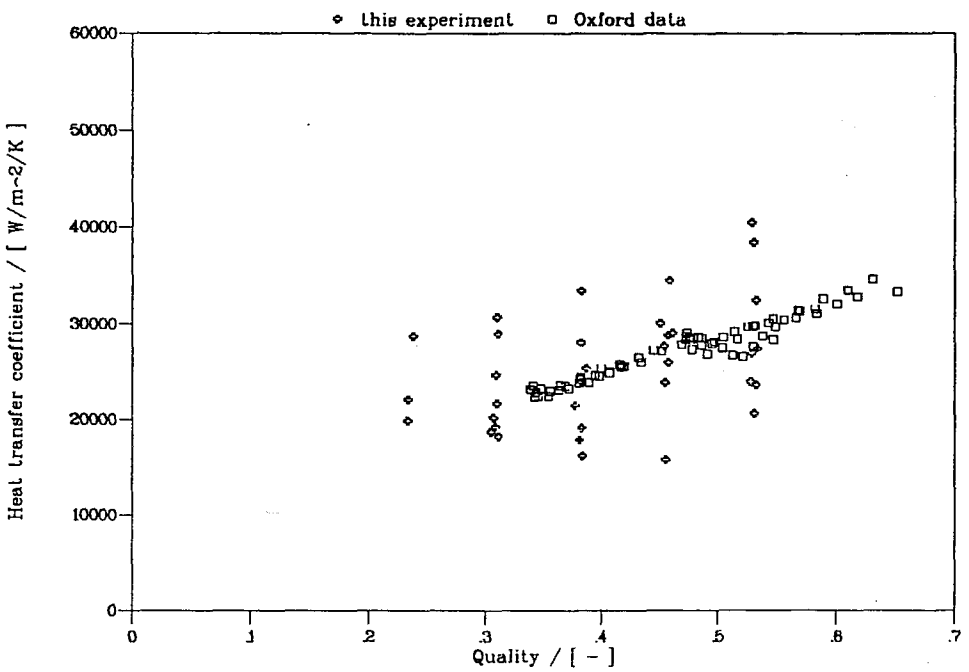

	test fluid	test section inside diameter / [mm]	total mass flux / [kg/m^{2}s]	pressure / [Bar]	Method of heating in test section
Present data	water	9.5	125	1	fluid
Oxford data	water	9.6	123	1.63	electric

coefficient. In the present condensation experiments, incondensible gases could enter the test section by air dissolution in the two-phase circuit water tank with subsequent release of the air into the steam formed in the quality generation section. Could this small amount of inert gas have caused the condensation heat transfer coefficients to be significantly reduced? Calculation addressing this question are described in Appendix G. It was concluded that, in this one-dimensional flow situation and at the mass fluxes used, the effect of incondensible would be negligible.

(6) Direction of mass transfer. Condensation enhances and evaporation reduces the interfacial shear (see, for instance Collier, 1981) and this could change the heat transfer coefficient in the same directions. This is opposite of what is seen here. Calculation using the HANA code indicated, in any case, that mass transfer effects would be expected to be small at the low heat fluxes used.

(7) Primary nucleation and nucleate boiling. It was confirmed using the methods described in Section 2.2.1.3 that the heat fluxes were lower than those required for primary (wall) nucleation. This was also confirmed by the results of Kenning and Cooper (1989) who reported, for similar conditions, that no nucleate boiling was occurring at heat fluxes in excess of those reported here.

We must conclude, therefore, that the difference between evaporation and condensation are real and, as was stated above, this has far reaching implications. Existing theories of forced convective heat transfer would appear deficient and perhaps one does indeed have to look to the explanation of Mesler (1977) to describe the effect. That is, secondary nucleation arising from wave entrainment can have a very significant role even when wall nucleation has been suppressed. Of course, such a surprising conclusion will need much further investigation but a good prim facie case appears to have been established that the observed effects are real.

4.1.7.2 Pressure drop results

The pressure drop data were processed according to the procedure set out in Section 4.1.6.2 in order to calculate the frictional component. In fact, the pressure drop was normally dominated by this component.

The data for frictional pressure gradient in these experiments is presented in figures 4.1.7.2-1 to 4.1.7.2-30. The pressure drop was measured between tappings placed in flanges at the entrance and outlet of the 2m long adiabatic (calming) section placed between the electrically heated section and the test section, and between the tappings at each end of the test section itself (here the pressure tapping were spaced 0.327m apart). The data presented in two forms:

(a) In the form of measured pressure gradient (i.e. pressure drop divided the distance between the tappings) against the mean quality in the respective section.

(b) In the form of $\phi_{Lt} = [(dp_F/dz)/(dp_F/dz)_L]^{1/2}$ against

$X_{tt} = [(dp_F/dz)_L/(dp_F/dz)_G]^{1/2}$ where $(dp/dz)_L$ and $(dp_F/dz)_G$ are the frictional pressure gradients for the liquid and gas phases respectively flowing alone in the channel. This was the form proposed originally by Lockhart and Martinelli (1949) whose correlation curve is also plotted on each of the graphs.

The first pair of graphs (figure 4.1.7.2-1 and 4.1.7.2-2) show data for a mass flux of 241 kg/m^{2}s with no heat transfer in the test section. The test section pressure gradients are higher than those in the calming section. This is because the pressure of the vapour is lower there thus giving higher vapour velocities and higher pressure gradients. When plotted in the ϕ_{Lt}/X_{tt} form, the data are consistent and in good agreement with the Lockhart and Martinelli correlation. Indeed, the agreement with the correlation is remarkable in view of its known errors. However, these errors tend to be greater at higher mass fluxes than those used here.

In figures 4.1.7.2-3 to 4.1.7.2-26, the data for pressure gradient with heat transfer in the test section are presented for mass fluxes of 125 kg/m^{2}s (figures 4.1.7.2-3 to 4.1.7.2-10), 183 kg/m^{2}s (figures 4.1.7.2-11 to 4.1.7.2-18) and 241 kg/m^{2}s (figures 4.1.7.2-19 to 4.1.7.2-26). For each mass flux, the data are presented first for the copper tube experiments and then for the nickel tube experiments and, for each tube, the data are presented for condensation and then for evaporation. In examining the results shown in figures 4.1.7.2-3 to 4.1.7.2-26, the following main features emerge :

(a) The pressure gradient in the adiabatic (calming) section agrees well with the Lockhart-Martinelli correlation at mass fluxes of 241 kg/m^{2}s and 183 kg/m^{2}s but tends to fall somewhat below the correlation line at a mass flux of 125 kg/m^{2}s. In any case, the agreement with the correlation is remarkably good in view of the known scatter of published data compared to the correlation

(b) The agreement between test section pressure gradient data for the copper tube and nickel tube respectively is very good.

(c) Due to the positive change in qualities and consequent changes in local pressure, pressure gradient in evaporation tend to lie somewhat higher than those for the adiabatic section

Figure 4.1.7.2-1

Frictional pressure drop data in calming section and nickel tube test section under adiabatic condition
mass flux 241 kg/m~2/s

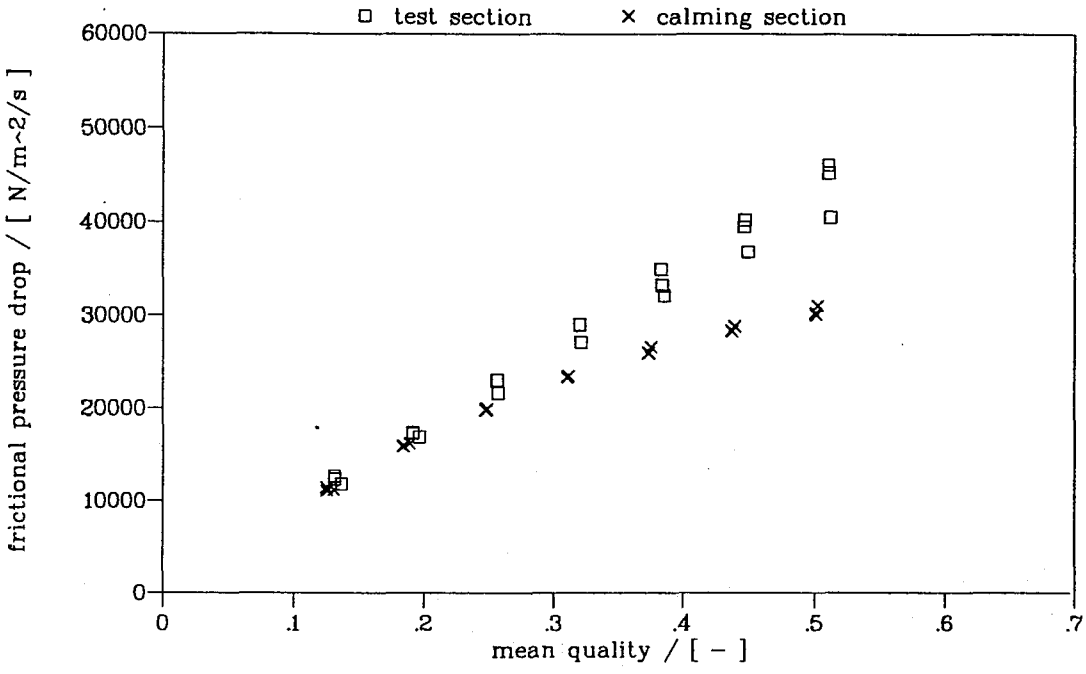

Figure 4.1.7.2-2

Frictional pressure drop data in calming section and nickel tube test section under adiabatic condition compared with Lockhart and Martinelli correlation
mass flux 241 kg/m~2/s

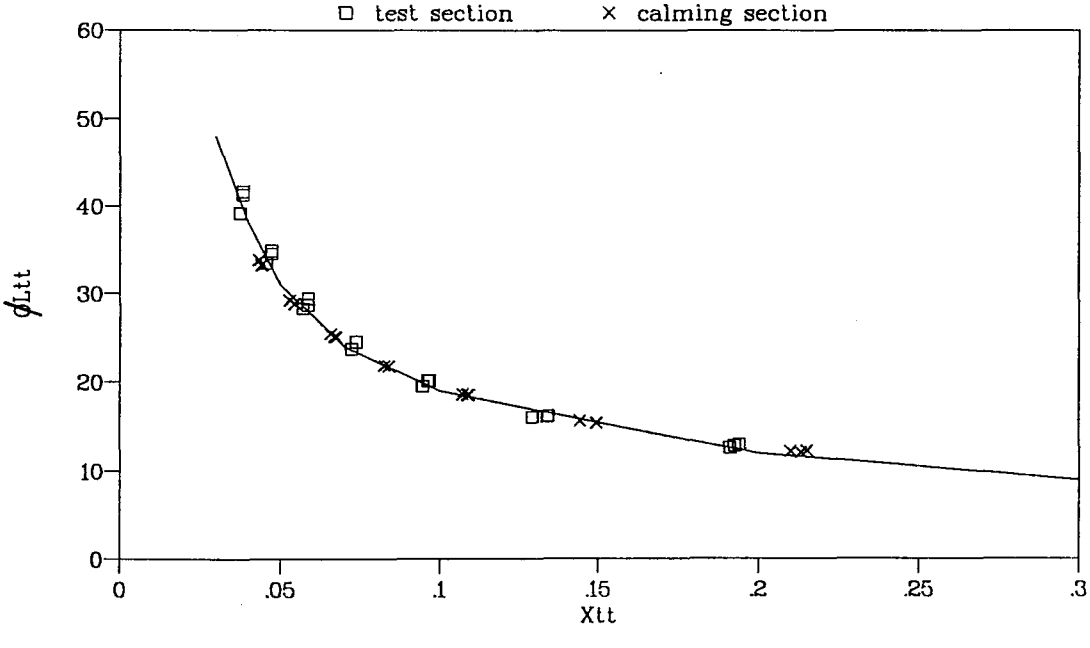

Figure 4.1.7.2-3

Frictional pressure drop data in calming section and copper tube test section with condensation
mass flux 125 kg/m~2/s

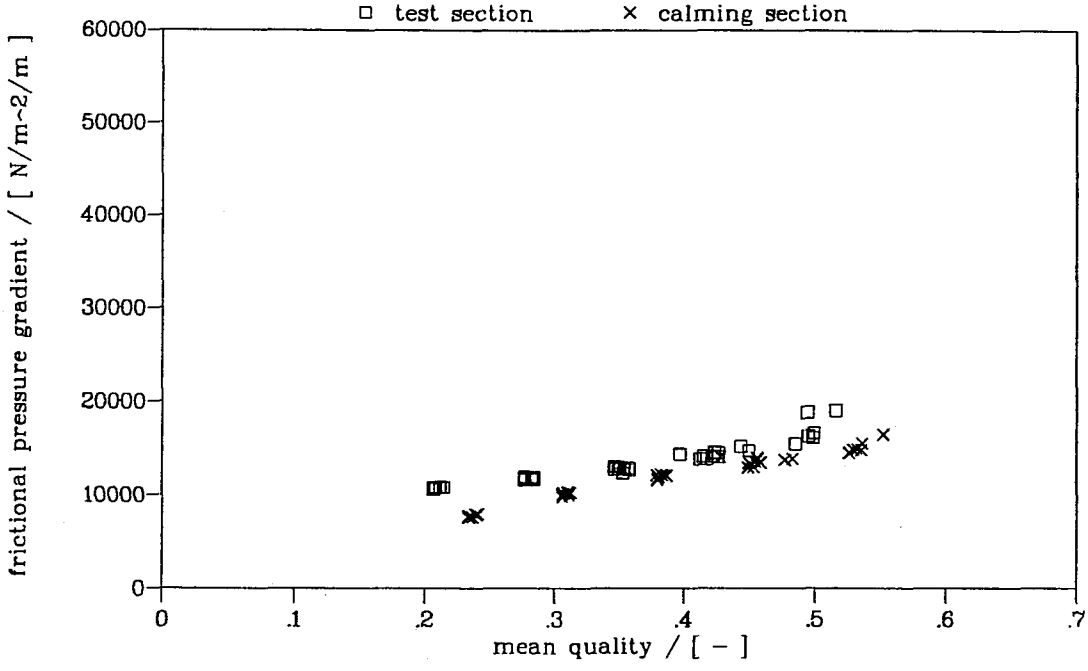

Figure 4.1.7.2-4

Frictional pressure drop data in calming section and copper tube test section with condensation compared with Lockhart and Martinelli correlation
mass flux 125 kg/m~2/s

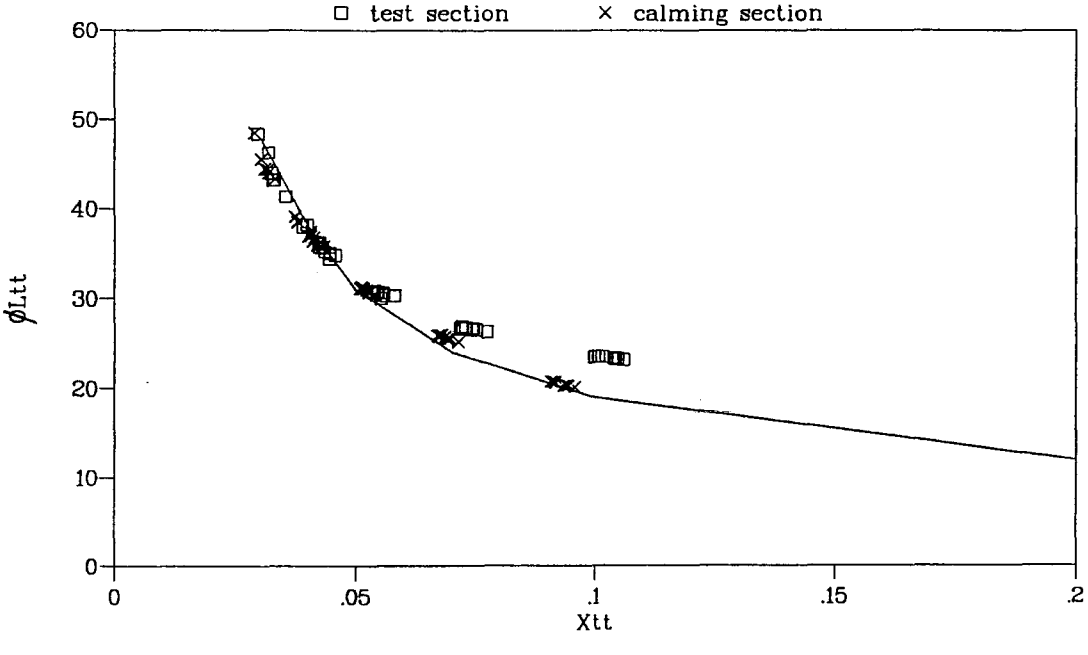

Figure 4.1.7.2-5

Frictional pressure drop data in calming section and copper tube test section with evaporation
mass flux 125 kg/m^2/s

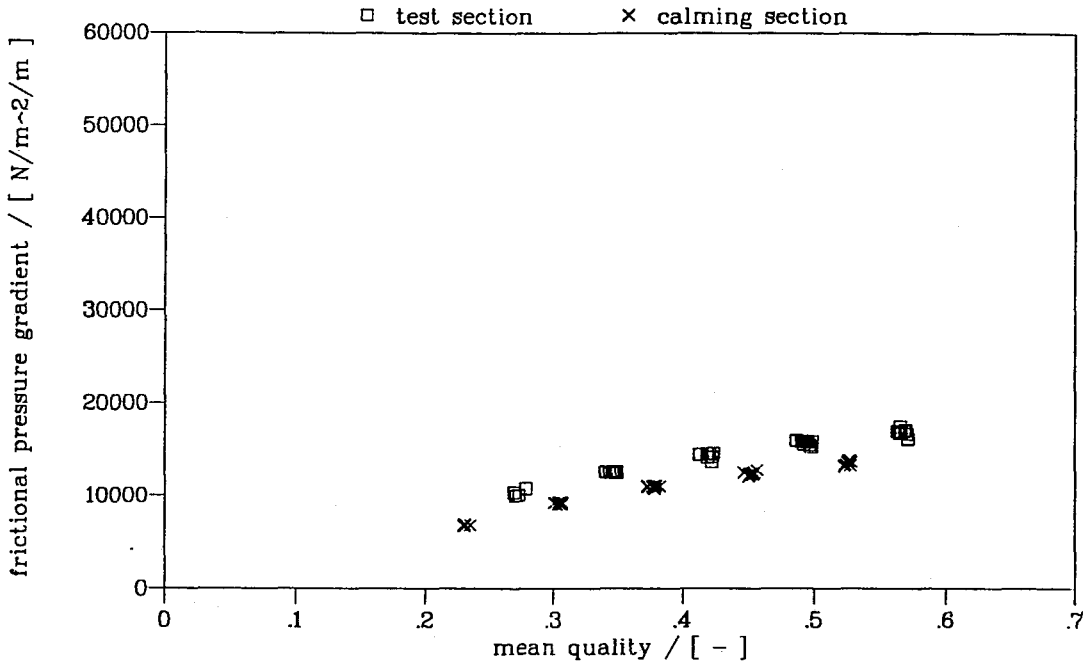

Figure 4.1.7.2-6

Frictional pressure drop data in calming section and copper tube test section with evaporation compared with Lochart and Martinelli correlation
mass flux 125 kg/m^2/s

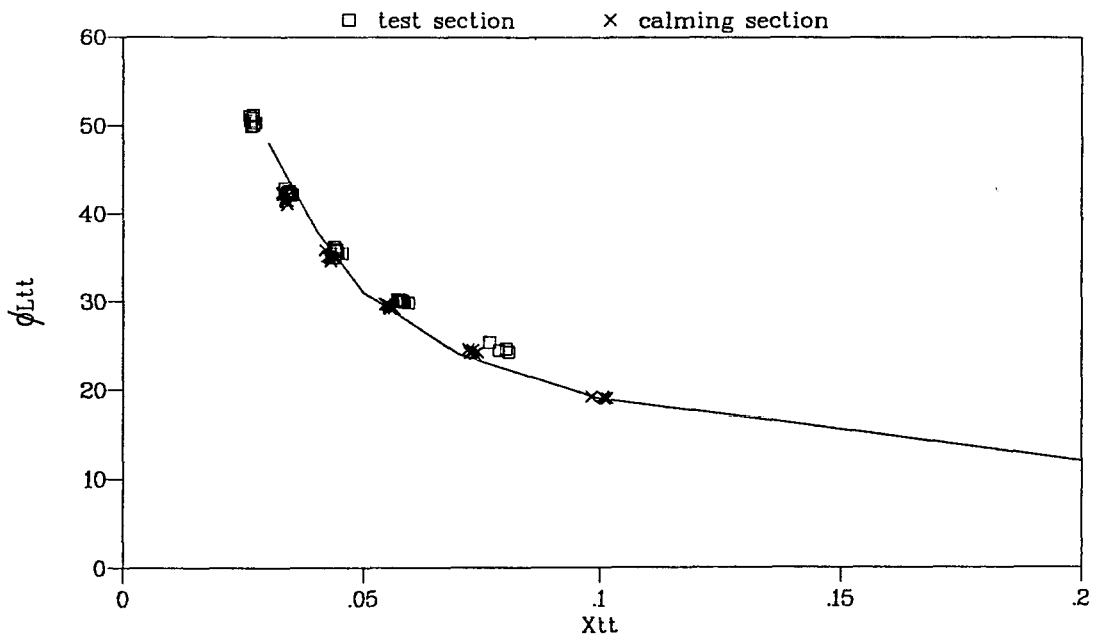

Figure 4.1.7.2-7

Frictional pressure drop data in calming section and nickel tube test section with condensation
mass flux 125 kg/m~2/s

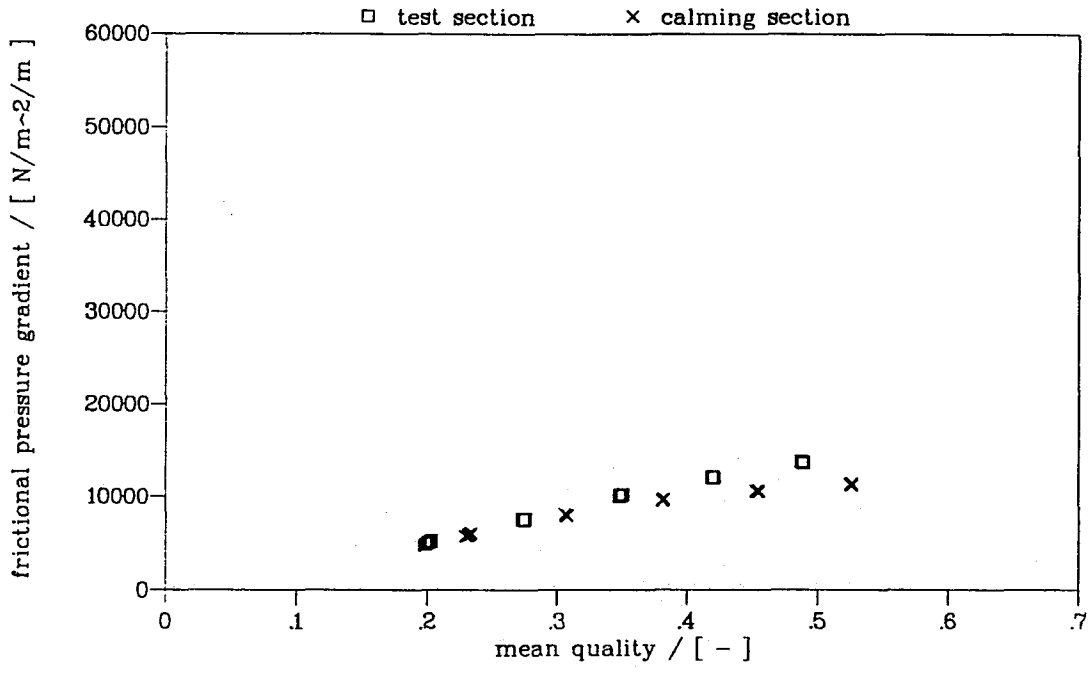

Figure 4.1.7.2-8

Frictional pressure drop data in calming section and nickel tube test section with condensation compared with Lockhart and Martinelli correlation
mass flux 125 kg/m~2/s

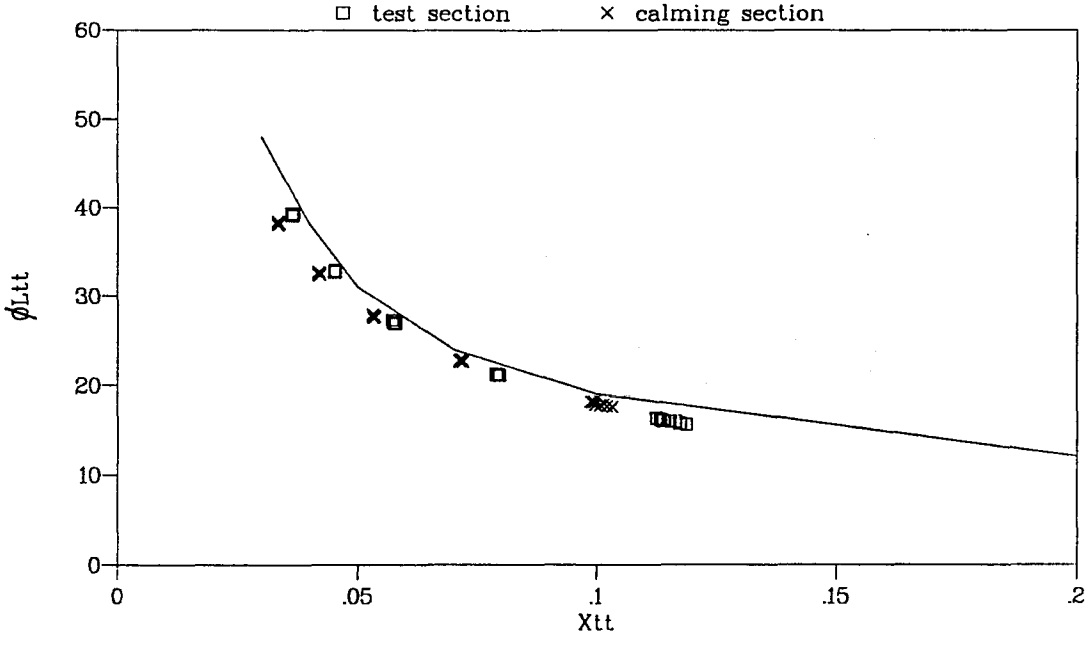

Figure 4.1.7.2-9

Frictional pressure drop data in calming section and nickel tube test section with evaporation
mass flux 125 kg/m~2/s

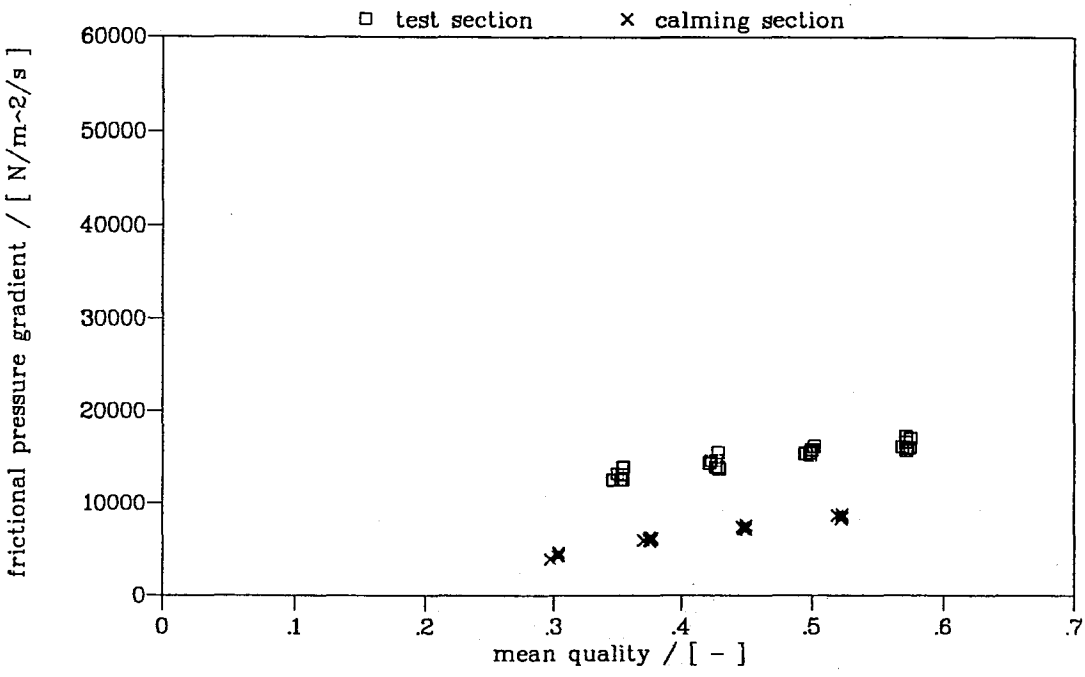

Figure 4.1.7.2-10

Frictional pressure drop data in calming section and nickel tube test section with evaporation compared with Lockhart and Martinelli correlation
mass flux 125 kg/m~2/s

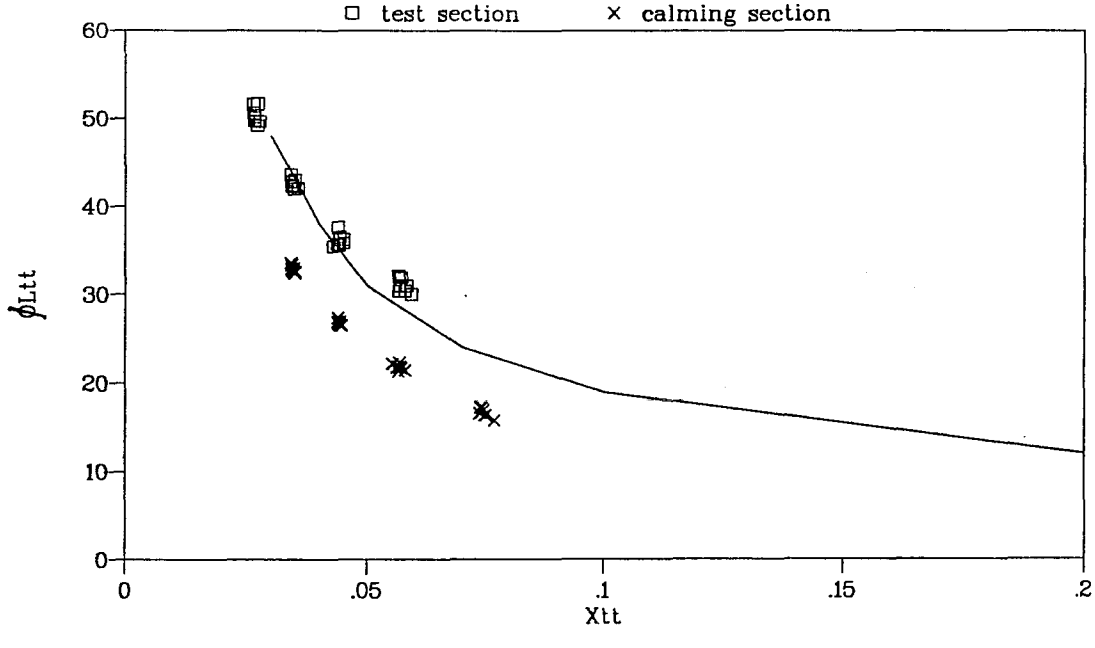

Figure 4.1.7.2-11

Frictional pressure drop data in calming section and copper tube test section with condensation
mass flux 183 kg/m^2/s

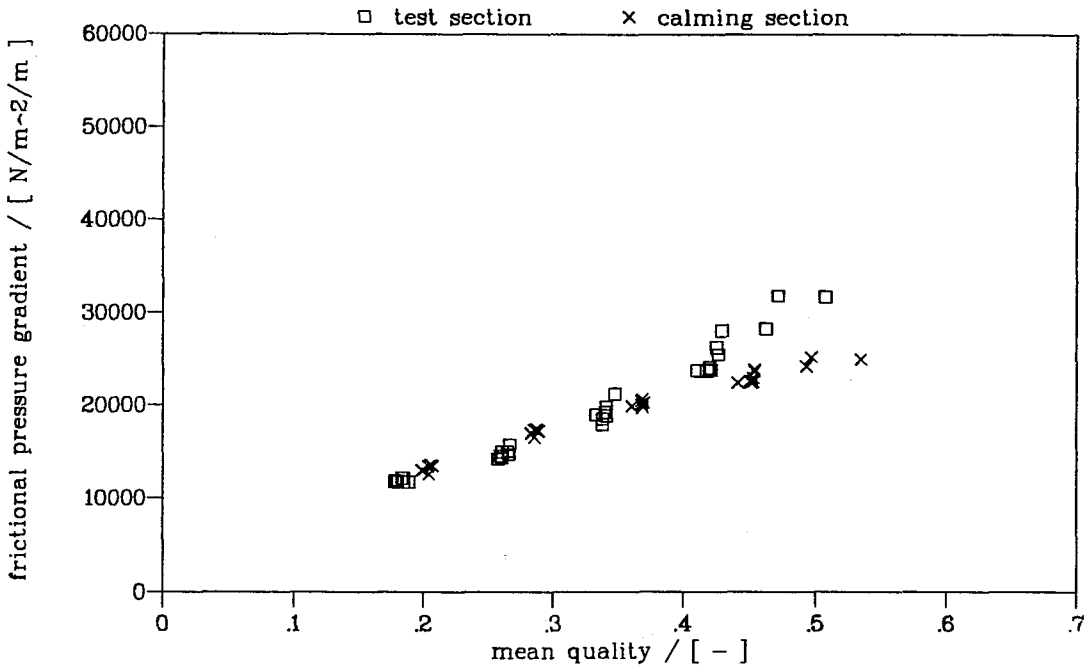

Figure 4.1.7.2-12

Frictional pressure drop data in calming section and copper tube test section with condensation compared with Lockhart and Martinelli correlation
mass flux 183 kg/m^2/s

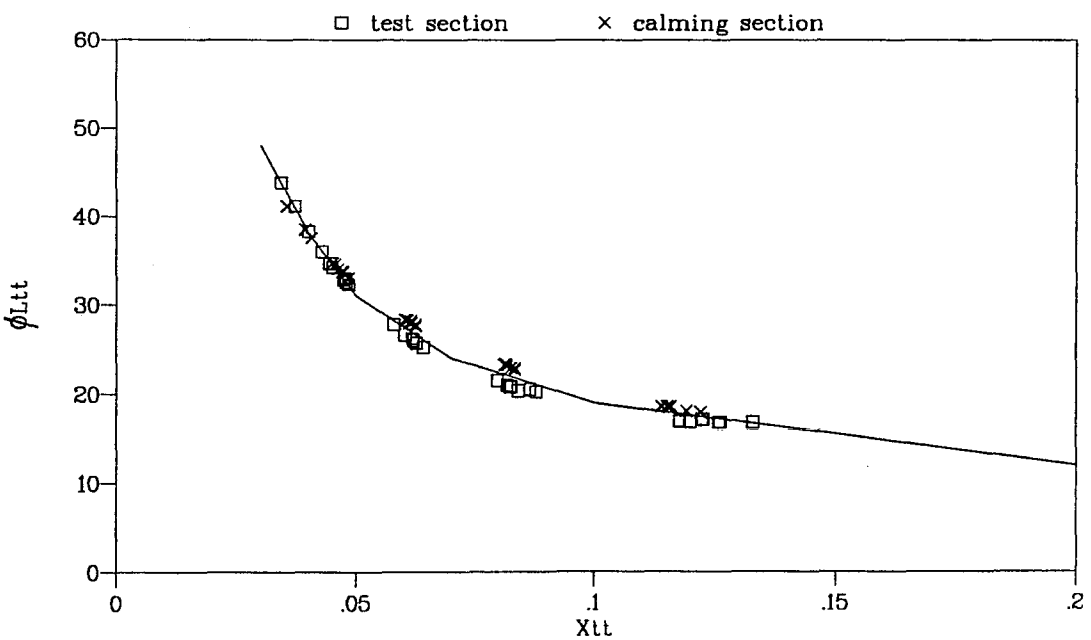

Figure 4.1.7.2-13

Frictional pressure drop data in calming section and copper tube test section with evaporation
mass flux 183 kg/m^2/s

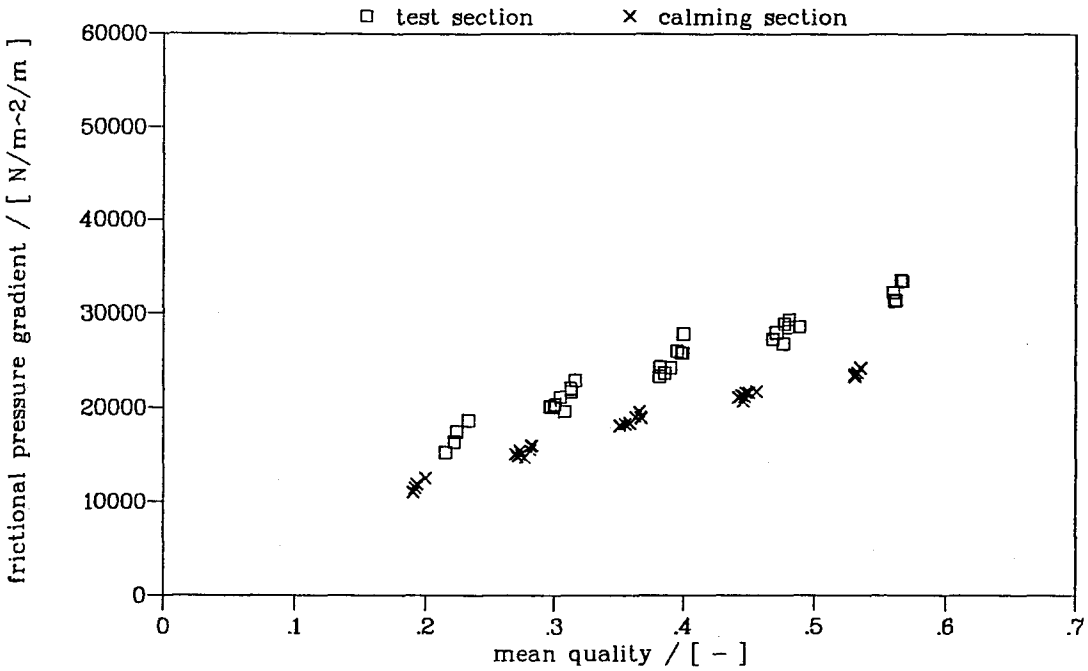

Figure 4.1.7.2-14

Frictional pressure drop data in calming section and copper tube test section with evaporation compared with Lochart and Martinelli correlation
mass flux 183 kg/m^2/s

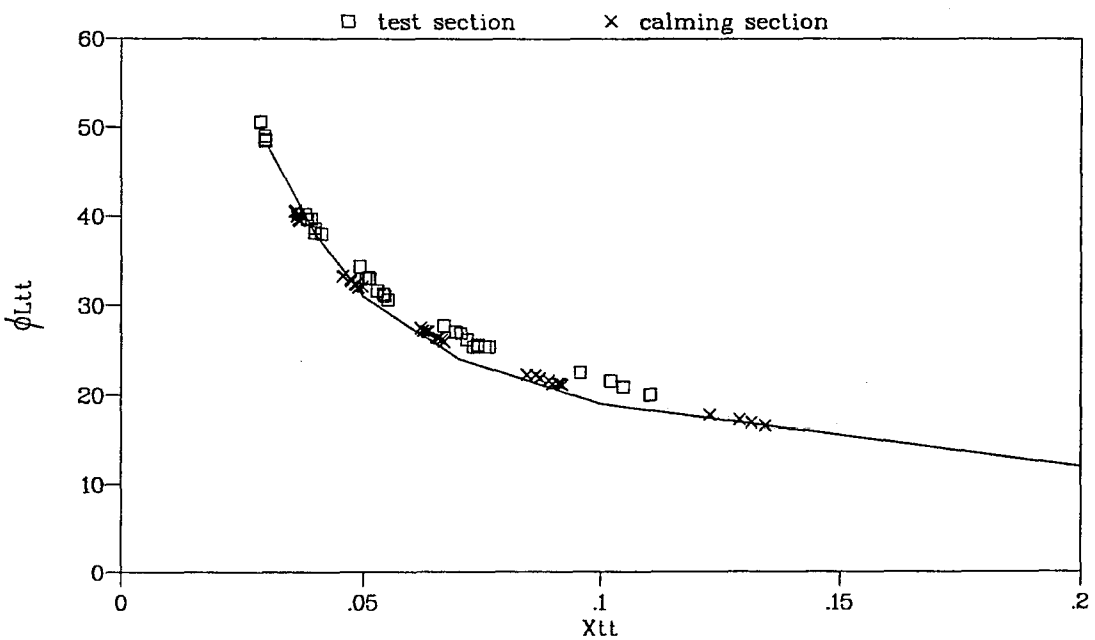

Figure 4.1.7.2-15

Frictional pressure drop data in calming section and nickel tube test section with condensation
mass flux 183 kg/m^2/s

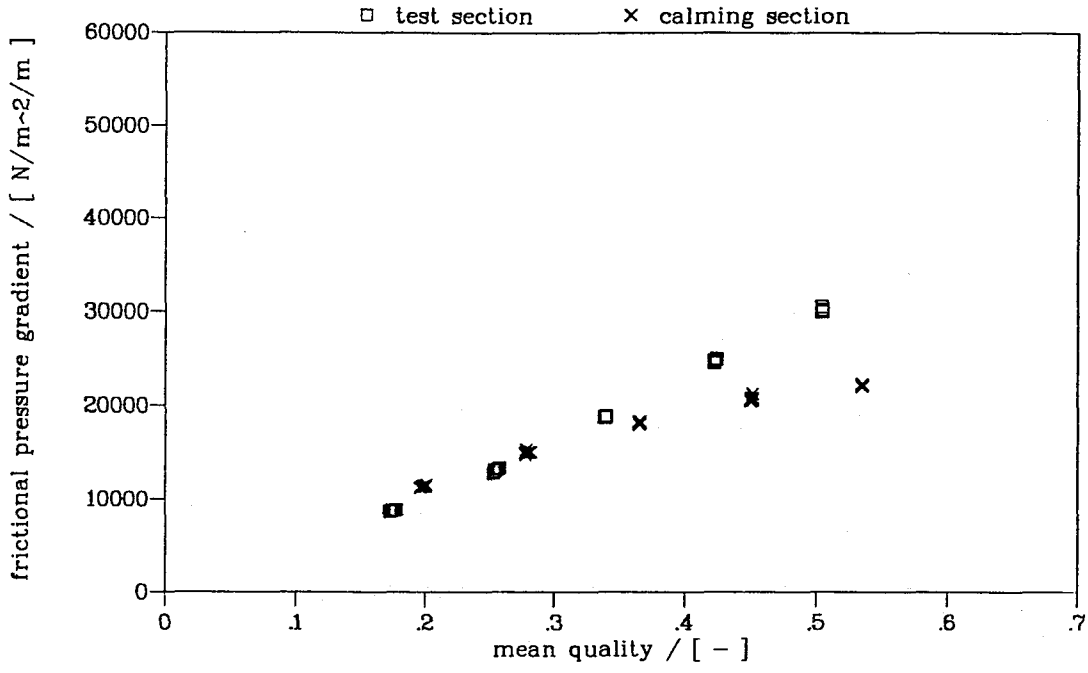

Figure 4.1.7.2-16

Frictional pressure drop data in calming section and nickel tube test section with condensation compared with Lockhart and Martinelli correlation
mass flux 183 kg/m^2/s

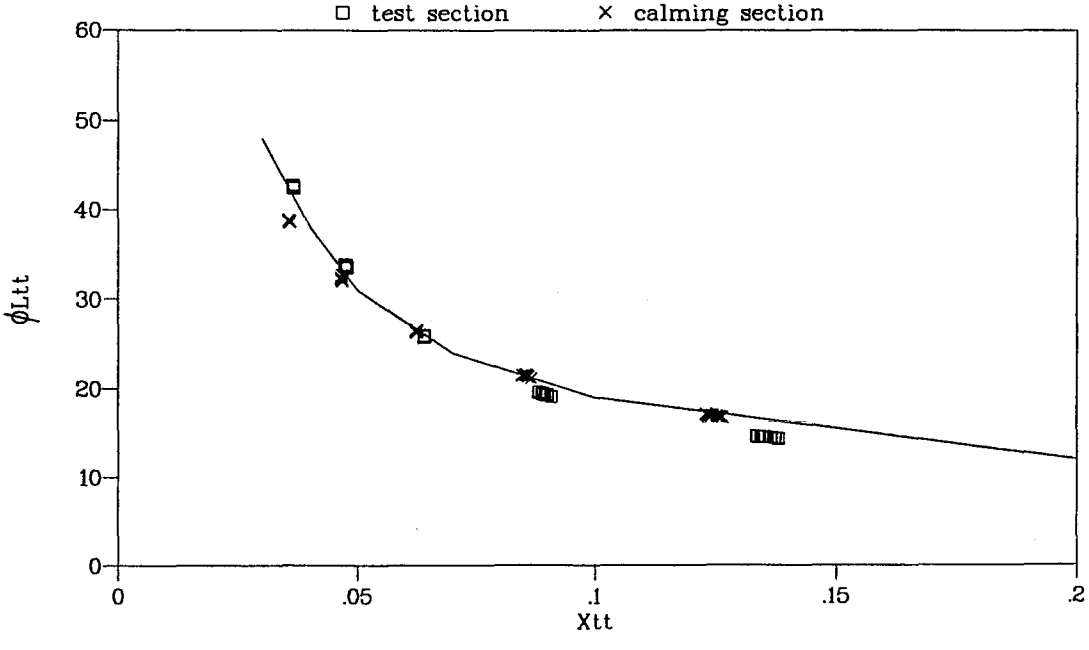

Figure 4.1.7.2-17

Frictional pressure drop data in calming section and nickel tube test section with evaporation
mass flux 183 kg/m~2/s

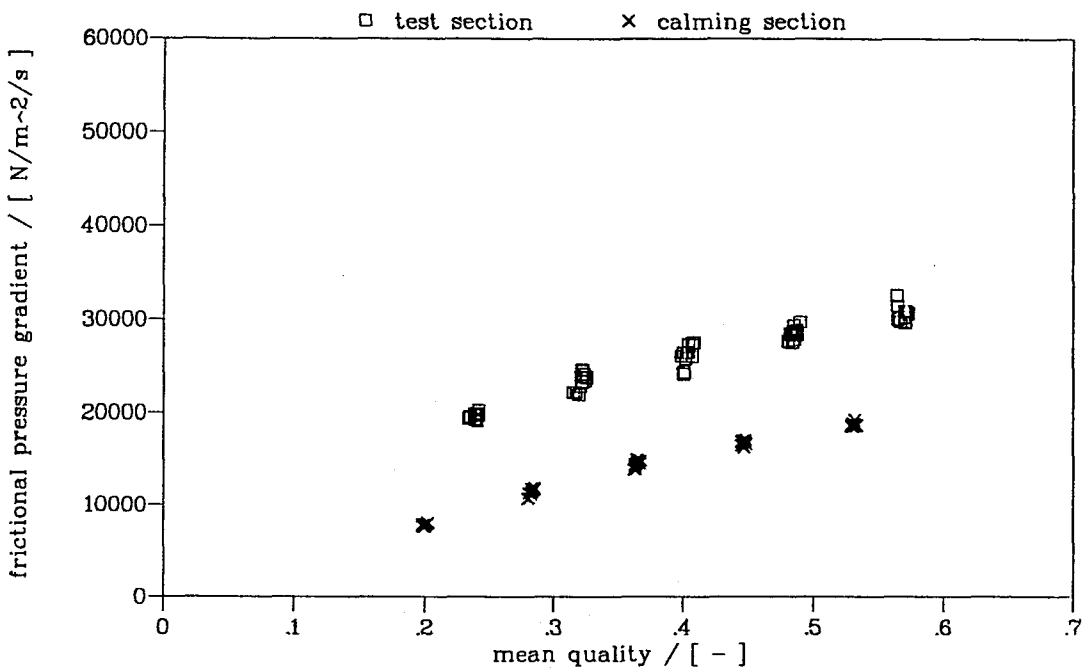

Figure 4.1.7.2-18

Frictional pressure drop data in calming section and nickel tube test section with evaporation compared with Lockhart and Martinelli correlation
mass flux 183 kg/m~2/s

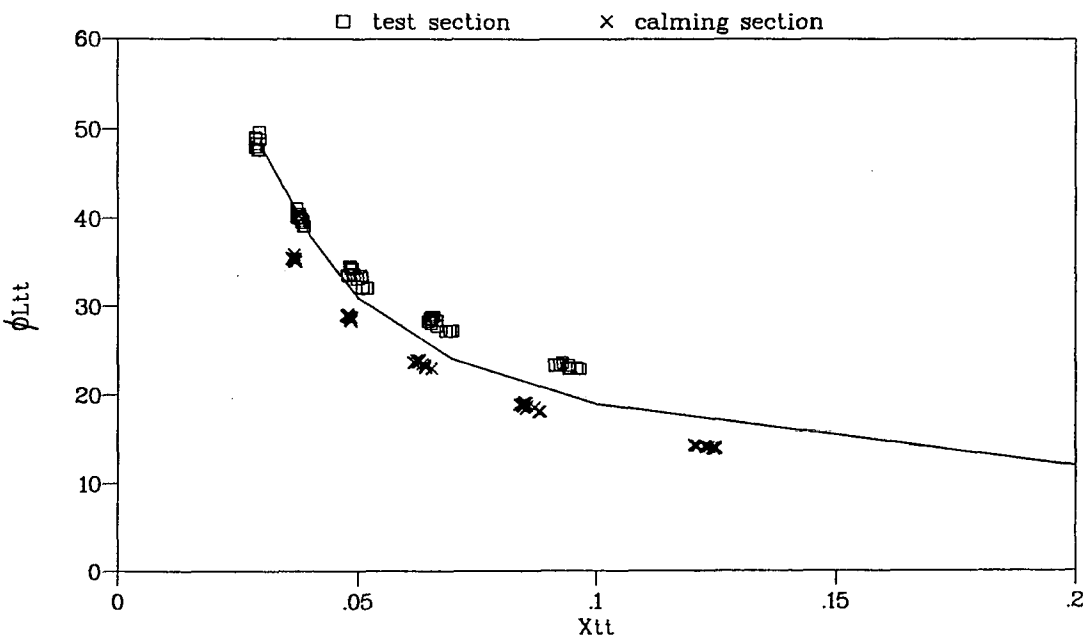

Figure 4.1.7.2-19

Frictional pressure drop data in calming section and copper tube test section with condensation
mass flux 241 kg/m^2/s

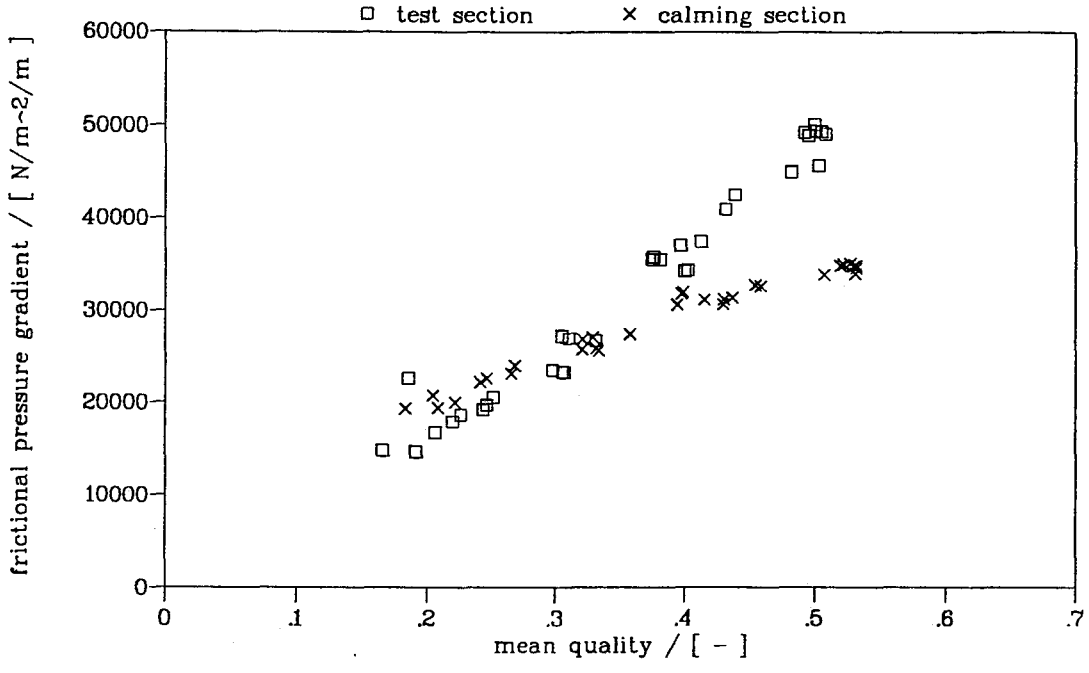

Figure 4.1.7.2-20

Frictional pressure drop data in calming section and copper tube test section with condensation compared with Lockhart and Martinelli correlation
mass flux 241 kg/m^2/s

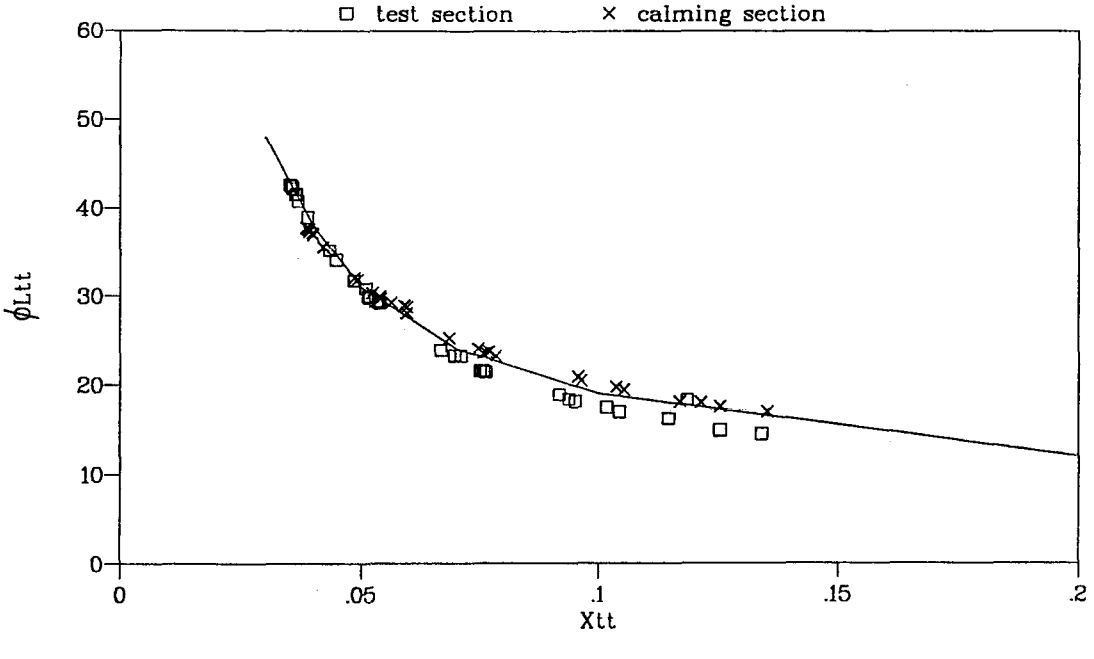

Figure 4.1.7.2-21

Frictional pressure drop data in calming section and copper tube test section with evaporation
mass flux 241 kg/m~2/s

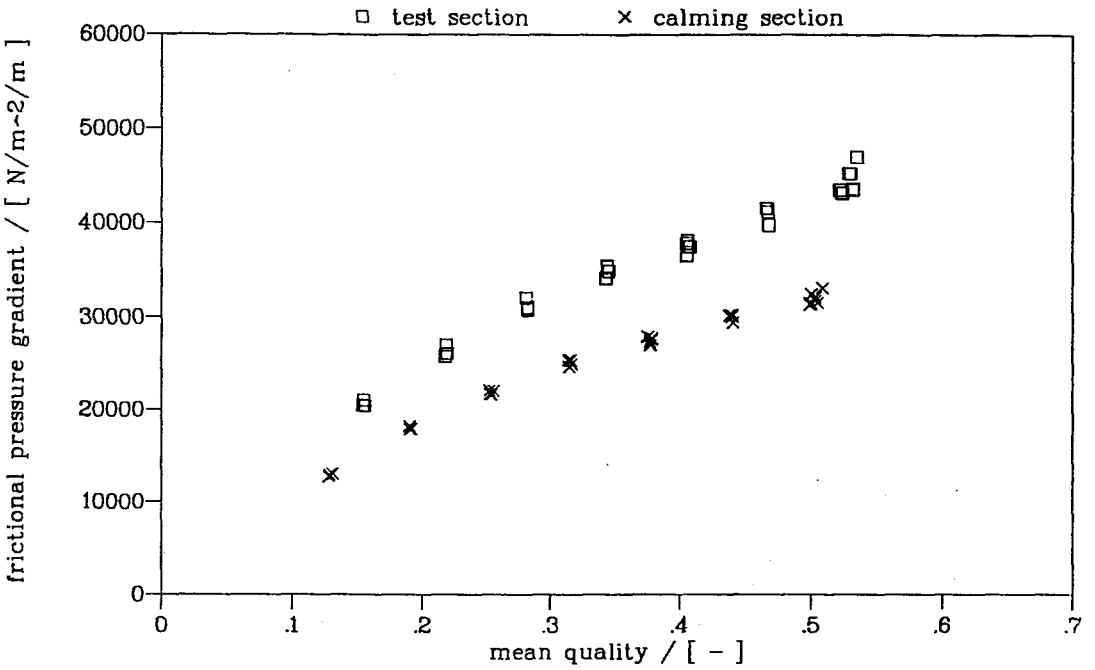

Figure 4.1.7.2-22

Frictional pressure drop data in calming section and copper tube test section with evaporation compared with Lochart and Martinelli correlation
mass flux 241 kg/m~2/s

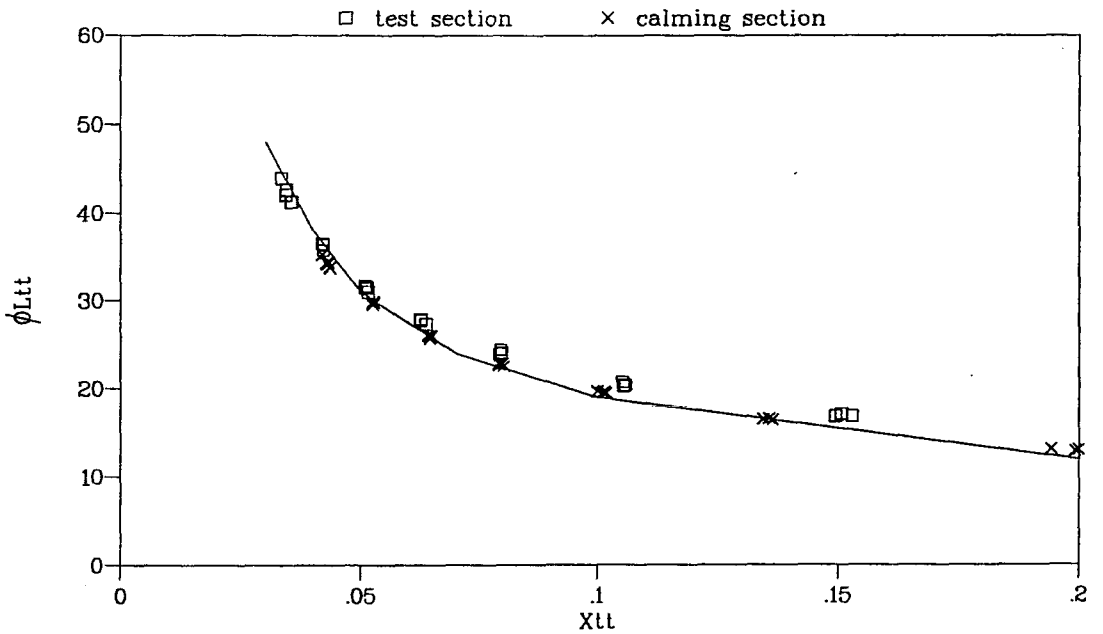

Figure 4.1.7.2-23

Frictional pressure drop data in calming section and nickel tube test section with condensation
mass flux 241 kg/m^2/s

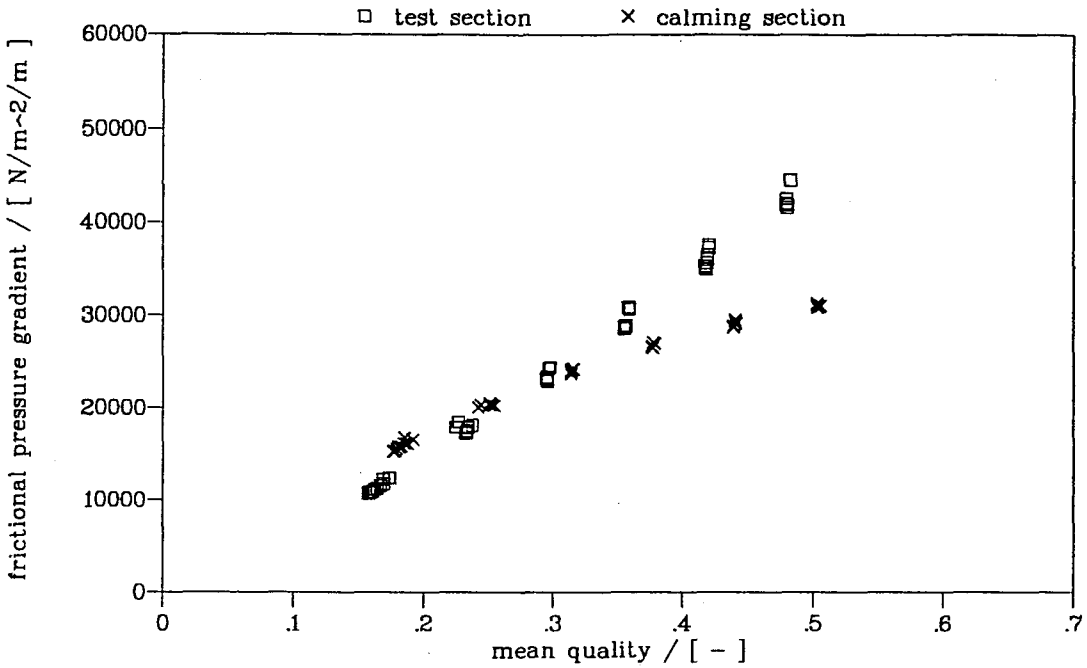

Figure 4.1.7.2-24

Frictional pressure drop data in calming section and nickel tube test section with condensation compared with Lockhart and Martinelli correlation
mass flux 241 kg/m^2/s

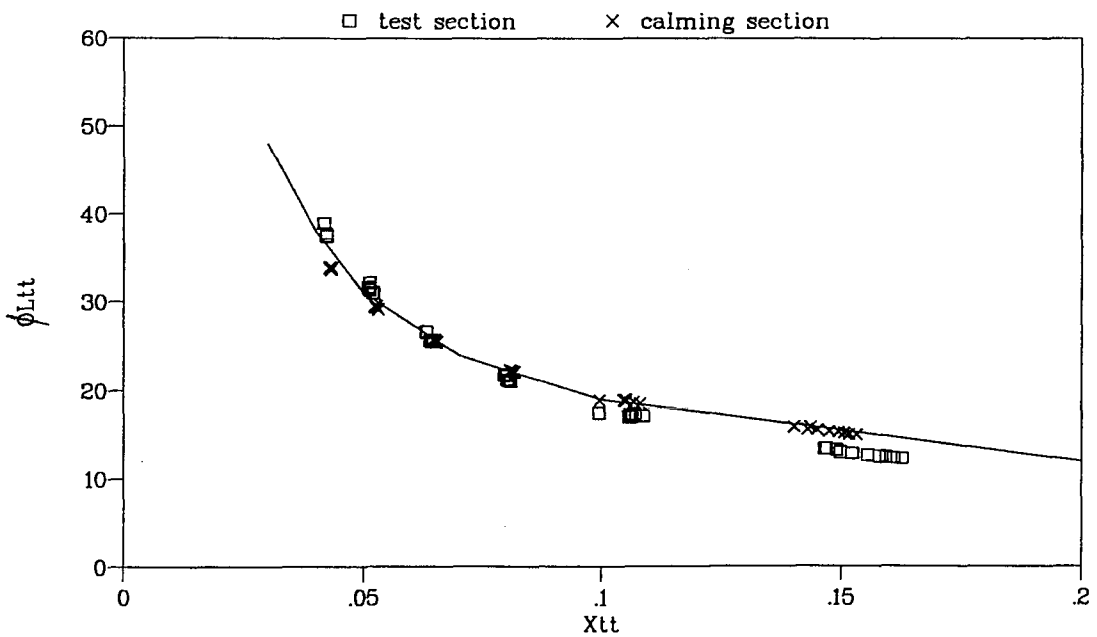

Figure 4.1.7.2-25

Frictional pressure drop data in calming section and nickel tube test section with evaporation
mass flux 241 kg/m~2/s

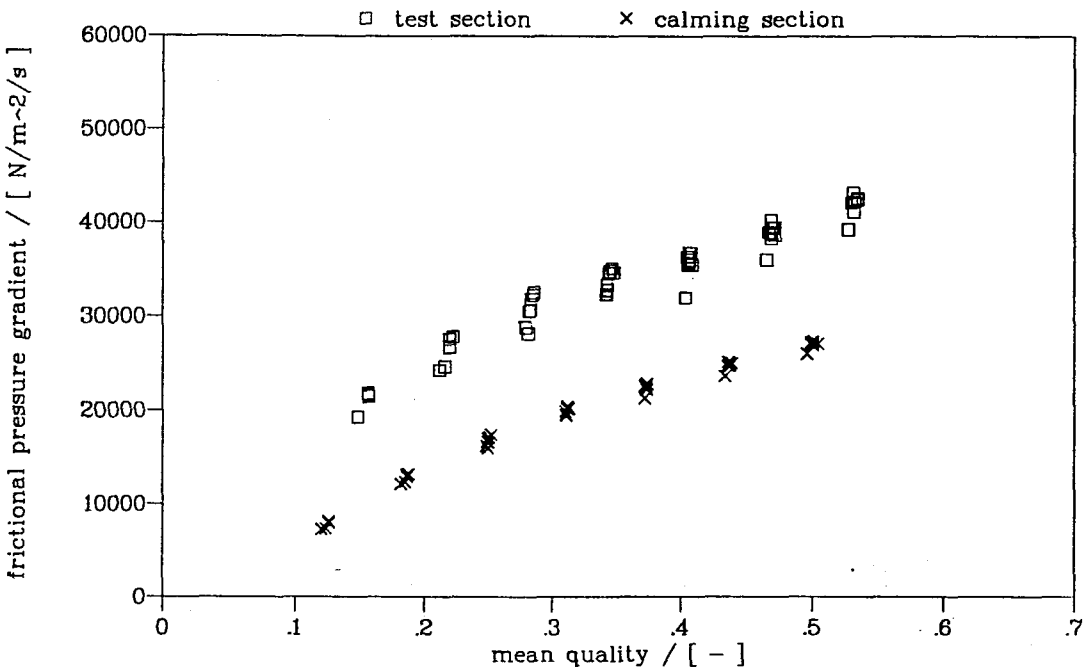

Figure 4.1.7.2-26

Frictional pressure drop data in calming section and nickel tube test section with evaporation compared with Lockhart and Martinelli correlation
mass flux 241 kg/m~2/s

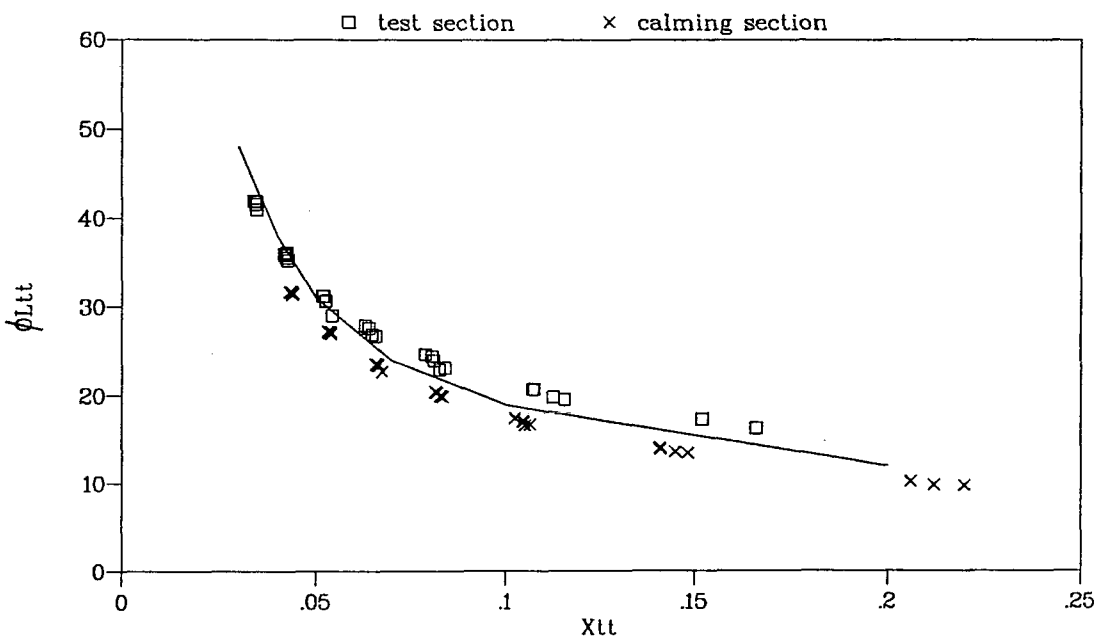

Figure 4.1.7.2-27

Frictional pressure drop data in calming section with heat transfer taking place in test section
mass flus 241 kg/m^2/s

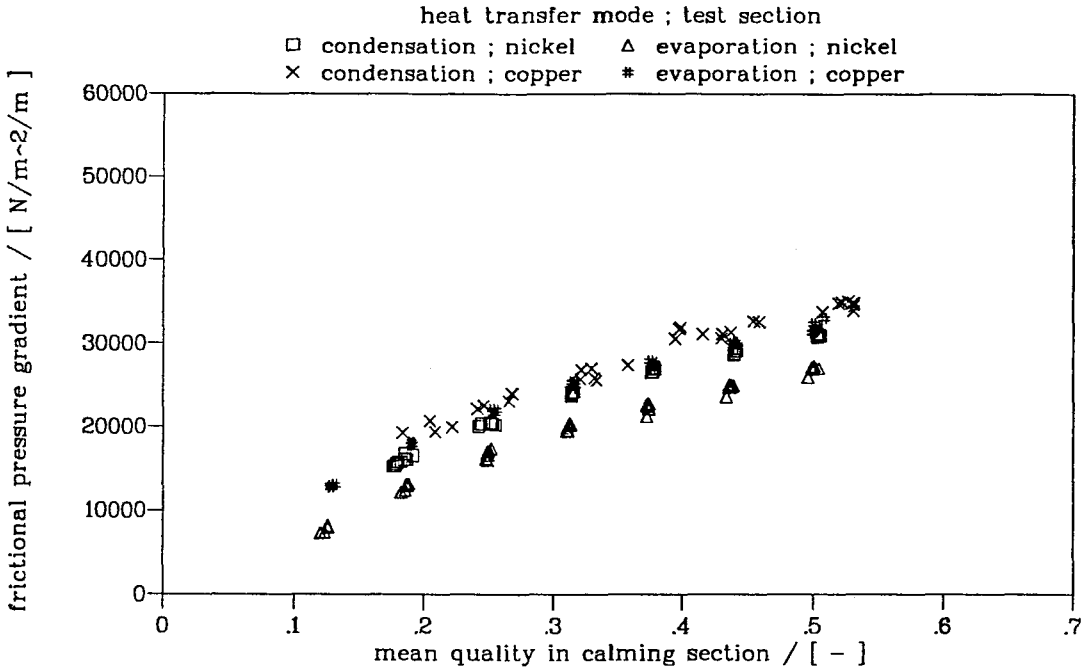

Figure 4.1.7.2-28

Frictional pressure data in calming section with heat transfer taking place in test section compared with Lockhart and Martinelli correlation
mass flux 241 kg/m^2/s

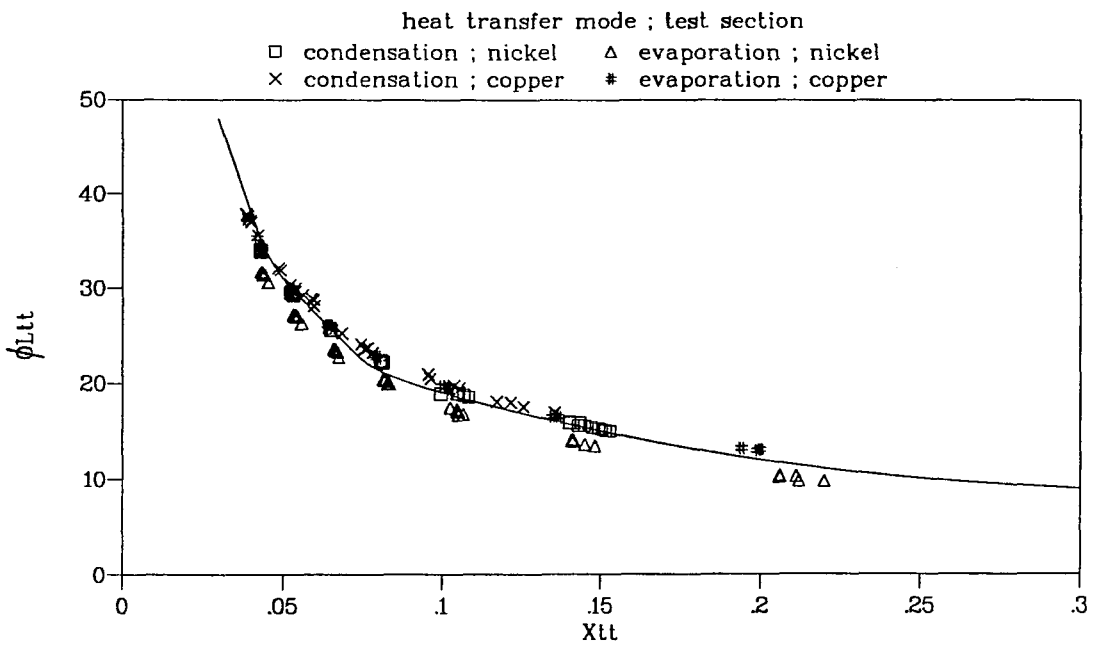

Figure 4.1.7.2-29

Frictional pressure drop data in test section with heat transfer taking place
mass flus 241 kg/m~2/s

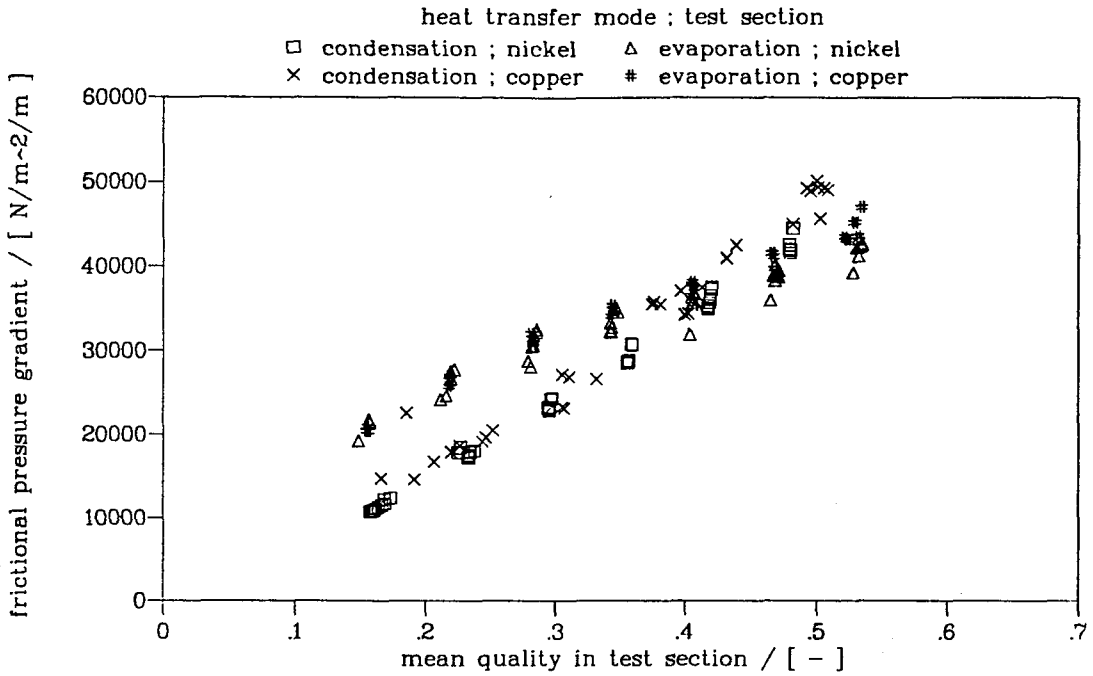

Figure 4.1.7.2-30

Frictional pressure drop data in test section with heat transfer taking place compared with Lockhart and Martinelli correlation
mass flux 241 kg/m~2/s

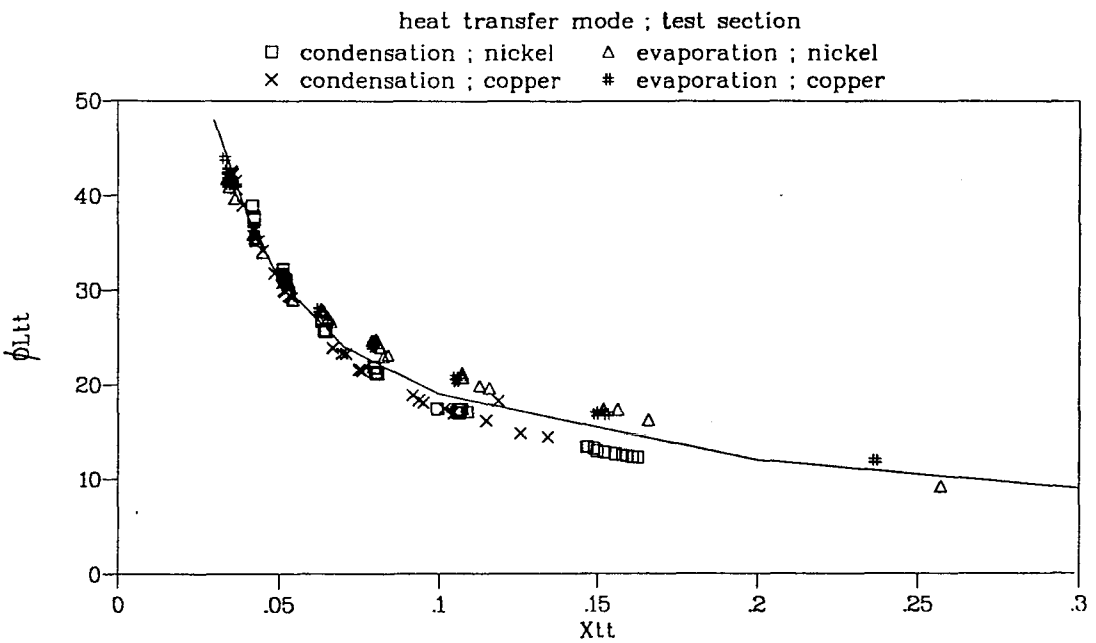

whereas those for condensation are (coincidentally) closer to the adiabatic section line. However, the difference persists even when the data are plotted in the form of ϕ_{Ln} against X_n with condensation tending to give lower pressure gradients than adiabatic flow and evaporation giving high pressure gradients. This point is further illustrated in figures 4.1.7.2-27 to 4.1.7.2-30. Here, the data for all test sections and heat transfer directions are presented together for a mass flux of 241 kg/m^{2}s. For the adiabatic section (figure 4.1.7.2-27 and 4.1.7.2-28), the results generally agree well with the correlation line, though the results obtained with evaporation occurring in the nickel test section above the adiabatic test section seem slightly anomalous. For the test section (figures 4.1.7.2-29 and 4.1.7.2-30) good agreement is obtained between the two tubes but the evaporation data lie slightly above the correlation line whereas those for condensation lie slightly below it.

It is well known (see for instance Hewitt and Hall Taylor, 1970) that, for given phase flow rates, the pressure gradient increases with increasing liquid film flowrate (i.e. with decreasing fraction of liquid entrained as droplets). In evaporation, starting from equilibrium, the film flowrate would tend to decrease with distance along the test section compared with equilibrium whereas the opposite would be true in condensation. Thus the trends seen in figure 4.1.7.2-30 are not consistent with those expected. The probable explanation lies in the fact that a linear average pressure gradient is taken whereas the pressure is not changing linearly in the test section. However, the difference between evaporation and condensation are at least partially consistent with the differences in heat transfer but are certainly not sufficient to explain them purely in terms of changes in shear stress. However, if bubble growth arising from secondary nucleation is indeed occurring in the liquid film, then this may lead to additional friction.

4.2 Experiments on non-equilibrium annular up-flow

Given the liquid and vapour phase flow rates, the hydrodynamics of the system can be characterized by the distribution of the liquid phase, namely the liquid film flow rate and the liquid entrainment. This liquid

phase distribution in turn is a result of the interaction between droplet entrainment and deposition. At equilibrium, the rate of deposition and entrainment are equal and the droplet concentration remains constant. In non-equilibrium flow, there is an imbalance between the deposition and entrainment processes. This imbalance is seen most severely in adiabatic flows where the fluids are mixed in an arbitary way at the channel inlet. For example, when the liquid phase is introduced through a porous wall (sinter) section, all the liquid is in the liquid film when it first meets the vapour phase. Interfacial waves are then induced and liquid entrainment then follows as the liquid at the wave crests breaks off because of the vapour shear. Entrainment rate is highest at the sinter mixer. As the droplet concentration increases, droplet deposition then comes into play. and an equilibrium state will be reached at some distance down-steam from the sinter mixer.

It is expected that interfacial waves will play a crucial role in the heat transfer process. Azzopardi and Martin (1985) have suggested that there is a link between turbulent bursts and disturbance wave formation in annular flow. The turbulent burst frequency in a single phase flow and the initial wave frequency in annular flow were shown to be similar. Downstream of the inlet, the waves coalesce and their frequency decreases. Could the failure of single-phase-flow-based convective heat transfer correlationsreflect the reduction in frequency ? The objective of the second series of measurements reported in this thesis was to investigate this question by examining heat transfer in annular flows with controlled non-equilibrium. This was achieved by separating the flows and then reinjecting the liquid around the periphery of the tube. By allowing different distances (120 mm and 320 mm) between the injector and the test section inlet (the same nickel tube test section was used as for the equilibrium experiments), the effect of waves development could be studied. The characteristics of the waves were investigated using flush-mounted concentric conductance probes and these measurements will be described in Chapter 5

4.2.1 Modifications of experimental rig

The calming section in the equilibrium flow experiments was replaced by the set-up as shown in figure 4.2.1.1 . The separator consisted of a QVF

Figure 4.2.1-1 Set-up for non-equilibrium annular flow experiments

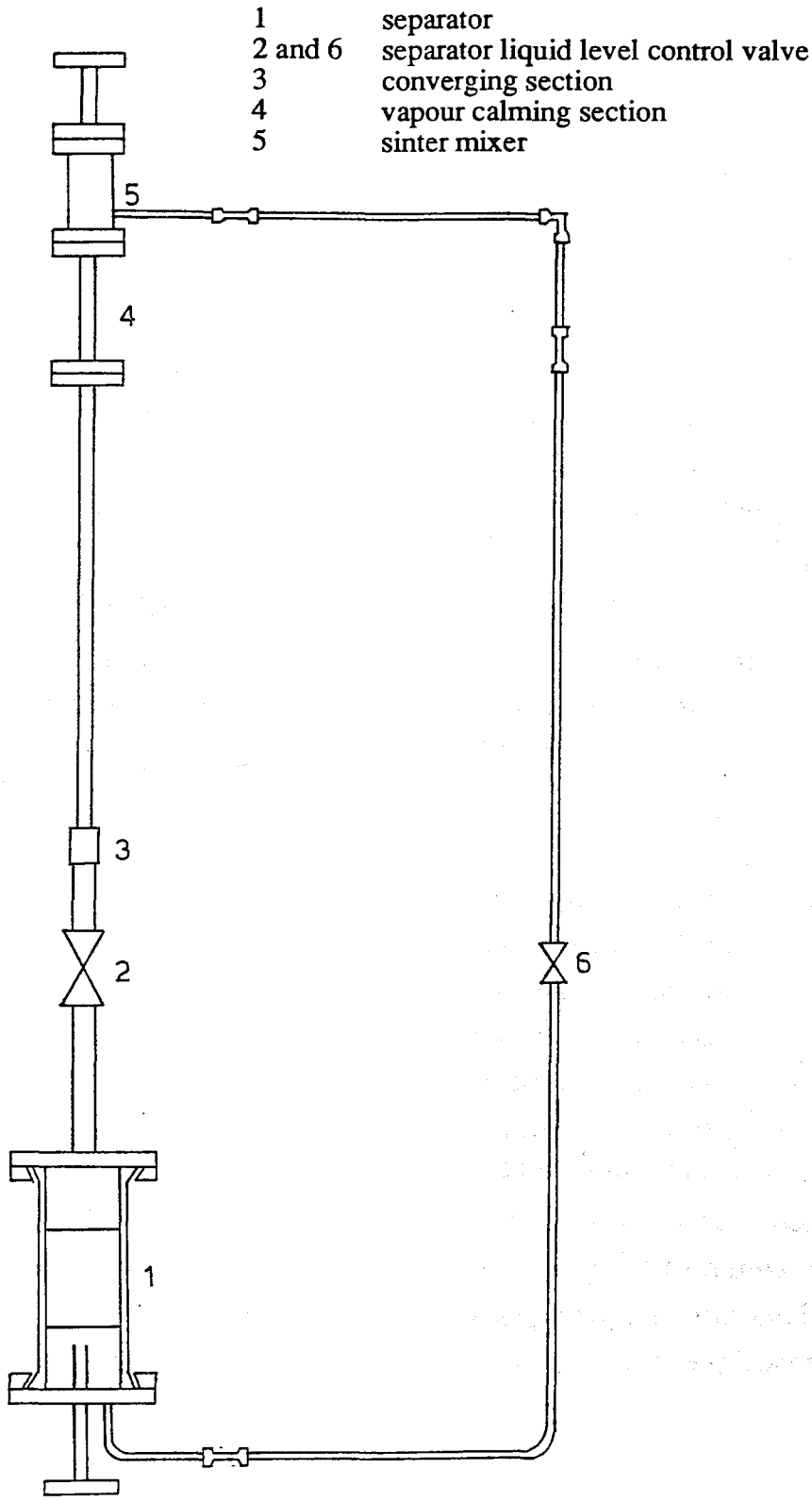

cylinder in which was mounted a highly porous "Knitmesh" pad made from woven stainless steel wire. The diameter and the depth of the "Knitmesh" are 100 mm and 150 mm respectively. Given the operating conditions, these dimensions were determined by the criteria recommended by the "Knitmesh" manufacturer. Due to limited space, the clearance above and below the "Knitmesh" did not follow the manufacturer's standard. To make sure that the separator worked satisfactorily, a separation efficiency test was carried out. The results of this test were satisfactory (see Appendix E).

The steam outlet pipe of the separator had an inside diameter of 12.7 mm. After the needle control valve, there was an converging section to reduce the diameter down to 9.5 mm. Before the test section, there were three sections with an inside diameter of 9.5 mm. The one just below the test section has a length of 120 mm. Below this section was the porous wall section (sinter mixer). Another straight section, which had a length of 300 mm, could be swapped with the porous wall section.

The water outlet pipe from the separator to the porous wall injector had an inside diameter of 4.9 mm. There was a needle control valve on this water line, which brought the water into the sinter mixer.

4.2.2 Operation

The operation was similar to the that in the equilibrium flow experiment. A run was started by priming the two-phase circuit, including the D.P. cell sensing lines. Then the power supply to the heating section was switched on. The cooling water flow rate in the condenser was adjusted while the power was raised to produce two-phase flow. Once the desired power was reached to produce the required quality, the control values on the steam line and the water lines were adjusted to maintain the water level in the separator below the "Knitmesh". Then water circulation in the single-phase circuit was started and set at a predetermined flow rate (0.0849 kg/s). The flow rate of the cooling water to the cooler in the single-phase circuit was adjusted to maintain the single-phase fluid at a predetermined temperature (about 60°C).

Temperatures and pressure differentials were continuously scanned by the computer. The wattmeter, flowmeters and pressure transducers were monitored manually. When the equilibrium state was reached, the computer would take the average values of the last nine scans for each channel. The readings of the wattmeter, flowmeters and pressure transducers were taken manually and typed into the computer for storage.

Runs were carried out at only one mass flux (241 kg/m^{2}s).

4.2.3 Results and discussion

4.2.3.1 Heat transfer results

The non-equilibrium data were processed in the same way as the equilibrium data (see Section 4.1.6).

The heat transfer results are shown in figure 4.2.3.1-1. The results from the equilibrium flow experiments were also plotted in the same figure for comparison. It can be seen that the three sets of data overlapped each other in good agreement. Thus, in the present experiments, there was no significant effect of entrance length, though a change in wave frequency had been expected from earlier data. However, later in the work, the wave frequency was measured using conductance probes (see Chapter 5) and was found not to vary significantly with position over the range measured. Earlier work had been with water at atmospheric pressure (see Hewitt and Hall Talyor, 1970) and perhaps the equilibrium value is attained more rapidly at higher temperature where the liquid viscosity is greatly reduced. To further investigate the proposed mechanism, therefore, shorter distances are required between the injector and the measurement station. This was not possible in the present work.

4.2.3.2 Pressure drop results

Pressure drop data for the test section were obtained with and without condensation in the test section. The results with no heat transfer are shown in figure 4.2.3.2-1 and 4.2.3.2-2 and those with condensation are shown in figure in 4.2.3.2-3 and 4.2.3.2-4. Again, the result are plotted as actual pressure gradient and also in the form of ϕ_{Lo} against X_{tt}.

Figure 4.2.3.1-1

Condensation heat transfer coefficients of annular up-flow of water and steam with and without sinter mixer up-stream of nickel tube test section

mass flux 241 kg/m^2/s

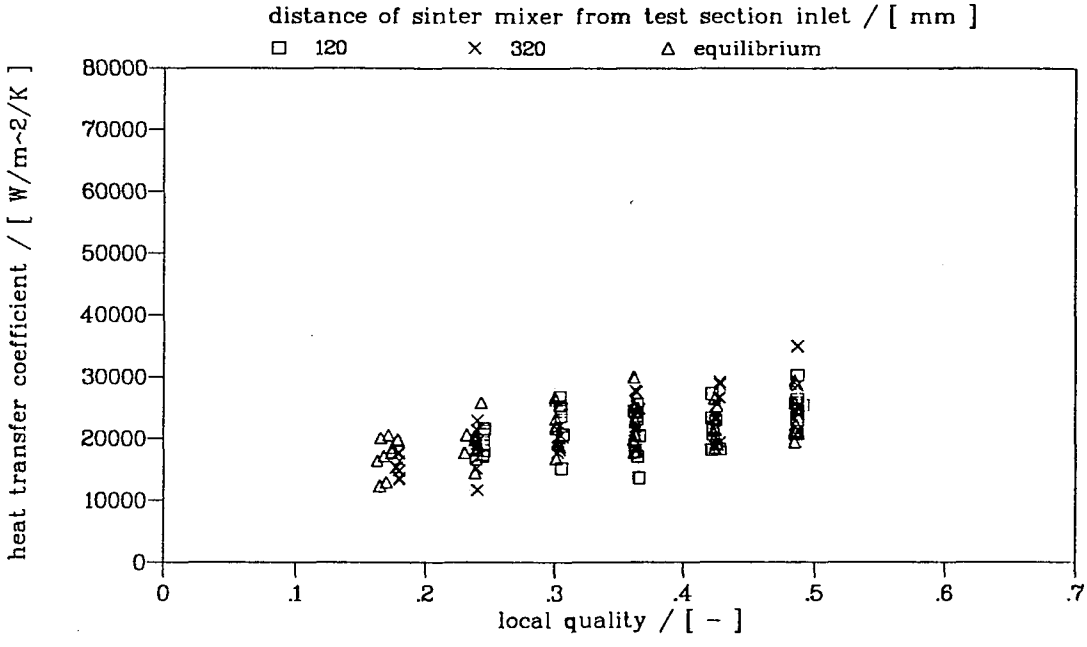

Figure 4.2.3.2-1

Frictional pressure drop data in nickel tube test section under adiabatic condition with sinter mixer up-stream of of test section inlet
mass flux 241 kg/m^2/s

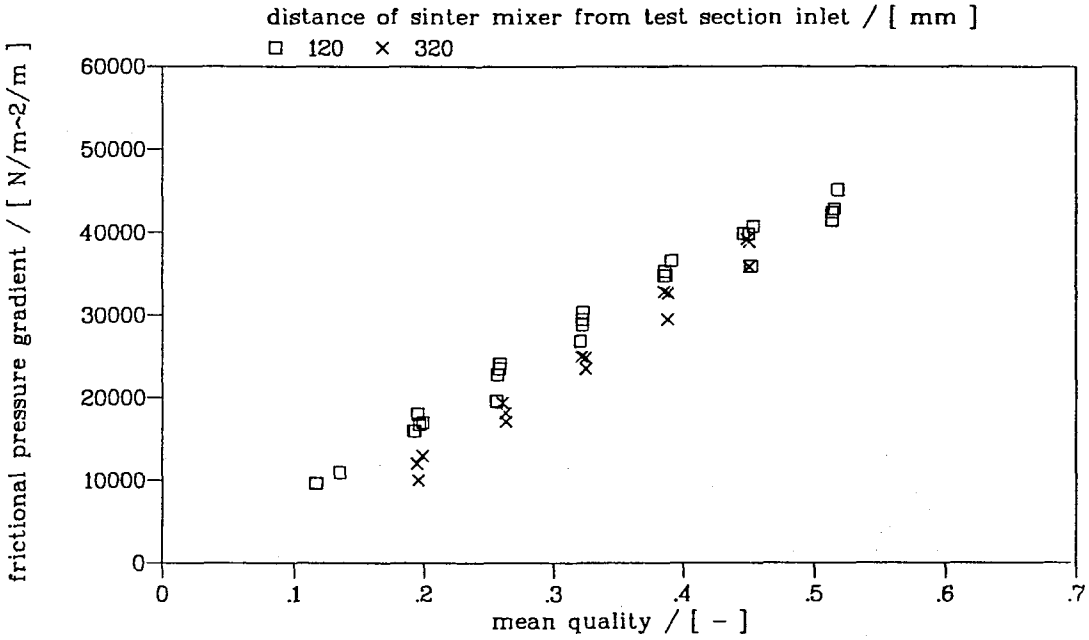

Figure 4.2.3.2-2

Frictional pressure drop data in nickel tube test section under adiabatic condition with sinter mixer up-stream of of test section inlet compared with Lockhart and Martinelli correlation
mass flux 241 kg/m^2/s

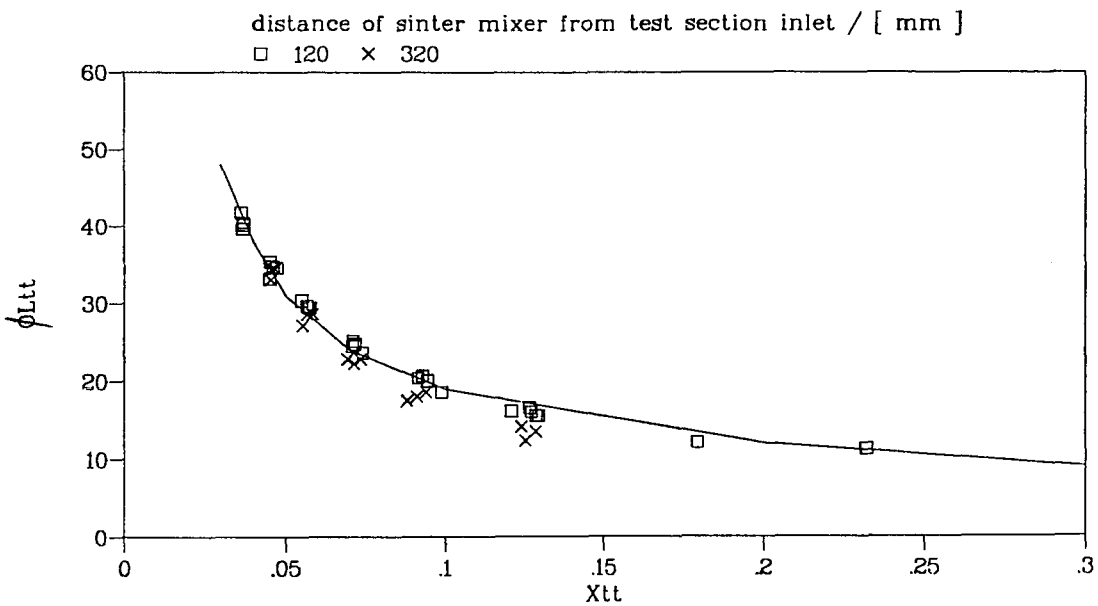

Figure 4.2.3.2-3

Frictional pressure drop data in nickel tube test section with condensation and with sinter mixer up-stream of test section inlet
mass flux 241 kg/m^2/s

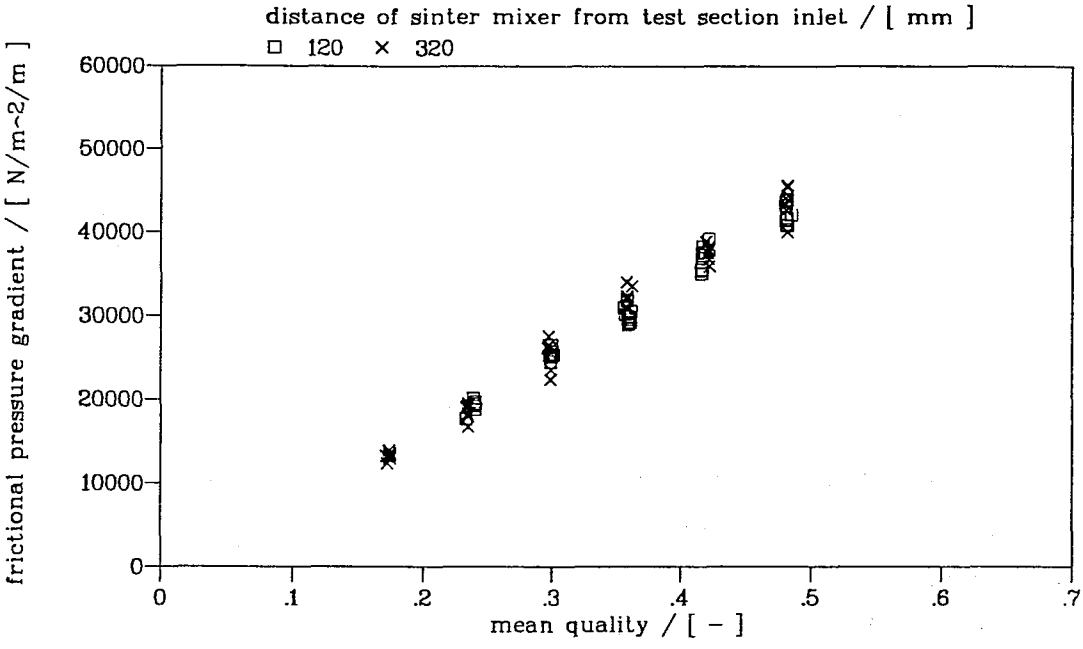

Figure 4.2.3.2-4

Frictional pressure drop data in nickel tube test section with condensation and with sinter mixer up-stream of test section inlet compared with Lockhart and Martinelli correlation
mass flux 241 kg/m^2/s

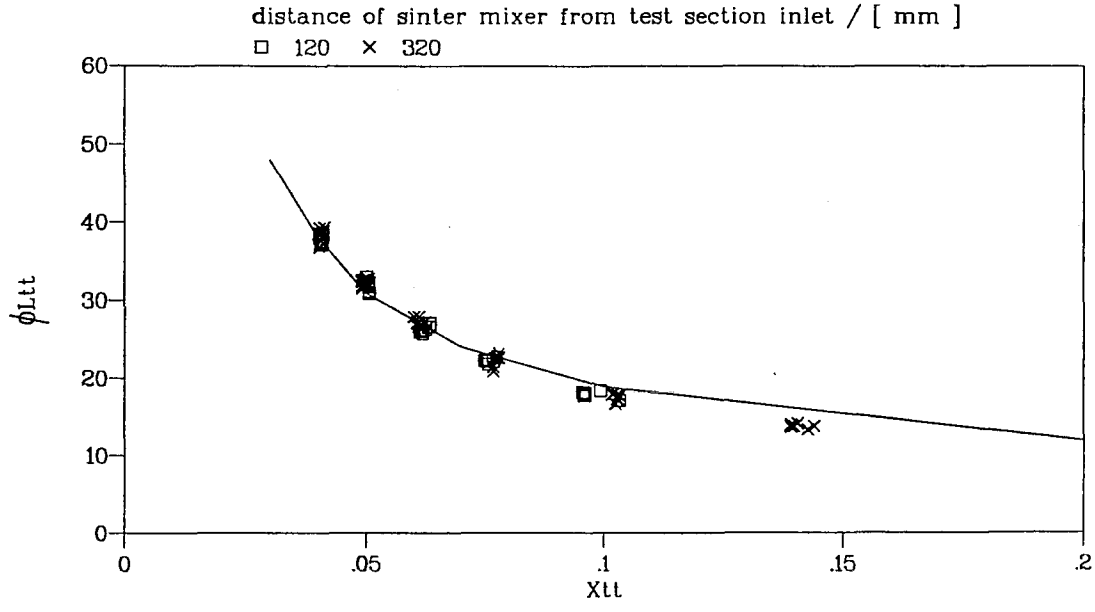

For the adiabatic conditions, the results with 120 mm upstream length are slightly higher than those with a 320 mm upstream length. This is consistent with the results of Gill et al (1963) who showed pressure gradient decreasing with length in the entrance region following porous-wall injection of the liquid. With condensation in the test section, there was less effect, presumably due to the competing effects of quality change and disequilibrium.

4.3 Conclusions

(1) In equilibrium annular flow, the heat transfer coefficient in evaporation is significantly higher than in condensation under similar hydrodynamic conditions. No obvious secondary cause for this difference could be identified and it must be concluded that the difference almost certainly represents a mechanistic difference, perhaps that of secondary nucleation as suggested by Mesler (1977).

(2) In the low quality region, the frictional pressure drop in evaporation is slightly higher than in condensation. The difference was not sufficient to explain the differences in evaporation and condensation heat transfer coefficients and may be due to an averaging effect over the test section.

(3) Some experiments were conducted on developing annular flow and, within the scatter of the present measurements, no significant difference was found between condensation heat transfer in developing and equilibrium annular flow.

CHAPTER 5

FILM THICKNESS MEASUREMENTS IN ANNULAR FLOW

Film thickness measurements are important in developing annular flow models. Measurements of average film thickness and of the time variation of film thickness (due to waves on the interface) are both important. Although there have been many such studies in low pressure (typically air-water) systems, there have been few measurements under the higher temperature conditions associated with evaporative or condensation heat transfer. The design of devices for these latter conditions is obviously more difficult. It was felt important to conduct measurements of this type in the present study since an understanding of interfacial structure is clearly significant in building fuller phenomenological models of heat transfer.

There are many techniques in film thickness measurements. Some techniques have general application and some have been developed to suit a particular condition. A review of these techniques has been made by Hewitt (1978). Most of the available techniques are unsuitable for application in high temperature systems. The technique chosen here for continuous film thickness measurement was the use of flush-mounted concentric conductance probes. However, when there is phase change, the local electrical conductivity of the liquid film is unknown and some other supporting technique is required. Here, we used the needle contact method to determine the average film thickness.

5.1 Needle contact probe

The principle of this technique is quite simple; a traversible needle probe (insulated except for its tip) is moved up to the film and the fraction of the time it spends in contact with the film is determined as a function of the distance between the tip and the wall. The mean film thickness is conventionally defined as that at which the tip is in contact with the film for 50% of the time. For a circular channel, the pre-requisites for a successful application of this technique are that the axis of the needle

coincides with the channel diameter and is at right angles to the axis of the channel, and the initial distance between the probe tip and the channel wall that it is facing must be known accurately.

A convenient initial distance can be set at zero. That is to bring the needle tip in contact with the channel wall initially. A time-trace record of the potential difference between the needle and the channel wall is then made for each step of retraction of the needle.

5.2 Flush-mounted concentric probe

The flush-mounted concentric probe is particularly convenient for application to metal-walled channels. The probe consists of a centre metallic pin surrounded by a circular insulation. When inserted through the wall of a metal-walled channel with its end flush with the inside surface of the channel, the centre pin acts as one electrode and the channel wall acts as the other. The conductance between the pin and the wall increases with the increasing film thickness. A review of such devices is given, for instance, by Hewitt (1982).

To avoid electrolytic corrosion, an A.C. carrier signal must be used. The probe can be operated in either the capacitance mode or the conductance mode. In practice, the liquid impedance has both capacitance and conductance components. While operating in one mode, the other unwanted component must be eliminated.

In this experiment, the conductance mode was used. In this mode, the frequency of the A.C carrier signal should be sufficiently high (for example, 20 to 50 kHz) to avoid formation of an electric double layer over the probe surface, while at the same time salt is added to the liquid to enhance the conductance.

In the capacitance mode, the specific conductance of the liquid should be as low as possible and the frequency of the A.C. carrier signal much higher than that used in the conductance mode in order to allow capacitance effects to dominate. Benn (1972), for instance, used frequencies in the order of 450 kHz.

The size of the probe is dictated by the maximum film thickness to be measured. Given a specific conductance in the liquid film, as the film thickness increases from zero, the conductance measured by the probe increases linearly up to a certain film thickness, after which point the measured conductance will approach an asymptotic value and becomes insensitive to any further change of film thickness. The linear range depends on the ratio of probe size to film thickness. The larger the ratio, the wider this linear range will become. However, the larger the ratio, the less localised is the measurement. Therefore, a compromise is necessary.

Brown et al (1975) has succeeded in using a concentric probe to measure wave frequency and velocity in annular up-flow in a channel. The size of that channel and the experimental conditions are similar to those in this experiment. The probe size that he chose was also adopted in this experiment. The diameter of the centre stainless steel pin is 0.8 mm and the outer diameter of the insulation is 3.2 mm. In his experiment, Brown (1976) did not convert the conductance signals into liquid film thickness due to the difficulty in calibration with very thin liquid films involved.

An analytical equation to describe the relation between the film thickness and the its conductance is not available for concentric probes.Calibration is necessary. However, using HANA, the film thickness in the experiment was estimated to be in the order of 0.1 mm. Common calibration methods using "plug in channel" or "falling film" are not able to produce such film thickness with acceptable accuracy.

Fortunately based on the principle of geometric similarity, the difficulty in film thickness calibration can be overcome. A scaled-up probe was used, in which the centre pin had a diameter of 3.3 mm and the outer diameter of the insulation was 13.2 mm . Thus the ratio of the outer diameter of the insulation to the centre pin diameter of the probe proper was maintained. Calibration of this scaled-up probe is described in Appendix F.

Using suitably defined non-dimensional variables, the calibration data were well correlated. The resulting non-dimensional data provides a basis for extrapolation for concentric probes of similar geometry.

Using a general purpose computer code (PHEONICS), a numerical simulation of the potential field in the liquid film over the concentric probe was carried out (see Appendix F). The results of the numerical

solution were in good agreement with the calibration data. The confidence in both the calibration data and the computer method was thus established.

The specific conductance of the liquid film must be known in the experiment in order to convert the conductance records into film thickness traces. Monitoring the specific conductance of the liquid phase in a two-component adiabatic system is not difficult. However, a problem arises in a one-component system where the specific conductance varies with the liquid fraction. By making measurements with the needle contact probe at the same axial location as the concentric conductance probe, it was possible to provide a calibration standard from which, using the non-dimensional calibration curve, it was possible to convert the conductance records to film thickness records.

5.3 Flush-mounted double concentric probe

The problem involved in diabatic system in obtaining film thickness values from conductance probes was discussed above. In the present work, the use of a needle contact probe to provide a calibration standard was adopted. However, an alternative, less intrusive, method was also investigated, namely the use of a double concentric probe. At large film thicknesses and / or very small spacing between the electrodes, probe conductance becomes insensitive to film thickness and depends only on the electric conductivity of the liquid. The principle of the double concentric probe is to use a centre pin separated by insulation from a concentric ring electrode which is in turn separated from the conducting channel wall by a further concentric ring of insulation. The whole unit is mounted flush with the channel wall. By spacing the centre pin and the concentric ring electrode close together, their response can be made sensitive only to the specific conductance whereas, if the gap between the wall and the ring electrode is larger, the conductance between it and the metal wall would be sensitive to both the film thickness and liquid specific conductance. The ratio of the conductance would depend only on the film thickness. In practice, there is a finite liquid film thickness below which the inner circuit is not saturated and the principle of the double concentric probe cannot be applied.

Since numerical simulation has shown good agreement with calibration results for the case of concentric probe, calibration of the double concentric probe may not be necessary. Furthermore, sizing of the probe for the maximum film thickness to be measured can be done numerically.

The option of using double concentric probe has been considered. The main difficulty was in making a small enough probe with precision for measuring liquid film with thickness in the order of 0.1 mm. Consequently, the needle contact probe was used as the calibration standard in these experiments.

5.4 Installation and instrumentation

Two flanges were specially made for housing the probes for film thickness measurements. One flange (called the dual-probe flange hereafter) accommodated a concentric probe and a needle contact probe. The other flange (called the single-probe flange hereafter) had only a concentric probe.

The traversing mechanism of the needle contact probe was attached to the dual-probe flange. This traversing mechanism had a combination of cogs for driving the needle probe and a reference plate against which the tip of a dial gauge stem can be pressed for registering the distance travelled by the needle tip. The axis of the needle was at right angles with the axis of the concentric probe. The stem of the dial gauge was also checked to make sure it was parallel with the line of movement of the needle contact probe.

The needle is a 0.5 mm nickel-chromium alloy wire with the tip ground flat. The geometric error in using a flat rather than a pointed tip is ± 0.14%. The needle was insulated by a PVC plastic sleeve with about 2 mm length at its tip exposed. In the course of the experiments, the plastic sleeve was found to be eroded very quickly. A PTFE sleeve was tried, but proved unsatisfactory. Consequently, the sleeve had to be changed regularly. An eroded sleeve might expose the needle to the liquid film on the "near" side of the channel. To avoid this happening, a series of runs was always started at the lowest quality with the thickest liquid film, which would protect the sleeve on the "near" side from steam erosion. As quality was increased, the liquid film was thinned and would not contact

the needle which was exposed by the deteriorating sleeve. After the experiment with the highest quality, the sleeve was replaced by a new one.

At the tip of the concentric probe, the centre stainless steel pin had a diameter of 0.8 mm. and the surrounding insulation had an outer diameter of 3.2 mm. The insulation material was polyphenolene (commercially called Noryl). With the concentric probes inserted, the bore of each of the two probe flanges was reamed to make the probe ends flush.

With the test section mounted, the dual-probe flange was placed at the outlet of the test section and the single-probe flange at the inlet. The concentric probes were on the same side of an axial plane. With this arrangement, experiments with condensation and those under adiabatic condition were carried out.

For those experiments without the test section, a dummy tube was used in its place. The dual probe flange was placed at the same location as that of the single-probe flange in the experiments with the test section in place. The single-probe flange was positioned above the dual-probe flange with a spacer flange between them. On top of the single-probe flange was the inlet to the dummy tube.

Unfortunately, the insulation cracked under the thermal conditions in the experiments. Polyacetal (commercially called Durin) was then used as the insulation. After inserting the new insulation into the flanges, their ends in the bore were scraped by scalpel to flushness. The new probe assembly is shown in 5.4-1 . The position of the pin end was controlled by adjusting the tension of the backing spring until the pin end was flush. After some experimental runs, the probe flanges were taken down for examination. The insulations of the concentric probes were found to be protruding while the flanges were hot. The insulations were scraped to flushness whilst still hot and the centre pins were re-positioned.

The two concentric probes had identical electric circuits. A schematic diagram of the electric circuit is shown in figure 5.4-2. The power supply unit delivered an output of ±15V to the circuit components. A 20 kHz constant amplitude voltage sine carrier signal was generated by the oscillator, then amplified and sent to the concentric probe. The amplitude of this carrier signal was modulated according to the change of

Figure 5.4-1 Assembly of flush-mounted concentric probe

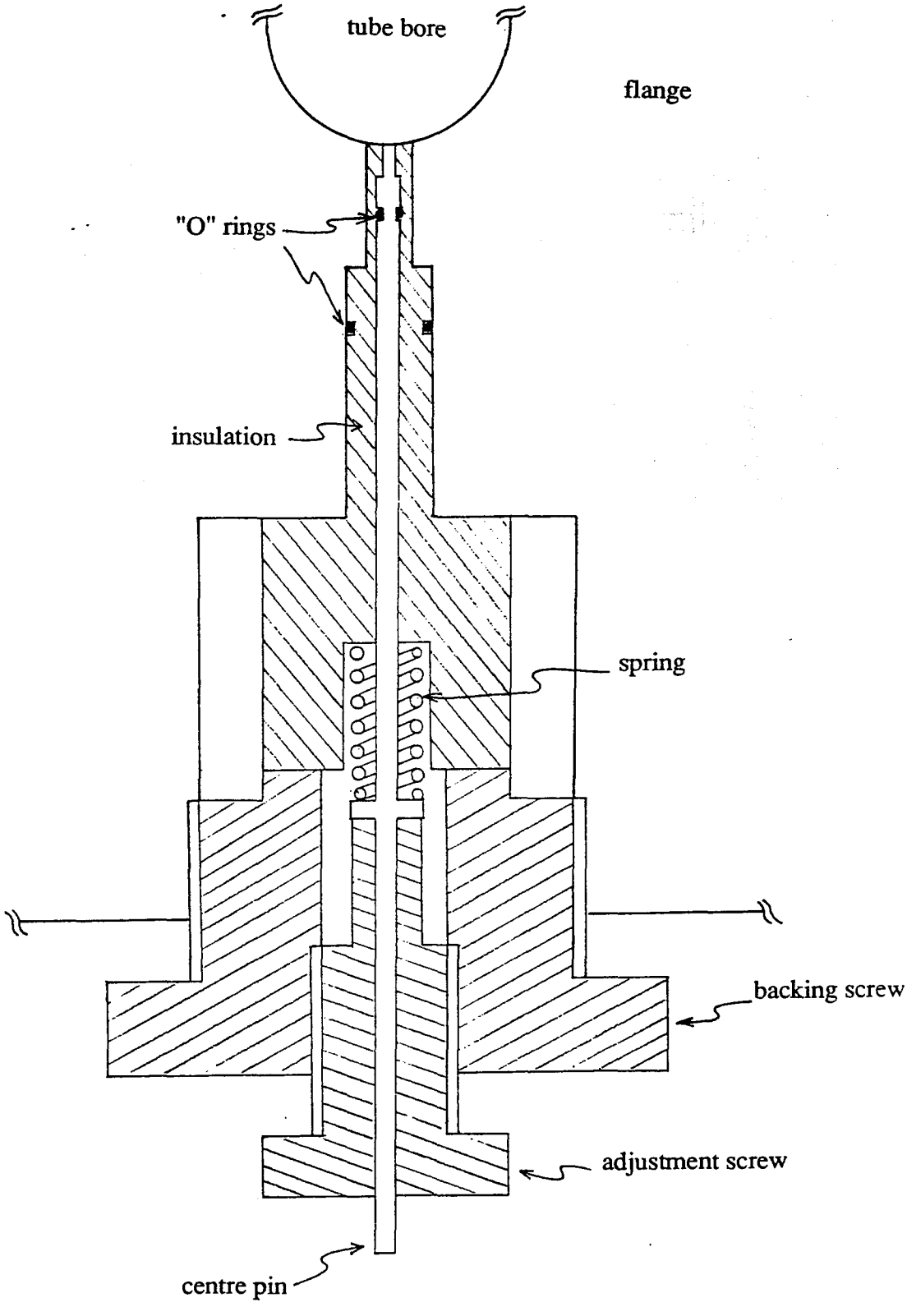

Figure 5.4-2 Electric circuit for concentric probe in conductance mode

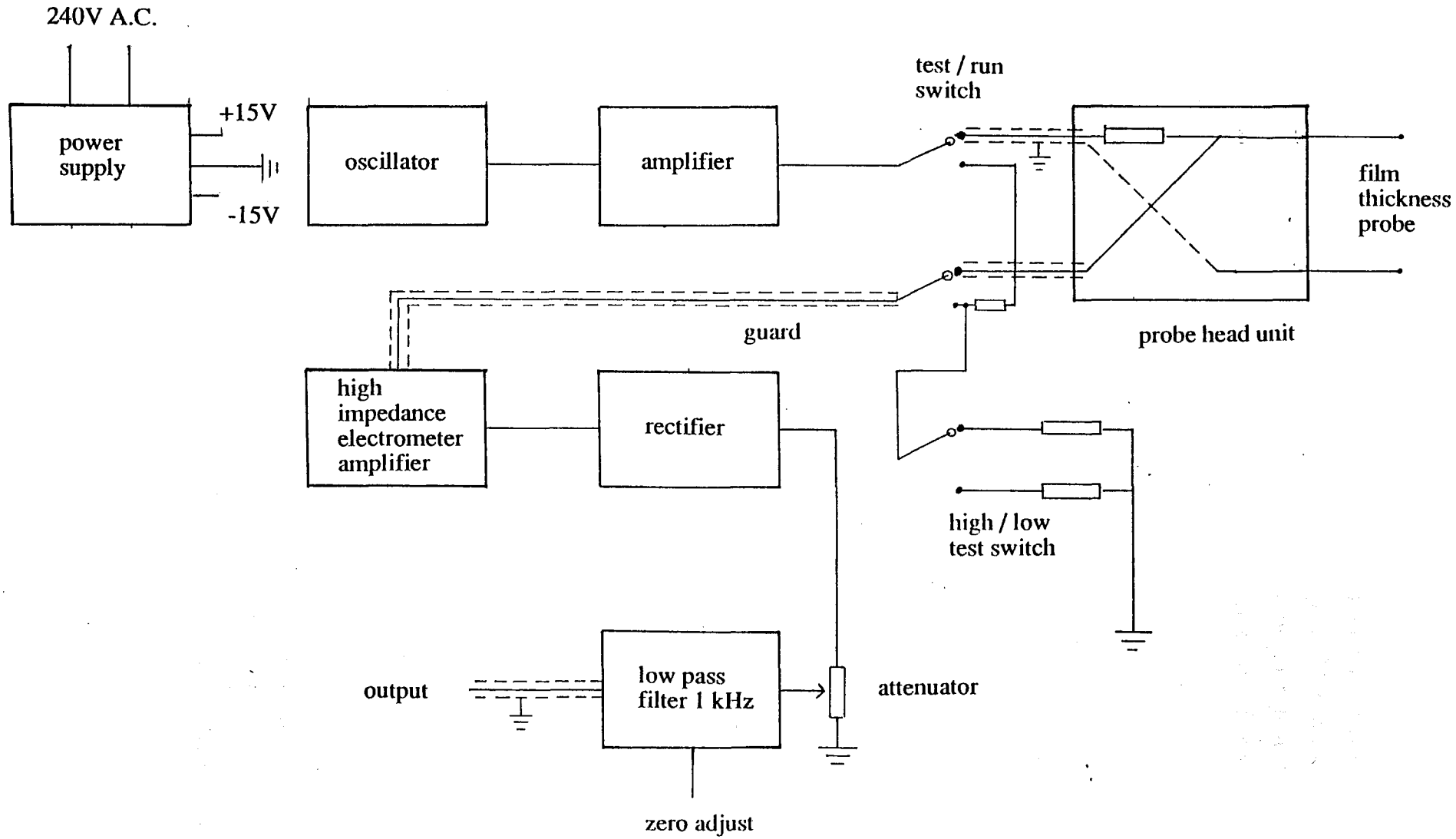

conductance in the liquid film as a result of the changing film thickness. The probe fed this modulated signal back to a high impedance electrometer amplifier, then a rectifier and a low pass filter with a cut-off frequency at 1000 Hz to remove the A.C. carrier signal. The variable resistor in the probe was adjusted (with the concentration of salt in the liquid taken into account) so that the output D.C. would not exceed 10V.

The D.C. outputs from the two probe circuits were taken simultaneously by a tape recorder using FM (frequency modulation) recording. The input range of the recorder was set at 0-10V. On play back, the output range was 0-1V. The tape speed of the recorder was set at 7.5 in/s, corresponding to a frequency band of 1250 Hz, which was comparable with the cut-off frequency of 1000 Hz for the probe circuit output. For each run, the length of recording time was about 40 seconds.

The same probe circuit was used for the needle contact probe. In this case, the probe circuit had a D.C. output range of 0-14V. In principle, the contact and break points of the needle probe should correspond to the minimum (0V) and maximum (14V) respectively of the output range. However, the steep signal fluctuation, compounded by the characteristics of the electronic components, caused some over and under shoot. A tape speed of 7.5 in/s was also used for recording the needle probe signals.

5.5 Data processing

A signal processing computer package (DATS) was used to digitise and analysis the film thickness signals.

The processing computer accepts signal in the range of ±10V, which is divided into 2048 levels. Since the recorder output has a maximum of 1V, its output was amplified by a factor of 5 during digitisation in order to increase the signal resolution in the computer.

The frequency band corresponding to the recording speed was 0-1250 Hz. A sampling rate in that order was set at 1000 s^{-1} for digitisation. The resulting frequency band of the digitised signals would be 500 Hz.

The digitised voltage signals were further processed for auto spectral and cross-correlation analysis with the assumption that they were ergodic. These digitised signals were first normalised by using the following expression :

$$x_n = x - \mu_x \qquad (5.5\text{-}1)$$

The normalised signals were then digitally filtered with the high and low pass frequencies set at 10 Hz and 490 Hz respectively. Using a finite Fourier transform technique, the frequency spectrum of the filtered signals was calculated using the following equation (Bendat and Piersol, 1971) for $f \geq 0$ and $t \geq 0$.

$$G_{xx}(f) = \frac{2}{T} \sum_{n=1}^{N=T/\Delta t} \left| \int_t^{t+\Delta t} x(t) e^{-j2\pi ft} dt \right|^2 \qquad (5.5\text{-}2)$$

where T is the total record time and Δt is the interval in the time domain over which the finite Fourier transform is performed. The smaller Δt , the smoother the frequency spectrum will be but the more details will be lost. An optimum frequency resolution of 5 Hz was specified. This means that the auto spectral density function, G_{xx} , was calculated at each interval of 5 Hz. Using equation 5.5-2. for each frequency interval in the range from zero up to the Nyquist frequency (which is equal to half the sampling rate), an autospectral density distribution can be established.

Cross-correlation analysis was carried out on the filtered signals using a fast Fourier transform technique. The input / output relation of this analysis can be simply defined as :

$$R_{12}(\tau) = \frac{1}{T} \int_0^T x_1(t) x_2(t+\tau) dt \qquad (5.5\text{-}3)$$

For a pair of ergodic processes, the length of the record time, T, should approach infinity; but, in practice, T must be finite. Using equation 5.5-3. for a specified range of displacement time τ , a distribution of the cross correlation function, R_{12} against the displacement time, τ, can be established. The displacement time corresponding to the peak in the distribution is the time separation between the passage of the waves over the two successive probes. Knowing the separation distance of the two concentric probes, the velocity of the dominant waves was calculated.

The signals of the needle contact probe have been attenuated by a ratio of 20 : 1 at the recording stage. During digitisation, play-back signals were amplified by a factor of 10. Therefore, in the digitised signals, 0V and 7V represent the contact and break points of the needle respectively, disregarding the under and over shoots. Since, the square-wave shaped

signals have very sharp and symmetrical descending and ascending slopes, one cut point at 3.5V was used to separate the contact and break points.

For each experimental run, a cumulative probability distribution was calculated for the time trace of each needle position. The results of a typical run is shown in figure 5.5-1. The intersection points of the 3.5V cut-off line and the distribution curves represent the fraction of time in which the needle was in contact with the liquid film at different positions.

A typical contact time fraction distribution for different needle positions is shown in figure 5.5-2. In principle, the mean film thickness can be found by taking the mean of the integration of the distribution with respect to the time fraction. However, for low qualities, the distributions have long tails stretching to long distances. This phenomenon is due to the large amplitude waves or strands of liquid passing between the needle tip and the liquid film. Because of the lack of data points at long distances, the integration method in calculating the mean film thickness is not possible. On the other hand, the distributions for high qualities have very steep slopes and approach zero time fraction fairly rapidly. If a certain time fraction at the region of the steep slope is chosen to define the mean film thickness, the result should not be sensitive to the choice. For an idealised wave shape such as sine wave, the choice should be the 50% contact time fraction. Hewitt et al (1962) have shown that mean film thickness obtained from this technique is in good agreement with the mean value from conductance probes. Thus, the 50% contact position was used in the present experiments as a calibration standard for the conductance probes.

In the experiments, the specific conductance of the liquid film over the concentric probes was unknown. However, the mean film thickness was measured by the needle contact probe at each of the concentric probe positions. Since the response of the conductance probes is non-linear, an iterative process is required to establish the calibration. A value of specific conductance is assumed and the mean film thickness determined from the non-dimensional calibration described in Appendix F. This is compared with the needle probe 50% contact value, the specific conductance adjusted and the calculation repeated until the values agree.

Figure 5.5-1 Typical cumulative time fraction distribution as a function of the needle probe voltage signals.

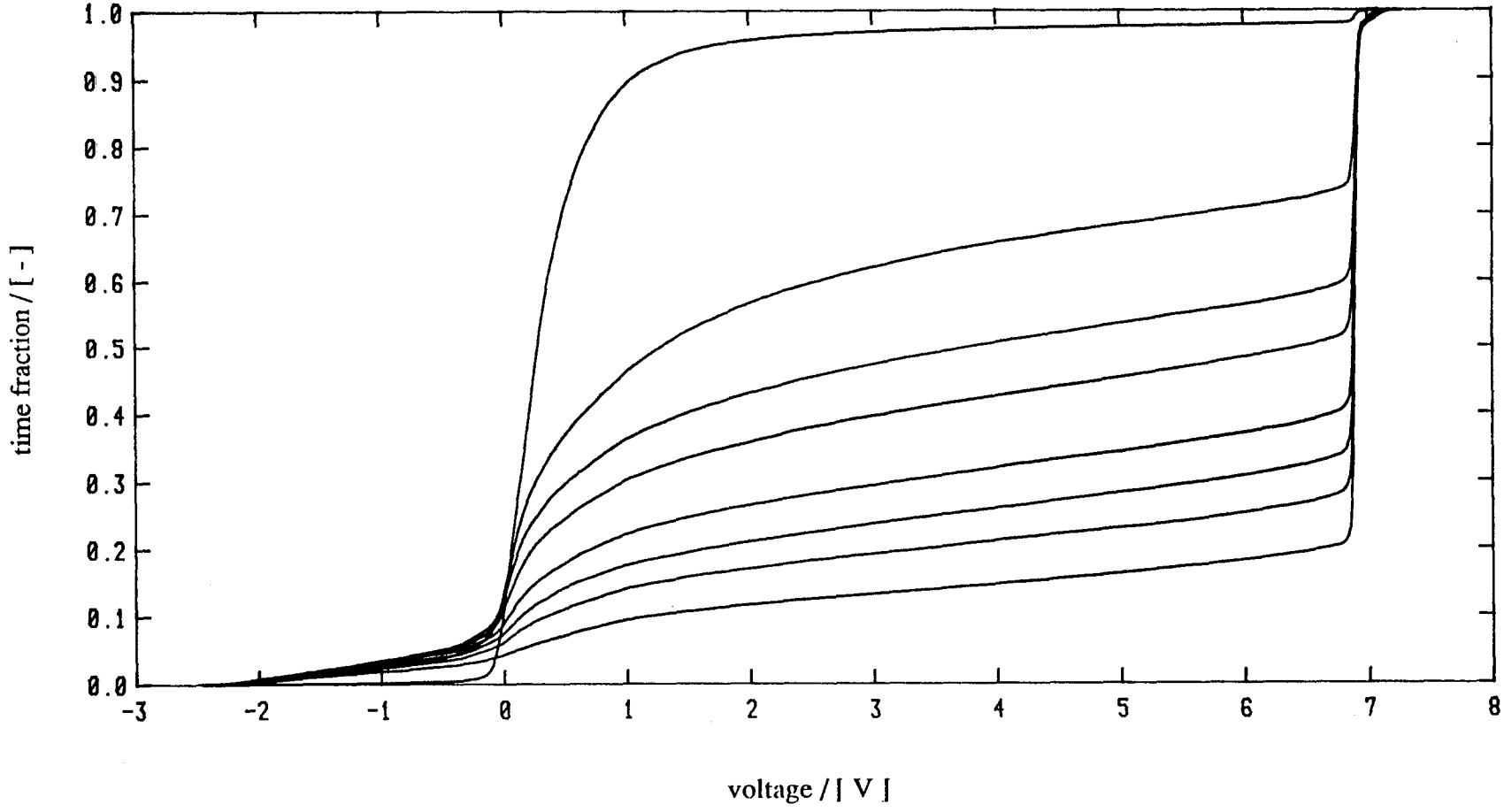

Figure 5.5-2

Data of needle contact probe in equilibrium adiabatic annular up-flow of water and steam
mass flux 241 kg/m^2/s
probe at test section inlet

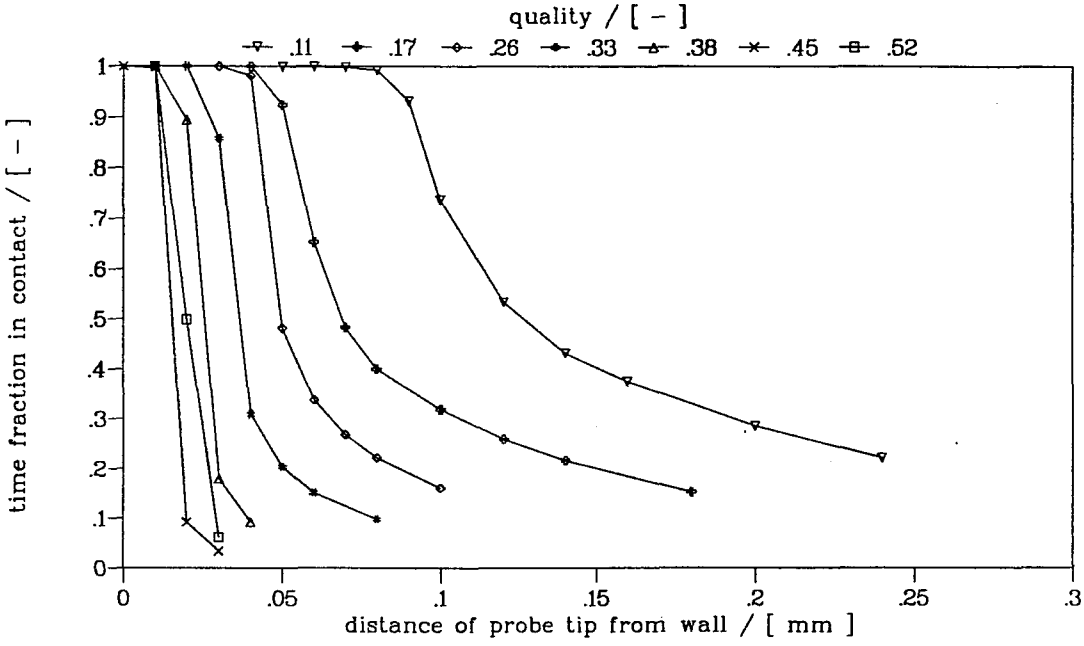

5.6 Results and discussion

5.6.1 Needle contact probe measurements

The data of the needle contact probe measurements are presented in figures 5.6.1-1. to 5.6.1-4. For equilibrium flow (see figure 5.6.1-1), the data appear to be fairly consistent at different measurement positions and different thermal conditions, although there is some scatter at low quality region. The amount of condensation does not seem to have added to the mean film thickness significantly, though this reflects the relatively small change in quality in the test section.

For the case of the sinter mixer being at 120 mm up-stream of the test section inlet, the scatter in figure 5.6.1-2. is more significant. Under adiabatic condition, the mean film thickness at the test section outlet appears to be larger than at the inlet. This could be due to the disturbance depleting the liquid film at the inlet.

Large scatter occurred in the measurements at the outlet under adiabatic condition with the 320 mm upstream length (see figure 5.6.1-3). These errors were very likely due to a deteriorated sleeve. Entrained liquid could have intermittently bridged the liquid film on the "near" side with the exposed needle.

In figure 5.6.1-4, the film thickness measurements for equilibrium and developing annular flow are compared with the predictions from the annular flow theory described in Chapter 2 and 3. Specifically, the Owen and Hewitt (1987) model was used for the liquid film and interfacial shear and the Govan et al (1988) correlation was used for predicting the entrainment fraction. The prediction of film thickness is quite encouraging.

5.6.2 Conductance probe results

Conversion of conductance trace to film thickness trace

In general, the conductance vs. time records were used directly in the spectral and cross-correlation analysis. However, the traces were converted to film thickness for the case of equilibrium condensation with a mass flux of 241 kg/m^2s. The reference film thickness data to be converged on in the calculation were the mean values taken from figure

Figure 5.6.1-1

Mean liquid film thickness measured by needle contact probe in equilibrium annular up-flow of water and steam
mass flux 241 kg/m^2/s

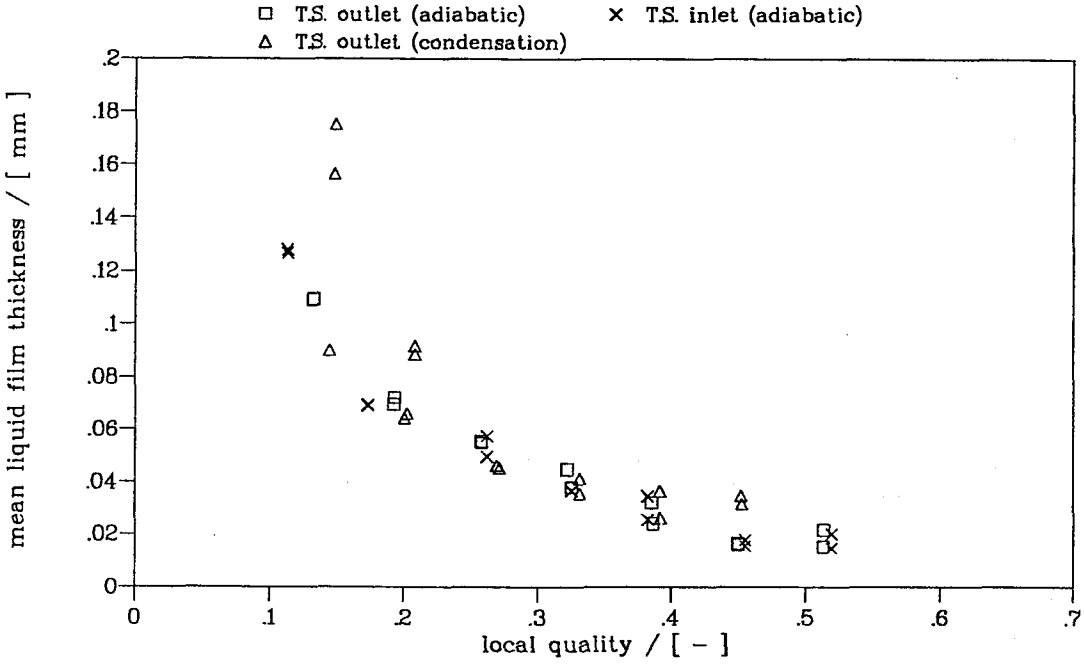

Figure 5.6.1-2

Mean liquid film thickness measured by needle contact probe in annular up-flow of water and steam with sinter mixer at 120 mm up-stream of test section inlet
mass flux 241 kg/m^2/s

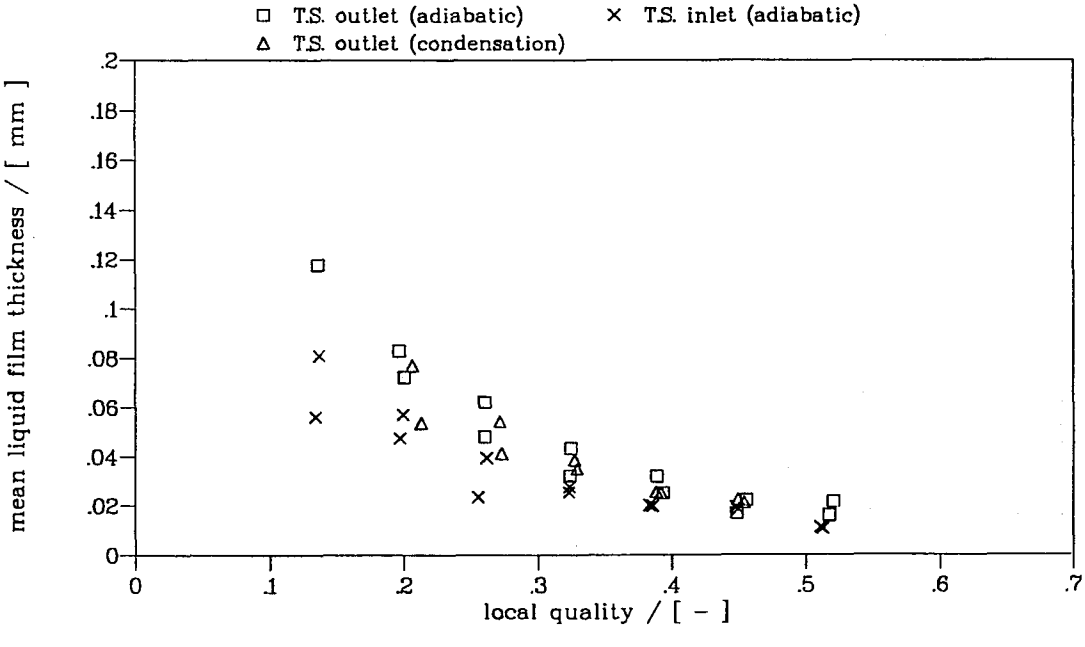

Figure 5.6.1-3

Mean liquid film thickness measured by needle contact probe in annular up-flow of water and steam with sinter mixer at 320 mm up-stream of test section inlet
mass flux 241 kg/m^2/s

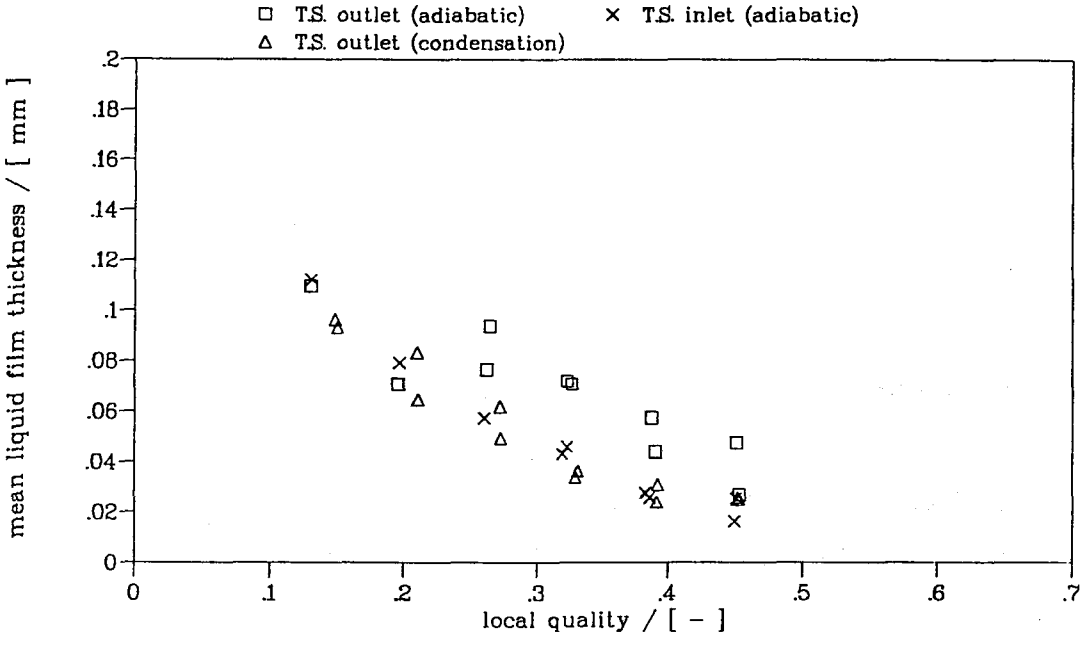

Figure 5.6.1-4

Mean liquid film thickness measured by needle contact probe compared with values calculated by Owen-Hewitt model based on experimental conditions
mass flux 241 kg/m^2/s

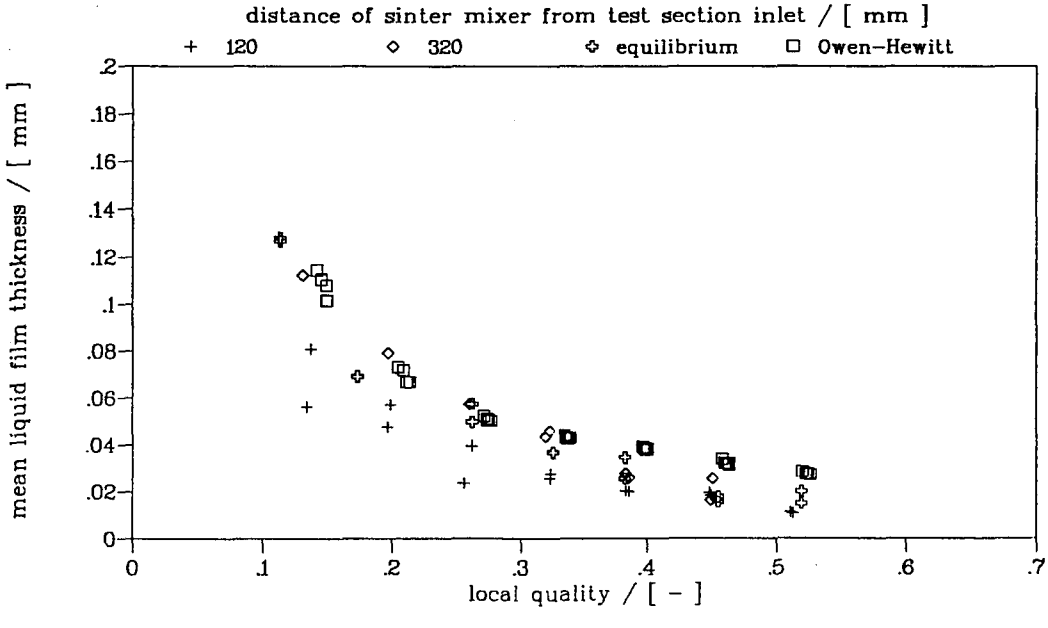

5.6.1-1 The time traces of the converted film thickness at the inlet and outlet of the test section are presented in figures 5.6.2-1 and 5.6.2-2. Bearing in mind that the calculation was subject to errors in the needle contact probes measurements, the traces look reasonable. The effect of quality on the wave frequency and the liquid film thickness can be clearly seen. Ripple and disturbance waves are also distinguishable.

A simple check was done to verify the specific conductance calculated in the film thickness signal conversion process. A sample of the salted water was taken from the storage tank. Its specific conductance was measured at various temperatures in a temperature-controlled bath. The results are shown in figure 5.6.2-3. The extrapolated specific conductance at 100°C is 2267 μS.

With the assumptions that the salt concentrations in the liquid film and the entrained droplets are the same, and the relation between salt concentration and the specific conductance is linear, a simple relation between the quality and the specific conductance at 100°C can be expressed as follows :

$$c = \frac{2267}{1-x} \qquad (5.6.2\text{-}1)$$

A comparison between equation 5.6.2-4 and the electrical conductance calculated from the film thickness conversion process are given in figure 5.6.2-4. Bearing in the assumptions made, the agreement is fair.

Auto spectral and cross-correlation analysis

The auto spectral and cross-correlation analysis were carried out directly on the conductance vs. time records. Since frequencies and time differences were being determined, there was no need to process the tape into film thickness vs. time record.

A typical set of results from the autospectral analysis is shown in figure 5.6.2-5. The effect of quality is clearly seen. As quality decreases, the autospectral density distribution becomes more peaked and more skewed. The dominant frequencies have been shown in earlier air-water flow studies to correspond to "disturbance waves" (Hall Taylor et al, 1963). At higher qualities, these waves have low amplitudes and the peak frequency is less well defined

Figure 5.6.2-1

Film thickness trace converted from signals of concentric probe at test section inlet

conditions equilibrium condensation in test section

mass flux 241 kg/m^{2}s

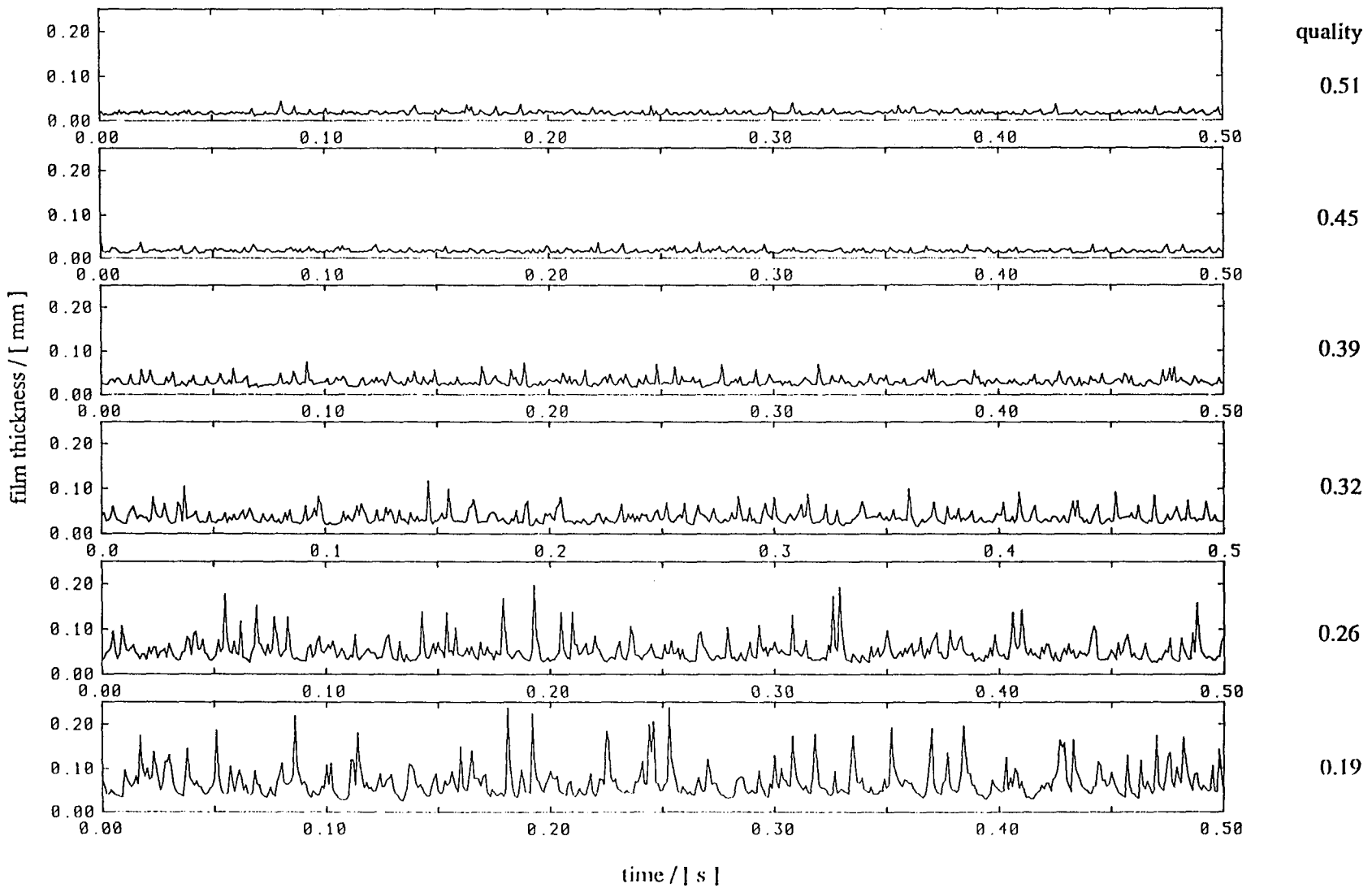

Figure 5.6.2-2

Film thickness trace converted from signals of concentric probe at test section outlet

conditions equilibrium condensation in test section

mass flux 241 kg/m^{2}s

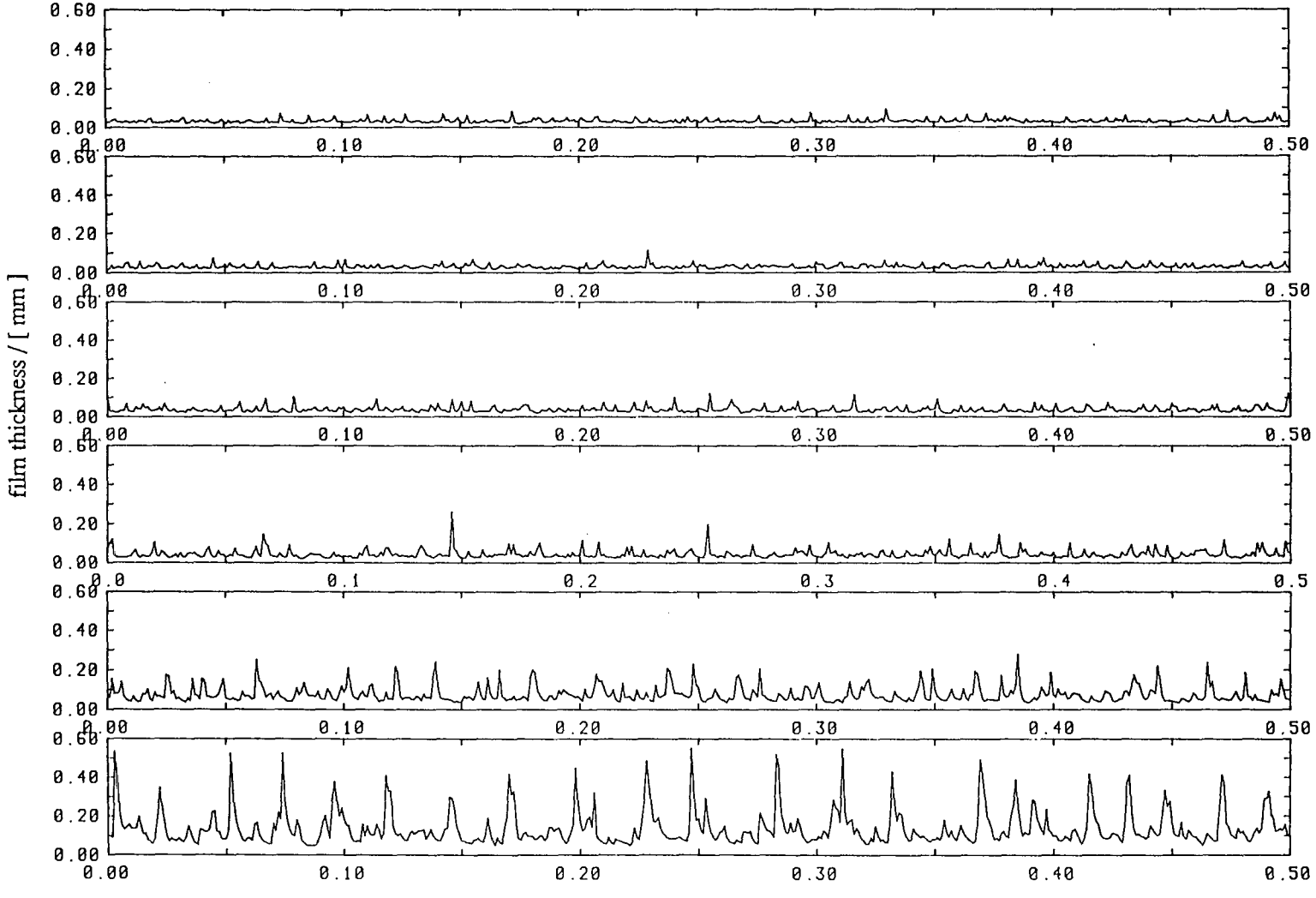

quality

0.45

0.39

0.33

0.27

0.21

0.14

Figure 5.6.2-3

Measured variation of specific conductance with temperature in potassium nitrate solution

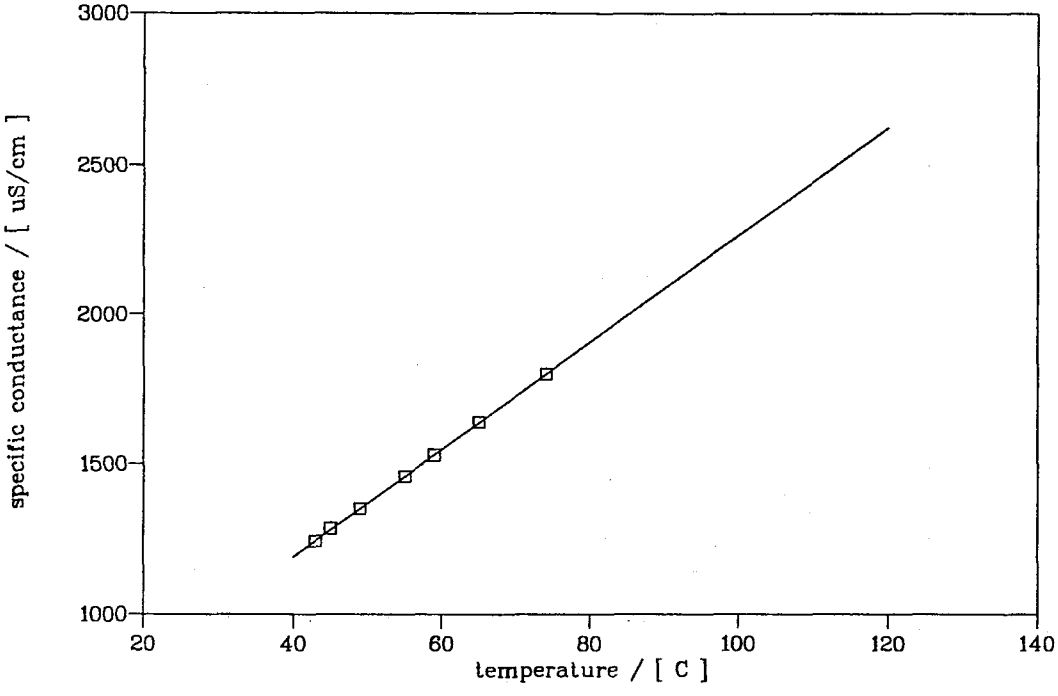

Figure 5.6.2-4

Specific conductance calculated by film thickness conversion procedure and by a simple extrapolation method

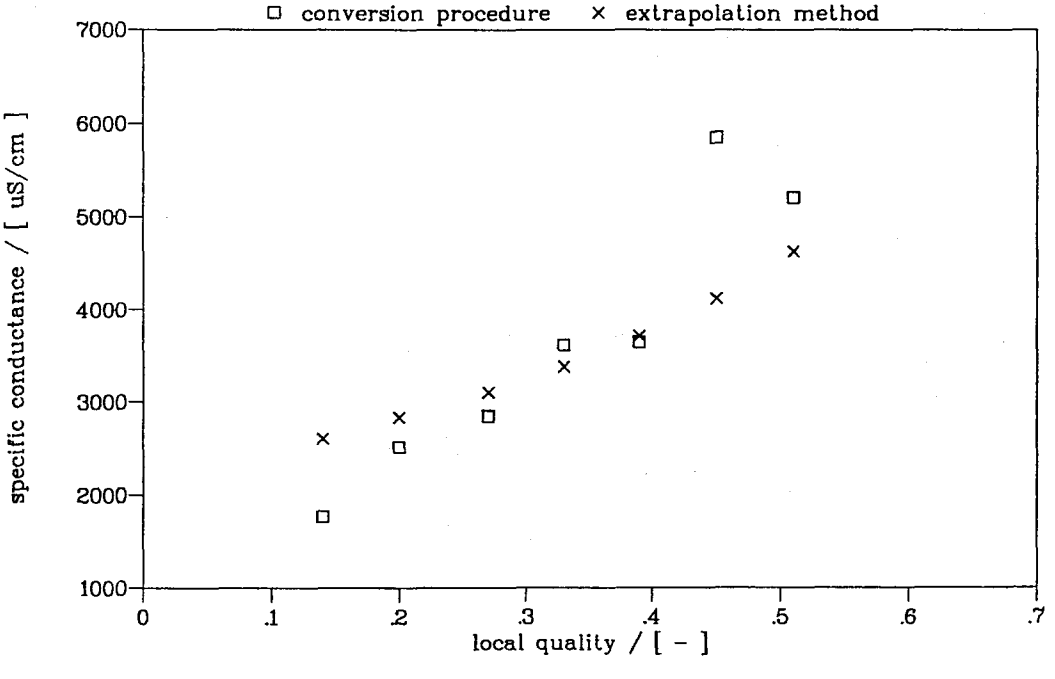

Figure 5.6.2-5 Typical variation of auto spectral density function with wave frequency and quality.
measurements taken at test section inlet
mass flux 241 kg/m^{2}s

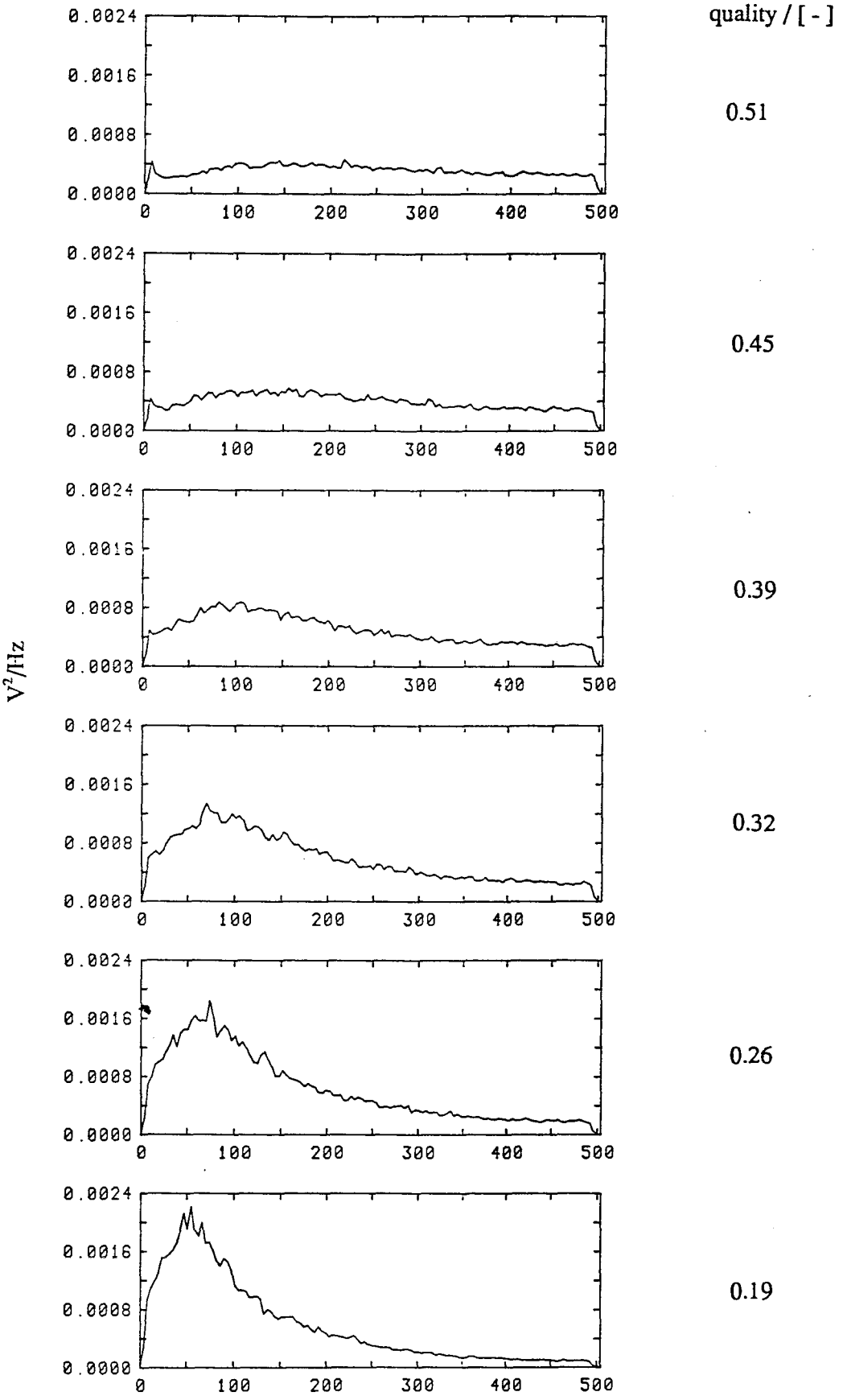

Following Brown's suggestion (1975), the parameters used to describe the autospectral density distribution are the frequency at maximum power (called the peak frequency hereafter) and the frequency range with power more than half of the maximum power. The upper limit of this frequency range will be called the high range frequency and the lower limit called the low range frequency. These defined parameters are plotted (see figures 5.6-6 to 5.6-27) against local quality for the conditions as shown in Table 5.6.2-1:

Table 5.6.2-1

Figure numbers	Thermal condition	hydrodynamic condition or distance of sinter mixer from test section inlet / [mm]	probe separation distance / [mm]	mass flux / [kg/m^2]
5.6.2-6 & 7	condensation	equilibrium	0.327	125
5.6.2-8 & 9	condensation	equilibrium	0.327	183
5.6.2-10 & 11	condensation	equilibrium	0.327	241
5.6.2-12 & 13	adiabatic	equilibrium	0.327	241
5.6.2-14 & 15	adiabatic	equilibrium	0.04	241
5.6.2-16 & 17	condensation	120	0.327	241
5.6.2-18 & 19	adiabatic	120	0.327	241
5.6.2-20 & 21	adiabatic	120	0.04	241
5.6.2-22 & 23	condensation	320	0.327	241
5.6.2-24 & 25	adiabatic	320	0.327	241
5.6.2-26 & 27	adiabatic	320	0.04	241

From the plots for the equilibrium condensation experiments, it can be observed that increase in mass flux and quality increase the peak frequency and the high range frequency. It should be remembered that, for the pair of concentric probes in the same experimental run, there is a shift in quality due to condensation, the inlet quality being higher than the outlet quality. The local quality seems to correlate well the inlet and outlet conditions for the peak and range frequencies, especially in the low quality region. The discrepancies in the high quality region are due to the flatness of the autospectral density distribution (see figure 5.6.2-5).

For the experiments with the sinter mixer installed, a disturbance with frequency of about 2 Hz was noticed from the concentric probe signals. In the high quality region, the liquid film at the bottom concentric probe was depleted intermittently at the same frequency as the disturbance. This liquid film depletion could have damped out the high frequency waves. The high range frequency at the test section inlet is lower than that at the outlet and the peak frequency at the inlet probe is lower than that at the outlet probe in the high quality region. This is contrary to other experimental findings that in developing annular flow, which is generated by sinter mixer, the high range frequency and the peak frequency are monotonically decreasing with increasing distance from the sinter mixer.

There are three possible causes for the disturbance : one is the pressure fluctuation in the separator being transmitted through the steam, or through the water or through both; the second is the higher pressure in the water line causes flashing at the sinter mixer; the third is that the water could have flashed much earlier at the water line control valve and the disturbance generated there was transmitted down-stream.

Despite the disturbance, some interesting observation can be made, the most important of which is that there is no significant effect of the sinter position on the peak frequency under adiabatic conditions. This is contrary to previous observations and may explain why the heat transfer data show no variation with entrance conditions.

Typical cross-correlation analysis results are presented in figures 5.6.2-28 and 5.6.2-29 which were for concentric probe spacing of 0.327 m and 0.04 m respectively. The correlation function for the shorter probe separation distance is much stronger as expected but, for a short separation distance,

the transit time of the waves between the successive probes was small (typically 0.01 s) and the resolution (typically 0.001 s) of the electronic system was such as to produce large errors in this case. Results for adiabatic flow with the two separation distances are compared in figure 5.6.2-30 and some discrepancy is observed, reflecting this fundamental limitation. All the results presented below are for the 0.327 m spacing (i.e. with the probes at each end of the test section).

Wave velocity data for equilibrium flows is presented in figure 5.6.2-31. As will be seen, wave velocity increases systematically with mass flow and quality.

Wave velocity data taken in the "non-equilibrium" experiments are shown in figures 5.6.2-32 and 5.6.2-33 respectively. Without condensation in the test section, the wave velocities (see figure 5.6.2-32) were not significantly affected by entrance length and were in good agreement with those measured in the equilibrium experiments. It seems, therefore, that equilibrium is reached much more rapidly in high temperature steam-water flows than in air-water flows. This implies that much shorter length would be required to properly study non-equilibrium effects. Condensation in the test section had relatively little effect on the observed wave velocities. (see figure 5.6.2-33).

5.7 Conclusions

(1) Both needle contact and concentric conductance probe methods of film thickness measurement have been successfully developed and applied to steam-water annular flow. Calibration of the conductance probe system was successfully achieved by using a model system, by using numerical prediction and by using the needle probe result as a reference standard

(2) Measurements of mean film thickness taken with the needle probe are in good agreement with annular flow theory.

(3) Measurement of wave frequency using autospectral analysis and of wave velocity using cross-correlation analysis indicated

that equilibrium was achieved quite quickly in steam-water flows. This is in accord with the heat transfer results reported in Chapter 5.

Figure 5.6.2-6

Frequency range with power more than half the maximum in the frequency spectrum of waves in equilibrium condensation of annular up-flow of water and steam
mass flux 125 kg/m^2/s
concentric conductance probes 0.327 apart

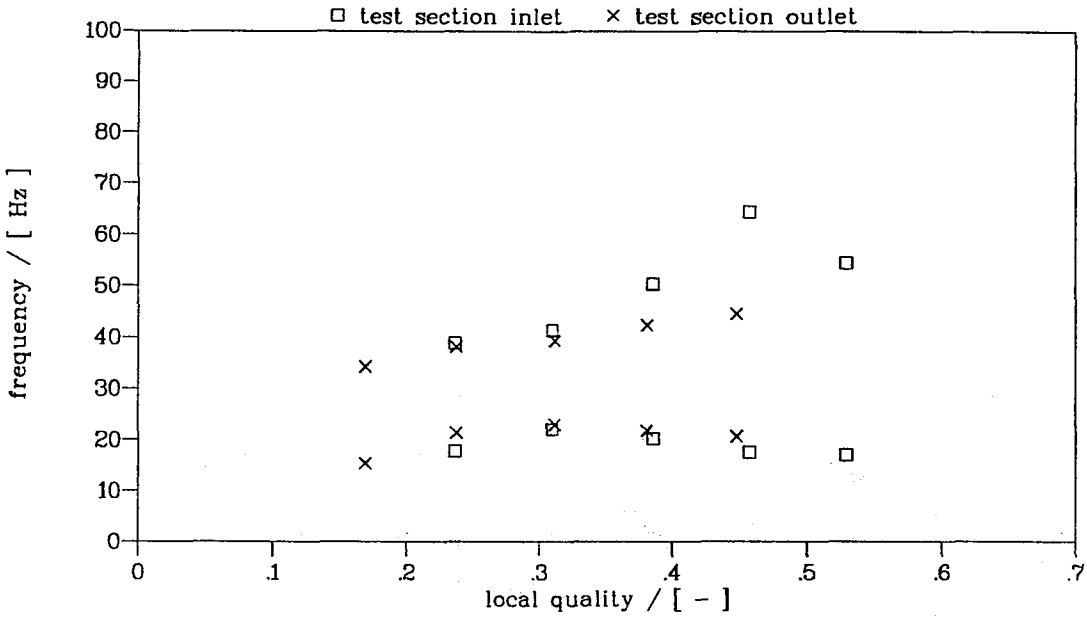

Figure 5.6.2-7

Frequency at maximum power in the frequency spectrum of waves in equilibrium condensation of annular up-flow of water and steam
mass flux 125 kg/m^2/s
concentric conductance probes 0.327 apart

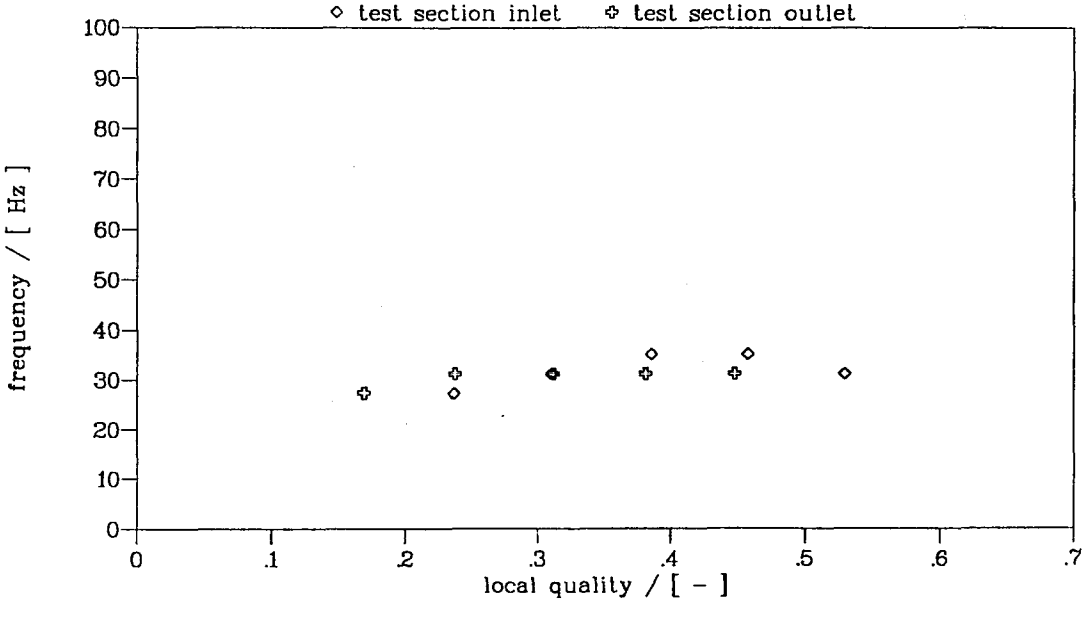

Figure 5.6.2-8

Frequency range with power more than half the maximum in the frequency spectrum of waves in equilibrium condensation of annular up-flow of water and steam
mass flux 183 kg/m^2/s
concentric conductance probes 0.327 apart

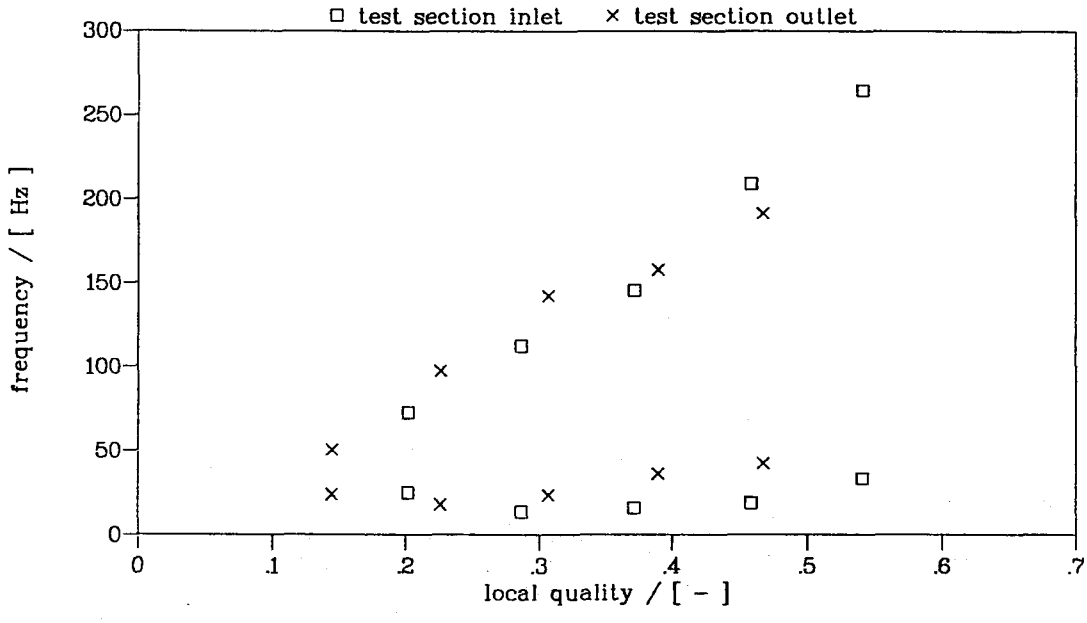

Figure 5.6.2-9

Frequency at maximum power in the frequency spectrum of waves in equilibrium condensation of annular up-flow of water and steam
mass flux 183 kg/m^2/s
concentric conductance probes 0.327 apart

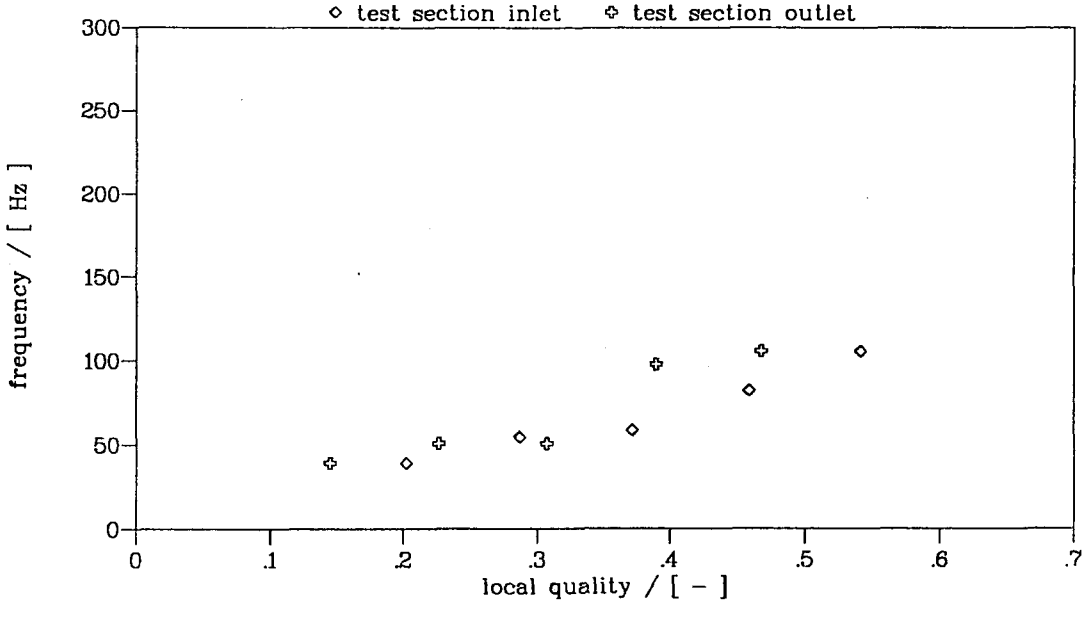

Figure 5.6.2-10

Frequency range with power more than half the maximum in the frequency spectrum of waves in equilibrium condensation of annular up-flow of water and steam
mass flux 241 kg/m^2/s
concentric conductance probes 0.327 apart

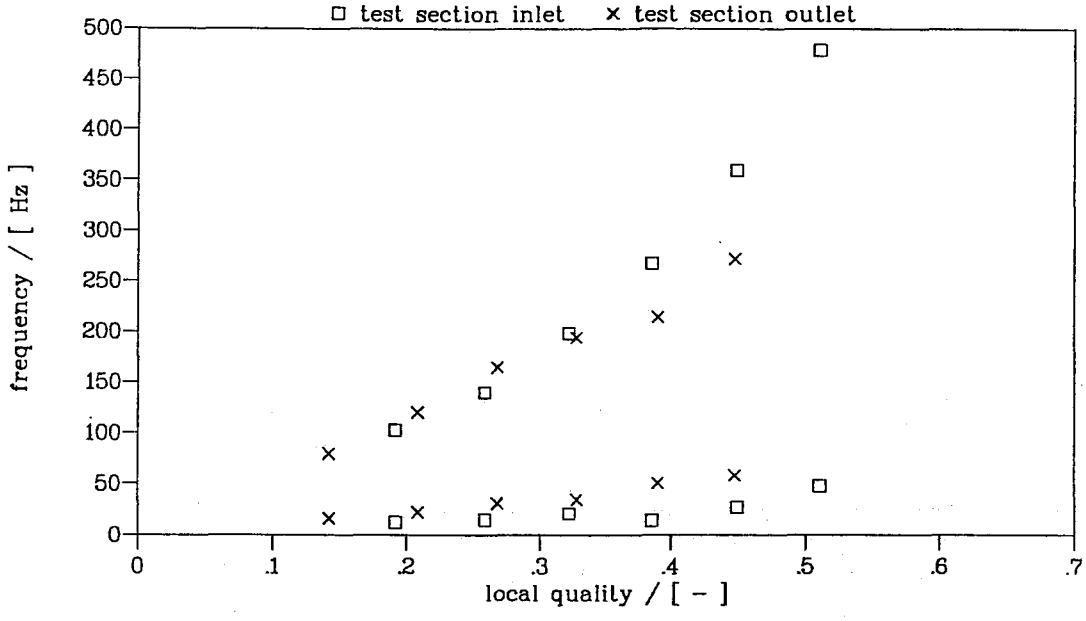

Figure 5.6.2-11

Frequency at maximum power in the frequency spectrum of waves in equilibrium condensation of annular up-flow of water and steam
mass flux 241 kg/m^2/s
concentric conductance probes 0.327 apart

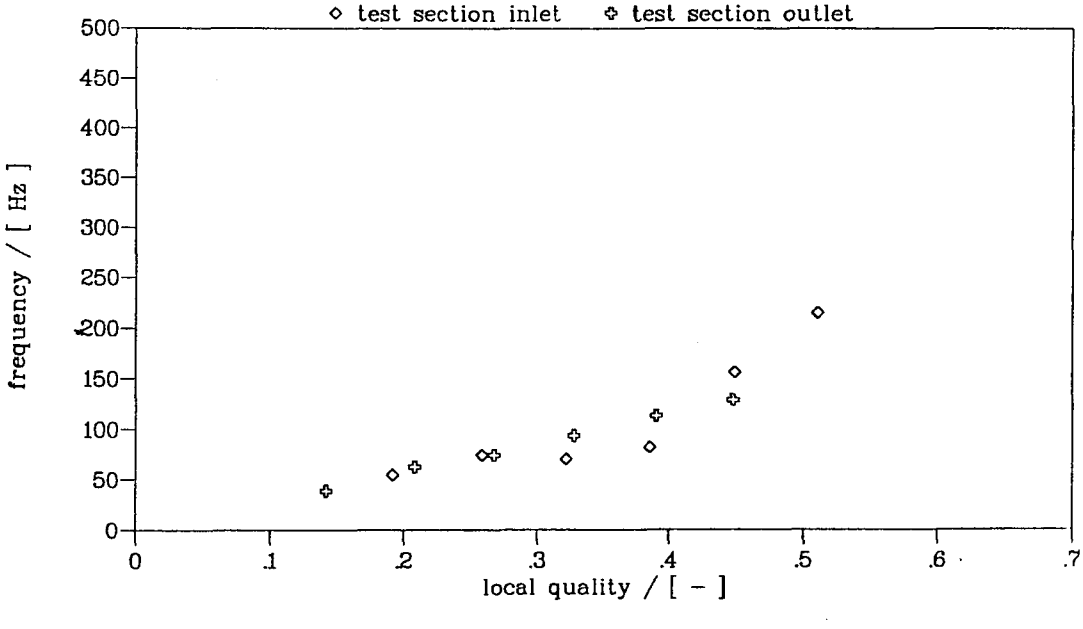

Figure 5.6.2-12

Frequency range with power more than half the maximum in the frequency spectrum of waves in adiabatic equilibrium annular up-flow of water and steam
mass flux 241 kg/m^2/s
concentric conductance probes 0.327 m apart

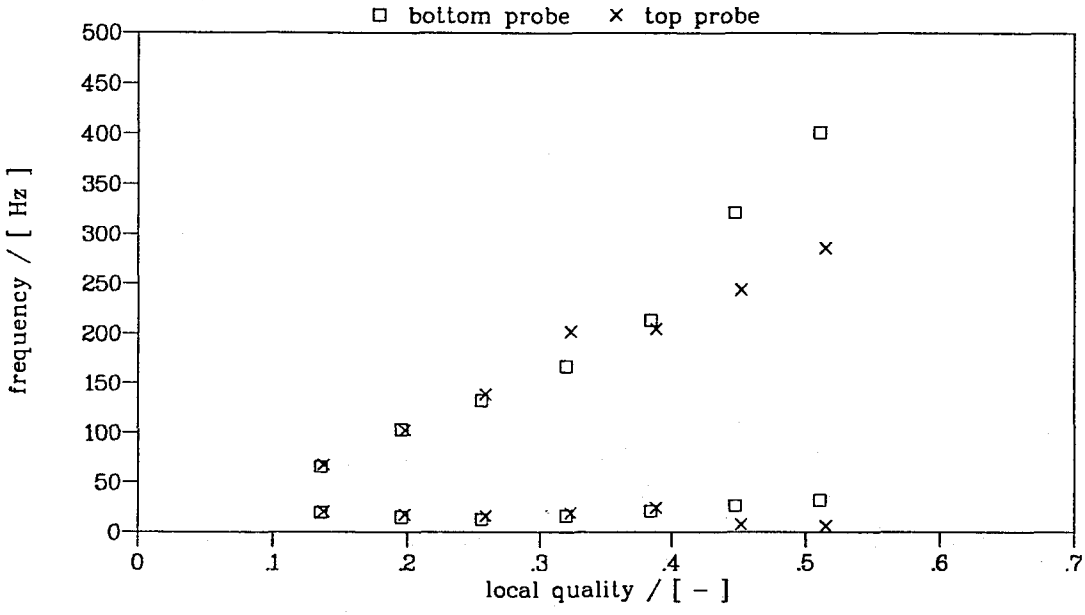

Figure 5.6.2-13

Frequency at maximum power in the frequency spectrum of waves in adiabatic equilibrium annular up-flow of water and steam
mass flux 241 kg/m^2/s
concentric conductance probes 0.327 m apart

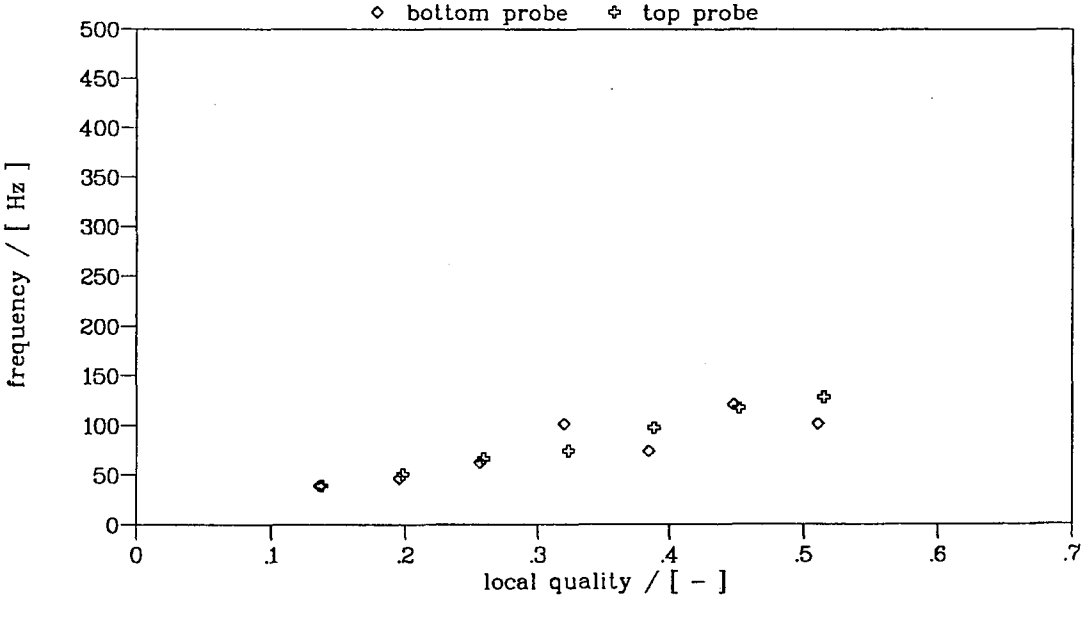

Figure 5.6.2-14

Frequency range with power more than half the maximum in the frequency spectrum of waves in adiabatic equilibrium annular up-flow of water and steam
mass flux 241 kg/m~2/s
concentric conductance probes 0.04 m apart

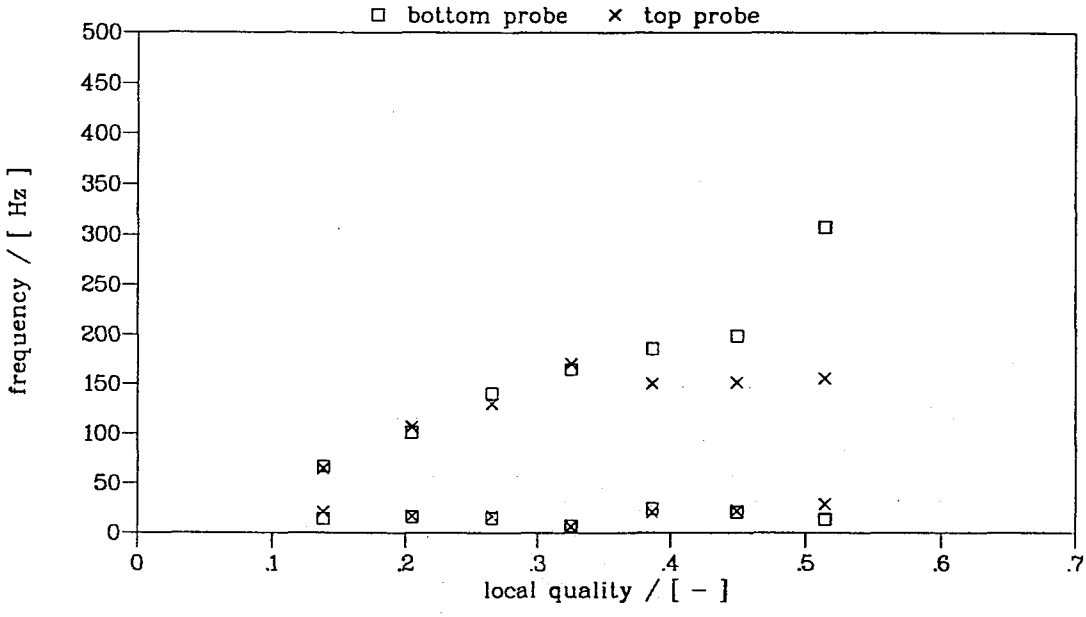

Figure 5.6.2-15

Frequency at maximum power in the frequency spectrum of waves in adiabatic equilibrium annular up-flow of water and steam
mass flux 241 kg/m~2/s
concentric conductance probes 0.04 m apart

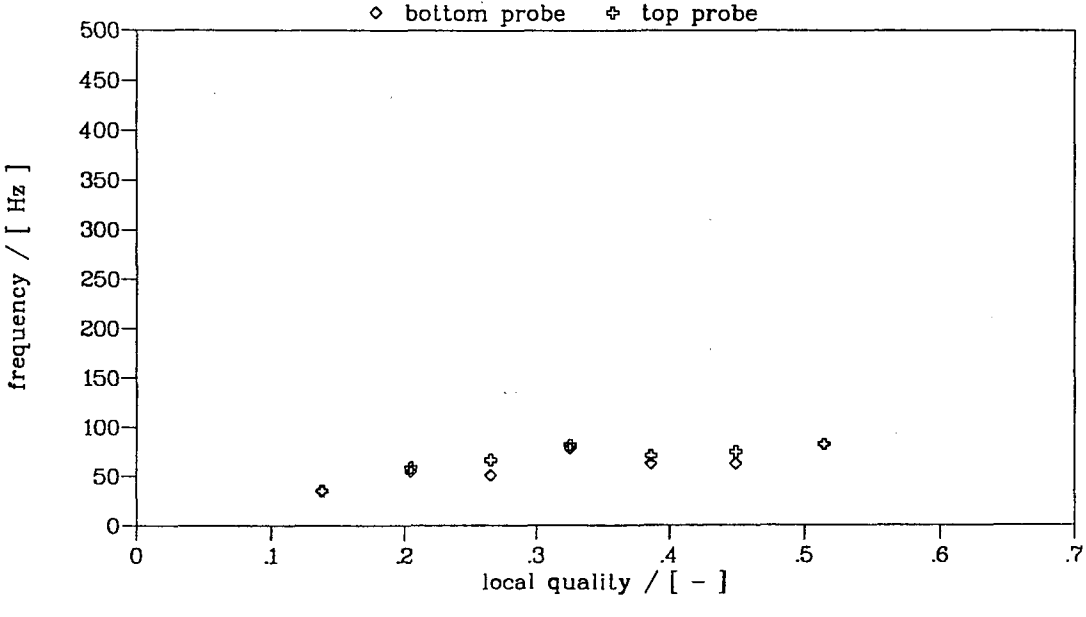

Figure 5.6.2-16

Frequency range with power more than half the maximum in the frequency spectrum of waves in condensation of annular up-flow of water and steam with sinter mixer at 120 mm up-stream of the test section inlet
mass flux 241 kg/m^2/s

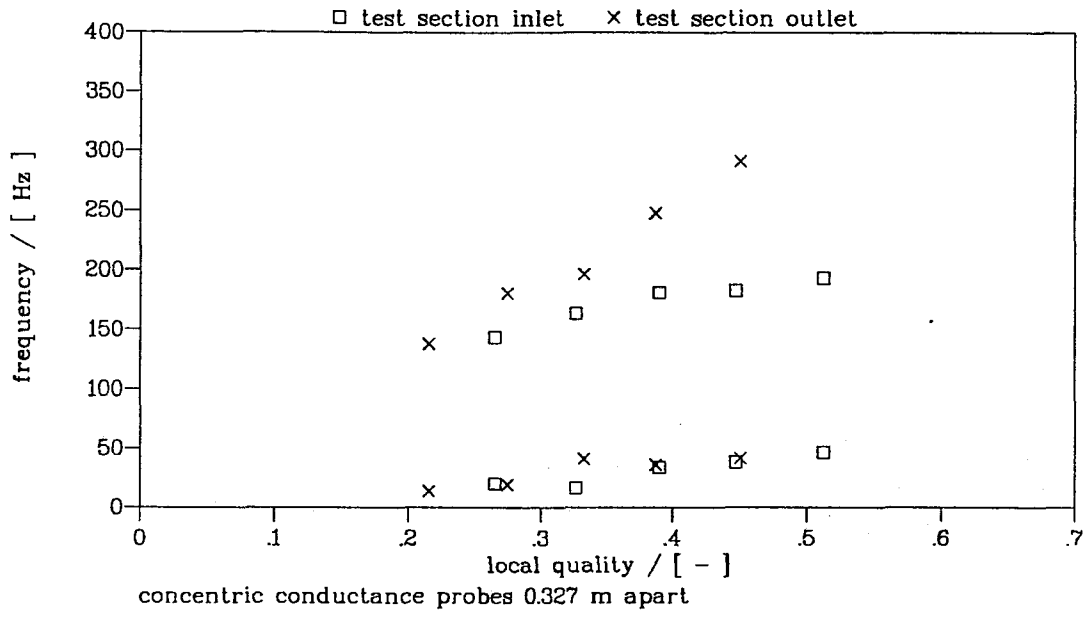

Figure 5.6.2-17

Frequency at maximum power in the frequency spectrum of waves in condensation of annular up-flow of water and steam with sinter mixer at 120 mm up-stream of the test section inlet
mass flux 241 kg/m^2/s

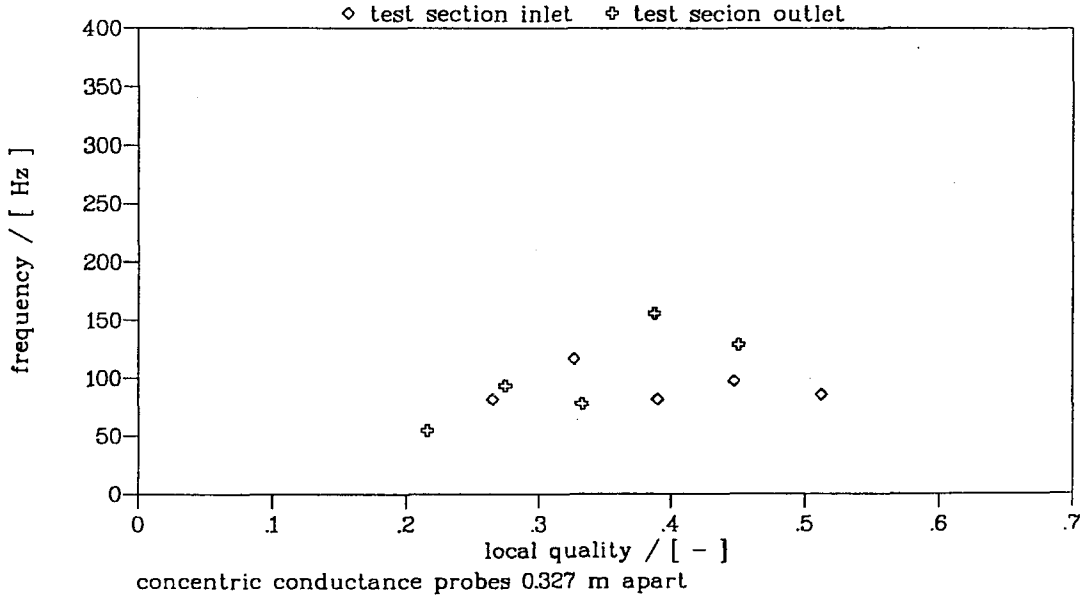

Figure 5.6.2-18

Frequency range with power more than half the maximum in the frequency spectrum of waves in adiabatic annular up-flow of water and steam with sinter mixer at 120 mm up-stream of test section inlet
mass flux 241 kg/m^2/s

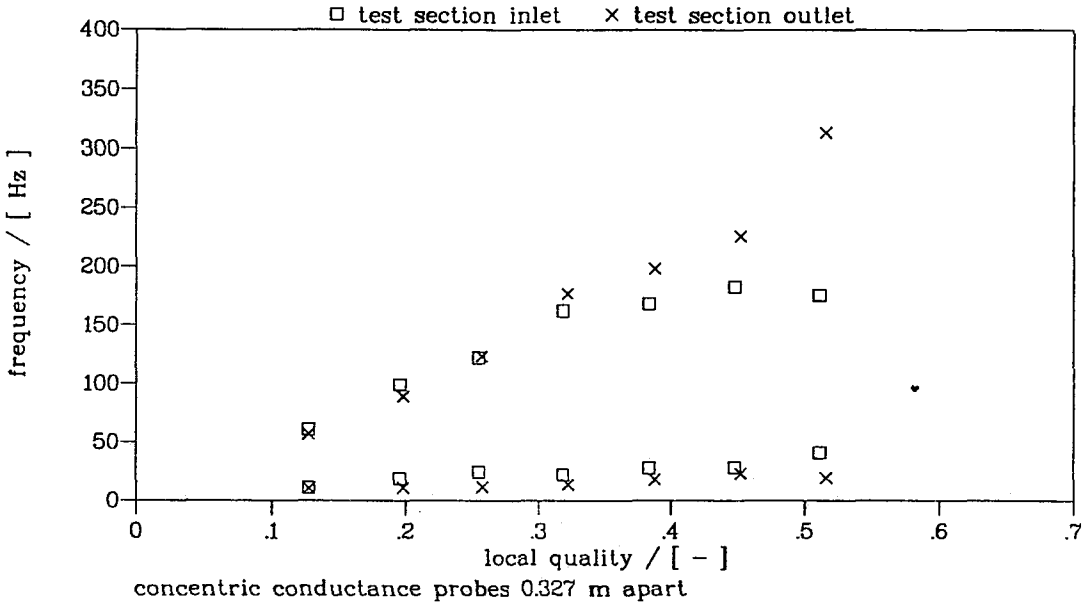

Figure 5.6.2-19

Frequency at maximum power in the frequency spectrum of waves in adiabatic annular up-flow of water and steam with sinter mixer at 120 mm up-stream of test section inlet
mass flux 241 kg/m^2/s

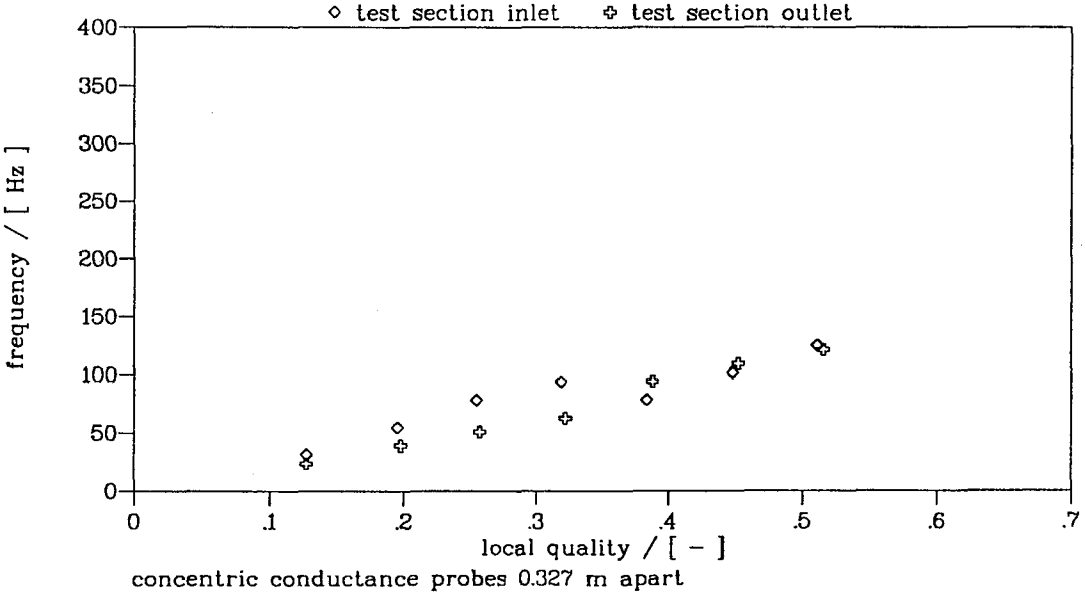

Figure 5.6.2-20

Frequency range with power more than half the maximum in the frequency spectrum of waves in adiabatic annular up-flow of water and steam with sinter mixer at 120 mm up-stream of test section inlet
mass flux 241 kg/m^2/s

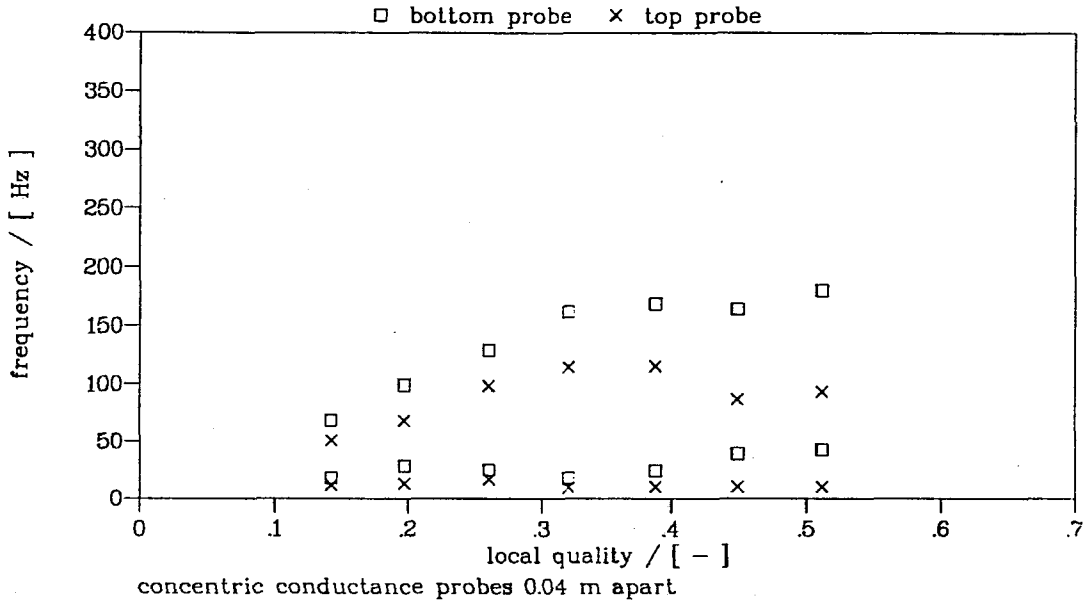

concentric conductance probes 0.04 m apart

Figure 5.6.2-21

Frequency at maximum power in the frequency spectrum of waves in adiabatic annular up-flow of water and steam with sinter mixer at 120 mm up-stream of test section inlet
mass flux 241 kg/m^2/s

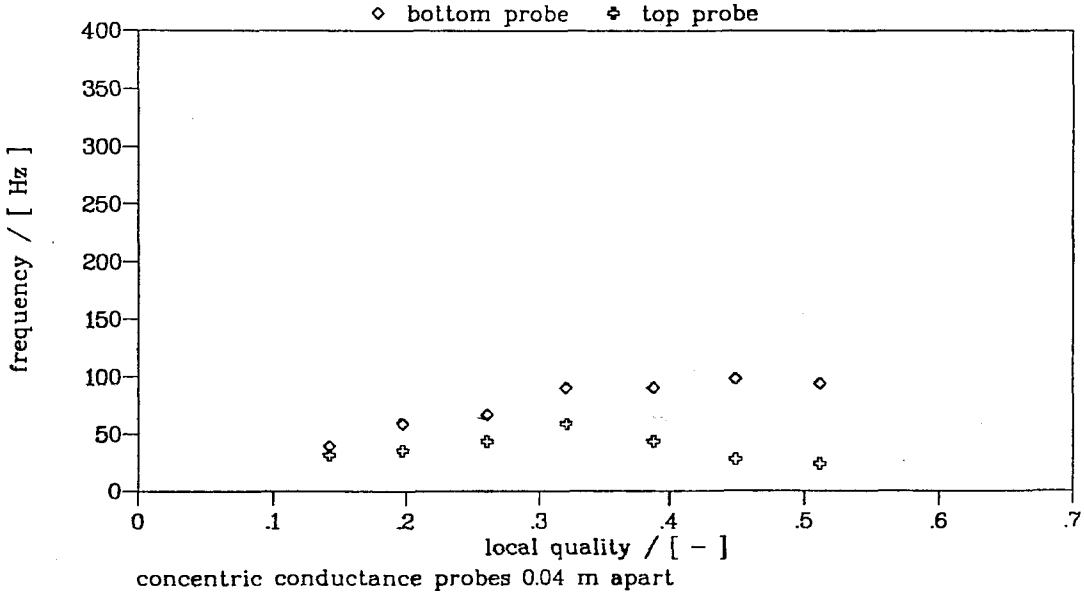

concentric conductance probes 0.04 m apart

Figure 5.6.2-22

Frequency range with power more than half the maximum in the frequency spectrum of waves in condensation of annular up-flow of water and steam with sinter mixer at 320 mm up-stream of the test section inlet
mass flux 241 kg/m^2/s

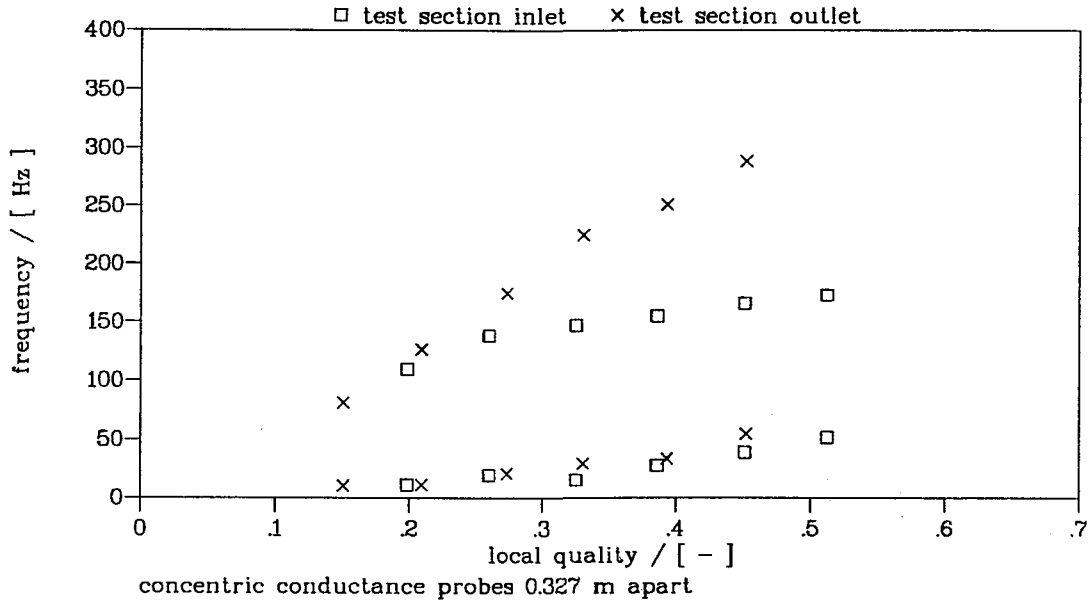

Figure 5.6.2-23

Frequency at maximum power in the frequency spectrum of waves in condensation of annular up-flow of water and steam with sinter mixer at 320 mm up-stream of the test section inlet
mass flux 241 kg/m^2/s

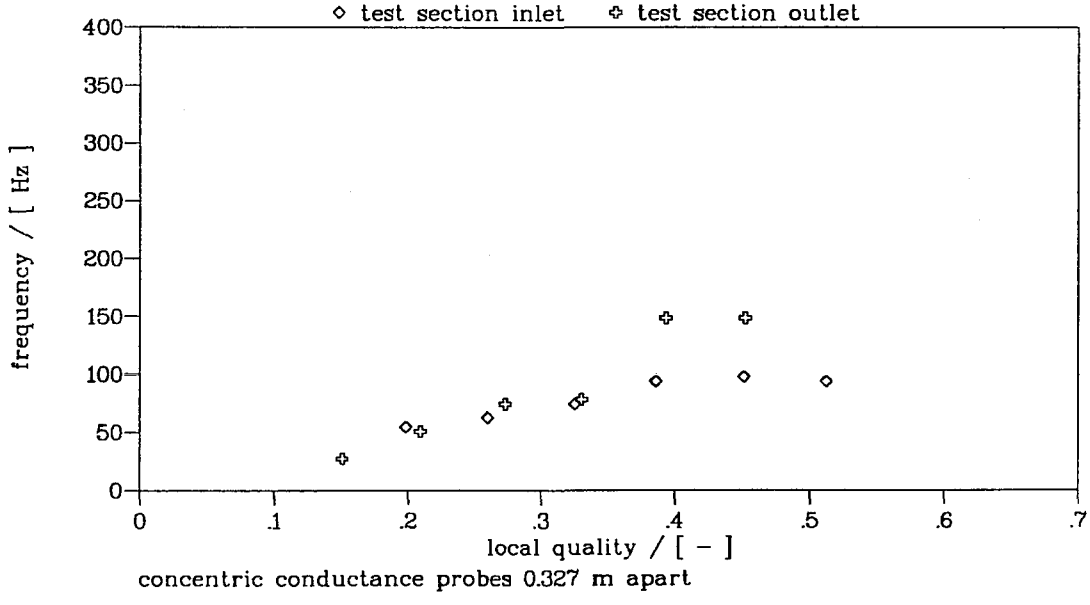

Figure 5.6.2-24

Frequency range with power more than half the maximum in the frequency spectrum of waves in adiabatic annular up-flow of water and steam with sinter mixer at 320 mm up-stream of test section inlet
mass flux 241 kg/m~2/s

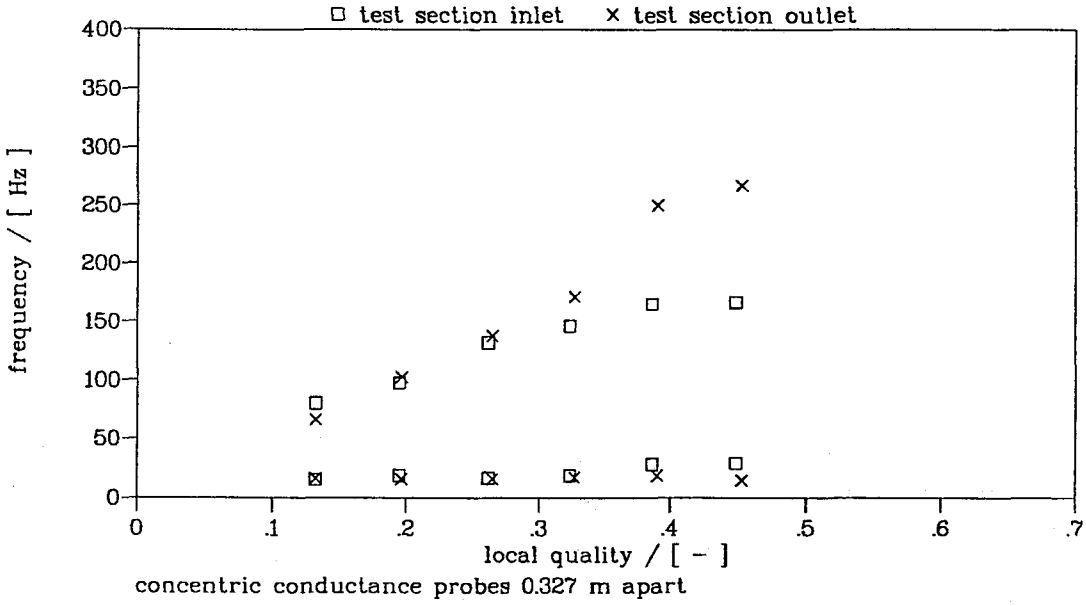

Figure 5.6.2-25

Frequency at maximum power in the frequency spectrum of waves in adiabatic annular up-flow of water and steam with sinter mixer at 320 mm up-stream of test section inlet
mass flux 241 kg/m~2/s

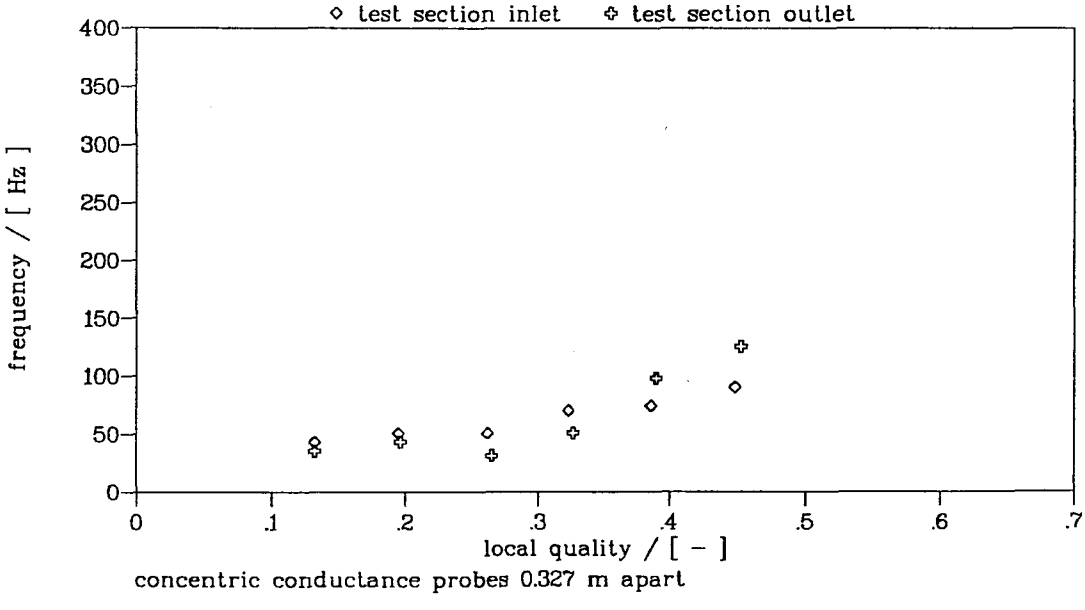

Figure 5.6.2-26

Frequency range with power more than half the maximum in the frequency spectrum of waves in adiabatic annular up-flow of water and steam with sinter mixer at 320 mm up-stream of test section inlet
mass flux 241 kg/m^2/s

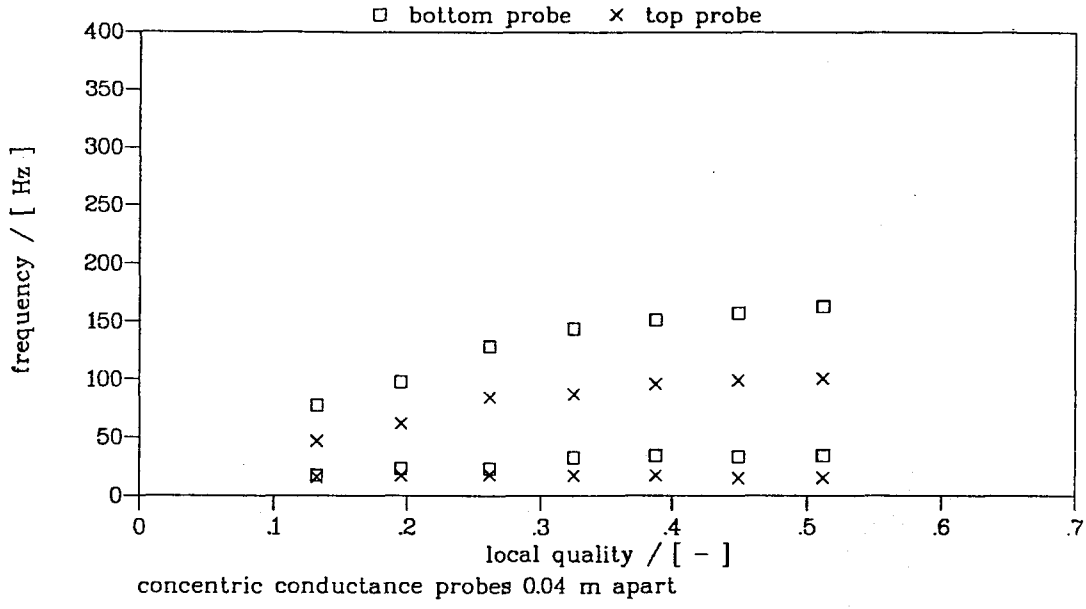

concentric conductance probes 0.04 m apart

Figure 5.6.2-27

Frequency at maximum power in the frequency spectrum of waves in adiabatic annular up-flow of water and steam with sinter mixer at 320 mm up-stream of test section inlet
mass flux 241 kg/m^2/s

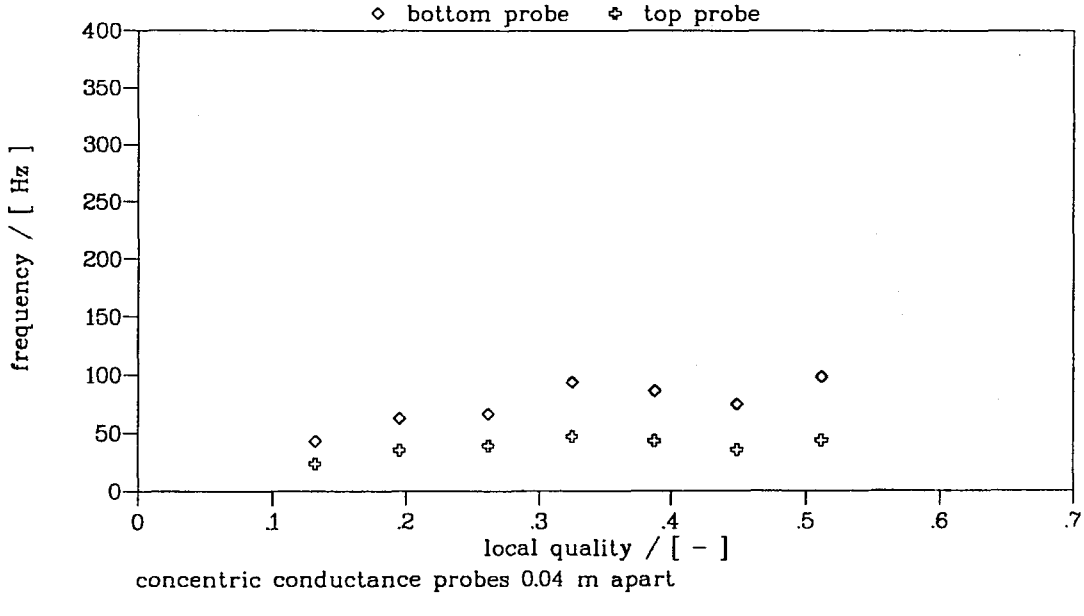

concentric conductance probes 0.04 m apart

Figure 5.6.2-28 Typical results of cross-correlation
conditions : adiabatic
sinter mixer at 120 mm upstream of test section inlet
probes 0.327 m apart

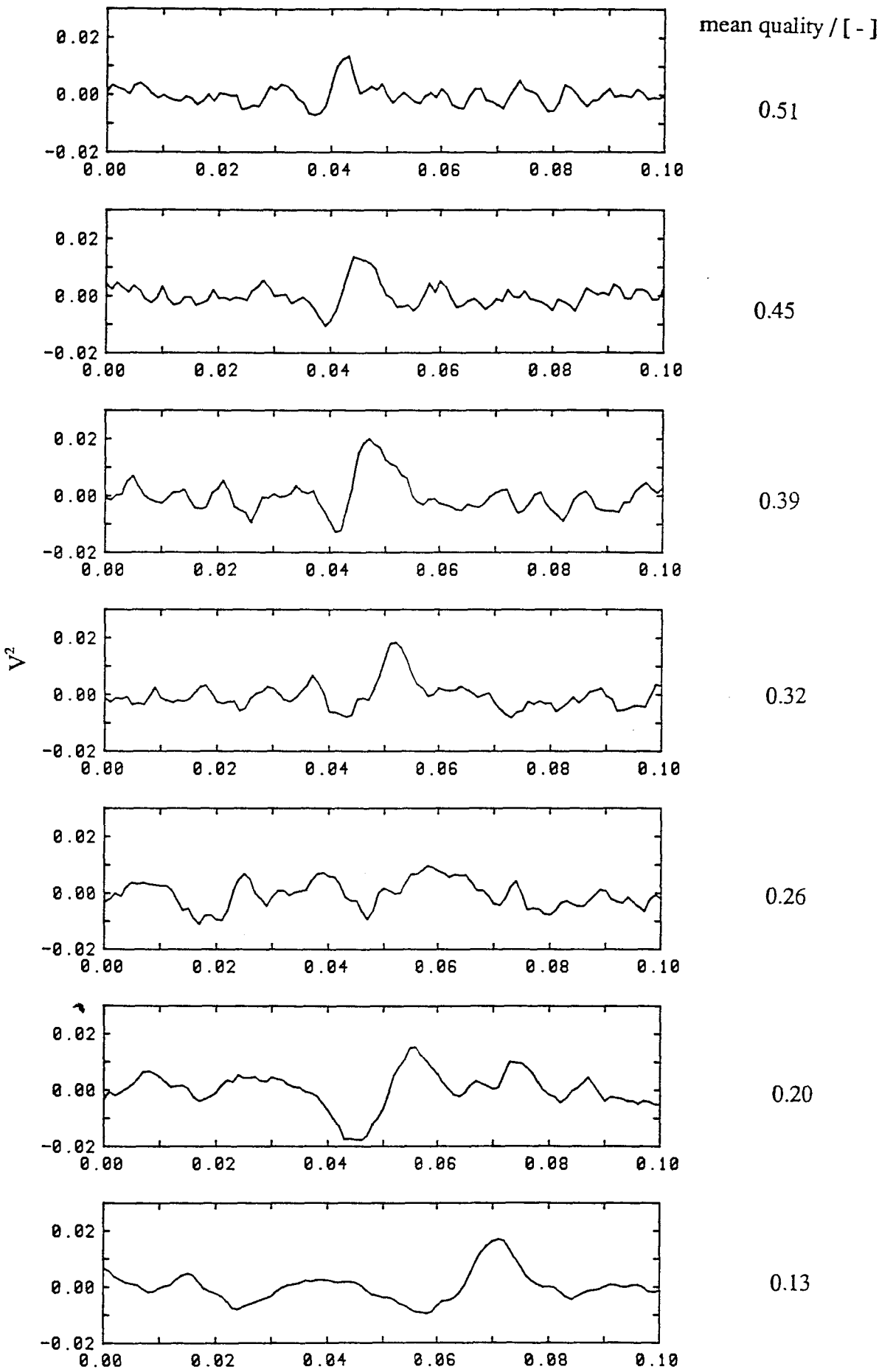

Figure 5.6.2-29 Typical results of cross-correlation
conditions : adiabatic
sinter mixer at 120 mm upstream of test section inlet
probes 0.04 m apart

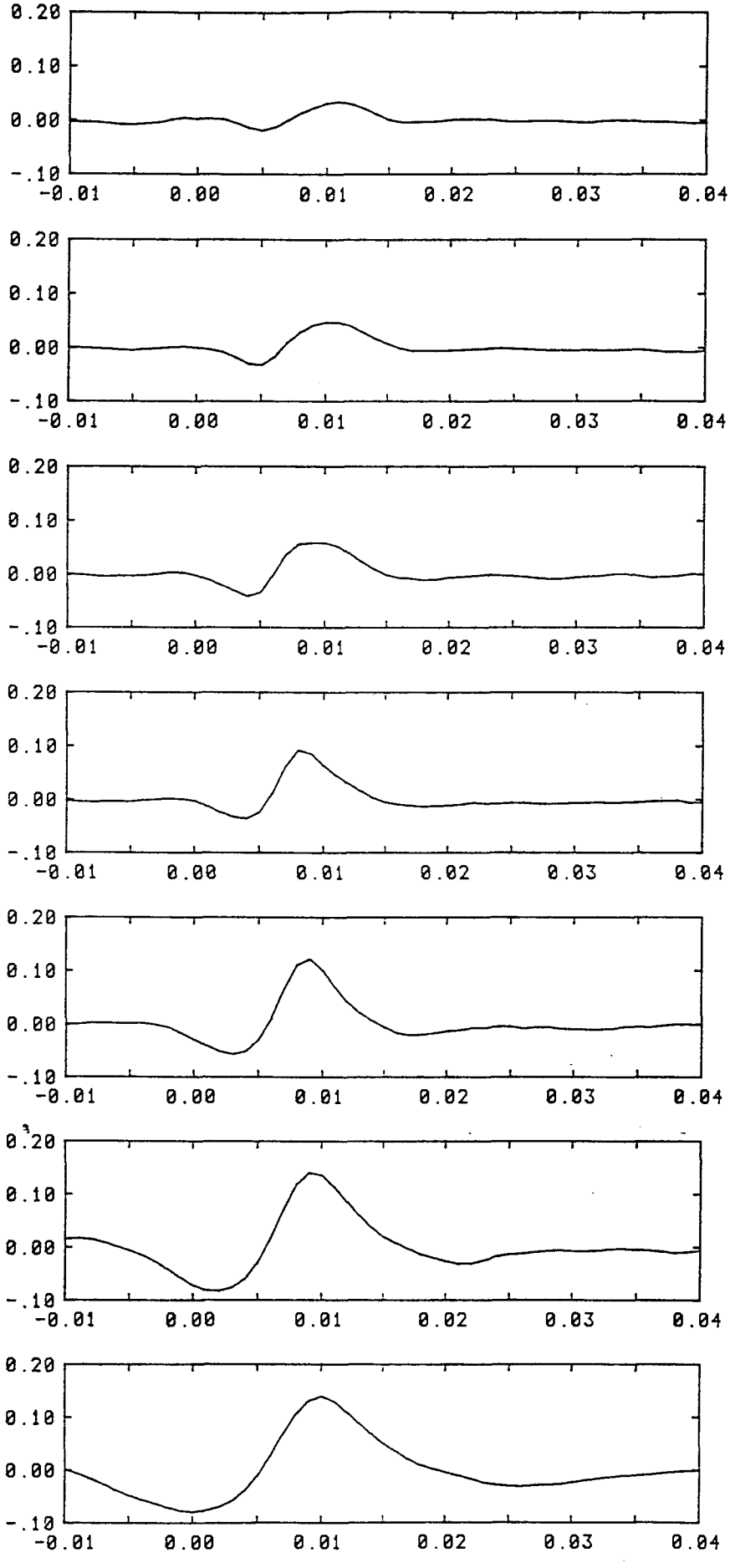

Figure 5.6.2-30

Wave velocity in adiabatic equilibrium annular up-flow of water and steam
mass flux 241 kg/m^2/s

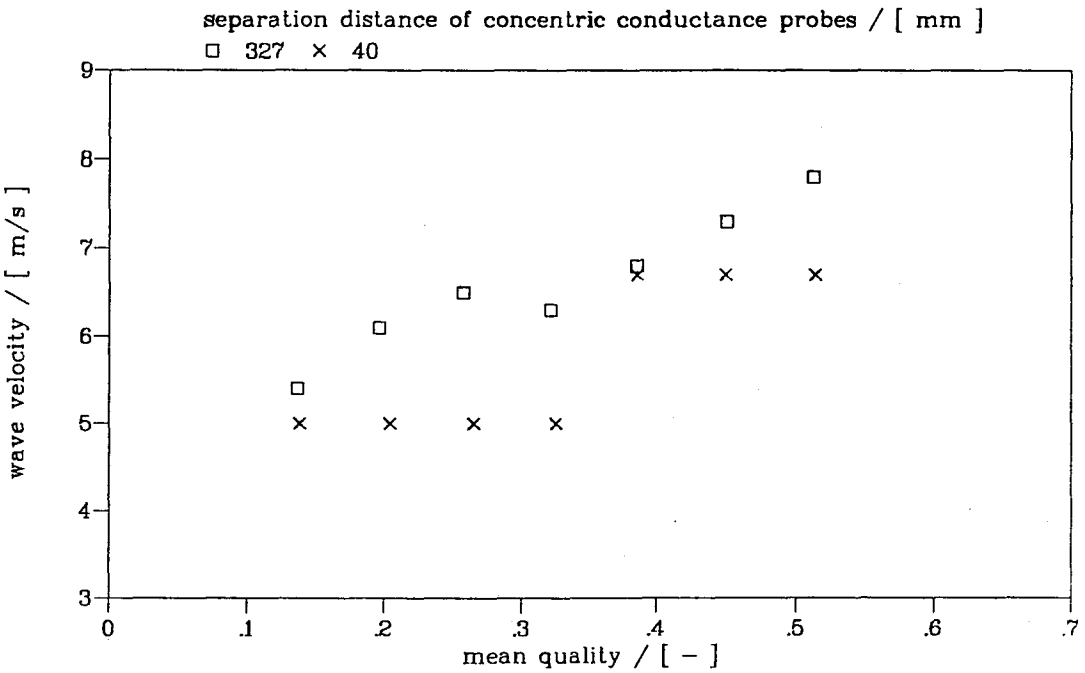

Figure 5.6.2-31

Wave velocity in equilibrium condensation of annular up-flow of water and steam

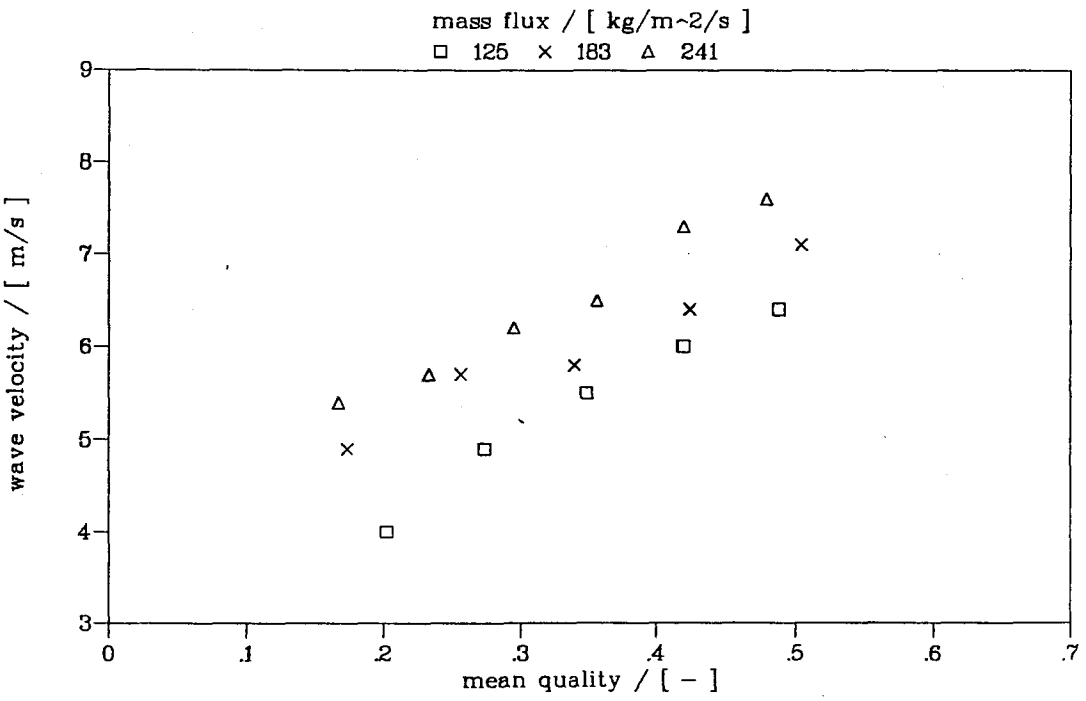

Figure 5.6.2-32

Wave velocity in adiabatic annular up-flow of water and steam with and without sinter mixer up-stream of test section inlet
mass flux 241 kg/m^2/s

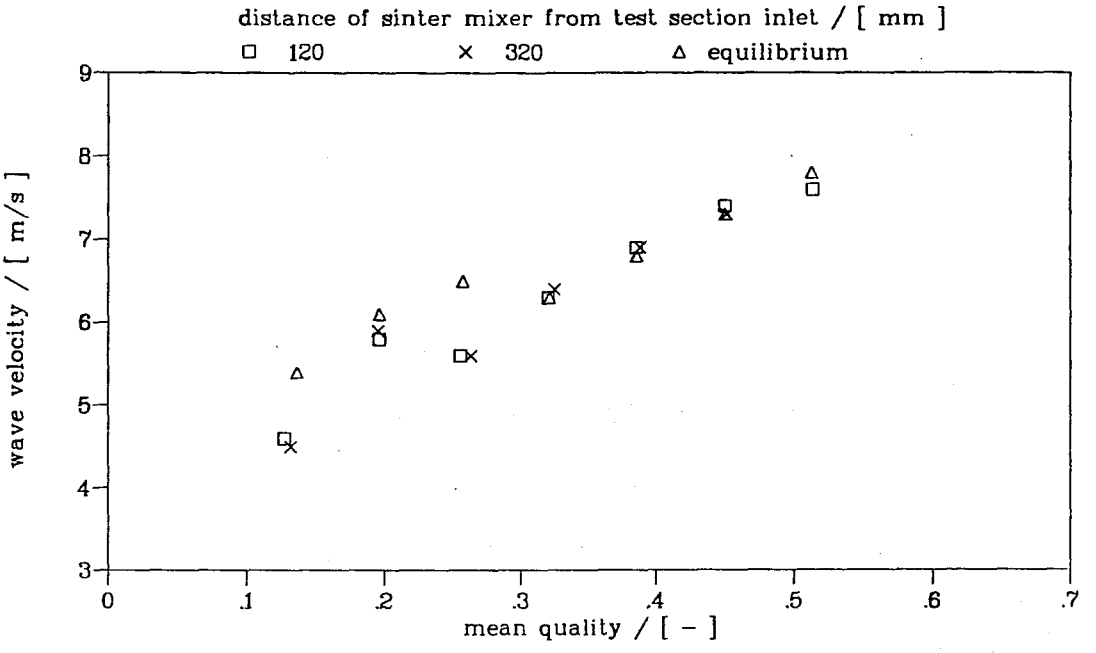

Figure 5.6.2-33

Wave velocity in condensation of annular up-flow of water and steam with and without sinter mixer up-stream of test section inlet
mass flux 241 kg/m^2/s

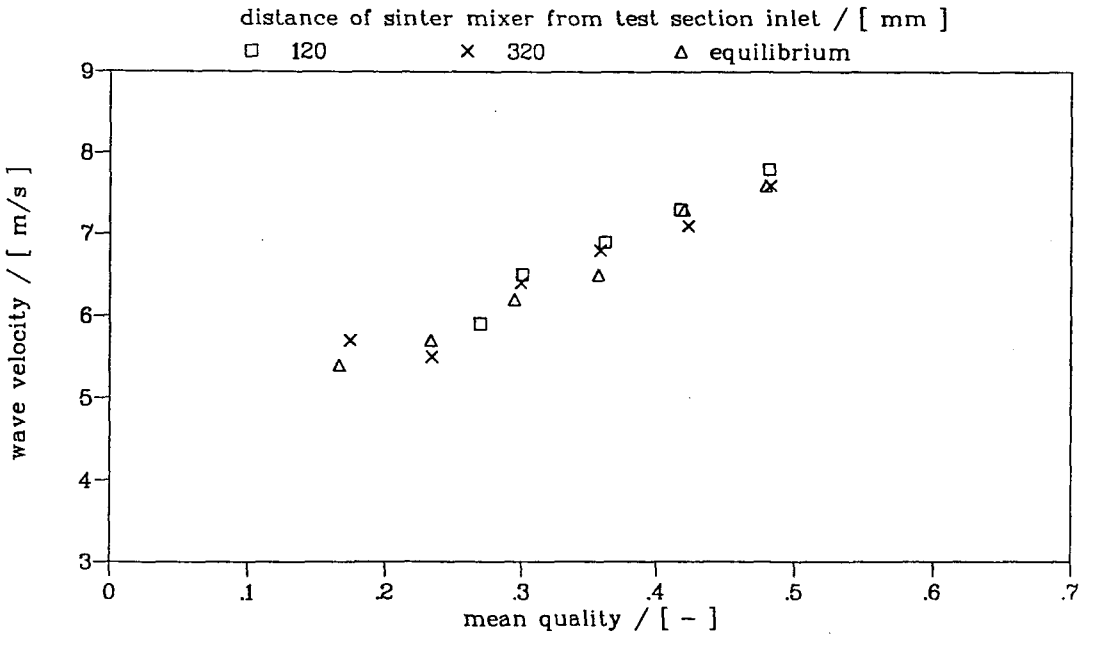

CHAPTER 6

CONCLUSIONS AND RECOMMENDATIONS FOR FURTHER WORK

Detailed conclusions and indications for further development are given throughout this thesis. Here, we shall state the most important results and suggestions and it is convenient to do so in terms of the principal objectives listed in Chapter 1.

6.1 Heat transfer in equilibrium annular flow

Conclusions

(1) Data taken for heat transfer in equilibrium annular flow indicate that the heat transfer coefficients for forced convective evaporation are considerably higher than those for condensation.

(2) A number of factors which might have influenced the measurements, leading to the difference between the evaporation and condensation being spurious, have been carefully considered and it is concluded that there is a strong prima facie case that the difference are real. This finding is, therefore, consistent with the secondary nucleation mechanism proposed by Mesler (1977).

Recommendations for further work

(1) It view of the far reaching implications of the findings of these experiments, further confirmation of the result is required as a first priority, preferably with a wider range of fluids and flow conditions

(2) If secondary nucleation is indeed important, then attempts should be made to visualise it under annular flow condition.

(3) Efforts should be made to improve the accuracy of the fluid heated evaporation experiments. Specifically, the use of a heating fluid with lower viscosity than the glycerol used in the present work would allow turbulent condition to be attained at lower flow rate and large annulus temperature difference to be achieved, thus increasing the accuracy.

6.2 Heat transfer and wave characteristics in developing annular flow

Conclusions

(1) Heat transfer in condensation was studied with two different channel lengths (120 mm and 320 mm) separating the porous wall liquid injector and the test section. The results were identical to each other and to those obtained in equilibrium flow.

(2) The measurements of film thickness, disturbance wave frequency and disturbance wave velocity showed that the film and wave characteristics developed much more rapidly in the present stem-water flows than had been expected from the previous air-water studies. The wave frequency and velocity appeared fully developed after 120 mm. This explains conclusion (1) but, of course, means that the objective of studying non-equilibrium flow could not be met in the present experiment.

Recommendations for further work

(1) Further investigation of equilibrium phenomena are required for steam-water annular flow. This would involve using shorter length between the injector and the measurement station.

(2) Subject to the results of (1), the original objective should be pursued, namely that of making heat transfer measurements in non-equilibrium.

6.3 Prediction of flow boiling

Conclusions

(1) A fully consistent model for flow boiling has been developed which takes account of both forced convective evaporation and nucleate boiling.

(2) Closure of the model required bubble burst sizes which were many time greater than the film thickness; a constant burst size of 1.5 mm was used in closing the present model. Investigation of the cine film of Hewitt et al (1963) showed that the bubble burst size was, indeed, many times the mean liquid film thickness.

Recommendations for further work

(1) The model developed here should be tested against a wider range of data.

(2) Efforts should be made to obtain a better correlation of bubble burst diameter, preferably based on further visual observations of the bubble growth and release cycle in annular flow.

(3) Attempts should be made to include secondary nucleation into the forced convective part of the model in order to reflect the observations in the present work.

APPENDIX A

CALIBRATION OF ANNULUS THERMOCOUPLES

Accurate calibrations of the thermocouples was essential to achieve the measurement precision required, in particular, for the annulus thermocouples. The chromel-constantan annulus thermocouples were calibrated in two modes, one differential and the other absolute. The calibration was done in a thermal bath with temperature-control. The fluid used for calibration was water for temperatures below 100°C, and oil for temperatures above. The sensing ends of the thermocouples were bunched and tied to the tip of a platinum resistance thermometer which was then immersed about 250mm below the fluid surface in the thermal bath.

A.1 Absolute mode

In absolute mode, the thermocouples were connected to some compensating wires. The cold-junction ends of the compensating wires were placed in a frigister which provided a 0°C reference. The leads of the compensating wires were connected to a scanner. The micro-volt signals read by the scanner were converted to nominal temperature readings in Celsius by a computer program using a ninth order British Standard polynomial. The form and the coefficients of this polynomial are as follows :

$$T = a_0 + a_1 v + a_2 v^2 + a_3 v^3 + a_4 v^4 + a_5 v^5 + a_6 v^6 + a_7 v^7 + a_8 v^8 + a_9 v^9$$

where

$a_0 = 9.96908663 \times 10^{-3}$

$a_1 = 1.70177406 \times 10^{1}$ $\quad$ $a_2 = -2.04044924 \times 10^{-1}$

$a_3 = -1.76835221 \times 10^{-4}$ $\quad$ $a_4 = 6.1660763 \times 10^{-4}$

$a_5 = -3.22396725 \times 10^{-5}$ $\quad$ $a_6 = 1.48182138 \times 10^{-7}$

$a_7 = 4.17895462 \times 10^{-8}$ $\quad$ $a_8 = -1.43809321 \times 10^{-9}$

$a_9 = 1.50731037 \times 10^{-11}$

The temperature readings of the thermocouples are compared with those of the platinum resistance thermometer. The results are shown in Figures A.1-1 and A.1-2. As will be seen, the nominal temperature readings show deviation from the (assumed true) platinum resistance thermometer values and, also, deviations between different thermocouples were also observed. However, repeated calibrations of the thermocouples showed that the readings of any individual thermocouple were very reproducible. Thus, each thermocouple can be individually corrected. Once this correction is made, it is estimated that the maximum error in any given reading is ±0.04°C. This means that the maximum error in terms of temperature difference would be ±0.08°C.

A.2 Differential mode

In differential mode, the leads of consecutive thermocouple pairs were wired to a switching device, which had a pair of extensions linked to a micro-voltmeter. The circuit of the switching device was such that, at any one time, the negative poles of a paired thermocouples were connected and the potential between their positive poles was measured by the micro-voltmeter. Under isothermal condition, a perfect pair of thermocouples connected in this way should not create any potential between them. In practice, there will be some residual potential. Over the same range of temperatures as in the absolute mode calibration, repeated measurements of these residual potentials were made. These readings can then be used to correct differential temperature measurements made in experiments.

The results of this calibration are typified by those shown in Figure A.2-1. The average uncertainty in the temperature difference is about ± 4 V x10^{-6}, which is equivalent to ± 0.06°C. Thus, this method is not significantly better than the absolute mode. Furthermore, it has a disadvantage of introducing disturbance to the circuit during switching. This disturbance takes time to die out. Therefore, it was decided to use the absolute mode in the experiments.

Figure A.1-1

Calibration of annulus thermocouples in thermal bath

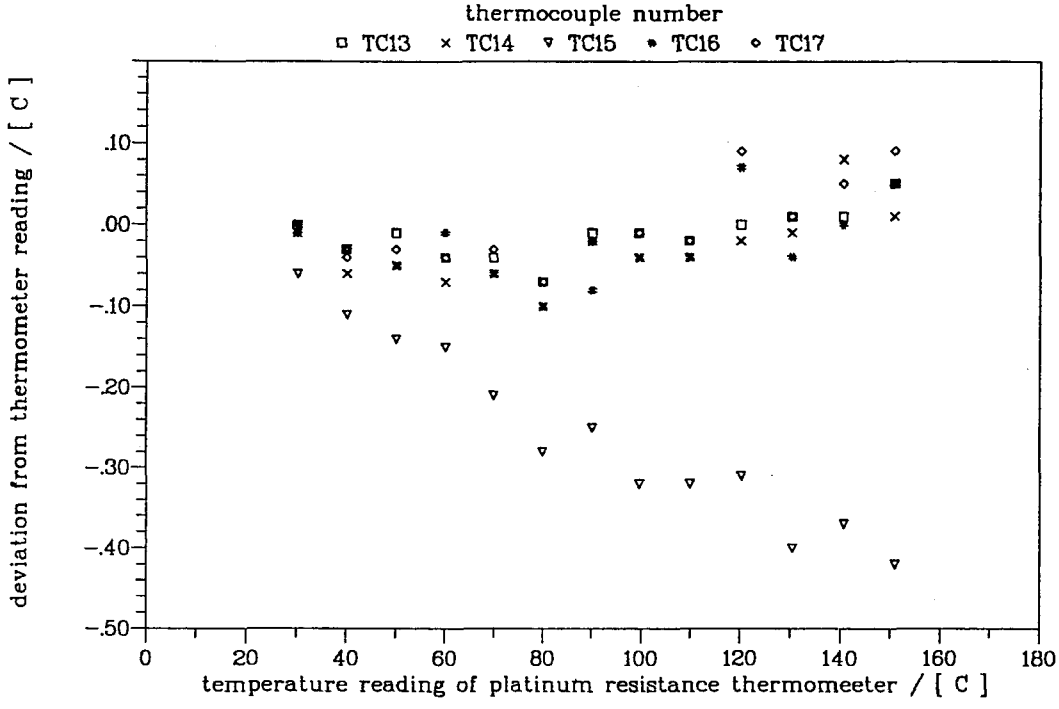

Figure A.1-2

Calibration of annulus thermocouples in thermal bath

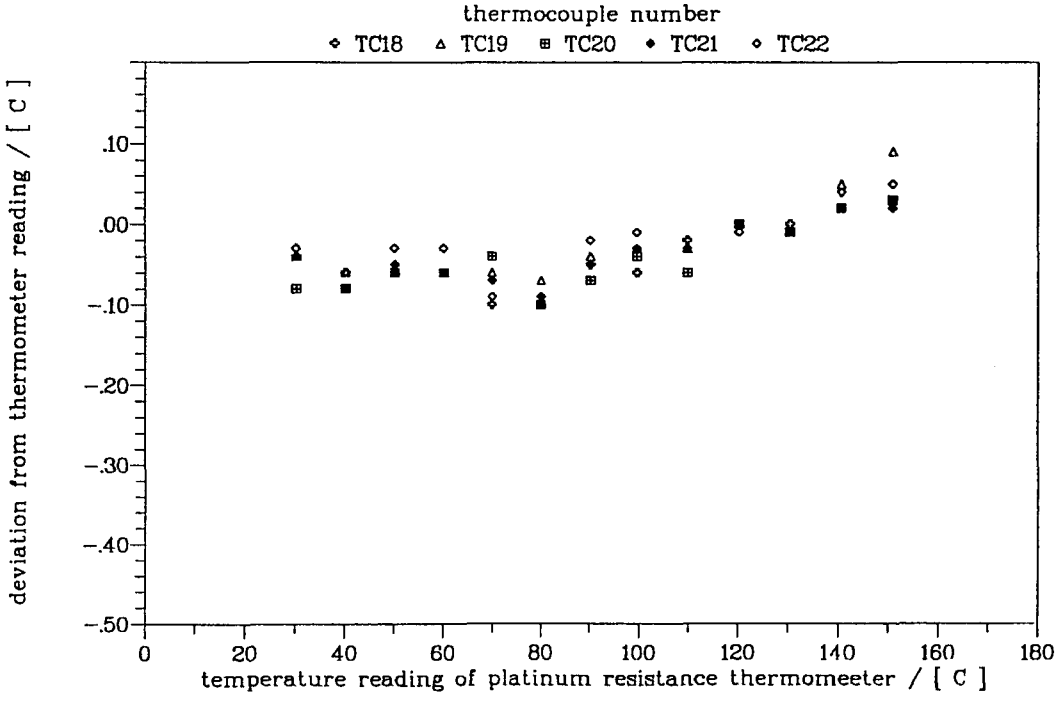

Figure A.2-1

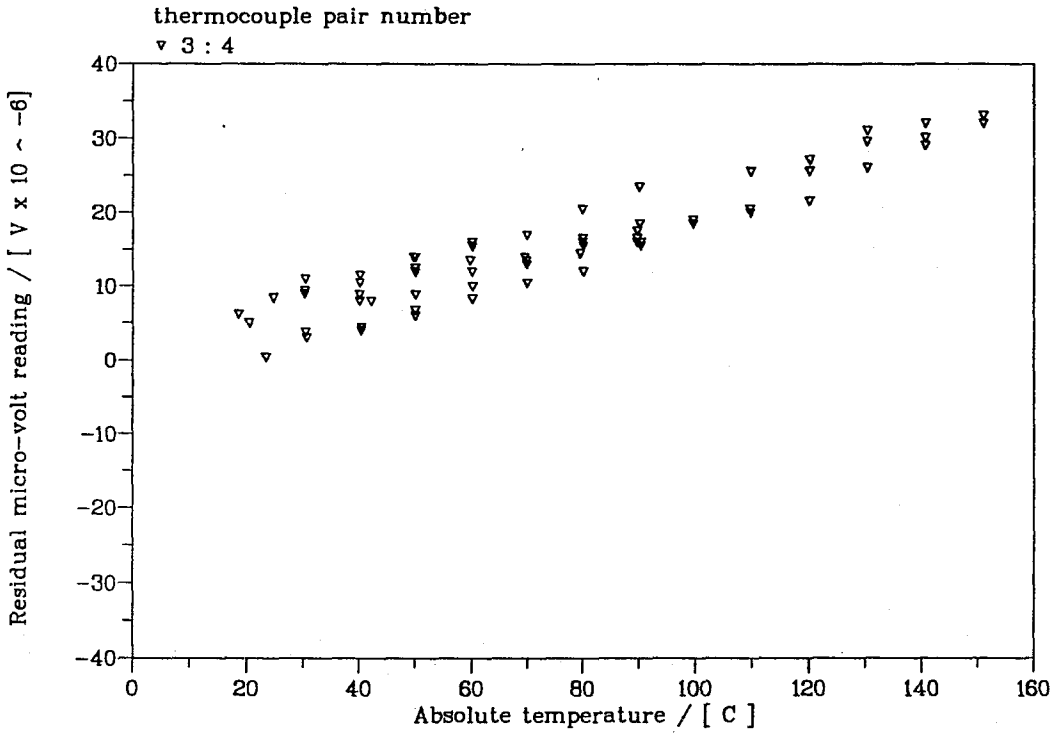
thermocouple pair number
▽ 3 : 4
Residual micro-volt reading / [V x 10 ^ -6]
40
30
20
10
0
-10
-20
-30
-40
0
20
40
60
80
100
120
140
160
Absolute temperature / [C]

APPENDIX B

CALIBRATION OF PRESSURE SENSORS

B.1 Calibration of differential pressure cells

All the D.P. cells were calibrated by "dead weight" method. The low pressure end of the cell was open to atmosphere. The high pressure end was connected to a "dead weight" tester. The applied weight was in terms of inches of water gauge. The output signal from the cell was read by a digital voltmeter. The data are presented in figures B.1-1, B.1-2 and B.1-3.

The following expressions are used to fit the data.

Test section low range D.P. cell $\Delta P = 0.25E - 5$

Test section high range D.P. cell $\Delta P = 2.5E - 50$

Calming section D.P. cell $\Delta P = 10E - 200$

where E is the voltage reading in terms of μV (i.e 1×10^{-6} V).

B.2 Calibration of pressure transducers

The pressure transducers were also calibrated by " dead weight " method. Since some of the operating pressures are below atmospheric pressure, a vacuum system was used to provide sub-atmospheric pressure.

The error shown in figures B.2-1 appear to be consistently small. They are used to correct the absolute pressure readings. However, during the course of the condensation experiments for the copper tube test section, the outlet pressure transducer was found to be drifting. Subsequently, both transducers were checked by a simple "water column" method. The results are shown in figure B.2-2. The jump in the data was caused by a small amount of air trapped in the transducer. This pocket of air expanded under sub-atmospheric pressure. A shorter water column would result in a bias towards a higher measured pressure.

The test section outlet pressure transducer was sent back to the manufacturer for repair. Later, it was re-installed for the evaporation experiments. Shortly after, the inlet pressure transducer became faulty. It was left un-repaired. The measurement of saturation temperature at the test section inlet could still be obtained from the readings of the outlet pressure transducer and the D.P. cells.

Figure B.1-1

Calibration of test section low range D.P. cell

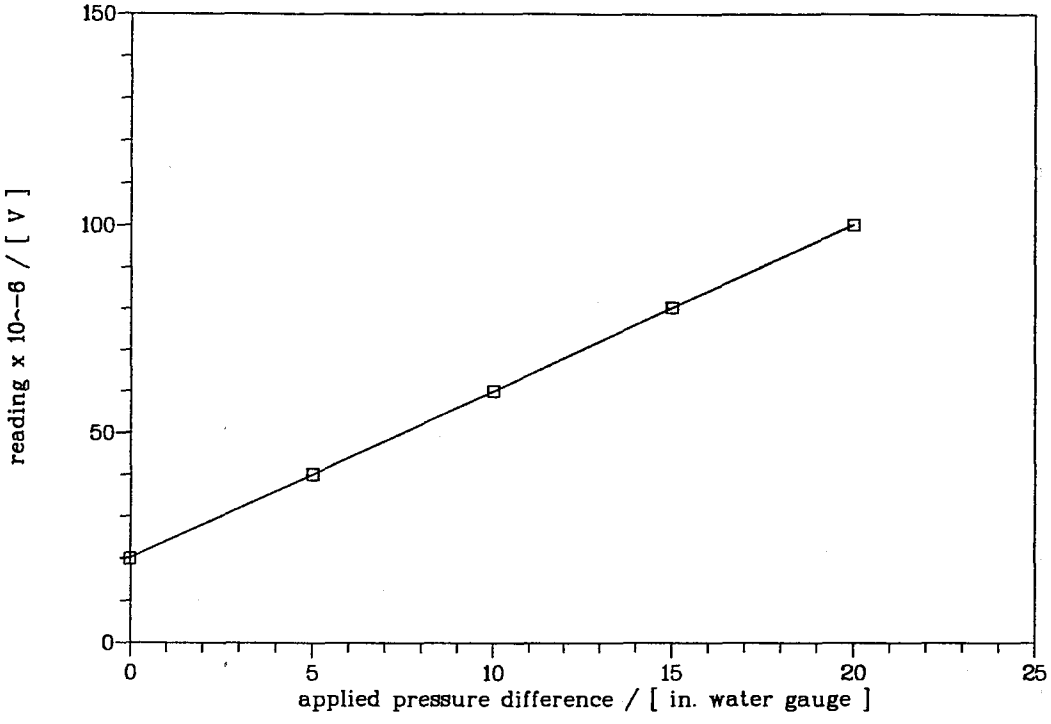

Figure B.1-2

Calibration of test section high range D.P. cell

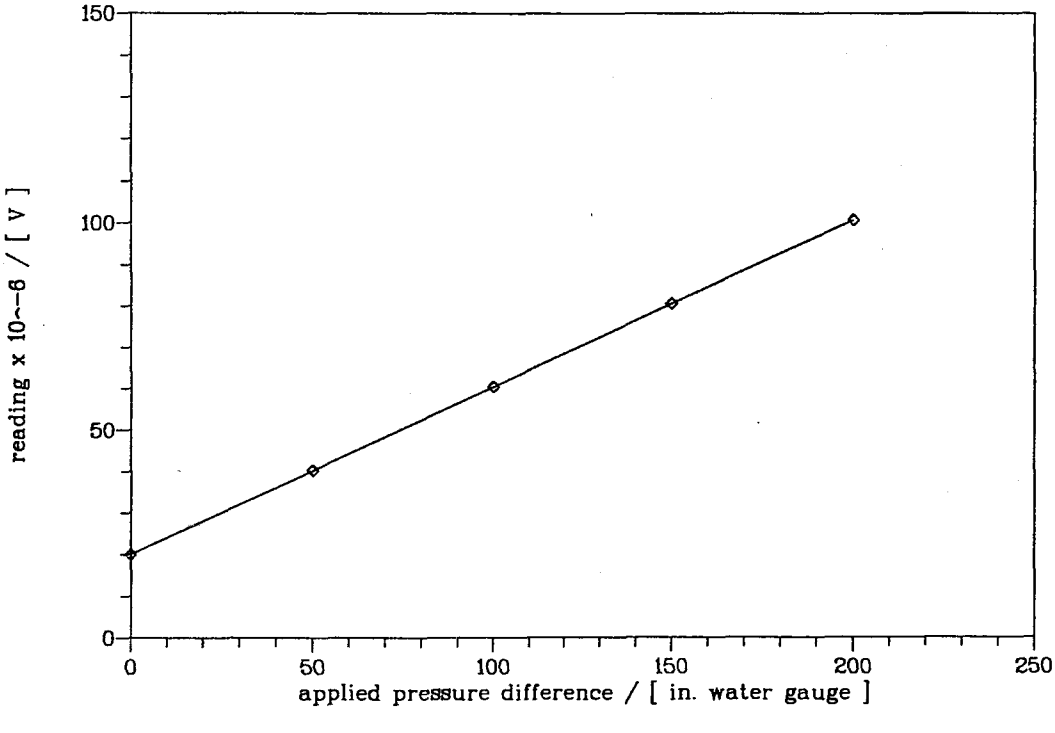

Figure B.1-3

Calibration of calming section D.P. cell

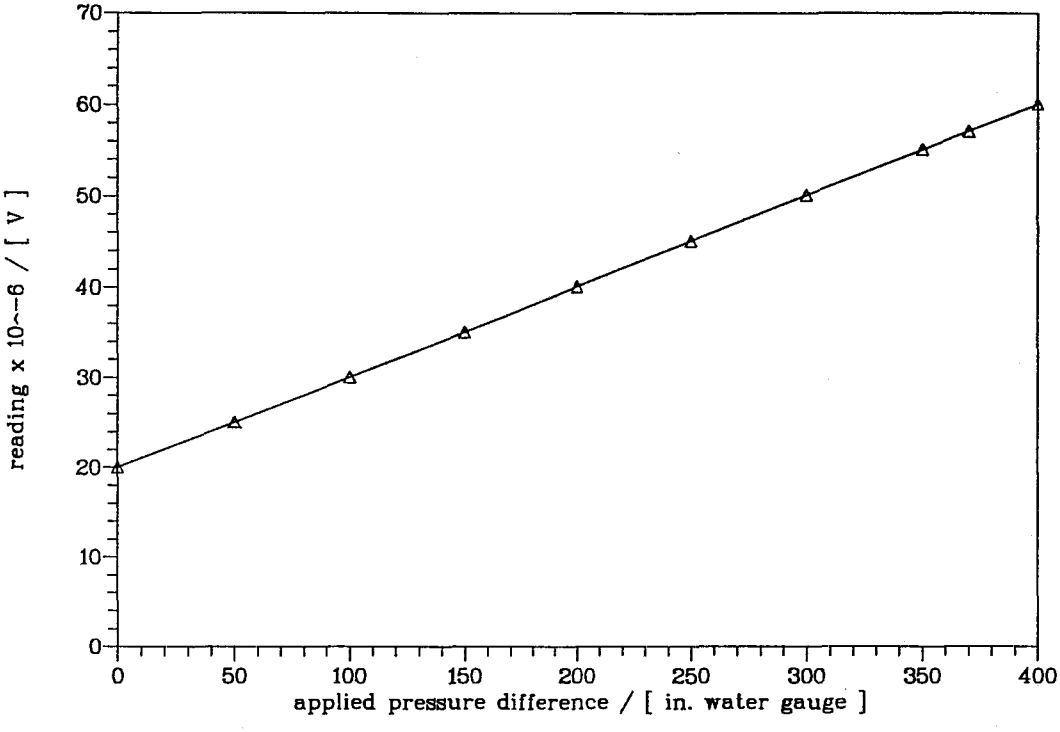

Figure B.2-1

Calibration of pressure transducers using "dead weight" method and a vacuum system

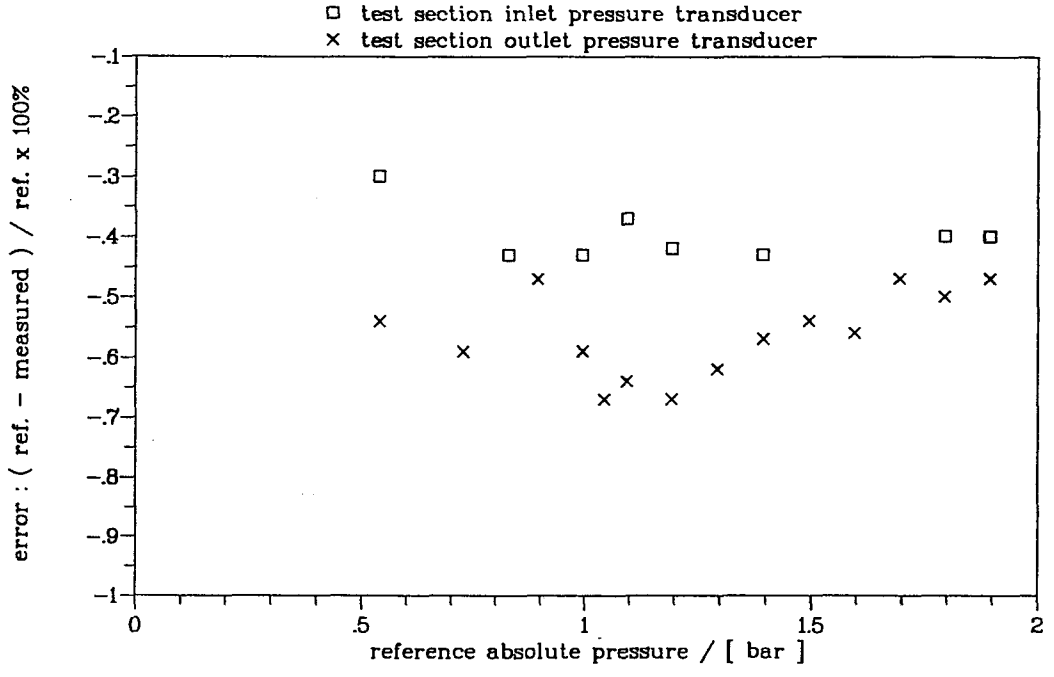

Figure B.2-2

Check on pressure transducers using "water column" method

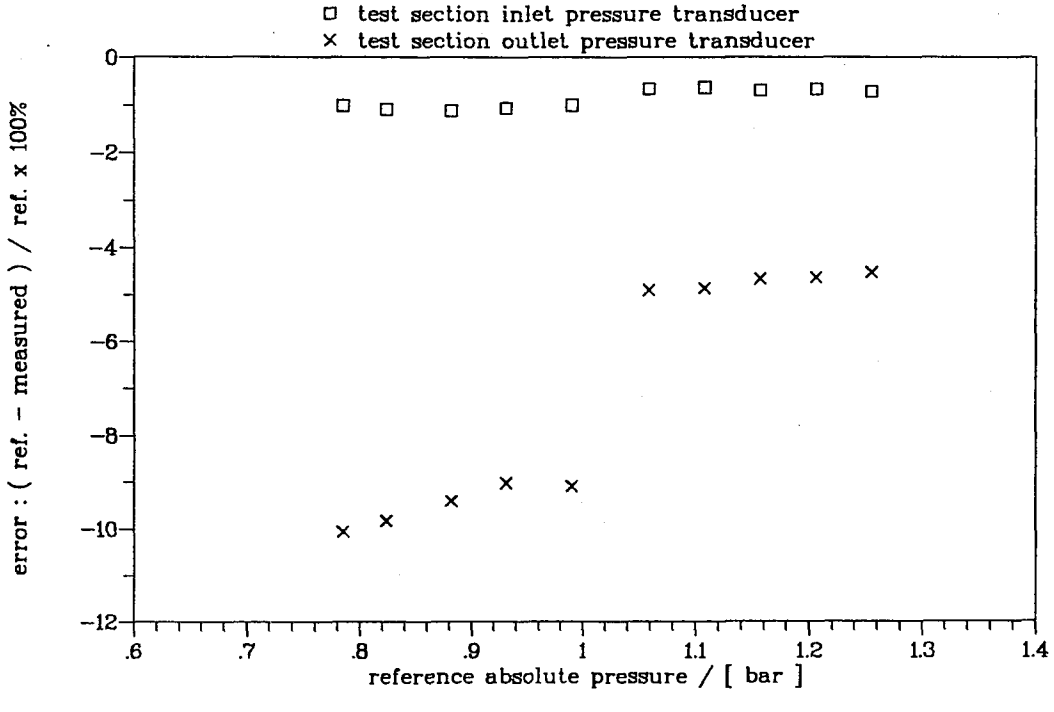

APPENDIX C

CALIBRATION OF FLOWMETERS

The flowmeters calibrated are listed in Table C-1 . The method used for calibration was of " bucket and stop-watch " type. The flow down-stream of the flowmeter was diverted by a temporary hose to a bucket. The mass flow rate was calculated from the time taken for a certain mass of liquid collected. The calibration results are shown in figures C-1, C-2 and C-3.

The single-phase Reynolds numbers at the flow rates in the two-phase circuit ranged from laminar to just within the turbulent region. For low flow conditions, the viscosity effect due to temperature change on flow measurement is significant. The 50°C data was used for the two-phase experiment, whereas the 20°C data was used for the single-phase heat balance test.

No calibration was done for glycerol flowing in the single-phase circuit because of the high temperature under normal operating conditions. Calculated flow rate data (see figure C-4) supplied by the flowmeter manufacturer was used. These calculated flow rate data are based on the physical property data of pure glycerol from the Glycerine Producers' Association (1975).

Table C-1 Conditions and results of flowmeter calibrations

Description	Float material	Single phase fluid used	Fluid temperature / (℃)	Polynomial to fit data
Two-phase circuit flowmeter	stainless steel	water	20	$\dot{M} = -1.9116 \times 10^{-3} + 9.9931 \times 10^{-4} F$
Two-phase circuit flowmeter	stainless steel	water	50	$\dot{M} = -1.4109 \times 10^{-3} + 1.02872 \times 10^{-3} F$
Single-phase circuit flowmeter	PTFE.	water	50	$\dot{M} = -5.7974 \times 10^{-3} + 1.50 \times 10^{-3} F$
Single-phase circuit flowmeter	PTFE.*	glycerol	160	$\dot{M} = 5.2339 \times 10^{-3} + 1.1742 \times 10^{-3} F + 1.4684 \times 10^{-6} F^2$
Single-phase circuit flowmeter	Stainless steel*	glycerol	160	$\dot{M} = 1.2174 \times 10^{-2} + 1.7897 \times 10^{-3} F + 2.04469 \times 10^{-6} F^2$
Condenser cooling water flowmeter	Ceramic	water	13	$\dot{M} = 1.2257 \times 10^{-2} + 3.9608 \times 10^{-3} F + 5.6869 \times 10^{-5} F^2$

* Data supplied by flowmeter manufacturer.

Figure C-1

Calibration of two–phase circuit flowmeter using single–phase water

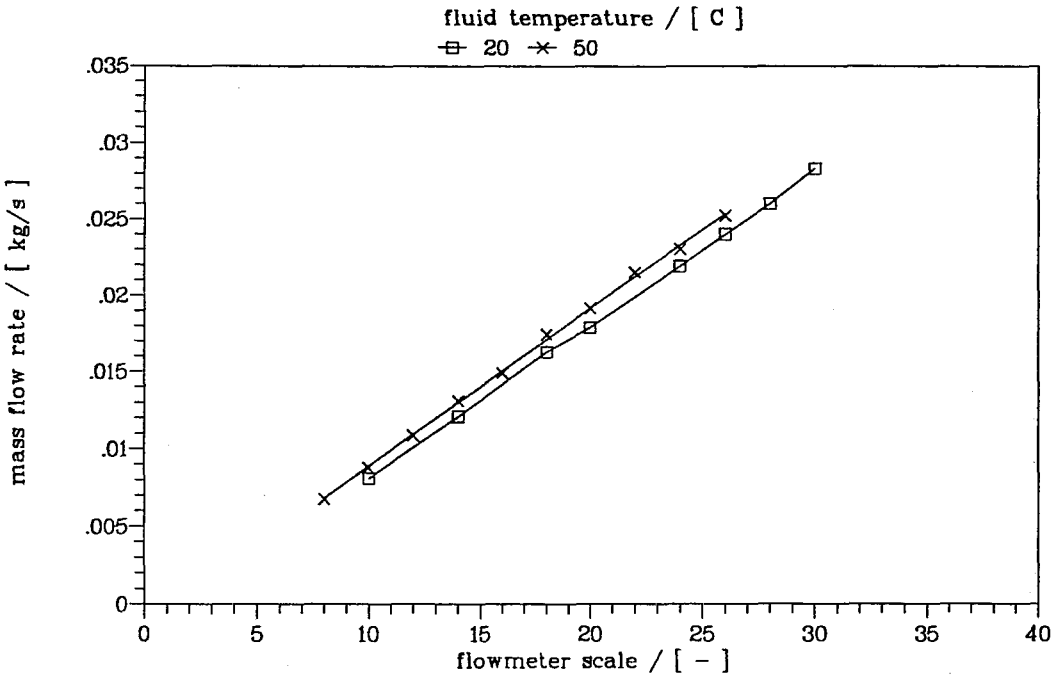

Figure C-2

Calibration of single–phase circuit flowmeter using water compared with flow rate curve supplied by manufacturer
fluid temperature at 50 C

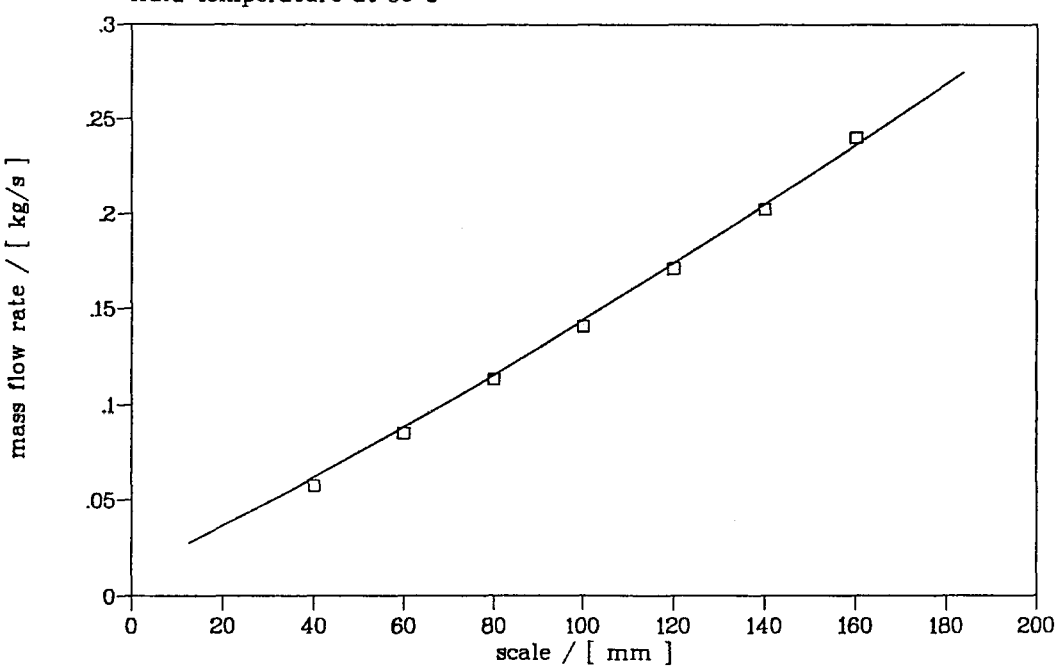

Figure C-3

Calibration of flowmeter for cooling water of total condenser
fluid temperature at 13 C

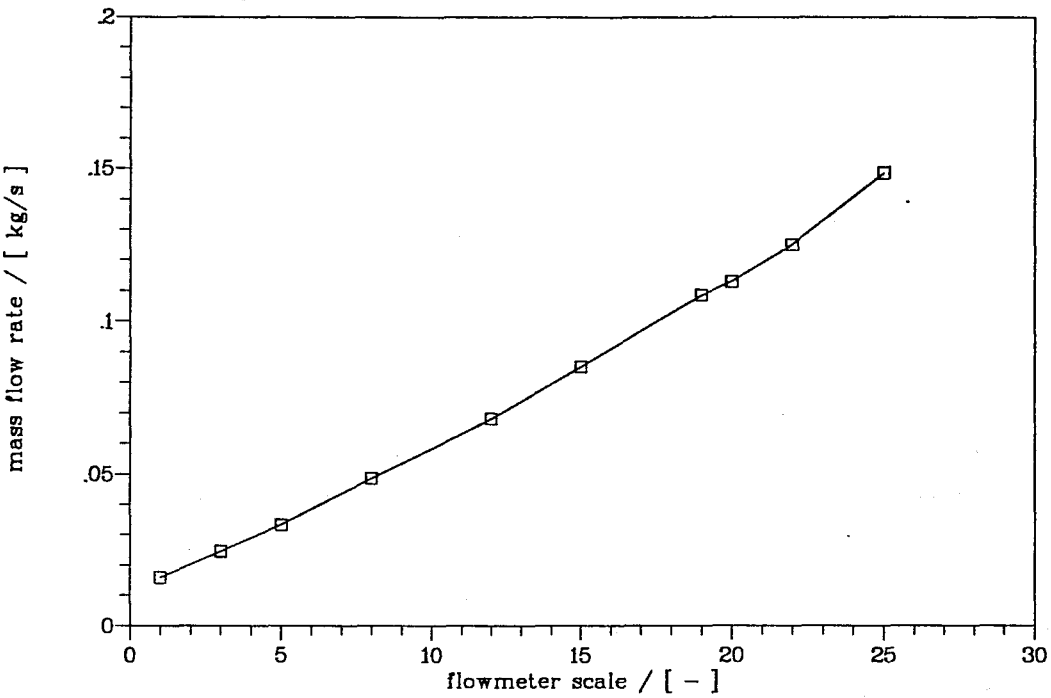

Figure C-4

Single-phase circuit flowmeter flow rate curve supplied by manufacturer for glycerol
fluid temperature at 150 C

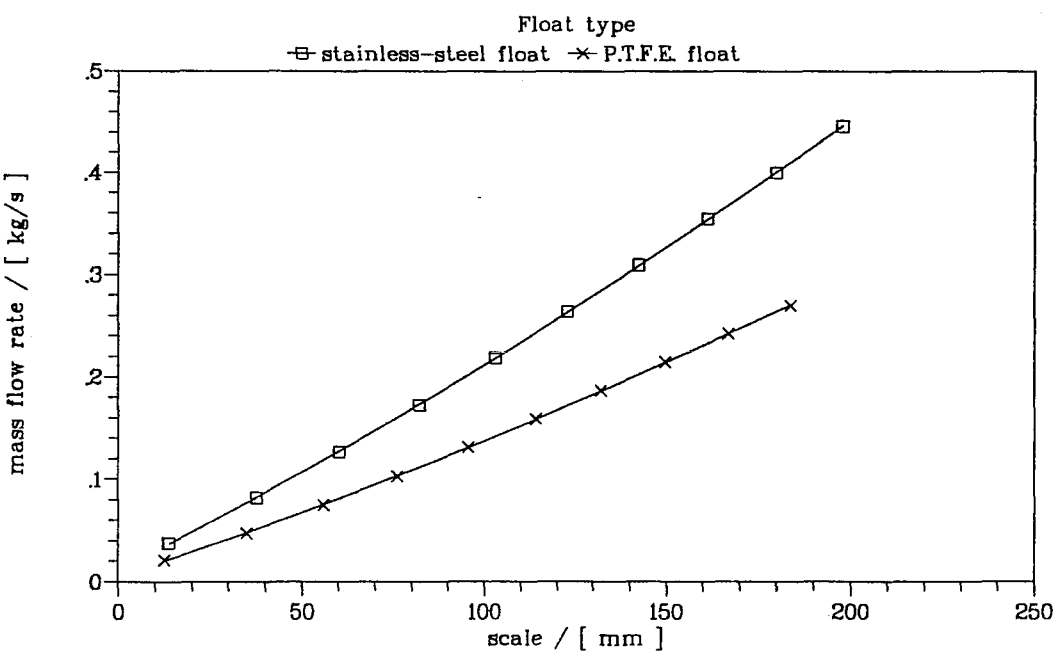

APPENDIX D

SINGLE PHASE HEAT BALANCE

D.1 Objectives

In heat transfer measurements, heat balance assessments are traditionally a means of an overall check on the instrumentation etc in the experimental apparatus and to quantify heat losses. In the present experiments, the electrical heating system for the quality-generation section is an important part of the overall system. Although the heating section and the calming section were covered by about 1.5 in. thick insulation, the copper blocks with the connecting power cables at the heating section were expected to be potential areas of heat loss. There was also concern over the test section because its end flanges were large relative to its length. In addition, the wall-thermocouple extensions that came out from the top flange could vitiate the insulation contact. In the experiment for non-equilibrium annular flow, the calming section was replaced by a separator, some straight sections and a sinter mixer. Heat balance tests for this set-up were also desirable.

Thus, as part of the present work, a number of single phase heat balance tests were carried out and are reported here.

D.2 Conditions of tests

Three main types of tests were carried out to check heat balances :

(a) Experiments with water in both circuits with electrical heat input into the water flowing in the two-phase (tube) circuit. Here, the heat input $\dot{Q}_1$ is known from the electrical measurements. Initially, all of this heat ($\dot{Q}_1$) is deposited in the water in the two-phase circuit but then some of this heat ($\dot{Q}_3$) is transferred via the test section to the water flowing in the annulus circuit. Of the original heat input, $\dot{Q}_1$, an amount $\dot{Q}_2$ remains in the two-phase circuit stream. $\dot{Q}_2$ and $\dot{Q}_3$ are determined by the relationships :

$$\dot{Q}_2 = \dot{M}_{tp} C_{pLtp} (T_{tpi} - T_{tpo}) \qquad \text{(D.2-1)}$$

$$\dot{Q}_3 = \dot{M}_a C_{pLa}(T_{ao} - T_{ai}) \qquad \text{(D.2-2)}$$

where $\dot{M}_{tp}$ and $\dot{M}_a$ are the mass rates of flow of water in the two-phase and annulus circuits respectively, C_{pLtp} and C_{pLa} the respective specific heat capacities. T_{tpi} is the water temperature entering the electrically heated section, T_{tpo} the water temperature leaving the test section on the tube side, and T_{ao} and T_{ai} the outlet and inlet temperatures of the annulus respectively. The percentage heat loss is defined as :

$$\left(\frac{\dot{Q}_1 - \dot{Q}_2 - \dot{Q}_3}{\dot{Q}_1}\right) \times 100 \qquad \text{(D.2-3)}$$

(b) Experiments with hot (150°C) glycerol on the annulus side and cold (unheated) water flowing through the two-phase (tube) circuit. Here, we define $\dot{Q}_1$ and $\dot{Q}_2$ as :

$$\dot{Q}_1 = \dot{M}_a C_{pLa}(T_{ai} - T_{ao}) \qquad \text{(D.2-4)}$$

$$\dot{Q}_2 = \dot{M}_{tp} C_{pLtp}(T_{tpo} - T_{tpi}) \qquad \text{(D.2-5)}$$

and the percentage heat loss is given by :

$$\left(\frac{\dot{Q}_1 - \dot{Q}_2}{\dot{Q}_1}\right) \times 100 \qquad \text{(D.2-6)}$$

(c) Experiments similar to (a) above but with the experimental arrangement corresponding to that used in the non-equilibrium experiments.

D.3 Results and discussions

The results from the three different series of tests are given in Tables D.3-1, D.3-2 and D.3-3 respectively. The results for water on the annulus side (see Tables D.3-1 and D3-3) show heat loses of around 5% whereas the results for glycerol show higher heat losses, of the order of 17-20%. This is not surprising in view of the much higher temperature involved. However, the heat losses are not likely to significantly affect the results of the experiments on evaporating annular flow, bearing in mind that the measurement methodology adopted where localised temperature differences are employed.

Table D.3-1 Heat balance tests with heat input at heating section and water flowing in annulus (annulus water mass flowrate at 0.0849 kg/s and temperature at 60°C)

Water mass flowrate in two-phase circuit / [kg/s]	Heat input at heating section Q_1 / [W]	Heat into water in two-phase circuit Q_2 / [W]	Heat into water in annulus, Q_3 / [W]	Heat loss $(Q_1 - Q_2 - Q_3)/Q_1$ x 100
0.00806	2500	1876	529	3.80
0.01407	4000	3356	465	4.48
0.01808	5000	4219	526	5.1

Table D.3-2 Heat balance tests on test section with glycerol flowing in annulus (glycerol mass flowrate at 0.3521 kg/s and temperature at 150°C at annulus inlet; water temperature at 27°C in two-phase circuit before flowmeter)

Water mass flowmeter in two-phase circuit / [kg/s]	Heat from glycerol Q_1 / [W]	Heat into water Q_2 / [W]	Heat loss $(Q_1 - Q_2)/Q_1$ x 100
0.01607	2083	1684	19.77
0.01207	1963	1580	19.52
0.00806	1827	1502	17.79

Table D.3-3 Heat balance tests on set-up for non-equilibrium annular flow experiment. (water mass flowrate in the annulus at 0.0849 kg/s and temperature at about 26°C)

Water mass flowmeter in two-phase circuit / [kg/s]	Heat input to heating section Q_1 / [W]	Heat into water in two-phase circuit Q_2 / [W]	Heat into water in annulus Q_3 / [W]	Heat loss $(Q_1 - Q_2 - Q_3)/Q_1$ x 100
0.01808	3000	2268	633	3.30
0.01407	3600	2667	770	4.53
0.01808	4000	3045	732	5.58

APPENDIX E

EFFICIENCY TEST ON WATER-STEAM SEPARATOR USING WATER AND AIR

For the non-equilibrium experiments, steam-water separation and recombination was employed. The geometry of the rig did not allow the separator to be designed fully to the recommendations of the manufacturer of the "Knitmesh" gauze which was used in the separator. Thus it was considered important to carry out tests on the separation efficiency and it was convenient to do this with air-water mixtures. An existing air-water facility at Harwell was used for this purpose. The porous wall (sinter) mixer section was mounted at the inlet of the separator so that water could be injected into an air stream to simulate the entry flow. Pressure transducers were fitted at positions between the sinter mixer and the separator and at the air outlet pipe of the separator. Plastic hoses were connected to the water and air outlet pipes and were open to atmosphere. The water from the water outlet pipe was collected.

Except the temperature, the test conditions were set close to the actual conditions in the experiment proper. The temperatures of the water and air supplies were at 18°C. The total mass flow rate was set close to 0.02 kg/s. The individual phase flow rates were varied to achieve different air mass fractions. The inlet pressure after the sinter varied with the air mass fraction in a similar way to the pressure at the heating section exit in the experiment proper.

The performance of the separator proved to be satisfactory. The test results are shown in the Table E-1 below. Efficiency more than 100% is obviously not correct, and is only due to error in the flow rate measurements.

Table E-1. Results of efficiency test on water-steam separator using water and air

Run number	Air flow rate / [kg/s]	Water flow rate / [kg/s]	Total mass flow rate / [kg/s]	Air mass fraction / [-]	Flow rate of water at outlet pipe / [kg/s]	Efficiency / [%]	Inlet pressure / [N/m^2]	Pressure drop / [N/m^2]
1	0.012	0.00804	0.02004	0.6	0.00804	100	210200	17000
2	0.01	0.0103	0.0203	0.49	0.0102	99	210800	15500
3	0.008	0.0121	0.0201	0.4	0.0122	101	190000	13700
4	0.006	0.0144	0.0204	0.29	0.0144	100	170200	10700
5	0.004	0.0166	0.0206	0.19	0.0167	101	150300	7500
6	0.002	0.0181	0.0201	0.1	0.0182	101	130100	2900

APPENDIX F

CALIBRATION OF FLUSH-MOUNTED CONCENTRIC PROBES

Flush-mounted concentric probes are widely used for liquid film thickness measurements. Since no analytical equation for the relationship between the liquid film thickness and the liquid conductance was available for the concentric probes used in the present experiments, calibration is necessary. A commonly used method is the "plug insert" technique, by which a static liquid film is generated by filling liquid in a gap formed between a plug and the wall of the probe housing. In view of the small bore pipe used in the experiment and the very thin liquid film (about 0.1 mm thickness) to be measured, the precision requirement in making the calibration plugs to generate such a thin liquid film could not be met. Subsequently, a scaled-up probe four times the size of the probe proper was made for calibration using precision made plugs. Based on the principle of geometric similarity and by choosing suitably defined non-dimensional variables for plotting the calibration data, a universal correlation for the concentric probe can be established.

F.1 Calibration equipment and procedure

There were ten PTFE plugs of different diameters used in this calibration. Each plug had channels near its bottom and top running radially to a central vertical channel. This arrangement would let excess liquid escape through the plug being inserted. While not in use, the plugs were always soaked in demineralised water to maintain their constant size in the "wet" state.

Each plug diameter at the axial position corresponding to the probe in the assembly was measured at two diametric positions 90° apart. The inside

diameter of the assembly was measured in the same way. The range of liquid film thickness that can be generated is 0.14 to 3.28 mm with an uncertainty of ±0.02 mm.

Potassium nitrate solutions were used for calibrating the scaled-up probe. The concentration ranged from 0.1 to 0.8 g/l , which made use of most of the voltage scale provided by the probe electric circuit (see Section 5.4 for a description of the probe electric circuit).

The probe electric circuit has a full voltage scale of 0-14V. Zero voltage corresponds to very small resistance in the liquid film and 14V represents infinite resistance or open circuit. A non-inductive variable resistance box was used to calibrate the probe electric circuit.

A Radiometer CDM83 conductivity meter was used for measurements of specific conductance. The meter was checked with sodium chloride solution, using a procedure recommended by the manufacturer. The results agreed well with the calibration data published in the operation manual.

The calibration of the scaled-up concentric probe involved the following steps. The plugs (which were soaked in beakers containing demineralised water), bottles of potassium nitrate solutions and the probe assembly (which was insulated with a surrounding plastic bag and filled with demineralised water) were left in a temperature-controlled bath to attain thermal equilibrium. When thermometer indicated that the required temperature was reached, calibration was started. Each plug was first wiped and shaken dry, then dipped in a beaker of prepared solution. The demineralised water in the probe assembly was discarded. The interior of the assembly was wiped dry and then filled with the prepared solution. During insertion of the plug, care was taken to make sure no bubble was trapped. Once the plug was in place, the "live" wire of the probe head (see figure 5.4-2 in Section 5.4) was connected to the centre pin of the concentric probe and the earth wire was connected to the metal body of the probe assembly. After the first voltage reading was taken, the plug was turned 90° and a second reading taken. Then the probe assembly and another plug were prepared in the same way as before for subsequent calibration.

The calibrations have been carried out at 30°C and 40°C.

F.2 Calibration results and predictions by numerical method

The voltage readings from the calibration of the scaled-up concentric probe was converted into conductance of the liquid film, using the calibration data of the probe electric circuit.

The results of the probe calibration are presented in figures F.2-1 to F.2-4. The variables for the non-dimensional plots in figures F.2-2 and F.2-4. are defined as follows :

$$G^* = \frac{G}{c(d_2 - d_1)} \qquad \text{(F.2-1)}$$

$$h = \frac{\delta}{d_2 - d_1} \qquad \text{(F.2-2)}$$

where G is the dimensional film conductance, c is the specific conductance of the liquid film, d_1 if the centre pin diameter of the concentric probe and d_2 is the outer diameter of the insulation.

The non-dimensional plots correlate the data quite well though the specific conductance appears to have a small residual effect. This may be due to stray capacity in the circuit.

Numerical prediction of the calibration data was carried out, using a computer package (PHEONICS) developed by CHAM Ltd. and licensed to Imperial College. This computer package employs finite difference methods to model transport processes by solving the general material, force and heat balance equations. Based on the analogy between temperature and potential field, this computer package can calculate the liquid film conductance. The basic equation that describes the potential field in the liquid film is

$$\nabla^2 V = 0 \qquad \text{(F.2-3)}$$

where the potential field, V, is analogous to a temperature field, T.

The tip of the concentric probe was assumed flat, being flush with an infinite plane wall. This assumption implied axisymetry and enabled the use of polar coordinates for a sector with its origin coinciding with the probe centre. Then equation F.2-3 can be written as

$$\frac{\partial^2 V}{\partial r^2}+\frac{1}{r}\frac{\partial V}{\partial r}+\frac{\partial^2 V}{\partial z^2}=0 \qquad \text{(F.2-4)}$$

The boundary conditions are as follows :

$$0 \le r \le \frac{d_1}{2} \quad \text{and} \quad z=0 \qquad V=10 \qquad \text{(F.2-5)}$$

$$\frac{d_1}{2} \le r \le \frac{d_2}{2} \quad \text{and} \quad z=0 \qquad \frac{\partial V}{\partial z}=0 \qquad \text{(F.2-6)}$$

$$\frac{d_2}{2} \le r \le r_\infty \quad \text{and} \quad z=0 \qquad V=0 \qquad \text{(F.2-7)}$$

$$z=\delta \qquad \frac{\partial V}{\partial z}=0 \qquad \text{(F.2-8)}$$

The value of 10 assigned to V in equation F.2-5 is arbitrary. A value of r_∞ in equation F.2-7 was set large enough to approximate infinity. In addition, the angle of the sector was set arbitrarily small. Once these arbitrary values were fixed, they were used in calculations for different δ.

After the potential field was solved, the total current, I, can be calculated by summing the current of each cell over the probe sector :

$$I = c\,\Sigma\left(A\frac{\Delta V}{\Delta z}\right) \qquad \text{(F.2-9)}$$

where c is the specific conductance of the liquid film and A the surface of a cell on the probe.

The resistance and conductance was then calculated by the following relation :

$$G=\frac{1}{R}=\frac{I}{V} \qquad \text{(F.2-10)}$$

The predictions of PHEONICS compares very well with the calibration data in figures F.2-2 and F.2-4. Since the prediction line coincides with the mean of the data points, it was subsequently used in converting the concentric probe signals into liquid film thickness trace.

The followings are polynomials fitted to the PHEONICS line :

$$h = 0.23791114G^* + 0.040041532G^{*2} + 0.12861566G^{*3} + 0.45472267G^{*4} \qquad 0 \le G^* < 0.4617 \qquad \text{(F.2-11.a)}$$

$$h = 37.633455G^* - 281.55124G^{*2} + 794.24897G^{*3} - 994.47977G^{*4} + 467.77149G^{*5} \qquad 0.4617 \le G^* < 0.6413 \qquad \text{(b)}$$

$$h = -1.2060856 + 2.4326923G^* \qquad 0.6413 \le G^* \qquad \text{(c)}$$

Figure F.2-1

Calibration data of a scaled up flush mounted concentric conductance probe (temperature at 30 C)

centre pin diameter : 3.2 mm ; outer diameter of insulation : 12.8 mm
concentration range of potassium nitrate solution : 0.1 to 0.8 grams/litre

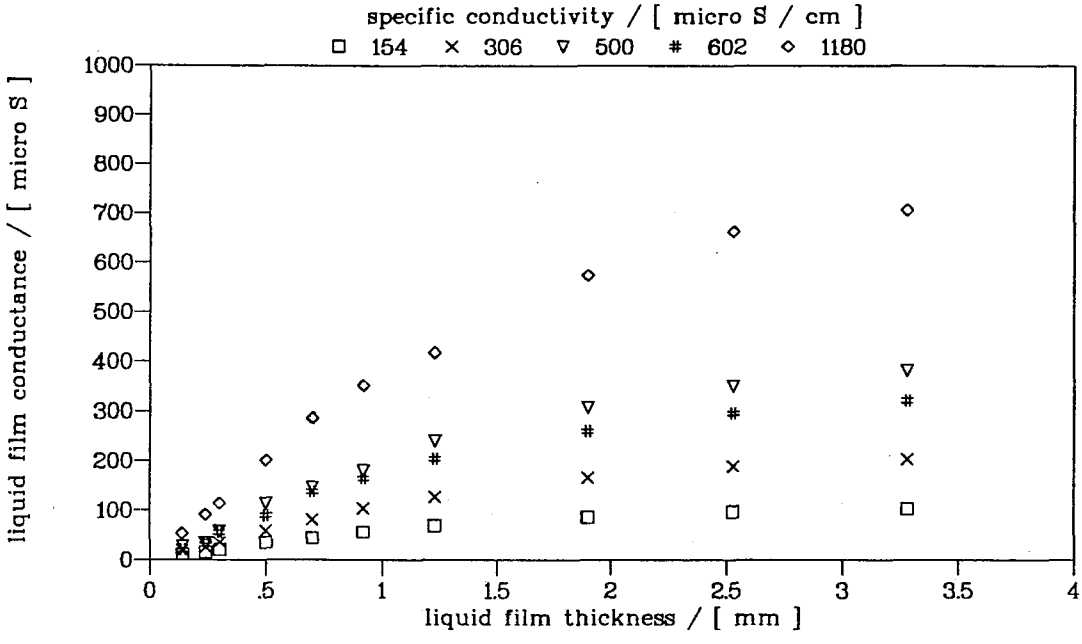

Figure F.2-2

Non-dimensionalised calibration data of a scaled up flush mounted concentric conductance probe (temperature at 30 C)

centre pin diameter : 3.2 mm ; outer diameter of insulation : 12.8 mm
concentration range of potassium nitrate solution : 0.1 to 0.8 grams/litre

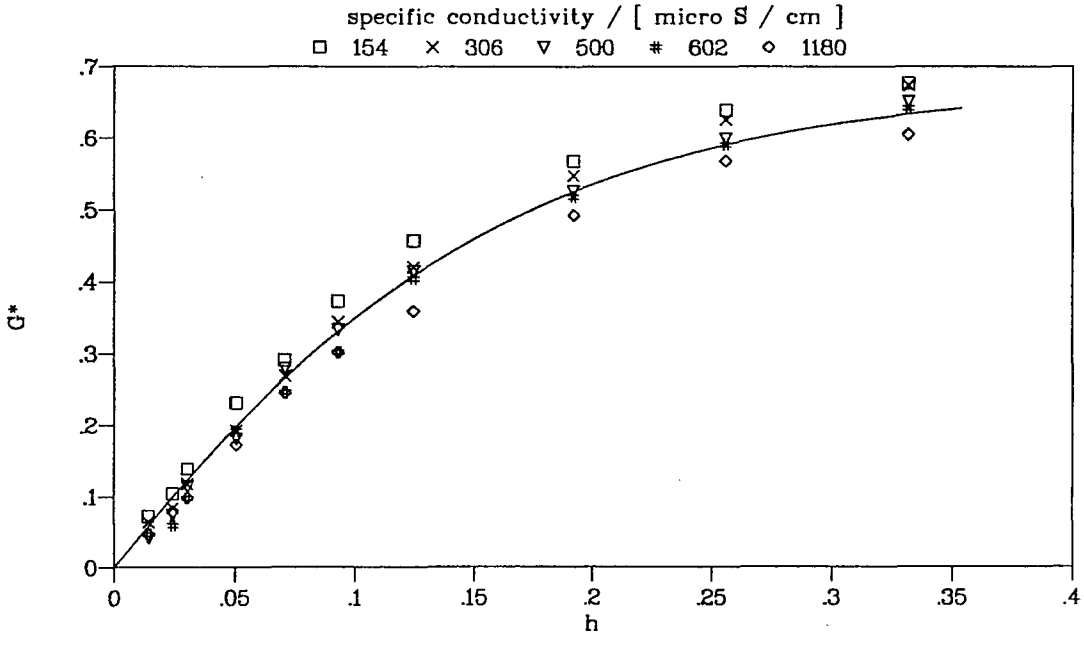

Figure F.2-3

Calibration data of a scaled up flush mounted concentric conductance probe (temperature at 40 C)

centre pin diameter : 3.2 mm ; insulation outer diameter : 12.8 mm
concentration range of potassium nitrate solution : 0.1 to 0.8 grams/litre

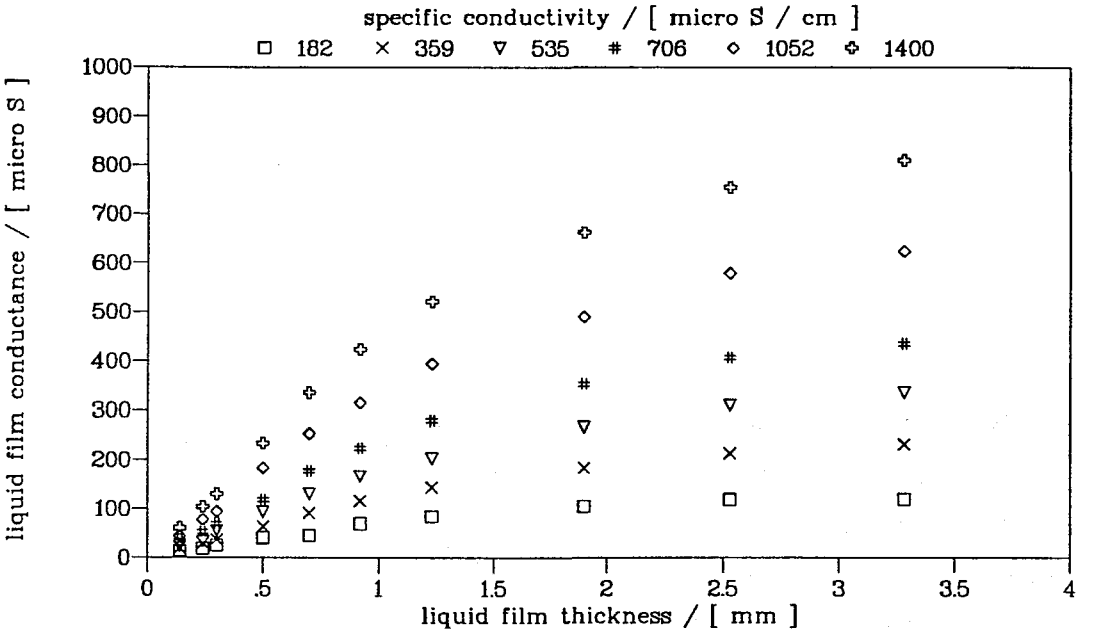

Figure F.2-4

Non–dimensionalised calibration data of a scaled up flush mounted concentric conductance probe (temperature at 40 C)

centre pin diameter : 3.2 mm ; insulation outer diameter : 12.8 mm
concentration range of potassium nitrate solution : 0.1 to 0.8 grams/litre

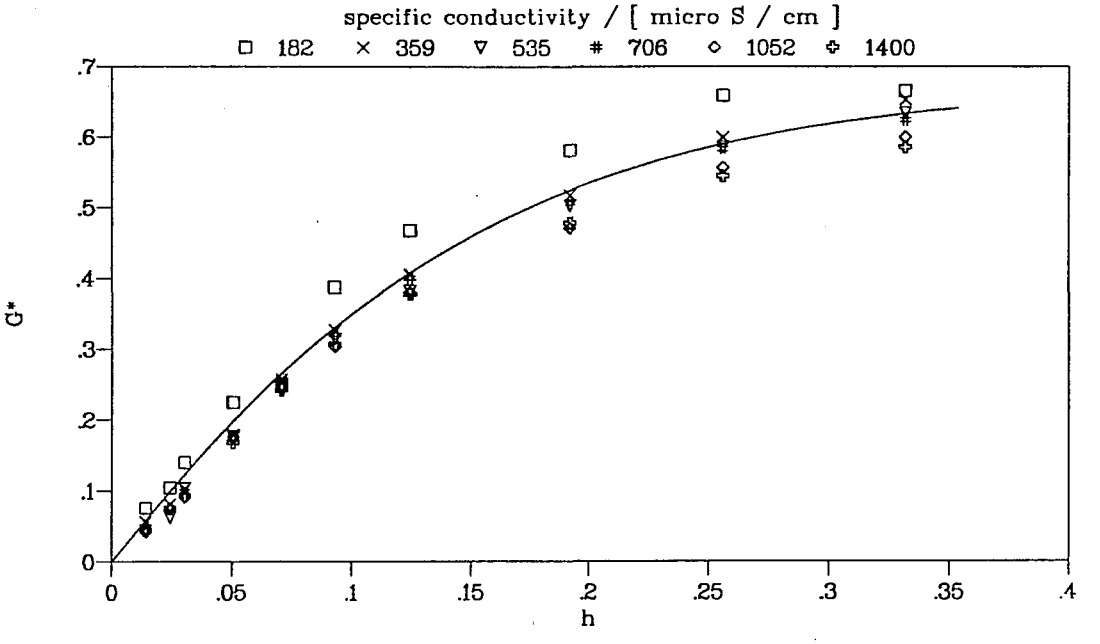

APPENDIX G

ASSESSMENT OF THE EFFECT OF INCONDENSIBLES ON CONDENSATION HEAT TRANSFER UNDER NORMAL OPERATION

The experimental data for both copper and nickel test sections showed a higher heat transfer coefficient in evaporation than in condensation. It was important to consider whether a contributory factor to this difference could be the influence of incondensible gases. Air, which was originally dissolved in the demineralised water, could be released during the evaporation process in the heating section and subsequently affect the condensation in the test section. Such dissolved air is likely since the demineralised water tank is open to atmosphere.

During condensation, there is a radial mass flow of vapour towards the interface. This mass flow carries incondensibles (air) which accumulate at the interface. This accumulation reaches equilibrium, when the incondensibles at the interface diffuse back towards the core at the same rate as they are carried towards the interface. While the total pressure remains constant radially, there is partial pressure gradients for both the steam and the incondensibles in a layer adjacent to the interface. The steam flows by bulk motion and by diffusion through this layer which presents resistance to the heat and mass transfer processes.

In contrast, there is no accumulation of incondensibles at the interface during evaporation. In fact, the steam generated at the interface carries the incondensibles towards the core where both are brought away by the axial bulk motion.

Therefore, the incondensibles presents resistance to mass and heat transfer in condensation but not in evaporation. The following analysis will consider the effect of incondensibles on condensation heat transfer.

G.1 Analysis

The mass transfer resistance can be modelled as an equivalent laminar layer at the interface. Gradients of partial pressure for both the vapour and the incondensibles are built up in this layer while the local total pressure remains constant. Mass transfer takes place under these pressure gradients by bulk motion and diffusion. The molar flux of the vapour towards the interface can be expressed as :

$$\dot{n}_G = \dot{n}\,\bar{y}_G - \mathcal{D}_{AG}\bar{c}\frac{d\bar{y}_G}{dy} \qquad \text{(G.1-1)}$$

In the above equation the first term on the right hand side represents the bulk flow, while the second term pertains to diffusion.

The bulk molar flux of the incondensibles towards the interface is counter-balanced by the incondensibles diffusing from the interface. Therefore, the total molar flux of the incondensibles is zero.

$$\dot{n}_A = 0 \qquad \text{(G.1-2)}$$

For constant local pressure across the horizontal plane, the following relations hold

$$p = p_G + p_A = \text{constant} \qquad \text{(G.1-3a)}$$

$$1 = \bar{y}_G + \bar{y}_A \qquad \text{(b)}$$

$$\frac{d\bar{y}_G}{dy} = -\frac{d\bar{y}_A}{dy} \qquad \text{(c)}$$

From the above equations, the molar flux of the vapour can be expressed as :

$$\dot{n}_G = -\mathcal{D}_{AG}\bar{c}\frac{d\bar{y}_G}{dy}\left(\frac{1}{1-\bar{y}_G}\right) \qquad \text{(G.1-4)}$$

Integrating the above equation between the interface ($y = 0$) and the edge of the equivalent laminar layer ($y = \delta_M$)

$$\dot{n}_G = \frac{\mathcal{D}_{AG}\bar{c}}{\delta_M}\ln\left(\frac{1-\bar{y}_{Gc}}{1-\bar{y}_{Gi}}\right) \qquad \bar{y}_{Gc} > \bar{y}_{Gi},\ \dot{n}_G < 0 \qquad \text{(G.1-5)}$$

For small concentration difference, equation G.1-5 reduces to

$$\dot{n}_G = \mathcal{D}_{AG}\frac{\Delta c_G}{\delta_M} = \beta_{AG}\Delta c_G \qquad \text{(G.1-6)}$$

where $\beta_{AG} = \mathcal{D}_{AG}/\delta_M$ is the mass transfer coefficient which can be estimated from the usual equation :

$$Sh_G = 0.023 Re_G^{0.8} Sc_G^{0.3} \qquad \text{(G.1-7)}$$

where

$$Sh_G = \frac{\beta_{AG} D_i}{\mathcal{D}_{AG}} = \frac{D_i}{\delta_M} \qquad \text{(G.1-8)}$$

$$Sc_G = \frac{\eta_G}{\rho_G \mathcal{D}_{AG}} \qquad \text{(G.1-9)}$$

The sensible heat transfer in the resistance layer can be modelled in a similar fashion. The sensible heat flux consists of a conductive term and a convective term.

$$\dot{q}_{sen} = -\lambda_G \frac{dT}{dy} + \dot{n}_G \mathcal{M}_G C_{pG}(T - T_i) \qquad \text{(G.1-10)}$$

After integrating from $y = 0$ to $y = \delta_T$

and using $\alpha_G = \lambda_G/\delta_T$

$$\dot{q}_{sen} = \frac{a}{1 - e^{a}}\alpha_G(T_C - T_i) = \alpha'_G(T_C - T_i) \qquad \text{(G.1-11)}$$

$a < 0$, $\dot{q}_{sen} < 0$

where

$$a = \frac{\dot{n}_G \mathcal{M}_G C_{pG}}{\alpha_G} \qquad \text{(G.1-12)}$$

The total heat flux at the interface is a sum of the sensible heat and latent heat transferred.

$$\dot{q} = \dot{q}_{sen} + \dot{q}_{lat} = \alpha'_G(T_C - T_i) + \dot{n}_G \mathcal{M}_G h_{LG} \qquad \text{(G.1-13)}$$

δ_T is defined in a similar way as in the mass transfer case, that is

$$\dot{q}_{sen} = \frac{\lambda_G \Delta T}{\delta_T} = \alpha_G \Delta T \qquad \text{(G.1-14)}$$

For the turbulent core, the well-known Dittus-Boelter equation can also be applied.

$$Nu_G = 0.023\, Re_G^{0.8} Pr_G^{0.3} \qquad \text{(G.1-15)}$$

where

$$Nu_G = \frac{\alpha_G D_i}{\lambda_G} = \frac{D_i}{\delta_T} \qquad \text{(G.1-16)}$$

It can be seen that

$$\frac{\delta_M}{\delta_T} = \left(\frac{Pr_G}{Sc_G}\right)^{0.3} \qquad \text{(G.1-17)}$$

Ignoring any fouling on both sides of the copper tube in the test section, the overall heat transfer coefficient between the interface and the bulk in the annulus can be expressed as:

$$\frac{1}{U'} = \frac{D_i}{\alpha_a D_o} + \frac{D_i \ln(D_o/D_i)}{2\lambda_w} + \frac{1}{\alpha_{tp}} \qquad \text{(G.1-18)}$$

therefore

$$\dot{q}' = U'(T_i - T_a) \qquad \text{(G.1-19)}$$

Fully developed condition is considered here. In the annulus, the single-phase heat transfer coefficient recommended by Wiegand (1945) is used :

$$Nu_a = \frac{\alpha_a D_e}{\lambda_L} = 0.023\, Re_a^{0.8} Pr_a^{0.4} \left(\frac{D_2}{D_1}\right)^{0.45} \qquad \text{(G.1-20)}$$

The convective part of the Chen correlation is used for the two-phase heat transfer coefficient.

At steady state,

$$\dot{q} = \dot{q}' \qquad \text{(G.1-21)}$$

G.2 Calculation

To effect the calculation, some variables of the above equations are substituted with numerical values based on operating conditions, of which a set is given below.

(a) Temperature in storage tank at 50°C.
(b) Total pressure in test section at 1 atm.
(c) Total mass flux of two-phase at 242 kg/m^{2}s.
(d) Quality in test section at 0.5.
(e) Bulk temperature of water in annulus at 60°C.
(f) Mass flowrate of water in annulus at 0.0849 kg/s.

Data for properties are as follows :

(i) The proportionality constant, $\mathcal{H}$, of Henry's Law, i.e. $p_A = \mathcal{H}x_A$, for air in water is 9.46x10^4 atm at 50°C and 1 atm (Perry 1973).
(ii) Humidity in the plenum of the storage tank is 0.09 kg water / kg air at 50°C and 1 atm (Perry 1973).
(iii) Diffusivity of water vapour through air at 373.15 K and 1 atm is 36.4x10^{-6} m^2/s. (Incropera 1985).
(iv) Thermal conductivity of copper is 377 W/mK (Coulson 1977).
(v) Molecular weight of water and air are 18 and 28.84 kg/kmol respectively.

From (ii) and (v), p_A = 0.874 atm.

From (i), x_A = 9.24x10^{-6}.

Assuming the air is released at the same rate as evaporation, $\bar{y}_{AC}$ = 9.24x10^{-6}.

As $\bar{y}_{AC} \ll \bar{y}_{GC}$, the core temperature is assumed saturated for water vapour at 1 atm and 373.15 K.

For such low pressure in the test section, the total molar concentration can be found using the ideal gas law. Therefore $\bar{c} = p/(\mathcal{R}T_{sat})$ = 3.27x10^{-2} kmol/m^3.

For a range of assumed values of T_i, the values of the heat transfer rate from the vapour to the interface $\dot{q}$ and the heat transfer rate from the interface to the cooler $\dot{q}'$ were calculated. The results are shown in the following table :

T_i/ [K]	373.1498	373.1497	373.1496
$\dot{q}$ / [W/m^2]	174915.2	-173648.0	-367613.0
$\dot{q}'$ / [W/m^2]	-243418.6	-243418.0	-243417.6

The solution for $\dot{q} = \dot{q}'$ is obtained at a value of T_i between 373.1497 and 373.1496. It should be clear that $T_i \approx T_{sat} = 373.15K$, which means that the thermal resistance at the interface (due to incondensibles) is negligible. Therefore, it can be concluded that the incondensibles did not cause the difference in the heat transfer coefficients in evaporation and condensation in the annular flow experiments.

APPENDIX H

FORMATION OF BUBBLES IN A LIQUID FILM : ANALYSIS OF EXPERIMENTS OF HEWITT ET AL (1963)

Hewitt et al (1963) described an experiment using an annular channel with a vertical upflow of saturated water and steam. Their aim was to investigate burn-out and nucleation in climbing film flow. The channel was formed by a centre stainless steel tube and an outer glass cylinder. The liquid (water) was introduced onto the centre tube through a porous wall (sinter) section of the same outside diameter. The steam was introduced into the annular channel separately. The annular channel was enclosed by another glass cylinder. Hot air was passed through the outer annulus to prevent condensation on the inside wall of the inner glass cylinder, thus facilitating observation. The flow was saturated and fully developed at the point where observations were made. High speed cine film (4000 frames/s) was taken during an experimental run and it was this high speed cine film which was analysed during the present work to elucidate the process of nucleate boiling and bubble formation in annular flow.

A cine film analyser was used to measure bubble size and frequency during the nucleation process. Typical sequences of bubble growth (from the first observed appearance of the bubble to bursting), as obtained from the cine film is shown in figure H-1. The bubble burst size averaged between 1 to 2 mm in diameter. The observed bubble frequency was in the order of 500 s^{-1} at one active nucleation site.

The liquid film thickness was not measured in the Hewitt et al (1963) experiments. However, measurements of liquid film flow rate were made. One of the surprising results to emerge from the analysis reported in Chapter 3 was that the bubble burst diameter needed to be an order of magnitude greater than the film thickness to obtain consistency. Thus, to establish whether the bubble burst size was consistent in the Hewitt et al experiments,

Figure H-1

Observed bubble growth and translation in climbing liquid film

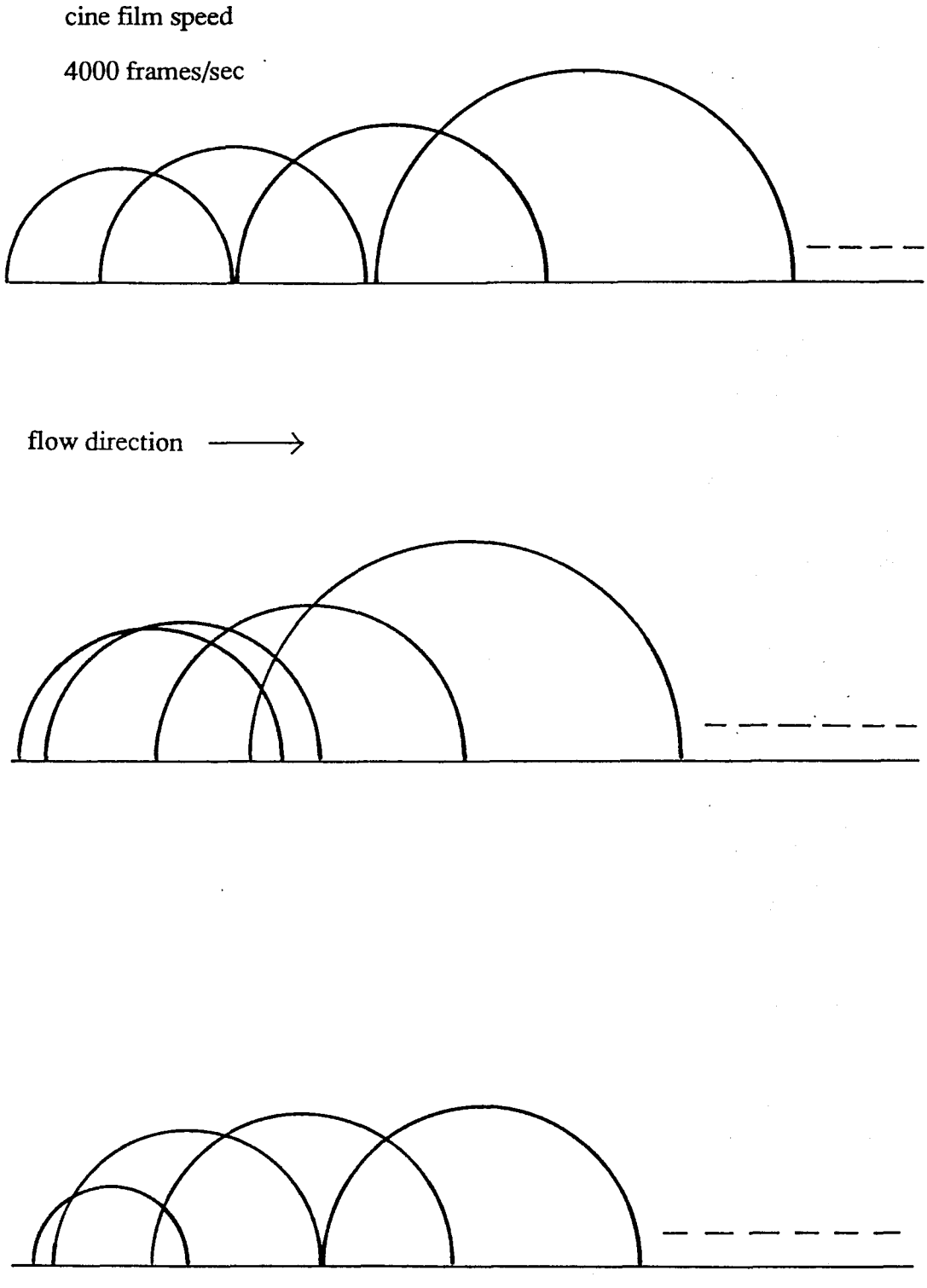

it was necessary to calculate the thickness of the liquid film. Here, a theory due to Hewitt (1964) for single-phase flow in annuli with one rough and one smooth wall is invoked; the theory had already been applied to annular flow in an annulus by Hewitt et al (1965) where the liquid film was on the outer surface only.

H.1 Theory

The model being considered is represented in figure H.1-1. Liquid entrainment was ignored and the interface was assumed flat. The shear stress is assumed zero at a cylindrical plane in the radial direction where the gas-phase velocity is maximum. This plane divides the annular channel into two regions. That nearer to the centre tube is called region 1, and region 2 is on the other side of the plane. The equivalent diameters of these regions are defined as follows:

$$D_{e1} = \frac{2[r_m^2 - (r_1 + \delta)^2]}{r_1 + \delta} \qquad \text{(H.1-1)}$$

$$D_{e2} = \frac{2(r_2^2 - r_m^2)}{r_2} \qquad \text{(H.1-2)}$$

In terms of these equivalent diameters, the Reynolds numbers are :

$$Re_1 = \frac{\rho_G U_1 D_{e1}}{\mu_G} \qquad \text{(H.1-3)}$$

$$Re_2 = \frac{\rho_G U_2 D_{e2}}{\mu_G} \qquad \text{(H.1-4)}$$

Hewitt used the Kao equation to calculate the friction factor in the region without the liquid film. For region 2 in this case, the Kao equation is in the form of

$$f_2 = 0.0007 + 0.0625 Re_2^{-0.32} \qquad \text{(H.1-5)}$$

If region 1 has no liquid film, an equation similar to equation H.1-5 applies :

$$f_{s1} = 0.0007 + 0.0625 Re_1^{-0.32} \qquad \text{(H.1-6)}$$

The Wallis' (1970) correlation for interfacial friction factor was developed from data of annular flow in round tubes. It was assumed applicable in an annulus. Assuming uniform shear stress in the liquid film and substituting equivalent diameter for diameter :

$$f_1 = f_{s1}\left(1 + 360\frac{\delta}{D_{e1}}\right) \qquad \text{(H.1-7)}$$

The friction factors in the Kao equation and the Wallis' correlations followed the conventional definition. In region 1, the friction factor can be expressed as :

$$\tau_1 = f_1 \rho_G U_1^2 \qquad \text{(H.1-8)}$$

Assuming the frictional component of the total pressure drop is much larger than the acceleration and gravitational components added together, then

$$\frac{f_1}{f_2} = \frac{D_{e1} U_2^2}{D_{e2} U_1^2} \qquad \text{(H.1-9)}$$

The average velocity of the gas phase is related to its mass flowrate as follows :

$$U = \frac{\dot{M}_G}{\pi[r_2^2 - (r_1 + \delta)^2]\rho_G} \qquad \text{(H.1-10)}$$

A mass balance for the gas-phase can show that

$$U[r_2^2 - (r_1 + \delta)^2] = U_1[r_m^2 - (r_1 + \delta)^2] + U_2[r_2^2 - r_m^2] \qquad \text{(H.1-11)}$$

Hewitt (1964) integrated the von Karman 'deficiency' velocity profile in the gas-phase for each region to obtain the mean gas velocities in their respective regions. The ratio of these mean velocities is

$$\frac{U_2}{U_1} = \frac{\frac{\sqrt{f_1}}{k}\left[\frac{r_m + 3(r_1 + \delta)}{2r_m + 2(r_1 + \delta)}\right] + 1}{\frac{\sqrt{f_2}}{k}\left[\frac{r_m + 3r_2}{2r_m + 2r_2}\right] + 1} \qquad \text{(H.1-12)}$$

The average liquid film thickness is small compared with the centre tube diameter. Integrating von Karman's universal velocity profile over a flat plate, one can obtain the film flowrate equation, which, in non-dimensional form, is as follows :

$$\dot{M}_{LF}^{+} = \frac{\delta^{+2}}{2} \qquad \delta^{+} \leq 5 \qquad \text{(H.1-13a)}$$

$$\dot{M}_{LF}^{+} = 12.5 - 8\delta^{+} + 5\delta^{+}\ln\delta^{+} \qquad 5 < \delta^{+} \leq 30 \qquad \text{(b)}$$

$$\dot{M}_{LF}^{+} = -64 + 3\delta^{+} + 2.5\delta^{+}\ln\delta^{+} \qquad 30 < \delta^{+} \qquad \text{(c)}$$

Given the mass flowrates of both phases, the size of the channel and the saturation temperature or pressure, the above set of equations provides a model for climbing liquid films on the outer surface of the centre tube in an annulus. The variable of interest here is the average liquid film thickness.

H.2 Results and discussion

It was felt that it was necessary to verify Hewitt's original model with the data of Hewitt et al (1965), that is the case of liquid film flowing on the inner surface of the outer tube. Pressure drop predictions of the model is shown to have good agreement with data in figure H.2-1 . The range of mass flowrate for each phase was quite wide in the data set. However, the resulting range of vapour mass fraction fell on the high quality region. Figure H.2-2 showed that the predicted liquid film thickness correlates quite well with quality regardless of the mass flowrate of each phase.

The satisfactory performance of Hewitt's model has lent some confidence to the prediction of liquid film thickness by the modified model, which was then used in the following calculation .

Data available :

(a) Saturated pressure at 1 atm.
(b) Outside diameter of centre tube is 0.5 in.
(c) Inside diameter of the inner glass cylinder is 0.866 in.
(d) Mass flowrates of water and steam are 50 and 50 lb/hr respectively.

The calculated mean liquid film thickness is 0.127 mm. Bearing in mind that negligible liquid entrainment was assumed, this result only represents an upper bound.

Therefore, based on this analysis, the observed bubble burst size is much larger than the mean liquid film thickness and this is consistent with the finding in Chapter 3.

Figure H.1-1

Climbing film on centre tube in an annular channel

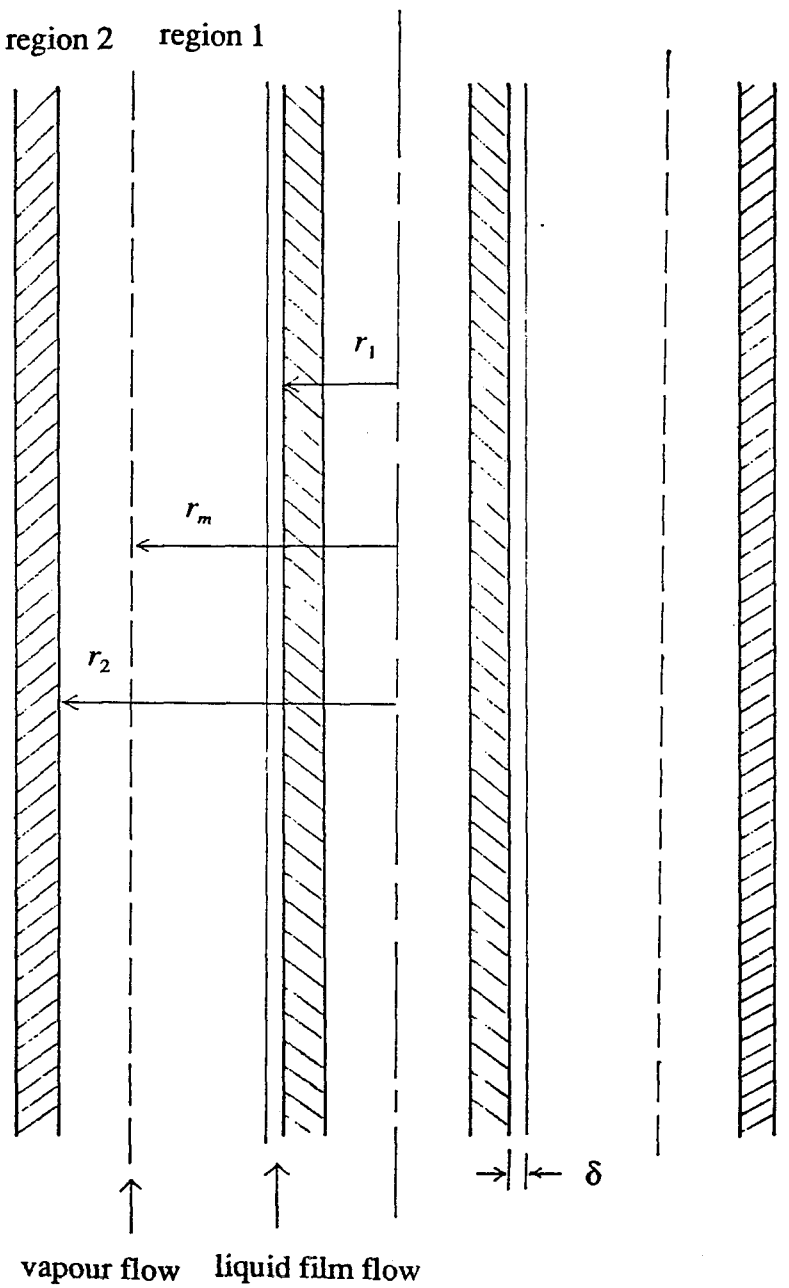

Figure H.2-1

Prediction of pressure gradient using Hewitt's model compared with experimental data for air-water flow in an annular channel
liquid film on the inner surface of the outer tube

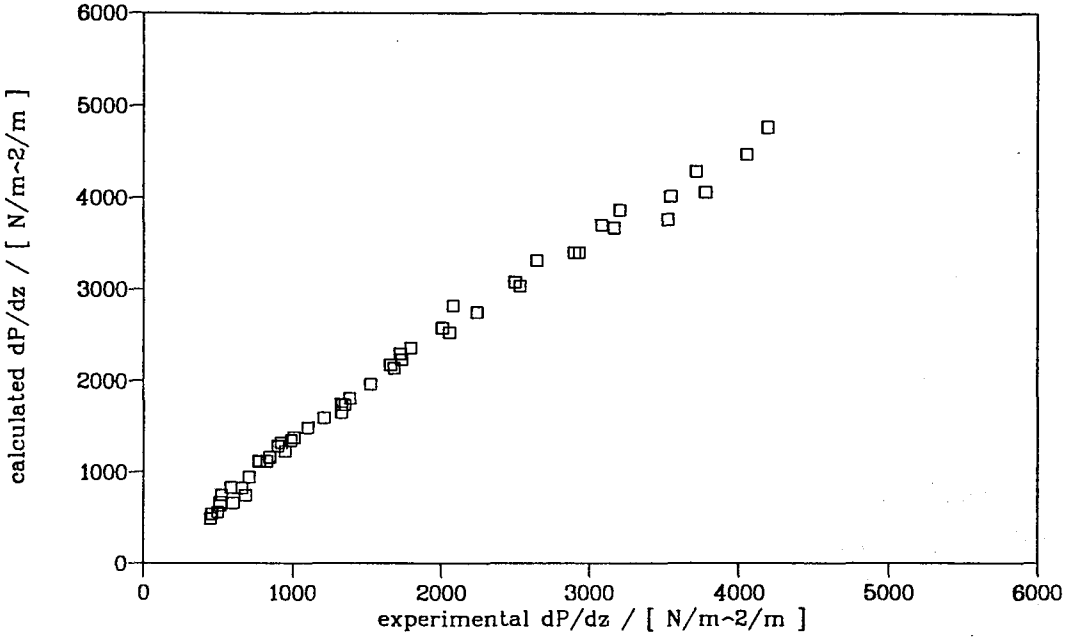

Figure H.2-2

Prediction of liquid film thickness using Hewitt's model
liquid film on the inner surface of the outer tube
of the the annular channel

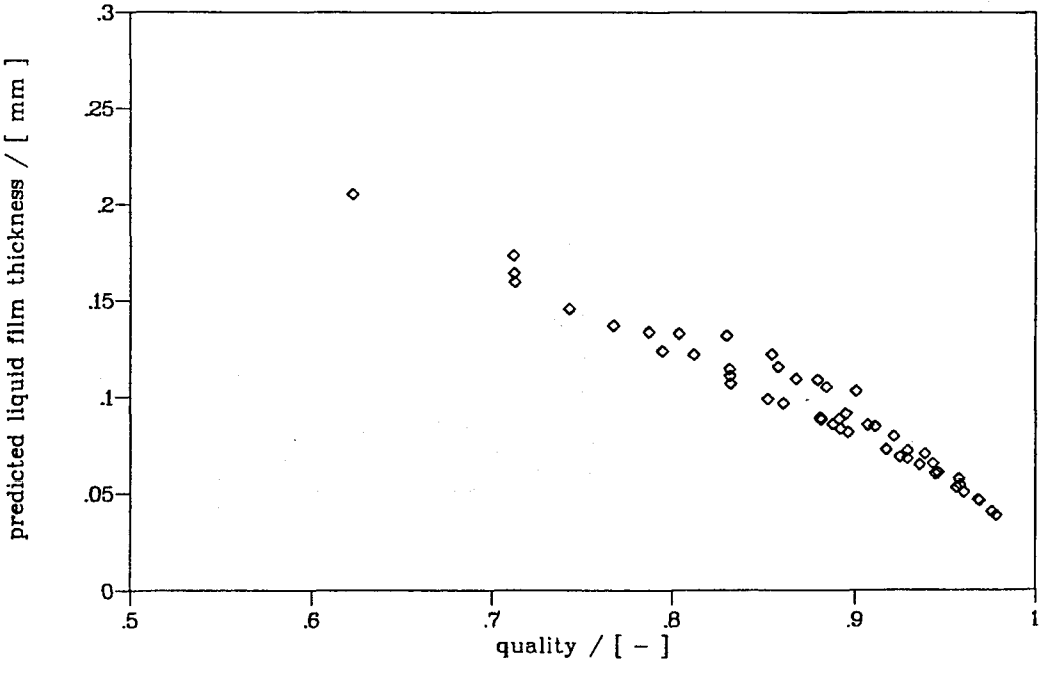

REFERENCES

Al-Hayes R.A.M. and Winterton R.H.S.(1981). Bubble Diameter on Detachment in Flowing Liquids, Int.J. Heat Mass Transfer, 24(2),223-230

Anderson G.H. Haselden G.G. and Mantzouranis B.G. (1961). Two-phase (Gas-Liquid) Flow Phenomena-III, The Calculation of Heat Transfer in a Vertical Long-tube Evaporator. Chem. Eng. Sci. 16,222-230

Aounallah Y., Kenning D.R.B., Whalley P.B. and Hewitt G.F.(1982). Boiling Heat Transfer in Annular Flow, Proc. 7th Int. Heat Transfer Conf.,Munich, paper FB3

Asali J.C.(1984). Entrainment in Vertical Gas-Liquid Annular Flows, PhD. Thesis, University of Illinois, Urbana, Illinois, U.S.A.

Bandel J. (1973). Pressure Drop and Heat Transfer in the Vaporation of Boiling Refrigerants Flowing through a Horizontal Tube. Ph.D. Thesis, 140pp. U. Karlsruhe.

Bankoff S.G. (1958). Entrapment of Gas in a Spreading of a Liquid over a Rough Surface. A.I.Ch.E. Journal 4,24.

Bendat J.S. and Piersol A.G.(1971). Random Data: Analysis and Measurement Procedures, Published by Wiley-Interscience

Benn D.N.(1972). Ab Experimental Capacitance Liquid Film Thickness Monitor, Operating Instructions and Circuit Details, Rept. AERE-R7155, UKAEA

Bennett D.L. and Chen J.C.(1980). Forced Convective Boiling in Vertical Tubes for Saturated Pure Components and Binary Mixtures, AIChE J. 26(3),454-461

Bennett D.L. and Hertzler B.L.(1980). The Suppression of Saturated Nucleate Boiling by Forced Convective Flow, AICHE Symp. 76(199),91-103

Bennett D.L.(1976). A Study of Internal Forced Convective Boiling Heat Transfer For Binary Mixtures, PhD. Thesis, Lehigh University, Pennsylvania,USA

Berensen P.J.(1962). Experiments on Pool Boiling Heat Transfer, Int. J. Heat Mass Transfer, 5,985

Bergles A.E. and Rohsenow W.M. (1964). The Determination of Forced-Convection Surface-Boiling Heat Transfer. J. of Heat Transfer. Trans. ASME Ser. C., 86, 365-372.

Blangetti F. and Krebs R.(1981). Film Condensation and Evaporation in Vertical Tubes with Superimposed Vapour Flow, ICHMT Int. Seminar on Advancement in Heat Exchangers, Dubrovnik, Yugoslavia

Brown W.T.(1967). Study of Flow Surface Boiling, Phd Thesis, Mechanical Engineering Department, M.I.T.

Burns A.D., Wilkes N.S.,Jones I.P. and Kightley J.R. (1986). FLOW 3D : Body Fitted Coordinates. AERE Report 12262. HMSO London.

Butterworth D.(1974). A Comparision of Some Void-Fraction Relationship, AERE-M 2619

Cerza M. and Sernas V.(1985). A Bubble Growth Model for Nucleate Boiling in Thin,Falling,Superheated,Laminar,Water Films, Int.J. Heat Mass Transfer, 28 (7),1307-1316

Chawla J.M. (1967). Wärmeübergang und Druckabfall in waagerechten Rohren dei der Strömung von verdampfenden Kältemitteln. Forsch Hft. Ver. Dt. Ing. 523.

Chen J.C.(1963). A Correlation for Boiling Heat Transfer to Saturated Fluids in Convective Flow, ASME-AIChE Heat Transfer Conf., Boston, Paper 63-HT-34

Chen J.C.(1966). Correlation for Boiling Heat Transfer to Saturated Fluids in Convective Flow, I&EC Process Design & Development, 5(3).

Cole R. and Shulman H.L.(1966). Bubble Growth Rates at High Jakob Numbers, Int.J. Heat Mass Transfer, 9,1377-1390, Pergamon Press.

Collier J.G. (1983). Heat Exchanger Design Handbook 2 : Fluid Mechanics and Heat Transfer, Section 2.7.2. Hemisphere Publishing Corporation.

Collier J.G. (1981). Convective Boiling and Condensation. 2nd Ed. McGraw-Hill Book Company.

Cooper M.G. and Lloyd A.J.P.(1969). The Microlayer in Nucleate Pool Boiling, Int.J. Heat Transfer, 12,895-913, Pergamon Press.

Cooper M.G. and Vijuk R.M.(1970). Bubble Growth in Nucleate Pool Boiling, Proceedings of the 4th International Heat Transfer Conference, Paris-Versailles, V.B 2.1

Cooper M.G.(1969). The Microlayer and Bubble Growth in Nucleate Pool Boiling, Int.J. Heat Mass Transfer, 12,915-933, Pegamon Press.

Cooper M.G.(1983). Heat Flow Rates in Saturated Nucleate Pool Boiling -A Wide-Ranging Examination Using Reduced Properties, Advances in Heat Transfer, 16,157-239.

Coulson J.M. and Richardson J.F. (1977). Chemical Engineering. Vol. 1. 3rd edition. Pergamon Press.

Davis E.J. and Anderson G.H.(1966). The Incipience of Nucleate Boiling in Forced Convection Flow, A.I.Ch.E. Journal, 12 (4),774-780.

Deissler R.G. (1952). Analytical and Experimental Investigation of Adiabatic Turbulent Flow in Smooth Tube, National Advisory Committe for Aeronautics Report Number NACA -TN-2138

Dengler C.E. and Addoms J.N.(1956). Heat Transfer Mechanism for Vaporization of Water in a Vertical Tube, Chemical Engineering Progress Symp. 52(18).

Dergarabedian P.(1953). Paper No. 53-SA-10, Heat Transfer and Fluid Mechanics Institute, California

Dicksen A.J., Gouse S.W. (1966). Heat Transfer and Fluid Flow inside a Horizontal Tube Evaporator. Phase III Report DSR 9649-3

van Driest E.R. (1956). On Turbulent Flow Near a Wall. Journal of the Aeronautical Sciences.

Dukler A.E.(1959). Dynamics of Vertical Falling Film Systems, Chemical Engineering Progress, 55(10).

Dwyer O.E.(1976). Boiling Liquid-Metal Heat Transfer, Monograph Series on Nuclear Science and Technology, Published by American Nuclear Society

Forster H.K. and Zuber N.(1954). Growth of a Vapour Bubble in a Superheated Liquid, Journal of Applied Physics, 25(4).

Forster H.K. and Zuber N.(1955). Dynamics of Vapour Bubbles and Boiling Heat Transfer, A.I.Ch.E. Journal, 1(4),531-535

Fujita T. and Ueda T.(1978). Heat Transfer to Falling Liquid Films and Film Breakdown-II,Saturated Liquid Films with Nucleate Boiling, Int.J. Heat Mass Transfer, 21,109-118

Fyodorov M.V. and Klimenko V.(1989). Vapour Bubble Growth in Boiling Under Quasi-Stationery Heat Transfer Conditions in a Heating Wall, Int. J. Heat Transfer, 32(2),227-242.

Glycerine Producers' Association. (1975). Physical Properties of Glycerine and Its Solutions.

Govan A.H., Hewitt G.F., Owen D.G. and Bott T.R. (Sept. 1988). An Improved CHF Modelling Code. 2nd National U.K. Heat Transfer Conference, Glasgow. Paper No. C175

Guerrieri S.A. and Talty R.D.(1966). A Study of Heat Transfer to Organic Liquid in Single-Tube,Natural-Circulation,Vertical-Tube Boilers, Chem. Eng. Prog. Symp. Series, 52(18),69-77.

Gungor K.E. and Winterton R.H.S.(1987). Simplified General Correlation for Saturated Flow Boiling and Comparisons of Correlations with Data, Chem Eng Res Des, 65.

Gungor K.E., Winterton R.H.S. (Sept 1985). A General Flow Boiling Correlation. 15th HTFS Res. Symp. Univ. Sussex U.K. Paper RS617, 553-567

Hall Taylor N.S., Hewitt G.F. and Lacey P.M.C.(1963). The Motion and Frequency of Large Disturbance Waves in Annular Two-Phase Flow of Air-Water Mixtures, Chem. Engng. Sci. 18,537-52

Hewitt G.F. (1982). Correlations for Deposition and Entrainments Rates, in Handbook of Multiphase Systems, Editer-in-Chief Hetsroni G. Chapter 2.2.4.4

Hewitt G.F. and Hall-Taylor N.(1970). Annular Two-Phase Flow, Pergamon Press, Oxford.

Hewitt G.F. and Lacey P.M.C.(1965). The Breakdown of the Liquid Film in Annular Two-phase Flow, Int.J. Heat Mass Transfer, 18,781-791

Hewitt G.F.(1961). Analysis of Annular Two-Phase Flow Application of the Dulker Analysis to Vertical Upward Flow in a Tube, AERE-R3680

Hewitt G.F.(1964). Interpretation of Pressure Drop Data from an Annular Channel, A.E.R.E. R4340

Hewitt G.F.(1978). Measurement of Two Phase Flow Parameters, Academic, New York.

Hewitt G.F., Kearsey H.A., Lacey P.M.C. and Pulling D.J.(1965). Burnout and Nucleation in Climbing Film Flow, Int.J. Heat Mass Transfer, 8,793-814

Hewitt G.F., King R.D.A. and Lovegrove P.C. (1962). Techniques for Liquid Film and Pressure Drop Studies in an Annular Two-phase Flow. UKAEA Report No. AERE-R3921.

Hodgson A.S. (1969). Hysteresis Effects in Surface Boiling of Water. J. Heat Mass, 91,160-162.

Hooper F.C. and Abdelmessih A.H.(1966). The Flashing of Liquids at a Higher Superheats, Proc. 3rd Int. Conf. Heat Transfer.

Hus Y.Y. and Graham R.W.(1963). A Visual Study of Two-phase Flow in a Vertical Tube with Heat Addition, NASA Technical Note D-1564

Idelchik I.E. (1986). Handbook of Hydraulic Resistance. 2nd edition. Hemisphere Publishing Corporation.

Incropera F.P. DeWitt D.P. (1981). Fundamentals of Heat and Mass Transfer. 2nd edition, John Wiley & Sons.

Jackson C. (1976). A Wheatstone Bridge Burnout Detector. UKAEA Harwell, Report No. AERE-R8363

von Karman T. (1930). Mechanical Theory of Turbulence, 3rd Int. Cong. Appl. Mech., Stockholm, Vol.1 p.85

von Karman T.(1939). The Analogy Between Fluid Friction and Heat Transfer, Trans. ASME, 61,705-710

Kenning D.B.R. and Cooper M.G.(1965). Flow Pattern Near Nuclei and the Initiation of Boiling During Forced Convection Heat Transfer, Paper 11 presented at the Symp. on Boiling Heat Transfer in Steam Generating Units and Heat Exchangers held in, Manchester, IMechE (London).

Kenning D.B.R. and Cooper M.G.(1989). Saturated Flow Boiling of Water in Vertical Tubes, Int.J. Heat Mass Transfer, 32(3),225-458

Kosky P.G. and Staub F.W.(1971). Local Condensing Heat Transfer Coefficients in the Annular Flow Regime, AIChE Journal, 17(5),1037-1043

Koumoutsos N., Moissis R. and Spyridonos A.(1968). A Study of Bubble Departure in Forced-Convection Boiling, Journal of Heat Transfer, Transactions of the ASME, 90C(2)

Levich V.G.(1962). Physicochemical Hydrodynamics, Chap.XII, Prentice-Hall Inc., Englewood Cliffs, New Jersey.

Liu Z. and Winterton R.H.S.(1988). Wet Wall Flow Boiling Correlation with Explicit Nucleate Term, 5th Miami Int. Symp. Multiphase Transport.

Lockhart R.W. and Martinelli R.C.(1949). Proposed Correlation of Data for Isothermal Two-Phase,Two-Component Flow in Pipes, Chemical Engineering Progrees, 45(1),39-48

Martin C.J. and Azzopardi B.J. (1985). Waves in Vertical Annular Flow. PCH PhysicoChemical Hydrodynamics, 6(1/2), pp.257-265

McAdams W.H. et al. (1949). Heat Transfer at High Rates to Water with Surface Boiling. Ind. Eng. Chem, 41,1945-1953.

Macbeth R.V., Trenberth R. and Wood R.W. (1971). An Investigation into the Effects of Crud Deposits on Surface Temperature, Dryout and Pressure Drop with Forced Convection Boiling of Water at 69 bar in an Annular Test Section. AEEW-R705

Mesler R.B.(1977). An Alternative to the Dengler and Addoms Convection Concept of Forced,Convection Boiling Heat Transfer, AIChE, 23(4),448-453

Mikic B.B. and Rohsenow W.M. (1969). Bubble Growth Rates in Non-uniform Temperature Field. Progress in Heat and Mass Transfer 2,283-293.

Mikic B.B. and Rohsenow W.M.(1969). A New Correlation of Pool-Boiling Data Including the effect of Heating Surface Characteristics, J. Heat Transfer, 91,245-250.

Mikic B.B., Rohsenow W.M. and Griffith P.(1970). On Bubble Growth Rates, Int.J. Heat Mass Transfer, 13,657-666, Pergamon Press .

Mudawwar A. and El-Masri M.A.(1986). Momentum and Heat Transfer Across Freely-Falling Turbulent Liquid Films, Int.J. Multiphase Flow. 12(5),771-790.

Owen D.G. and Hewitt G.F. (1987). An Improved Annular Two-phase Flow Model. Proceedings of the 3rd International Multiphase Flow Conference, The Hague, Netherland. Paper No. C1

Owen D.G.(1986). An Experimental and Theoretical Analysis of Equilibrium Annular Flows, PhD. Thesis, University of Birmingham.

Perry R.H. and Chilton C.H. (editors, 1973). Chemical Engineer's Handbook. 5th edition. McGraw-Hill Book Company.

Plesset M.S. and Zwick S.A.(1954). The Growth of Vapour Bubbles in Superheated Liquids, Journal of Applied Physics, 25(4)

Prandtl L., Z. Ver.(1933). Neuere Ergebnisse der Turbulenzforschung deut. Ing. 77,10

Rayleigh O.M. (1917). On the Pressure Developed in a Liquid during the Collapse of a Spherical Cavity, philos. Mag. 34(200),94-98

Robertson J.M. and Wadekar V.V. (Sept. 1988). Vertical Upflow Boiling of Ethanol in a 10 mm Diameter Tube. 2nd U.K. Nat. Conf. on Heat Transfer. Univ. Strathclyde, Glasgow U.K. IMechE, IChemE (Spons.) ISBN 0 85298 666 1, 1, 67-77, Paper No. C189/88.

Rohsenow W.M.(1970). Nucleation with Boiling Heat Transfer, ASME Symp. The Role of Nucleation in Boiling and Cavitation, Detroit, Paper 70-HT-18.

Saitoh T. and Shima A.(1977). Numerical Solution for the Spherical Bubble Growth Problem in a Uniformly Ultraheated Liquid, Journal Mechanical Engineering Science, 19(3).

Sato T. and Matsumura H. (1964). On the Conditions of Incipient Subcooled-Boiling and Forced-Convection. Bulletin of JSME, 7(36), 392-398.

Schrock V.E. and Grossman L.M.(1962). Forced Convection Boiling in Tubes, Nuclear Science and Engineering, 12,474-481.

Shah M.M. (1982). Chart Correlation for Saturated Boiling Heat Transfer : Equation and Further Study. ASHRAE Trans. 88,185-196.

Shah M.M.(1976). A New Correlation for Heat Transfer During Boiling Flow Through Pipes, ASHRAE Trans. 82(2), 66-86.

Singh A., Mikic B.B. and Rohsenow W.M.(1977). Effect of Superheat and Cavity Size on Frequency of Bubble Departure in Boiling, J.Heat Transfer, 99(2) Series C,246-249

Steiner D.(1988). Evaporation in Horizontal Tubes , in Multiphase Science and Technology , Vol.3 (Ed. Hewitt G.F., Delhaye J.M., Zuber N.) Hemisphere Publishing Corporation, New York.

Stephan K. and Abdelsalam. (1980). Heat Transfer Correlations for Natural Convection Boiling. Int. J. Heat Mass Transfer, 23,73-87.

Stephan K. and Auracher H.(1981). Correlation for Nucleate Boiling Heat Transfer in Forced Convection, Int.J. Heat Mass Transfer, 24,99-107

Stewart J.K. and Cole R.(1972). Bubble Growth Rates during Nucleate Boiling at High Jakob Numbers, Int.J. Heat Mass Transfer, 15,655-663, Pergamon Press.

Thirunavukkarasu K.(1970). Bubble Growth from a Cavity at a Solid Surface, ASME Symp. Detroit,paper 70-HT-13

Wallis G.B. (1961). Flooding Velocities for Air and Water in Vertical Tubes. U.K.A.E.A. Report No. AEEW-R123

Wallis G.B.(1970). Annular Two-Phase Flow-Part I, A Simple Theory and Part II. Additional Effects, J Basic Engng., 92,59-82

Whalley P.B. and Hewitt G.F.(1978). The Correlation of Liquid Entrainment Fraction and Entraiment Rate in Annular Two-Phase Flow, AERE R9187.

Whalley P.B. Hutchinson P. and Hewitt G.F. (1974). The Calculation of Critical Heat Flux in Forced Convection Boiling, Heat Transfer. 4,290-294, Scripta Book Co.

Whalley P.B.(1988). Boiling, Condensation and Gas-Liquid Flow, Oxford Engineering Science Series 21.

Whalley P.B., Azzopardi B.J., Pshyk L. (June 1977). Axial View Photography of Waves in Annular Two-Phase Flow, European Two-phase Flow Group Meeting, Grenoble, Paper No. A5, 26pp.

Wiegand J.H.(1945). Discussion of Paper by McMillen and Larson, Trans. AIChE, 41,147.

Winterton R.H.S.(1972). Sizes of Bubbles Produced by Dissolved Gas, Chem. Engng. Sci. 27,1223-1230.

Yin S.T. and Abdelmessih A.H.(1977). Prediction of Incipent Flow Boiling from a Uniformly Heated Surface, AICHE Symp. Ser., 73(164),236-243.

Missing References:

Gill L.E., Hewitt G.F. and Hitchon J.W. (1962), Sampling Probe Studies of the Gas core in Annular Two-phase Flow Part I the Effect of Length on Phase and Velocity Distribution. A.E.R.E. R - 3954

Witze C.P., Schrock V.E. and Chambre P.L. (1968),Flow about a Growing Sphere in Contact with a Plane Surface. Int. J. Heat Mass Transfer **11** pp 1637-1652

Brown D.J., Jensen A. and Whalley P.B. (1975), Non Equilibrium Effects in Heated and Unheated Annular Two-phase Flow. A.S.M.E. paper no. 75 - WA/HT7

NOMENCLATURE

Roman letters	Descriptions	Dimensions
A	channel cross sectional area	m^2
C	droplet concentration in gas core of annular flow	kg/m^3
C_d	drag coefficient	-
Co	parameter in Shah correlation	-
C_p	specific heat capacity	J/kgK
c	specific conductance	μS/cm
$\bar{c}$	molar concentration	$kmol/m^3$
D	tube diameter	m
D_1	annulus inner diameter	m
D_2	annulus outer diameter	m
D_d	droplet deposition rate	kg/m^2s
D_e	annulus equivalent diameter	m
D_h	hydraulic diameter	m
$\mathcal{D}_{AG}$	binary diffusivity of air and water vapour	m^2/s
d	bubble break-off diameter in liquid pool	m
d_1	diameter of centre pin of concentric conductance probe	m
d_2	outer diameter of insulation of concentric conductance probe	m
E	two-phase convective heat transfer enhancement factor defined by Gungor and Winterton (1985)	-
F	force	N

F	two-phase convective heat transfer enhancement factor defined by Chen (1963)	-
f	frequency	Hz
f	friction factor	-
f_i	interfacial friction factor in annular flow	-
f_{sgc}	friction factor for gas phase (in annular flow) flowing as a single-phase	-
G	conductance	μS
G_{xx}	auto spectral density function	V^2/Hz
G^*	dimensionless conductance	-
g	gravitational constant	m/s^2
$\mathcal{H}$	Henry's constant	atm.
h_{LG}	latent heat of evaporation	J/kg
I	current	amp.
k	droplet mass transfer coefficient	m/s
k	von Karman universal constant	-
k_{tp}	two-phase von Karman universal constant	-
$\dot{M}$	mass flow rate	kg/s
$\dot{M}_{LF}^+$	dimensionless liquid film flowrate	-
$\mathcal{M}$	molecular weight	kg/kmol
$\dot{m}$	mass flux	kg/m^2s
$\dot{m}_E$	liquid entrainment mass flux	kg/m^2s
$\dot{m}_{LFC}$	critical liquid film mass flux for entrainment incipience	kg/m^2s
$\dot{m}_{LF}$	liquid film mass flux	kg/m^2s
$\dot{n}$	molar flux	$kmol/m^2s$
n	number of cavities on surface	$1/m^2$

n_a	number of potentially active nucleation sites on surface	$1/m^2$
p	pressure	N/m^2
p_r	reduced pressure	-
$\dot{Q}$	heat transfer rate	W
$\dot{q}$	heat flux	W/m^2
R	bubble radius	m
R	resistance	kΩ
R_{12}	cross-correlation function	V^2
R_p	surface roughness specified according to Glättungstiefe DIN 4762	μm
$\mathcal{R}$	universal gas constant	J/kmol K
r	radial coordinate	m
r_c	radius of cavity mouth	m
r_m	radial position of zero shear stress in an annular channel	m
r_o	tube internal radius	m
S	channel wetted perimeter	m
S	suppression factor for nucleate flow boiling defined by Chen (1963)	-
T	temperature	K
T^+	dimensionless	-
ΔT_{sat}	wall superheat temperature	K
t	time	s
U	average velocity	m/s
U	radial velocity of bubble surface	m/s
U'	overall heat transfer coefficient	W/m^2K
u	local velocity	m/s
u^*	friction velocity	m/s
u^+	dimensionless velocity	-

v_G	specific volume of gas phase	m^3/kg
X_n	Martinelli parameter for turbulent liquid and turbulent gas two-phase flow	-
x	quality	-
x	mole fraction in liquid phase	-
x	signals of concentric conductance probe	V
y	distance from wall	m
$\bar{y}$	mole fraction in vapour phase	-
y^+	dimensionless distance parameter	-
z	axial distance	m

Dimensionless groups

Bo	Boiling number
Fr	Froude number
Gz	Graetz number
Ja	Jakob number
N	Nusselt number
Pe	Peclet number
Pr	Prandtl number
Re	Reynolds number
Sc	Schmidt number
Sh	Sherwood number
St	Stanton number
We	Weber number

Greek letters

α	heat transfer coefficient	W/m^2K
δ	film thickness	m
ε	volumetric fraction	-

ε_m	liquid eddy diffusivity of momentum	m^2/s
ε_h	liquid eddy diffusivity of heat	m^2/s
η	viscosity	kg/ms
θ	contact angle	degree
θ_o	equilibrium contact angle	degree
θ_a	advancing contact angle	degree
θ_r	receding contact angle	degree
κ	thermal diffusivity	m^2/s
λ	thermal conductivity	W/mK
μ_x	mean of concentric conductance probe signals	V
ρ	density	kg/m^3
σ	surface tension	kg/s^2
τ	shear stress	N/m^2
τ	displacement time	s
υ_L	liquid kinematic viscosity	m^2s
ϕ	cavity included angle	degree
ϕ_{Ltt}	two-phase pressure drop multiplier for turbulent gas and turbulent liquid	-

Subscripts

a	annulus
avg	average
B	bubble burst
b	bubble
b	buoyancy
C	gas core in annular flow
C	critical
con	convective
d	bubble departure

d	drag
E	equilibrium
F	friction
LF	liquid film
f	fully developed
G	gas phase
H	homogeneous
hs	heating section
i	nucleation incipience
i	inlet
i	inner
i	gas-liquid interface
int	bubble surface
L	liquid phase
lat	latent heat
max	maximum
np	nucleate pool boiling
nuc	nucleate boiling in forced flow
o	outlet
s	surface tension
sat	saturation
sen	sensible heat
ts	test section
w	wall